Intrinsic contributions to the anomalous Hall conductivity in multiband chiral superconductors

Author:
Mathew DENYS

Supervisor:
Dr. Philip BRYDON

A thesis submitted in fulfillment of the requirements for the degree of Master of Science

August 2020

Abstract

Intrinsic contributions to the anomalous Hall conductivity in multiband chiral superconductors

by Mathew DENYS

The anomalous Hall conductivity is a material property that can quantify time-reversal symmetry breaking in bulk materials. It is closely related to the polar Kerr effect, which is used as an experimental probe of such states, including in unconventional superconductors such as Sr_2RuO_4 and UPt_3. In such materials there is controversy as to the origin of the effect: is it due to an extrinsic mechanism such as scattering, or is the underlying mechanism intrinsic to the clean superconductor. Previous work in single-band models has indicated that an intrinsic contribution to the anomalous Hall conductivity is vanishing, and much of the theoretical literature has focussed on extrinsic contributions. However, recent work has shown that an intrinsic contribution is possible in multi-band superconductors. This thesis builds on previous work to develop an understanding as to the general conditions under which a two-band Hamiltonian will exhibit an anomalous Hall conductivity. Our results can be applied to explain experiments in order to gain insight into the pairing states of various unconventional superconductors. Substantial attention is paid towards strontium ruthenate as an illustrative model.

Acknowledgements

First and foremost, a massive shout out to Dr. Philip Brydon for everything you have done. For giving me a fascinating project, for answering my questions and explaining the same concepts week after week, and for all the miscellaneous life advice along the way. It has been a pleasure working with you. I would also like to acknowledge all of the other support I have received from within the physics department, especially from Bev and Sandra, and to thank all my friends and colleagues, in particular Peter and Emily for providing more than enough distraction whenever it was needed.

Thank you to my family: Mum, Dad, Kate, Anna, and I suppose Rocket too. I could not have chosen a better group of people to spend a six week lockdown with. Thank you Fiordland for providing me a place to escape to, and to Josephine for being there ever since I began my journey into physics five and a half years ago.

Contents

List of symbols and abbreviations

$\hat{a}_i^\dagger, \hat{a}_i$	electronic creation and annihilation operators	
$\mathcal{O}, \mathcal{U}, \mathcal{S}, \Theta$	operators (general, unitary, point-symmetry, time-reversal)	§1.2, §2.2
$\mathcal{H}, \mathcal{H}_0, \mathcal{H}^{\text{int}}, \mathcal{H}^{\text{MF}}$	Hamiltonians (full, normal state, interaction, mean-field)	(2.1), (2.2), (2.11)
$\mathcal{H}^\uparrow, \mathcal{H}^\downarrow$	"spin-up" and "spin-down" sectors of $\mathcal{H}$	§6.1.1
V	interaction potential of the electron–electron attraction	(2.2)
$f_{\nu,\boldsymbol{k},ij}$	pairing structure in the ν channel	(6.38)
$\lambda_{\nu\nu'}$	interaction strength between the ν and ν' channels	(6.38)
σ_i, η_i	Pauli matrices in spin and orbital space	§3
γ^n, γ^i	Gamma matrices (with and without including γ^0)	§4.1.1
Ψ, Ψ^e, Ψ^h	Nambu spinors (full, electron-only, hole-only)	(3.1), (5.18), (5.19)
H	Bogoliubov de Gennes Hamiltonian matrix	(2.16)
H_Δ	superconducting part of the BdG Hamiltonian	(5.32)
$H_0, \tilde{H}_0$	normal state BdG Hamiltonian (and its "flattened" form)	(2.1), (4.7), (4.8)
v^i, v^{ei}, v^{hi}	velocity matrices	(5.22), (5.9), (5.10)
$h_{\alpha\beta}\ [c_n]$	momentum coefficient of $\eta_\alpha \otimes \sigma_\beta$ normal-state matrix $[\gamma^n]$	(3.2), (4.7)
$\hat{h}_{\alpha\beta}\ [\hat{c}_n]$	flattened form of $h_{\alpha\beta}\ [c_n]$	(4.8)
$\Delta, \tilde{\Delta}$	the pairing potential and the transformed pairing potential	(2.8), (2.31)
$\Delta_{\alpha\beta}$	momentum coefficient of $\eta_\alpha \otimes \sigma_\beta$ pairing matrix	(3.3)
Δ_ν	the pairing potential in the ν channel	(6.42)
$\Delta_0, \Delta_{0,\nu}$	amplitude of the pairing potential (full, specific channel)	§3.4, (6.43)
$E, E_\pm, E_{\alpha\pm}$	single-particle eigenenergies (general, H_0, H)	(3.39), (6.31)
$\mathcal{G}$	Green's function corresponding to H	(5.23), (5.25)
$\mathcal{G}_0, \mathcal{G}_0^e, \mathcal{G}_0^h$	normal state Green's function (full, electron-part, hole-part)	(5.41)
N	number of lattice points ($= N_{\text{lat}}$ in Appendix A)	
β	$= 1/k_B T$ (k_B is Boltzmann's constant, T is temperature)	
T_c	critical temperature of the superconducting transition	
ω	angular frequency	
ω_n	Bose Matsubara frequency, $= 2n\pi/\beta$ for $n \in \mathbb{Z}$	
ν_m	Fermi Matsubara frequency, $= (2m+1)\pi/\beta$ for $m \in \mathbb{Z}$	
π	current-current correlator	(5.4)–(5.6)
σ, σ_H	conductivity tensor; Hall conductivity	§1.2.2, (5.1)
F_+, F_-	intra- and interband superconducting fitness	(4.19)
$\nu_{\mathcal{S}}$	the character of a given "object" under $\mathcal{S}$	§2.2
U_S	matrix describing the transformation of H_0 and $\tilde{\Delta}$ under $\mathcal{S}$	§2.2.1
TRSB	*time-reversal symmetry breaking*	p. 4
BdG	*Bogoliubov de Gennes*	p. 12
irrep	*irreducible representation*	p. 13
TROB	*time-reversal-odd bilinear*	p. 51

Chapter 1

Introduction

1.1 A brief overview of superconductivity

The phenomenon of superconductivity was first observed in 1911 by Heike Kamerlingh Onnes when he found that the electrical resistance of a sample of mercury abruptly dropped to zero when cooled below 4.2 K [1]. In the following decades the same behaviour was observed in a variety of other materials [2], and in 1933 Meissner and Ochsenfeld [3] discovered that superconducting samples of tin and lead expel magnetic fields. These two phenomena, vanishing electrical resistance and the expulsion of magnetic fields, are the defining characteristics of a superconducting state.

The microscopic origin of superconductivity remained a mystery for a long time, although a number of early phenomenological theories were put forward. The most successful of these were those constructed by Ginzburg and Landau [4] regarding the condensation energy of the superconducting state transition, and by London and London [5] regarding the expulsion of magnetic fields. The Ginzburg–Landau theory is still used as the basis of phenomenological descriptions of superconductivity to this day, in cases when a microscopic theory is impractical. In 1956 Leon Cooper published a seminal paper outlining a mechanism by which electrons in a crystal lattice could bind together into energetically favoured pairs [6]. This laid the road to a comprehensive microscopic theory known as BCS theory [7, 8], named after its creators, Bardeen, Cooper, and Schrieffer.

1.1.1 BCS theory

BCS theory applies to systems with a Fermi sea of weakly-interacting electrons in their normal state. Cooper showed that interactions between electrons and phononic excitations of the lattice could result in an *attractive* electron–electron interaction, as long as both electrons are within some particular energy of the Fermi surface [6]. While an attractive interaction in three dimensions does not lead to a bound state in general [9], the presence of a Fermi sea can be shown to imply that, no matter how small the attractive interaction, any electrons outside the occupied Fermi sea will pair together into stable bound states. These are referred to as Cooper pairs, and under the electron–phonon mechanism of BCS theory the most energetically favoured pairs are formed from electrons of opposite momentum and spin. Cooper pairs are bosons, so the ground state of a superconductor is one in which each pair is in the same lowest-energy state. This phenomenon is analogous to Bose–Einstein condensation, and results in a highly correlated system [9].

The formation of Cooper pairs destabilises the Fermi surface and results in an energy gap separating the paired states from those corresponding to free electrons, such that a finite amount of energy is required to break apart a Cooper pair. This is exemplified in Figure 1.1 A, where a single electronic energy band is present in the normal state because spin states are degenerate in

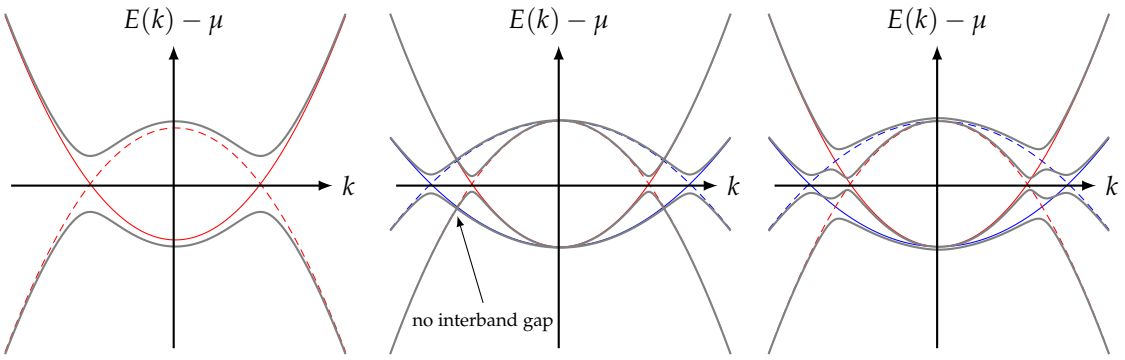

(A) Single band (B) Intraband pairing (C) Intra- and interband pairing

FIGURE 1.1: The normal state and superconducting state band structures of three one-dimensional toy models. Solid [dashed] red and blue lines indicate the normal state dispersion of electrons [holes]. Solid grey lines indicate quasiparticle dispersions in the superconducting state.

the absence of a magnetic field. In the superconducting state the excitations of the system are no longer electrons themselves, but rather quasiparticles composed of a superposition of electrons and their antiparticles, *holes* [9]. The superconducting dispersion arises from the hybridisation of the normal state electron and hole dispersions.

Due to the highly correlated nature of the BCS ground state, breaking one pair disturbs all other Cooper pairs, and therefore requires a significantly greater amount of energy than the binding energy of a single Cooper pair. For this reason it is the opening of the band gap that stabilises the superconducting state. In the presence of an electric field Cooper pairs may pick up a finite centre-of-mass momentum. They will no longer occupy their true ground state, but the system is still highly coherent. As the motion of one electron is correlated to the motion of all other paired electrons, it cannot easily be scattered into a different momentum state without a significant energy cost. This explains why electrical resistance drops to zero in the superconducting state.

1.1.2 Unconventional superconductivity

For many of the earliest discovered superconducting materials BCS theory provided accurate predictions, and seemed to be shaping up as a universally applicable theory. Significant deviations were first observed in the heavy fermion compounds [10, 11], which exhibited superconductivity despite localised magnetic moments that BCS theory predicted to be detrimental. In the 1980s superconductivity was observed in the "cuprates"[12, 13], a series of compounds sharing a copper-oxide structure. Some cuprates have critical temperatures on the order of 100 K, much larger than was thought possible at the time, and are hence referred to as "high-T_c" superconductors. Collectively, superconducting materials that do not obey BCS theory are said to be *unconventional* [14]. Other classes of unconventional superconductors include the heavy fermion superconductors [15, 16], the iron pnictides [17, 18], and the organic superconductors [19].

The microscopic origin of unconventional superconductivity remains an unsolved problem, but there has been success in explaining their behaviour using a classification scheme based on the different ways that electrons can bind into Cooper pairs. As electrons are fermions, one of the fundamental properties of Cooper pairs is that they must be *antisymmetric* under exchange of their constituent electrons. In conventional BCS theory the phonon mediated interaction leads to pairing states with an s-wave momentum dependence, which is *symmetric* under particle exchange [9]. For this reason, the two electrons must be paired in the spin-singlet configuration $|\uparrow\downarrow\rangle - |\downarrow\uparrow\rangle$,

such that the overall momentum-spin state is antisymmetric under particle exchange. Unconventional superconductors tend to arises from alternative pairing mechanisms, and as a result may permit the formation of Cooper pairs with different momentum dependences. Higher angular momentum pairing states (p-, d-, f-wave etc.) may be favoured so as to minimise the close-range Coulomb repulsion between electrons, and have been proposed to exist in various unconventional superconductors. For example, the cuprates are believed to be d-wave [20], and the heavy fermion superconductor UPt_3 is thought to have an f-wave state [21, 22].

If momentum and spin are the only degrees of freedom required to describe the Cooper pairs, fermionic antisymmetry requires that even-momentum states (s-, d-wave etc.) must be spin-singlet, while odd-momentum states (p-, f-wave etc.) must be spin-triplet (corresponding to the $|\uparrow\uparrow\rangle$, $|\uparrow\downarrow\rangle + |\downarrow\uparrow\rangle$, and $|\downarrow\downarrow\rangle$ states [23]). However, the electrons in some materials may be further differentiated by a third degree of freedom, such as the atomic orbital from which they originate [24–26], or a sublattice, layer, or valley degree of freedom [27–30]. For simplicity, I will always refer to this degree of freedom as an orbital one. In these systems the fermionic antisymmetry of the pairing state may be associated with the orbital degree of freedom, allowing for exotic pairing states. For example, a spin-triplet, s-wave state is allowed, as long as the orbital degree of freedom is antisymmetric with respect to particle exchange.

Unlike spin, orbital degrees of freedom tend to have non-degenerate states, leading to multiple energy bands. Further, the spin and orbital degrees of freedom are not typically good quantum numbers, which is to say that energy band eigenstates are a mixture of multiple orbital-spin states. The resulting Cooper pairs can be classified as being "intraband" or "interband", depending on which bands the electrons involved originate from. Intraband pairing is like conventional superconductivity in the sense that it opens band gaps across the Fermi surface, as shown for a two-band toy model in Figure 1.1 B. Interband pairing opens band gaps *away* from the Fermi surface, as shown in Figure 1.1 C. While the gap opened by intraband pairing is vital for stabilising the superconducting state, interband pairing is generally detrimental [31, 32].

1.2 Time-reversal symmetry

Symmetries play a major role in solid state physics, and in understanding unconventional superconductors in particular because a precise classification of the Cooper pairs is based on the symmetries that are broken by the superconducting state. These are typically crystal symmetries such as spatial inversion or rotation about a given axis, but states which break time-reversal symmetry are also possible. It could be argued that a more appropriate name here would be "motion-reversal", but at its core time-reversal is defined by its action of $t \to -t$. Time-reversal is *antiunitary* in nature, so is implemented in quantum theory by the operator $\Theta = \mathcal{U}_T\mathcal{K}$, where $\mathcal{U}_T$ is a unitary operator, and $\mathcal{K}$ is the complex conjugation operator [33]. If time is reversed particles will move in the opposite direction, and will hence have opposite momentum. Similarly, spin states are reversed, so we have

$$\Theta\,|\boldsymbol{k}\rangle = |-\boldsymbol{k}\rangle\,, \qquad \Theta\,|\uparrow\rangle = |\downarrow\rangle\,, \qquad \Theta\,|\downarrow\rangle = -\,|\uparrow\rangle\,, \tag{1.1}$$

where the factor of -1 in the last equation is due to the general result that $\Theta^2 = -1$ for systems of half-integer spin [33] (a general system must have $\Theta^2 = \pm 1$ as two successive applications of time-reversal will return us to the same physical state).

1.2.1 Time-reversal symmetry breaking and the polar Kerr effect

An operator $\mathcal{O}$ is said to be symmetric under time-reversal if $\Theta\mathcal{O}\Theta^{-1} = \mathcal{O}$, which is equivalent to saying that Θ and $\mathcal{O}$ commute. A physical system is symmetric under time-reversal if its Hamiltonian commutes with Θ. Equivalently, it breaks time-reversal symmetry if

$$\Theta\mathcal{H}\Theta^{-1} \neq \mathcal{H}. \tag{1.2}$$

This phenomenon is usually associated with magnetism, due to the action of time-reversal on spin states as given in (1.1). A magnetised system has a preferred spin direction, which is reversed under time-reversal.

Conventional (s-wave, spin-singlet) superconductors are inherently time-reversal symmetric because s-wave functions are even under the reversal of momentum, and (1.1) shows that the singlet state $|\uparrow,\downarrow\rangle - |\downarrow,\uparrow\rangle$ is symmetric under time-reversal. Unconventional superconductors, on the other hand, can form pairing states that break time-reversal symmetry [34]. Unfortunately, the experimental detection of time-reversal symmetry breaking (TRSB) in superconducting materials is complicated by the expulsion of magnetic fields mentioned in Section 1.1. Any intrinsic magnetic moment associated with the pairing state is screened such that the magnetic field is vanishing throughout the sample [35]. Although this screening is reduced at surfaces and defects, the measurable magnetic moment is weak, so we must resort to indirect probes [35, 36]. Muon spin relaxation has been developed as an experimental probe of the local magnetic environment of a material [37], and has detected TRSB in various superconductors [38, 39]. However, it is not always clear if the resulting signal is a bulk property or a localised effect about a defect. For this reason, it is desirable to have multiple complimentary experimental probes sensitive to TRSB. The detection of any magneto-optical effect, i.e. one arising from the interactions between photons and the spins of electrons, is an unambiguous indicator of TRSB in bulk materials [40]. The *polar Kerr effect*[1] is one such magneto-optical effect in which linearly-polarised, normally-incident light reflected from a TRSB material is elliptically polarised, and rotated by the Kerr angle [40, 41]

$$\theta_K = -\operatorname{Im}\left\{\frac{\tilde{N}_L - \tilde{N}_R}{\tilde{N}_L\tilde{N}_R - 1}\right\}, \tag{1.3}$$

where $\tilde{N}_L$ and $\tilde{N}_R$ are the complex indices of refraction of left- and right-circularly polarised light respectively. We see that a circularly birefringent material, i.e. one with $\tilde{N}_L \neq \tilde{N}_R$, is required to exhibit a non-zero Kerr angle, although it should be noted that (1.3) is in fact only valid if the difference between $\tilde{N}_L$ and $\tilde{N}_R$ is small. This circular birefringence is a result of TRSB [40]. In the context of superconductors we can use physically motivated approximations in the optical regime to write [41, 42]

$$\theta_K = \frac{4\pi}{\omega}\operatorname{Im}\left\{\frac{\sigma_H}{\tilde{n}(\tilde{n}^2 - 1)}\right\}, \tag{1.4}$$

where ω is the frequency of the incident light, σ_H is the antisymmetric part of the conductivity tensor (referred to as the Hall conductivity, and discussed in detail below), and $\tilde{n}$ is the complex refractive index of the material in the absence of any magneto-optical effect (i.e. the part of that does not contribute to the birefringence). The frequency dependence of the refractive index can lead to significant modulation of the Kerr angle, but (1.4) shows that the polar Kerr effect is observed if and only if the Hall conductivity is non-zero.

[1] More specifically this should be referred to as the *magneto-optic polar Kerr effect* so as not to be confused with the *electro-optic Kerr effect*, a non-linear optical effect in which an electric field affects the refractive index of a material.

1.2.2 Anomalous Hall conductivity

The current, $\boldsymbol{J}$, in a material is related to the electric field, $\boldsymbol{E}$, via $J_i = \sigma_{ij}E_j$, where σ is the conductivity tensor, and the Einstein summation convention applies to all repeated indices in this thesis. The off-diagonal elements of the conductivity can be written in terms of a symmetric and an antisymmetric tensor. The antisymmetric part is referred to as the *Hall conductivity*. In the context of an electromagnetic field propagating along the z axis, the electric field is restricted to the xy-plane, and we write

$$\sigma_H = \frac{\sigma_{xy} - \sigma_{yx}}{2}. \tag{1.5}$$

It is common to see σ_{xy} referred to as the Hall conductivity in the literature, although this is only consistent with (1.5) in the case that the conductivity tensor has no symmetric part. There are various underlying mechanisms that could lead to $\sigma_{xy} \neq \sigma_{yx}$, all of which require TRSB. For example, an applied magnetic field in the z direction can break time-reversal symmetry by lifting the degeneracy between spin-up and spin-down states. However, superconductors expel magnetic fields, so we are interested in the *anomalous* Hall conductivity, i.e. that which arises in the absence of an applied magnetic field.

In general, the Hall conductivity is dependent on both the frequency of the incident light and its wavevector, $\boldsymbol{q}$. The well known *Hall effect* [43] arises from the Hall conductivity in the $\boldsymbol{q} \to 0, \omega \to 0$ limit. For normally incident light the wavevector within the xy-plane is essentially zero, so we take the $\boldsymbol{q} \to \boldsymbol{0}$ limit in all calculations in this thesis. This is not entirely accurate as any finite-size incident beam will have an in-plane wavevector, but corrections due to this have been found to be negligible [42, 44]. Throughout this thesis we will also work in the "linear response regime", which is discussed in more detail in Chapter 5. This is equivalent to only considering single-particle contributions to the Hall conductivity. Higher order "vertex corrections" can contribute, but the energy scales involved are irrelevant to experimental endeavours [42].

While the breaking of time-reversal symmetry is a necessary condition for $\sigma_H \neq 0$, it is not sufficient. For example, the ($\boldsymbol{q} = \boldsymbol{0}$) external electric field only couples to the centre-of-mass momentum of Cooper pairs [26, 42], so if the TRSB is located in the relative momentum of the paired electrons there must be some mechanism by which this is coupled to the centre-of-mass coordinate. In a clean single-band superconductor these two coordinates are independent due to Galilean invariance [42]. In order to communicate TRSB in the pairing to the centre-of-mass coordinate, breaking of translation symmetry is required. This can be achieved by introducing impurities to the crystal lattice, and the resulting scattering can lead to an anomalous Hall conductivity via well understood mechanisms [34, 45–48]. Alternatively, in multiband superconductors, the relative and centre-of-mass coordinates are coupled [26], so it is feasible that a mechanism intrinsic to the clean superconductor can lead to an anomalous Hall conductivity [22, 26, 49–52]. In contrast to the impurity scattering mechanism, intrinsic contributions to the Hall conductivity are relatively poorly understood. It was recently proposed that an intrinsic contribution was dependent on the possibility of constructing a "time-reversal-odd bilinear" from the pairing potential, which was shown to neatly explain the Hall conductivity in a simple model of the honeycomb lattice [27]. The aim of this thesis is to generalise this result, so as to provide a better understanding as to the necessary conditions for an anomalous Hall conductivity in an arbitrary system. I take this general approach with the understanding that any specific results will depend on the details of a given system, such as the orbitals involved in the pairing. This inherently comes with many options, so I choose to also focus on a specific system, strontium ruthenate.

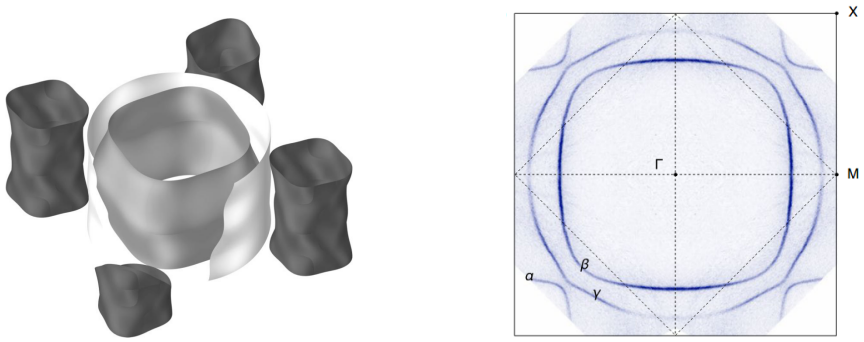

(A) 3D Fermi surface (modelled) (B) 2D cross-section (experimental)

FIGURE 1.2: The Fermi surface of strontium ruthenate consists of three bands, with only minor dispersion in the out-of-plane axis. (A) has out-of-plane dispersion exaggerated fifteen-fold. Reproduced from [35] and [55].

1.3 Strontium ruthenate[2]

Strontium ruthenate, Sr_2RuO_4, is a crystalline solid forming a tetragonal lattice belonging to the D_{4h} point symmetry group. It forms the same layered "perovskite" structure found in the undoped form of $La_{2-x}Ba_xCuO_4$, a high-T_c cuprate, which originally inspired investigation of strontium ruthenate as a superconductor. The normal state of strontium ruthenate behaves like a strongly two-dimensional Fermi liquid below 50 K [35, 53]; conductivity within the RuO_2 layers is of three orders of magnitude greater than the out-of-plane conductivity [53]. Three energy bands cross the Fermi energy, all of which derive from the Ru 4d orbitals. The "γ" band arises primarily from d_{xy} orbitals, while the "α" and "β" bands arise from hybridisation of d_{xz} and d_{yz}. Due to the highly two-dimensional nature of the normal state, these bands have very little dispersion in the out-of-plane axis, and form three nearly-cylindrical sheets [35, 54–56], as shown in Figure 1.2.

The superconducting transition in clean samples of strontium ruthenate occurs around 1.5 K [57], as shown in Figure 1.3. The exact critical temperature is strongly sensitive to the presence of impurities [58, 59], which is a strong indication that the superconductivity is unconventional [60]. The mechanism underlying Cooper pairing is thought to involve magnetic fluctuations, although phonon interactions may play a role [35, 61–63]. The superconducting state exhibits the same two-dimensional behaviour as the normal state, in the sense that the supercurrent is largely restricted to the RuO_2 plane. Ultrasonic probes of the strain tensor [64, 65] and tunnelling experiments [66] indicate that the superconducting state has two components. Multi-component states lend themselves to *chiral pairing states*, in which the relative phase between the two components winds as $\boldsymbol{k}$ is moved about a closed path across the Fermi surface. Chiral pairing states are TRSB, and indeed evidence from both muon spin relaxation [38] and polar Kerr experiments [40, 57] indicate that the superconducting state in strontium ruthenate breaks time-reversal. The TRSB coincides with the superconducting transition, as shown in Figure 1.3, and is observed in ultra-clean samples, indicating that it is likely to be intrinsic to the superconducting state, rather than the material or impurities respectively. This experimental evidence that strontium ruthenate exhibits an *intrinsic* anomalous Hall conductivity is backed up by theoretical work [26, 49, 50] and is the reason strontium ruthenate was chosen as an illustrative model for this thesis.

[2]For more discussions regarding strontium ruthenate, the interested reader is referred to the following highly informative review articles: "The superconductivty of Sr_2RuO_4 and the physics of spin-triplet pairing" by Mackenzie and Maeno [35], and "Chiral superconductors" by Kallin and Berlinsky [42].

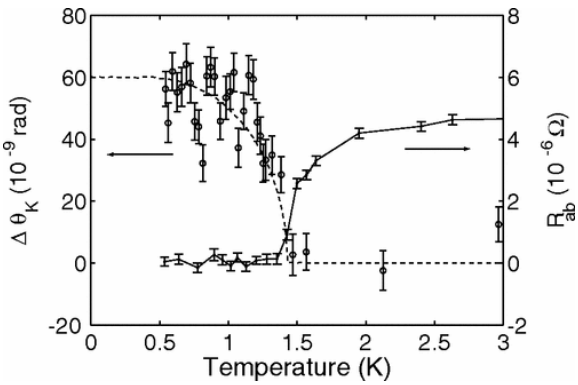

FIGURE 1.3: The conductivity (solid line) and Kerr angle (dashed line) of strontium ruthenate. We see that a non-zero Hall conductivity coincides with the superconducting transition. Reproduced from [57].

1.3.1 An ill-fated model

When I began work on this project the consensus in the literature was that the pairing in strontium ruthenate was likely to be a spin-triplet chiral p-wave state on the α and β bands [35, 67]. Specifically, it has been proposed that strontium ruthenate exhibits a "$k_x \pm ik_y$" pairing state, where k_x and k_y refer to the two p-wave components, and the chirality arises from the relative phase between these. This relative phase leads to a phase winding of $\pm 2\pi$ about the Fermi surface, and breaks time-reversal symmetry in the relative coordinate. In Chapter 3 I construct a model p-wave Hamiltonian using the Ru d_{xz} and d_{yz} orbitals. I restrict this model to two spatial dimensions, to reflect the highly two-dimensional nature of the pairing in strontium ruthenate. This is a simplified model as, for example, it completely neglects the d_{xy} orbital, but the hope was that it would be sophisticated enough to capture the important and relevant behaviour.

One of the core pieces of evidence for this pairing state was measurements of the spin susceptibility of the superconducting state, which indicated spin-triplet pairing [68–70]. However, recent work revisiting these measurements [71, 72] has cast serious doubt on the proposal of p-wave pairing in strontium ruthenate. Apart from having a massive impact in the community, this is unfortunate for us as it implies that our model is not physically justified. However, as strontium ruthenate was only chosen as an illustrative model, the core results of this thesis should apply broadly to more general systems anyway.

1.4 Outline

We begin in the next chapter with a general discussion of the mean-field theory of superconductivity. This includes a formal definition of the pairing potential, which describes the pairing state, and is directly related to the superconducting band gap. I take Section 2.2 to understand how the Hamiltonian transforms under point symmetry operations and time-reversal within the Bogoliubov de Gennes formalism. Chapter 3 focusses on constructing our model of strontium ruthenate, and Chapter 4 examines the stability of the various resulting pairing terms.

In Chapter 5 I derive some general results pertaining to the anomalous Hall conductivity. In particular, I derive a rather general formula in terms of bilinear products of the pairing potential. This applies within the high-frequency, small-gap limit, although I discuss its applicability away from this case. Calculations of the Hall conductivity within our model of strontium ruthenate are performed in Chapter 6, including application of the results of Chapter 5.

Chapter 2

Mean-field theory of superconductivity

In this chapter we begin our investigation by constructing a general superconducting Hamiltonian. Nothing in this chapter is particularly specific to strontium ruthenate. Once we have constructed the Hamiltonian I will dedicate some time to understanding its behaviour under various symmetry operations. These results are well known, and will be used in the next chapter in order to classify the terms that appear in our model of strontium ruthenate.

2.1 The superconducting Hamiltonian

We begin by writing the general Hamiltonian $\mathcal{H} = \mathcal{H}_0 + \mathcal{H}_{\text{int}}$, where [23, 73]

$$\mathcal{H}_0 = \sum_{\boldsymbol{k}} H_{0,\boldsymbol{k},\alpha_1\alpha_2}\, \hat{a}^\dagger_{\boldsymbol{k}\alpha_1} \hat{a}_{\boldsymbol{k}\alpha_2}, \tag{2.1}$$

$$\mathcal{H}_{\text{int}} = \frac{1}{2}\frac{1}{N} \sum_{\boldsymbol{k},\boldsymbol{k}'} V_{\boldsymbol{k},\boldsymbol{k}',\alpha_1\alpha_2,\alpha_3\alpha_4}\, \hat{a}^\dagger_{-\boldsymbol{k}\alpha_1} \hat{a}^\dagger_{\boldsymbol{k}\alpha_2} \hat{a}_{\boldsymbol{k}'\alpha_3} \hat{a}_{-\boldsymbol{k}'\alpha_4}, \tag{2.2}$$

$\hat{a}^\dagger_i$ and $\hat{a}_j$ are electronic creation and annihilation operators, N is the number of lattice points, the momentum summation covers the first Brillouin zone, and the Einstein summation convention applies to the α indices, which encapsulate the spin and any additional degrees of freedom. $\mathcal{H}_0$ is a single-particle "normal state" Hamiltonian, which can be derived from a tight-binding model in real-space. On the other hand, the interaction Hamiltonian is a two-particle operator. It describes the scattering of two opposite-momentum electrons (a Cooper pair) via the interaction potential, V, the details of which depend on the specific pairing mechanism. The factor of one half at the front of $\mathcal{H}_{\text{int}}$ is to avoid double counting due to the indistinguishably of electrons, so the $\frac{1}{2}\sum_{\boldsymbol{k}}$ in (2.2) should be interpreted as summing over half the Brillouin zone, rather than multiplying each eigenenergy by half.

The BCS Hamiltonian can be obtained as a limiting case of $\mathcal{H}$ by removing the additional degrees of freedom such that α_i encapsulate only spin, requiring the the spin indices in (2.1) to be the same, and taking $\alpha_1, \alpha_4 = \uparrow$ and $\alpha_2, \alpha_3 = \downarrow$ in (2.2). Additionally, BCS theory assumes the interaction potential is momentum-independent within a fixed energy of the Fermi surface (determined by the Debye frequency, a property of the crystal lattice), and vanishing outside this cutoff. In unconventional superconductivity there is much more freedom in the form of the interaction potential. In particular, the pairing mechanism does not necessarily have an energy cutoff, so we allow V to be non-zero across the entire Brillouin zone. However, there are still some physical results that place restrictions on its form. First of all, requiring $\mathcal{H}$ be Hermitian implies that

$$V_{\boldsymbol{k},\boldsymbol{k}',\alpha_1\alpha_2,\alpha_3\alpha_4} = V^*_{\boldsymbol{k}',\boldsymbol{k},\alpha_4\alpha_3,\alpha_2\alpha_1}, \tag{2.3}$$

which can be seen by taking the conjugate transpose of (2.2), then exchanging $\alpha_1 \leftrightarrow \alpha_4$, $\alpha_2 \leftrightarrow \alpha_3$, and $\boldsymbol{k} \leftrightarrow \boldsymbol{k}'$. Additionally, the creation and annihilation operators obey the fermionic anticommutation relations $\{\hat{a}_i, \hat{a}_j\} = \{\hat{a}_i^\dagger, \hat{a}_j^\dagger\} = 0$. These imply that

$$V_{\boldsymbol{k},\boldsymbol{k}',\alpha_1\alpha_2,\alpha_3\alpha_4} = -V_{-\boldsymbol{k},\boldsymbol{k}',\alpha_2\alpha_1,\alpha_3\alpha_4} = -V_{\boldsymbol{k},-\boldsymbol{k}',\alpha_1\alpha_2,\alpha_4\alpha_3}, \tag{2.4}$$

which is seen from (2.2) by exchanging $\{-\boldsymbol{k}, \alpha_1\} \leftrightarrow \{\boldsymbol{k}, \alpha_2\}$ and $\{-\boldsymbol{k}', \alpha_3\} \leftrightarrow \{\boldsymbol{k}', \alpha_4\}$ respectively.

2.1.1 The mean-field approximation

As it stands, this Hamiltonian is difficult to solve, in the sense of calculating eigenstates and eigenvalues. For this reason the standard approach is to perform a mean-field decoupling of the interaction term, which is achieved by writing

$$\hat{a}^\dagger_{-\boldsymbol{k}\alpha_1}\hat{a}^\dagger_{\boldsymbol{k}\alpha_2} = \langle \hat{a}^\dagger_{-\boldsymbol{k}\alpha_1}\hat{a}^\dagger_{\boldsymbol{k}\alpha_2}\rangle + \hat{\delta}, \tag{2.5}$$

$$\hat{a}_{\boldsymbol{k}'\alpha_3}\hat{a}_{-\boldsymbol{k}'\alpha_4} = \langle \hat{a}_{\boldsymbol{k}'\alpha_3}\hat{a}_{-\boldsymbol{k}'\alpha_4}\rangle + \hat{\epsilon}, \tag{2.6}$$

where $\langle\cdot\rangle$ denotes a thermal average. The expectation values in (2.5) and (2.6) are called *anomalous averages* because they would be vanishing when taken with respect to a state with a definite number of electrons. As a highly coherent system, the superconducting state can be written as the superposition of states with different numbers of Cooper pairs, so we can expect the anomalous averages to be non-vanishing. The "fluctuation operators", $\hat{\delta}$ and $\hat{\epsilon}$, describe how the operator products on the LHS of (2.5) and (2.6) differ from their corresponding anomalous averages. Together, (2.5) and (2.6) can be used to write the operator product in (2.2) as

$$\begin{aligned}\hat{a}^\dagger_{-\boldsymbol{k}\alpha_1}\hat{a}^\dagger_{\boldsymbol{k}\alpha_2}\hat{a}_{\boldsymbol{k}'\alpha_3}\hat{a}_{-\boldsymbol{k}'\alpha_4} &= \langle \hat{a}^\dagger_{-\boldsymbol{k}\alpha_1}\hat{a}^\dagger_{\boldsymbol{k}\alpha_2}\rangle\langle \hat{a}_{\boldsymbol{k}'\alpha_3}\hat{a}_{-\boldsymbol{k}'\alpha_4}\rangle + \langle \hat{a}_{\boldsymbol{k}'\alpha_3}\hat{a}_{-\boldsymbol{k}'\alpha_4}\rangle\hat{\delta} + \langle \hat{a}^\dagger_{-\boldsymbol{k}\alpha_1}\hat{a}^\dagger_{\boldsymbol{k}\alpha_2}\rangle\hat{\epsilon} + \hat{\delta}\,\hat{\epsilon} \\ &\approx \langle \hat{a}^\dagger_{-\boldsymbol{k}\alpha_1}\hat{a}^\dagger_{\boldsymbol{k}\alpha_2}\rangle\langle \hat{a}_{\boldsymbol{k}'\alpha_3}\hat{a}_{-\boldsymbol{k}'\alpha_4}\rangle + \langle \hat{a}_{\boldsymbol{k}'\alpha_3}\hat{a}_{-\boldsymbol{k}'\alpha_4}\rangle\hat{\delta} + \langle \hat{a}^\dagger_{-\boldsymbol{k}\alpha_1}\hat{a}^\dagger_{\boldsymbol{k}\alpha_2}\rangle\hat{\epsilon},\end{aligned}$$

where we have used the *mean-field approximation* by assuming that the fluctuations about the mean-field are small, and hence the $\hat{\delta}\,\hat{\epsilon}$ product can be safely ignored. While the mean-field approximation often over-estimates the critical temperature and other details of the transition, it tends to describe the electronic states in the superconducting phase well. We do not know how to deal with the fluctuation operators, but we can invert (2.5) and (2.6) to obtain $\hat{\delta} = \hat{a}^\dagger_{-\boldsymbol{k}\alpha_1}\hat{a}^\dagger_{\boldsymbol{k}\alpha_2} - \langle \hat{a}^\dagger_{-\boldsymbol{k}\alpha_1}\hat{a}^\dagger_{\boldsymbol{k}\alpha_2}\rangle$, and similarly for $\hat{\epsilon}$, which gives

$$\hat{a}^\dagger_{-\boldsymbol{k}\alpha_1}\hat{a}^\dagger_{\boldsymbol{k}\alpha_2}\hat{a}_{\boldsymbol{k}'\alpha_3}\hat{a}_{-\boldsymbol{k}'\alpha_4} = \langle \hat{a}^\dagger_{-\boldsymbol{k}\alpha_1}\hat{a}^\dagger_{\boldsymbol{k}\alpha_2}\rangle\,\hat{a}_{\boldsymbol{k}'\alpha_3}\hat{a}_{-\boldsymbol{k}'\alpha_4} + \langle \hat{a}_{\boldsymbol{k}'\alpha_3}\hat{a}_{-\boldsymbol{k}'\alpha_4}\rangle\,\hat{a}^\dagger_{-\boldsymbol{k}\alpha_1}\hat{a}^\dagger_{\boldsymbol{k}\alpha_2} - \langle \hat{a}^\dagger_{-\boldsymbol{k}\alpha_1}\hat{a}^\dagger_{\boldsymbol{k}\alpha_2}\rangle\langle \hat{a}_{\boldsymbol{k}'\alpha_3}\hat{a}_{-\boldsymbol{k}'\alpha_4}\rangle.$$

Substituting this expression into (2.2), we define the mean-field interaction Hamiltonian as

$$\begin{aligned}\mathcal{H}^{\mathrm{MF}}_{\mathrm{int}} = \frac{1}{2}\frac{1}{N}\sum_{\boldsymbol{k},\boldsymbol{k}'} V_{\boldsymbol{k},\boldsymbol{k}',\alpha_1\alpha_2,\alpha_3\alpha_4}\Big(&\langle \hat{a}^\dagger_{-\boldsymbol{k}\alpha_1}\hat{a}^\dagger_{\boldsymbol{k}\alpha_2}\rangle\,\hat{a}_{\boldsymbol{k}'\alpha_3}\hat{a}_{-\boldsymbol{k}'\alpha_4} \\ &+ \langle \hat{a}_{\boldsymbol{k}'\alpha_3}\hat{a}_{-\boldsymbol{k}'\alpha_4}\rangle\,\hat{a}^\dagger_{-\boldsymbol{k}\alpha_1}\hat{a}^\dagger_{\boldsymbol{k}\alpha_2} - \langle \hat{a}^\dagger_{-\boldsymbol{k}\alpha_1}\hat{a}^\dagger_{\boldsymbol{k}\alpha_2}\rangle\,\langle \hat{a}_{\boldsymbol{k}'\alpha_3}\hat{a}_{-\boldsymbol{k}'\alpha_4}\rangle\Big).\end{aligned} \tag{2.7}$$

The pairing potential: One of the core features of the mean-field theory of superconductivity is the *pairing potential*, which is essentially the expectation value of the annihilation of a Cooper pair,

and is defined component-wise as [23]

$$\Delta_{\boldsymbol{k},ij} = -\frac{1}{N}\sum_{\boldsymbol{k}'} V_{\boldsymbol{k},\boldsymbol{k}',ji,\alpha_3\alpha_4}\langle \hat{a}_{\boldsymbol{k}'\alpha_3}\hat{a}_{-\boldsymbol{k}'\alpha_4}\rangle. \tag{2.8}$$

The pairing potential can have an overall phase, but this can never be experimentally observed, so we have freedom over the overall phase of $\Delta_{\boldsymbol{k}}$ when describing measurable phenomena such as the Hall conductivity. Additionally, in order to satisfy the fermionic exchange antisymmetry, (2.4), the pairing potential must satisfy

$$\Delta_{\boldsymbol{k},ij} = -\Delta_{-\boldsymbol{k},ji}. \tag{2.9}$$

2.1.2 The Bogoliubov de Gennes Hamiltonian

If we take the complex conjugate of (2.8), apply (2.3), and relabel indices, we obtain

$$\Delta^*_{\boldsymbol{k},ij} = -\frac{1}{N}\sum_{\boldsymbol{k}'} V_{\boldsymbol{k}',\boldsymbol{k},\alpha_1\alpha_2,ij}\langle \hat{a}^\dagger_{-\boldsymbol{k}'\alpha_1}\hat{a}^\dagger_{\boldsymbol{k}'\alpha_2}\rangle. \tag{2.10}$$

Substituting (2.8) and (2.10) into the mean-field interaction Hamiltonian (2.7), making use of (2.9), taking $\boldsymbol{k} \to -\boldsymbol{k}$ in the first two terms, and relabelling indices to be consistent, we find

$$\mathcal{H}^{\mathrm{MF}}_{\mathrm{int}} = \frac{1}{2}\sum_{\boldsymbol{k}}\left(\Delta^*_{\boldsymbol{k},\alpha_2\alpha_1}\hat{a}_{-\boldsymbol{k}\alpha_1}\hat{a}_{\boldsymbol{k}\alpha_2} + \Delta_{\boldsymbol{k},\alpha_1\alpha_2}\hat{a}^\dagger_{\boldsymbol{k}\alpha_1}\hat{a}^\dagger_{-\boldsymbol{k}\alpha_2} + \Delta_{\boldsymbol{k},\alpha_2\alpha_1}\langle \hat{a}^\dagger_{-\boldsymbol{k}\alpha_1}\hat{a}^\dagger_{\boldsymbol{k}\alpha_2}\rangle\right). \tag{2.11}$$

We can also play some tricks on the form of the normal state Hamiltonian. We begin by using the anticommutation property $\{\hat{a}^\dagger_i, \hat{a}_j\} = \delta_{ij}$ to write

$$\mathcal{H}_0 = \frac{1}{2}\sum_{\boldsymbol{k}} H_{0,\boldsymbol{k},\alpha_1\alpha_2}\left(\hat{a}^\dagger_{\boldsymbol{k}\alpha_1}\hat{a}_{\boldsymbol{k}\alpha_2} + \delta_{\alpha_1\alpha_2} - \hat{a}_{\boldsymbol{k}\alpha_2}\hat{a}^\dagger_{\boldsymbol{k}\alpha_1}\right), \tag{2.12}$$

where $\frac{1}{2}\sum_{\boldsymbol{k}}$ is to be interpreted as a sum over half the first Brillouin zone, just as in $\mathcal{H}_{\mathrm{int}}$. Then, by taking $\boldsymbol{k} \to -\boldsymbol{k}$ in the last term and applying fermionic anticommutation, we obtain

$$\mathcal{H}_0 = \frac{1}{2}\sum_{\boldsymbol{k}}\left(H_{0,\boldsymbol{k},\alpha_1\alpha_2}\hat{a}^\dagger_{\boldsymbol{k}\alpha_1}\hat{a}_{\boldsymbol{k}\alpha_2} - H_{0,-\boldsymbol{k},\alpha_1\alpha_2}\hat{a}_{-\boldsymbol{k}\alpha_2}\hat{a}^\dagger_{-\boldsymbol{k}\alpha_1} + H_{0,\boldsymbol{k}\alpha_1\alpha_1}\right). \tag{2.13}$$

At this point, keeping track of the indices will be getting under any sane reader's skin, so it is the perfect time to introduce some convenient notation. In order to do this, note that the last term in each of (2.11) and (2.13) corresponds to a constant energy offset, so do not contribute to the dynamics of the system. It is conventional to neglect them, and to redefine the mean-field Hamiltonian as

$$\mathcal{H}^{\mathrm{MF}} = \frac{1}{2}\sum_{\boldsymbol{k}}\left(H_{0,\boldsymbol{k},\alpha_1\alpha_2}\hat{a}^\dagger_{\boldsymbol{k}\alpha_1}\hat{a}_{\boldsymbol{k}\alpha_2} - H_{0,-\boldsymbol{k},\alpha_2\alpha_1}\hat{a}_{-\boldsymbol{k}\alpha_1}\hat{a}^\dagger_{-\boldsymbol{k}\alpha_2} + \Delta^*_{\boldsymbol{k},\alpha_2\alpha_1}\hat{a}_{-\boldsymbol{k}\alpha_1}\hat{a}_{\boldsymbol{k}\alpha_2} + \Delta_{\boldsymbol{k},\alpha_1\alpha_2}\hat{a}^\dagger_{\boldsymbol{k}\alpha_1}\hat{a}^\dagger_{-\boldsymbol{k}\alpha_2}\right). \tag{2.14}$$

It is rather straightforward to verify that (2.14) can be written as

$$\mathcal{H}^{\mathrm{MF}} = \frac{1}{2}\sum_{\boldsymbol{k}} \Psi^\dagger_{\boldsymbol{k}} H_{\boldsymbol{k}} \Psi_{\boldsymbol{k}}, \tag{2.15}$$

where

$$H_{\boldsymbol{k}} = \begin{pmatrix} H_{0,\boldsymbol{k}} & \Delta_{\boldsymbol{k}} \\ \Delta^\dagger_{\boldsymbol{k}} & -H^T_{0,-\boldsymbol{k}} \end{pmatrix} \tag{2.16}$$

is the *Bogoliubov de Gennes (BdG) Hamiltonian*, and

$$\Psi_k = \begin{pmatrix} \hat{a}_{k\alpha_1} & \dots & \hat{a}_{k\alpha_n} & \hat{a}^\dagger_{-k\alpha_1} & \dots & \hat{a}^\dagger_{-k\alpha_n} \end{pmatrix}^T \tag{2.17}$$

is the *Nambu spinor*. Physically, the first n terms in Ψ_k correspond to the annihilation of electrons, while the last n correspond to the annihilation of holes. The block diagonal elements of H_k describe single-electron and single-hole dynamics respectively.

If desired, we could diagonalise H_k in order to solve for its eigenstates and eigenvalues. I will not go to the trouble of doing this analytically here, although it is done numerically for some specific models in later chapters. Instead, to exemplify some core results, I will briefly limit the discussion to BCS theory, in which case we have [9]

$$\mathcal{H}_k^{\text{BCS}} = \begin{pmatrix} \hat{a}^\dagger_{k\uparrow} & \hat{a}_{-k\downarrow} \end{pmatrix} \begin{pmatrix} \xi_k & \Delta \\ \Delta^* & -\xi_k \end{pmatrix} \begin{pmatrix} \hat{a}_{k\uparrow} \\ \hat{a}^\dagger_{-k\downarrow} \end{pmatrix}, \tag{2.18}$$

where $\xi_k = \epsilon_k - \mu$, ϵ_k is the normal state dispersion, μ is the chemical potential, and Δ is a momentum-independent pairing potential. This can be diagonalised to give

$$\mathcal{H}_k^{\text{BCS}} = \begin{pmatrix} \hat{\gamma}^\dagger_{k\uparrow} & \hat{\gamma}_{-k\downarrow} \end{pmatrix} \begin{pmatrix} E_k & 0 \\ 0 & -E_k \end{pmatrix} \begin{pmatrix} \hat{\gamma}_{k\uparrow} \\ \hat{\gamma}^\dagger_{-k\downarrow} \end{pmatrix}, \tag{2.19}$$

where $\hat{\gamma}_i^\dagger$ and $\hat{\gamma}_j$ correspond to the creation and annihilation of particle-hole quasiparticles with energies determined by

$$E_k = \sqrt{\xi_k^2 + |\Delta|^2}. \tag{2.20}$$

We see that, no matter the value of ξ_k, there will always be a band gap of $2|\Delta|$ about $E = \mu$, as was shown in Figure 1.1 A. Note that the phase of the pairing potential does not enter this expression. In this context the pairing potential is usually referred to as the "gap function", or just "the gap". I will use these terms somewhat interchangeably throughout this thesis. Further, (2.19) indicates that the many-particle Hamiltonian $\mathcal{H}$ has been reduced to a single-particle Hamiltonian, which was achieved by the mean-field approximation.

Both of these results can be generalised away from BCS theory and applied to (2.15). From this point on we deal exclusively with the single-particle problem by working with H_0 and Δ rather than $\mathcal{H}^{\text{MF}}$. It is important to note that H_0 and Δ are not operators in Fock space as $\mathcal{H}$ is, but rather matrices of (momentum-dependent) c-numbers; (2.15) is just a convenient shorthand for (2.14), and the matrix notation used here should not be mistaken as representing many-particle operators.

2.2 Point groups and irreducible representations

At this point I will take a lengthy aside to discuss point symmetries. The concepts introduced here will be used extensively in Chapter 3 in particular, as a means of classifying terms in the BdG Hamiltonian. A symmetry operation is any operation that leaves a given object or system unchanged. We restrict ourselves to spatial symmetries: those which affect the position or orientation of a system in space. Further, we restrict ourselves to *point symmetry operations*, which leave at least one coordinate fixed. These include rotations, reflections, inversion, and rotoinversions. All point symmetry operations can be implemented in quantum theory by unitary operators.

A *point group* is a mathematical group (satisfying the axioms of Closure, Associativity, Identity, and Inverse), the elements of which are point symmetry operations. In crystallography the set

of relevant point groups is restricted by the condition that they leave an entire periodic lattice invariant. There are a theoretically infinite number of point groups in three dimensions, but only 32 such *crystallographic point groups* [74]. To take a concrete example, which will be used extensively in this thesis due to its application to strontium ruthenate, consider the D_{4h} point group which contains the following set of symmetry operations:

$$\{E, 2\mathcal{C}_4, \mathcal{C}_2, \mathcal{C}_2', 2\mathcal{C}_2'', \mathcal{I}, 2\mathcal{S}_4, \sigma_h, 2\sigma_v, 2\sigma_d\}, \tag{2.21}$$

which can be combined via the operation of composition. E is the identity, $2\mathcal{C}_4$ are clockwise and counter-clockwise $\frac{\pi}{2}$ rotations about the z axis, $\mathcal{C}_2$ is a π rotation about the z axis, $2\mathcal{C}_2'$ are π rotations about the x and y axes, $2\mathcal{C}_2''$ are π rotations about the $x = y$ and $x = -y$ axes, $\mathcal{I}$ is inversion, $2\mathcal{S}_4$ are rotoinversions constructed from the $2\mathcal{C}_4$ rotations, σ_h is reflection in the $z = 0$ plane, $2\sigma_v$ are reflections in the $x = 0$ and $y = 0$ planes, and $2\sigma_d$ are reflections in the $x = y$ and $x = -y$ planes.

Each symmetry in D_{4h} can be constructed via the composition of three *generating symmetries*. The canonical choices are $\mathcal{C}_4, \mathcal{C}_2'$, and $\mathcal{I}$ (it does not matter which of the $\mathcal{C}_4$ and $\mathcal{C}_2'$ operations are chosen; we take $\mathcal{C}_4$ to be counter-clockwise, and $\mathcal{C}_2'$ to be about the x axis), although there are other possibilities such as $\{\mathcal{S}_4, \mathcal{I}, \sigma_v\}$. We say that a crystal lattice "belongs to D_{4h}" if it is invariant under each of the symmetry operations listed in (2.21), although it is sufficient to show that its unit cell is invariant under just the generating symmetries. This is the case for strontium ruthenate [35].

Given a group G, we say that the set of functions (or matrices, or whatever object you want to deal with) $\{\psi_i\}$ forms a basis of an *irreducible representation* (irrep) of G if the application of any $g \in G$ to ψ_i, denoted $g : \psi_i$, can be written as a linear combination of the elements of $\{\psi_i\}$ [23]. For example, the Cartesian functions $\{x, y\}$ form the basis of an irreducible representation of D_{4h}, since the generating symmetries of D_{4h} act on these spatial coordinates as

$$\begin{aligned} \mathcal{C}_4 &: x = y, & \mathcal{C}_4 &: y = -x, \\ \mathcal{C}_2' &: x = x, & \mathcal{C}_2' &: y = -y, \\ \mathcal{I} &: x = -x, & \mathcal{I} &: y = -y. \end{aligned}$$

In the $\{x, y\}$ basis we can represent these symmetry operations as unitary matrices. For example,

$$\mathcal{C}_4 \doteq \begin{pmatrix} 0 & 1 \\ -1 & 0 \end{pmatrix}, \qquad \mathcal{C}_2' \doteq \begin{pmatrix} 1 & 0 \\ 0 & -1 \end{pmatrix}, \qquad \mathcal{I} \doteq \begin{pmatrix} -1 & 0 \\ 0 & -1 \end{pmatrix}.$$

The *character* of this irrep under each of these generating symmetries is defined as the trace of the respective matrix, i.e.

$$\nu_{\mathcal{C}_4} = \mathrm{Tr}\left\{\begin{pmatrix} 0 & 1 \\ -1 & 0 \end{pmatrix}\right\} = 0, \quad \nu_{\mathcal{C}_2'} = \mathrm{Tr}\left\{\begin{pmatrix} 1 & 0 \\ 0 & -1 \end{pmatrix}\right\} = 0, \quad \nu_{\mathcal{I}} = \mathrm{Tr}\left\{\begin{pmatrix} -1 & 0 \\ 0 & -1 \end{pmatrix}\right\} = -2.$$

These characters uniquely determine the irreducible representation to which $\{x, y\}$ form a basis of. If we instead used the basis $\{x + y, x - y\}$ for example, we would still find $\nu_{\mathcal{C}_4} = 0$, $\nu_{\mathcal{C}_2'} = 0$, and $\nu_{\mathcal{I}} = -2$, and any other set of functions with the same set of characters belongs to the same irrep. We label this irrep in particular as E_u. Table 2.1 lists all the irreducible representations of D_{4h}, along with their character under each symmetry operation in D_{4h}. This is referred to as the character table of D_{4h}. The character of a given irrep under the identity operation E de facto tells us the dimension of the irrep, i.e. how many basis elements it has. We see that D_{4h} has only one- and two-dimensional irreps. When dealing with one-dimensional irreps the character simply tells us if

Irrep	E	$2C_4$	C_2	$2C_2'$	$2C_2''$	I	$2S_4$	$2\sigma_v$	$2\sigma_d$	σ_h
A_{1g}	1	1	1	1	1	1	1	1	1	1
A_{2g}	1	1	1	-1	-1	1	1	1	-1	-1
B_{1g}	1	-1	1	1	-1	1	-1	1	1	-1
B_{2g}	1	-1	1	-1	1	1	-1	1	-1	1
E_g	2	0	-2	0	0	2	0	-2	0	0
A_{1u}	1	1	1	1	1	-1	-1	-1	-1	-1
A_{2u}	1	1	1	-1	-1	-1	-1	-1	1	1
B_{1u}	1	-1	1	1	-1	-1	1	-1	-1	1
B_{2u}	1	-1	1	-1	1	-1	1	-1	1	-1
E_u	2	0	-2	0	0	-2	0	2	0	0

TABLE 2.1: The D_{4h} character table. Highlighted columns correspond to canonical generating symmetries, as discussed in the text.

the basis function is even or odd under the given symmetry operation. The meaning behind the labels for the irreps is ultimately unimportant for our purposes, although it is useful to note that g and u subscripts refer to the German words "gerade" and "ungerade", which translate to "even" and "odd". These refer to the character of the basis elements under inversion. Table 2.2 lists some possible bases for various D_{4h} irreps. Different bases are appropriate in for different applications; I have presented some simple possibilities chosen from Cartesian products and sinusoidal functions.

2.2.1 Transformation of H_0 and Δ under symmetry operations

With that crash course in symmetry operations and irreducible representations under our belt, we can apply these ideas to superconductivity. When dealing with the BdG Hamiltonian, a sensible question to ask is *how do point symmetry operations act on H_0 and Δ?* Answering this question will allow us to examine how H_0 and Δ behave under these symmetries within our model of strontium ruthenate in Chapter 3. Let us begin with the behaviour of $\mathcal{H}^{\mathrm{MF}}$ under *some* point symmetry operation $\mathcal{S}$, which acts on the creation and annihilation operators in Ψ_k to give

$$\mathcal{S}\mathcal{H}^{\mathrm{MF}}\mathcal{S}^{-1} = \frac{1}{2}\sum_k \mathcal{S}\Psi_k^\dagger\mathcal{S}^{-1}\, H_k\, \mathcal{S}\Psi_k\mathcal{S}^{-1}. \tag{2.22}$$

In order to understand how the spinor Ψ_k transforms under $\mathcal{S}$, let us first consider how a single creation operator is transformed. We approach this by considering the action of $\mathcal{S}$ on an electronic state. For simplicity, we will temporarily ignore the "additional" degrees of freedom. These can

Irrep	s	p	d	f	Sinusoidal
A_{1g}	1		$x^2+y^2+z^2$		$\cos x + \cos y$
A_{2g}					
B_{1g}			x^2-y^2		$\cos x - \cos y$
B_{2g}			xy		$\sin x \sin y$
E_g			$\{xz, yz\}$		
A_{1u}					
A_{2u}		z		z^3	$\sin z$
B_{1u}				xyz	
B_{2u}				$z(x^2-y^2)$	
E_u		$\{x, y\}$			$\{\sin x, \sin y\}$

TABLE 2.2: The symmetries of select Cartesian products and sinusoidal functions in D_{4h}. The Cartesian products are differentiated by the angular momentum of their corresponding spherical harmonics.

easily be reintroduced at the end as a generalisation of the result we will obtain, but for now we take spin to be the only internal degree of freedom. As an example we can write, quite generally, the action of $\mathcal{S}$ on a spin up state as

$$\mathcal{S}\left|\boldsymbol{k},\uparrow\right\rangle = c_{\boldsymbol{k},\uparrow\uparrow}\left|\mathcal{S}:\boldsymbol{k},\uparrow\right\rangle + c_{\boldsymbol{k},\uparrow\downarrow}\left|\mathcal{S}:\boldsymbol{k},\downarrow\right\rangle,$$

where the c coefficients are c-numbers, and $\mathcal{S}:\boldsymbol{k}$ denotes the transformation of the wavevector $\boldsymbol{k}$ under $\mathcal{S}$. To proceed, we write $\left|\boldsymbol{k},\alpha\right\rangle = \hat{a}^\dagger_{\boldsymbol{k}\alpha}\left|0\right\rangle$, where $\left|0\right\rangle$ is the vacuum state, which will be unaffected by $\mathcal{S}$:

$$\begin{aligned}
\mathcal{S}\hat{a}^\dagger_{\boldsymbol{k}\uparrow}\left|0\right\rangle &= c_{\boldsymbol{k},\uparrow\uparrow}\,\hat{a}^\dagger_{\mathcal{S}:\boldsymbol{k}\uparrow}\left|0\right\rangle + c_{\boldsymbol{k},\uparrow\downarrow}\,\hat{a}^\dagger_{\mathcal{S}:\boldsymbol{k}\downarrow}\left|0\right\rangle,\\
\mathcal{S}\hat{a}^\dagger_{\boldsymbol{k}\uparrow}\mathcal{S}^{-1}\mathcal{S}\left|0\right\rangle &= \left(c_{\boldsymbol{k},\uparrow\uparrow}\,\hat{a}^\dagger_{\mathcal{S}:\boldsymbol{k}\uparrow} + c_{\boldsymbol{k},\uparrow\downarrow}\,\hat{a}^\dagger_{\mathcal{S}:\boldsymbol{k}\downarrow}\right)\left|0\right\rangle,\\
\mathcal{S}\hat{a}_{\boldsymbol{k}\uparrow}\mathcal{S}^{-1}\left|0\right\rangle &= \left(c_{\boldsymbol{k},\uparrow\uparrow}\,\hat{a}^\dagger_{\mathcal{S}:\boldsymbol{k}\uparrow} + c_{\boldsymbol{k},\uparrow\downarrow}\,\hat{a}^\dagger_{\mathcal{S}:\boldsymbol{k}\downarrow}\right)\left|0\right\rangle.
\end{aligned}$$

From this we can conclude that the creation operator $\hat{a}^\dagger_{\boldsymbol{k}\uparrow}$ is transformed by $\mathcal{S}$ as

$$\mathcal{S}\hat{a}^\dagger_{\boldsymbol{k}\uparrow}\mathcal{S}^{-1} = c_{\boldsymbol{k},\uparrow\uparrow}\,\hat{a}^\dagger_{\mathcal{S}:\boldsymbol{k}\uparrow} + c_{\boldsymbol{k},\uparrow\downarrow}\,\hat{a}^\dagger_{\mathcal{S}:\boldsymbol{k}\downarrow}, \tag{2.23}$$

and, because $\mathcal{S}$ is unitary, we also see how the corresponding annihilation operator transforms:

$$\mathcal{S}\hat{a}_{\boldsymbol{k}\uparrow}\mathcal{S}^{-1} = c^*_{\boldsymbol{k},\uparrow\uparrow}\,\hat{a}_{\mathcal{S}:\boldsymbol{k}\uparrow} + c^*_{\boldsymbol{k},\uparrow\downarrow}\,\hat{a}_{\mathcal{S}:\boldsymbol{k}\downarrow}. \tag{2.24}$$

By generalising (2.23) and (2.24) to the corresponding results for spin-down operators, we find that the action of $\mathcal{S}$ on $\Psi_{\boldsymbol{k}}$ is given by

$$\mathcal{S}\begin{pmatrix}\hat{a}_\uparrow\\ \hat{a}_\downarrow\\ \hat{a}^\dagger_\uparrow\\ \hat{a}^\dagger_\downarrow\end{pmatrix}\mathcal{S}^{-1} = \begin{pmatrix} c^*_{\boldsymbol{k},\uparrow\uparrow} & c^*_{\boldsymbol{k},\uparrow\downarrow} & 0 & 0\\ c^*_{\boldsymbol{k},\downarrow\uparrow} & c^*_{\boldsymbol{k},\downarrow\downarrow} & 0 & 0\\ 0 & 0 & c_{\boldsymbol{k},\uparrow\uparrow} & c_{\boldsymbol{k},\uparrow\downarrow}\\ 0 & 0 & c_{\boldsymbol{k},\downarrow\uparrow} & c_{\boldsymbol{k},\downarrow\downarrow}\end{pmatrix}\begin{pmatrix}\hat{a}_{\mathcal{S}:\boldsymbol{k}\uparrow}\\ \hat{a}_{\mathcal{S}:\boldsymbol{k}\downarrow}\\ \hat{a}^\dagger_{\mathcal{S}:-\boldsymbol{k}\uparrow}\\ \hat{a}^\dagger_{\mathcal{S}:-\boldsymbol{k}\downarrow}\end{pmatrix} \equiv \begin{pmatrix} U_{\mathcal{S}} & 0\\ 0 & U^*_{\mathcal{S}}\end{pmatrix}\begin{pmatrix}\hat{a}_{\mathcal{S}:\boldsymbol{k}\uparrow}\\ \hat{a}_{\mathcal{S}:\boldsymbol{k}\downarrow}\\ \hat{a}^\dagger_{\mathcal{S}:-\boldsymbol{k}\uparrow}\\ \hat{a}^\dagger_{\mathcal{S}:-\boldsymbol{k}\downarrow}\end{pmatrix},$$

where $U_{\mathcal{S}}$ is a matrix which describes how the spin degree of freedom changes under $\mathcal{S}$, while the effect of $\mathcal{S}$ on the momentum dependence is being implemented explicitly. $U_{\mathcal{S}}$ can easily be generalised to include additional degrees of freedom. Returning to the transformation of $\mathcal{H}^{\mathrm{MF}}$, we find that we can now write (2.22) as

$$\mathcal{S}\mathcal{H}^{\mathrm{MF}}\mathcal{S}^{-1} = \frac{1}{2}\sum_{\boldsymbol{k}}\Psi^\dagger_{\mathcal{S}:\boldsymbol{k}}\begin{pmatrix}U^\dagger_S & 0\\ 0 & U^T_S\end{pmatrix}\begin{pmatrix}H_{0,\boldsymbol{k}} & \Delta_{\boldsymbol{k}}\\ \Delta^\dagger_{\boldsymbol{k}} & -H^T_{0,-\boldsymbol{k}}\end{pmatrix}\begin{pmatrix}U_S & 0\\ 0 & U^*_S\end{pmatrix}\Psi_{\mathcal{S}:\boldsymbol{k}}. \tag{2.25}$$

We now play a bit of a trick: instead of associating the U_S terms with the $\Psi_{\boldsymbol{k}}$ spinors, we associate them with the BdG Hamiltonian, such that we can isolate how $H_{\boldsymbol{k}}$ transforms under $\mathcal{S}$. If we also relabel the momentum index under the sum as $\boldsymbol{k}\to\mathcal{S}^{-1}:\boldsymbol{k}$, we have

$$\mathcal{S}\mathcal{H}^{\mathrm{MF}}\mathcal{S}^{-1} = \frac{1}{2}\sum_{\boldsymbol{k}}\Psi^\dagger_{\boldsymbol{k}}\begin{pmatrix}U^\dagger_S & 0\\ 0 & U^T_S\end{pmatrix}\begin{pmatrix}H_{0,\mathcal{S}^{-1}:\boldsymbol{k}} & \Delta_{\mathcal{S}^{-1}:\boldsymbol{k}}\\ \Delta^\dagger_{\mathcal{S}^{-1}:\boldsymbol{k}} & -H^T_{0,\mathcal{S}^{-1}:-\boldsymbol{k}}\end{pmatrix}\begin{pmatrix}U_S & 0\\ 0 & U^*_S\end{pmatrix}\Psi_{\boldsymbol{k}}, \tag{2.26}$$

which is to say that $\mathcal{S}$ acting on $\mathcal{H}$ can be effectively described by

$$H_{0,\boldsymbol{k}} \xrightarrow{\mathcal{S}} U_S^\dagger H_{0,\mathcal{S}^{-1}:\boldsymbol{k}} U_S, \tag{2.27}$$

$$\Delta_{\boldsymbol{k}} \xrightarrow{\mathcal{S}} U_S^\dagger \Delta_{\mathcal{S}^{-1}:\boldsymbol{k}} U_S^*. \tag{2.28}$$

It is worth noting that the wavevector $\boldsymbol{k} = (k_x, k_y, k_z)$ transforms just as the Cartesian coordinates (x, y, z) under point symmetries. In Chapter 3 we will spend some time determining the form of the U_S matrices within our model of strontium ruthenate, so that we can apply (2.27) and (2.28).

The time-reversal operation

The discussion so far has revolved around a general point symmetry operator $\mathcal{S}$. It is worth briefly discussing how the result differs for time-reversal. The crucial difference is that time-reversal is antiunitary. Referring to the discussion in Section 1.2, we remember that it is implemented by $\Theta = \mathcal{U}_T \mathcal{K}$, where $\mathcal{U}_T$ is unitary, and $\mathcal{K}$ is the complex conjugation operator. The presence of $\mathcal{K}$ slightly alters the form of (2.27) and (2.28) to give

$$H_{0,\boldsymbol{k}} \xrightarrow{\Theta} U_T^\dagger H_{0,-\boldsymbol{k}}^* U_T = U_T^\dagger H_{0,-\boldsymbol{k}} U_T, \tag{2.29}$$

$$\Delta_{\boldsymbol{k}} \xrightarrow{\Theta} U_T^\dagger \Delta_{-\boldsymbol{k}}^* U_T^*, \tag{2.30}$$

where I have used $\Theta : \boldsymbol{k} = -\boldsymbol{k}$ from (1.1), and the fact that H_0 is real-valued. Just as for point symmetries, U_T is a unitary matrix.

The transformed pairing potential

Examination of (2.27) and (2.28) show that there is a difference between how H_0 and Δ transform under point symmetry operations. For this reason it is convenient to define $\tilde{\Delta}_{\boldsymbol{k}}$, a slightly transformed version of the pairing potential:

$$\tilde{\Delta}_{\boldsymbol{k}} \equiv \Delta_{\boldsymbol{k}} U_T^\dagger \qquad \longleftrightarrow \qquad \Delta_{\boldsymbol{k}} = \tilde{\Delta}_{\boldsymbol{k}} U_T. \tag{2.31}$$

This transforms under a point symmetry operation in the same way as H_0:

$$\tilde{\Delta}_{\boldsymbol{k}} \xrightarrow{\mathcal{S}} U_S^\dagger \tilde{\Delta}_{\mathcal{S}^{-1}:\boldsymbol{k}} U_S. \tag{2.32}$$

Proof: We begin with the fact that time-reversal commutes with rotations and inversion [75], and therefore with all point symmetry operations, i.e. $\mathcal{S}\Theta = \Theta\mathcal{S}$ (as reflections can be constructed from a π rotation plus inversion). From (2.27) and (2.29) we have

$$H_{0,\boldsymbol{k}} \xrightarrow{\mathcal{S}\Theta} U_S^\dagger U_T^\dagger H_{0,\mathcal{S}^{-1}:-\boldsymbol{k}}^* U_T U_S, \tag{2.33}$$

$$H_{0,\boldsymbol{k}} \xrightarrow{\Theta\mathcal{S}} U_T^\dagger U_S^T H_{0,\mathcal{S}^{-1}:-\boldsymbol{k}}^* U_S^* U_T. \tag{2.34}$$

Setting these equal to each other, we conclude that

$$U_T U_S = U_S^* U_T \qquad \longleftrightarrow \qquad U_T U_S^* = U_S U_T. \tag{2.35}$$

Now let us substitute $\Delta = \tilde{\Delta} U_T$ into (2.28):

$$\tilde{\Delta}_{\boldsymbol{k}} U_T \xrightarrow{\mathcal{S}} U_S^\dagger \Delta_{\mathcal{S}^{-1}:\boldsymbol{k}} U_T U_S^* = U_S^\dagger \Delta_{\mathcal{S}^{-1}:\boldsymbol{k}} U_S U_T. \tag{2.36}$$

Finally, using $U_T \xrightarrow{\mathcal{S}} U_T$ (which can be seen by setting $\tilde{\Delta} = \mathbb{1}$ in the above equation), we reach (2.32) as a conclusion. Note that this result hinges upon the fact that the time-reversal operator is antiunitary, unlike the point symmetry operations, which is why U_T plays a special role in (2.31).

From its definition we see that the transformed pairing potential has a close connection to the operation of time-reversal. This will be examined in more detail in Section 3.2.1, once the form of U_T has been discussed. For now I note that in the BCS Hamiltonian (2.18) we have $\tilde{\Delta} = 1$, which physically implies that the pairing involves time-reversed states. As we will see in Section 3.2.1, this condition can be relaxed for more general pairing states.

Chapter 3

Modelling strontium ruthenate

In Chapter 2 we constructed the Bogoliubov de Gennes Hamiltonian, (2.15), for a general superconducting system involving an arbitrary number of internal degrees of freedom. We introduced the matrices H_0 and $\tilde{\Delta}$, which describe the normal state and superconducting state respectively, and showed how to act on them with point symmetries and time-reversal. In this chapter we take these results and apply them to modelling strontium ruthenate, which involves restricting ourselves to two internal degrees of freedom: the spin state of the electrons, and the orbital from which they originate. As discussed in Chapter 1, it is thought that Cooper pairing in strontium ruthenate arises primarily from electrons from the ruthenium d_{xz} and d_{yz} orbitals, so these are the only orbitals included in our model. In this case the Nambu spinor can be written as

$$\Psi_{\boldsymbol{k}} = \begin{pmatrix} \hat{a}_{\boldsymbol{k}x\uparrow} & \hat{a}_{\boldsymbol{k}x\downarrow} & \hat{a}_{\boldsymbol{k}y\uparrow} & \hat{a}_{\boldsymbol{k}y\downarrow} & \hat{a}^{\dagger}_{-\boldsymbol{k}x\uparrow} & \hat{a}^{\dagger}_{-\boldsymbol{k}x\downarrow} & \hat{a}^{\dagger}_{-\boldsymbol{k}y\uparrow} & \hat{a}^{\dagger}_{-\boldsymbol{k}y\downarrow} \end{pmatrix}^{T}, \tag{3.1}$$

where an x (y) index corresponds to d_{xz} (d_{yz}). H_0 and $\tilde{\Delta}$ are now 4×4 matrices. It is convenient to decompose them in terms of Pauli matrices in orbital and spin space, η_α and σ_β respectively:

$$H_{0,\boldsymbol{k}} = \sum_{\alpha,\beta=0}^{3} h_{\boldsymbol{k},\alpha\beta}\, \eta_\alpha \otimes \sigma_\beta, \tag{3.2}$$

$$\tilde{\Delta}_{\boldsymbol{k}} = \sum_{\alpha,\beta=0}^{3} \Delta_{\boldsymbol{k},\alpha\beta}\, \eta_\alpha \otimes \sigma_\beta. \tag{3.3}$$

In conjunction with the 2×2 identity matrix, $\sigma_0 = \mathbb{1}_2$, the Pauli matrices form a spanning basis of the 2×2 matrices, so we have lost no generality.

I begin in Section 3.1 by determining the forms of U_S within our model, for each of the D_{4h} generating symmetries. The same is done for U_T in Section 3.2. These results will allow us to explicitly implement (2.27)–(2.30). In Section 3.3 we apply some physical restrictions, as well as assumptions specific to our model, in order to restrict the terms that appear in (3.2) and (3.3), and specify forms for the momentum-dependent coefficients $h_{\boldsymbol{k},\alpha\beta}$ and $\Delta_{\boldsymbol{k},\alpha\beta}$. I finish in Section 3.4 with a discussion of the TRSB chiral pairing states that will be used later in this thesis. The analysis employed in this chapter is rather standard, so the results are not particularly novel, but should provide a robust understanding of the resulting model of strontium ruthenate.

3.1 Point symmetries

We can understand how the orbital $\otimes$ spin matrices in (3.2) and (3.3) are affected by the D_{4h} point symmetry operations by determining which irreducible representation they belong to. In order to achieve this we will use our physical understanding of the spin and orbital degrees of freedom to

Spin Pauli matrix	$\mathcal{C}_4 : \sigma_i$	ν_{C_4}	$\mathcal{C}_2' : \sigma_i$	$\nu_{C_2'}$	$\mathcal{I} : \sigma_i$	ν_I	Irrep
σ_0	σ_0	$+1$	σ_0	$+1$	σ_0	$+1$	A_{1g}
σ_3	σ_3	$+1$	$-\sigma_3$	-1	σ_3	$+1$	A_{2g}
$\{\sigma_1, \sigma_2\}$	$\{\sigma_2, -\sigma_1\}$	0	$\{\sigma_1, -\sigma_2\}$	0	$\{\sigma_1, \sigma_2\}$	$+2$	E_g

TABLE 3.1: The symmetry classification of the spin Pauli matrices in D_{4h}. The irreducible representations are determined from Table 2.1.

determine the irreps to which each of η_α and σ_β matrices belong to respectively. These can then be combined using a "direct product table". The behaviour of spin-$\frac{1}{2}$ under point symmetries is well known, so we will begin by considering the spin degree of freedom.

3.1.1 Determining the spin irreps

In order to determine which irrep each of the spin Pauli matrices belongs to, we must know the form of $U_S^{[s]}$, the spin part of U_S, for each of the D_{4h} generating symmetries, $\mathcal{C}_4$, $\mathcal{C}_2'$, and $\mathcal{I}$. In the basis defined by $\{\uparrow, \downarrow\}$ these are known to be [76]

$$U_{C_4}^{[s]} = \begin{pmatrix} e^{i\pi/4} & 0 \\ 0 & e^{-i\pi/4} \end{pmatrix}, \tag{3.4}$$

$$U_{C_2'}^{[s]} = \begin{pmatrix} 0 & -i \\ -i & 0 \end{pmatrix} = -i\sigma_1, \tag{3.5}$$

$$U_I^{[s]} = \begin{pmatrix} 1 & 0 \\ 0 & 1 \end{pmatrix} = \sigma_0. \tag{3.6}$$

Of these results I note in particular that (3.6) implies that neither $|\uparrow\rangle$ nor $|\downarrow\rangle$ is affected by inversion:

$$\mathcal{I}\,|\uparrow\rangle \doteq \begin{pmatrix} 1 & 0 \\ 0 & 1 \end{pmatrix} \begin{pmatrix} 1 \\ 0 \end{pmatrix} = \begin{pmatrix} 1 \\ 0 \end{pmatrix} = |\uparrow\rangle\,, \tag{3.7}$$

$$\mathcal{I}\,|\downarrow\rangle \doteq \begin{pmatrix} 1 & 0 \\ 0 & 1 \end{pmatrix} \begin{pmatrix} 0 \\ 1 \end{pmatrix} = \begin{pmatrix} 0 \\ 1 \end{pmatrix} = |\downarrow\rangle\,. \tag{3.8}$$

We can now use (2.27), and equivalently (2.32), in order to determine how each of the spin Pauli matrices in H_0 and $\tilde{\Delta}$ transform under the D_{4h} generating symmetries. As an example, consider how σ_3 transforms under $\mathcal{C}_4$:

$$U_{C_4}^{[s]\dagger} \sigma_3 U_{C_4}^{[s]} = \begin{pmatrix} e^{-i\pi/4} & 0 \\ 0 & e^{i\pi/4} \end{pmatrix} \begin{pmatrix} 1 & 0 \\ 0 & -1 \end{pmatrix} \begin{pmatrix} e^{i\pi/4} & 0 \\ 0 & e^{-i\pi/4} \end{pmatrix} = \begin{pmatrix} 1 & 0 \\ 0 & -1 \end{pmatrix} = \sigma_3. \tag{3.9}$$

This is to say that σ_3 has a character of $+1$ under $\mathcal{C}_4$. As a second example, consider the action of σ_1 under the same $\mathcal{C}_4$ rotation:

$$U_{C_4}^{[s]\dagger} \sigma_1 U_{C_4}^{[s]} = \begin{pmatrix} e^{-i\pi/4} & 0 \\ 0 & e^{i\pi/4} \end{pmatrix} \begin{pmatrix} 0 & 1 \\ 1 & 0 \end{pmatrix} e^{i\pi/4} \begin{pmatrix} e^{i\pi/4} & 0 \\ 0 & e^{-i\pi/4} \end{pmatrix} = \begin{pmatrix} 0 & -i \\ i & 0 \end{pmatrix} = \sigma_2. \tag{3.10}$$

We see that σ_2 is transformed into σ_1. It is neither symmetric nor antisymmetric under C_4, but instead σ_1 and σ_2 form the basis of a two-dimensional irrep.

This process can be repeated for each generating symmetry acting on each spin Pauli matrix, and the results are collated in Table 3.1. The irreducible representation to which each term belongs

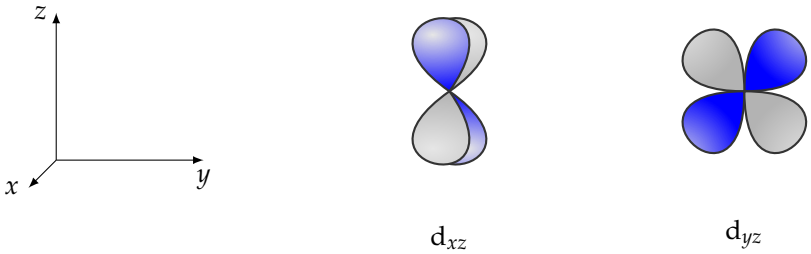

FIGURE 3.1: Visualisations of the d_{xz} and d_{yz} orbitals, which are involved in the pairing in our model.

is determined by comparing the characters in Table 3.1 to the D_{4h} character table, Table 2.1.

3.1.2 Determining the orbital irreps

When it comes to characterising the orbital Pauli matrices, we follow the same process as was just applied to the spin degree of freedom. However, the $U_S^{[o]}$ matrices are not well known, and must instead be determined specifically for the orbitals included in our model. As shown in Section 2.2.1, the form of U_S arises from how the single-electron states behave under the point symmetry $\mathcal{S}$. So we can determine the elements of, say, $U_{C_4}^{[o]}$ by acting on each of the d_{xz} and d_{yz} orbital states with C_4. These orbitals are shown diagrammatically in Figure 3.1. As spherical harmonics they are written in terms of Cartesian coordinates as

$$d_{xz} = \sqrt{\frac{15}{4\pi}} \frac{xz}{x^2+y^2+z^2}, \tag{3.11}$$

$$d_{yz} = \sqrt{\frac{15}{4\pi}} \frac{yz}{x^2+y^2+z^2}. \tag{3.12}$$

It is fairly straightforward to use the diagrams in Figure 3.1 to determine how these orbitals transform under the generating symmetries. For example, C_4, a quarter rotation about the z axis, will take $d_{xz} \to d_{yz}$ and $d_{yz} \to -d_{xz}$. This can be verified by acting C_4 on the Cartesian coordinates that appear in (3.11) and (3.12). Under C_4 we have $x \to y$, $y \to -x$, and $z \to z$, so

$$d_{xz} \xrightarrow{C_4} \sqrt{\frac{15}{4\pi}} \frac{yz}{(x^2+y^2+z^2)} = d_{yz}, \tag{3.13}$$

$$d_{yz} \xrightarrow{C_4} \sqrt{\frac{15}{4\pi}} \frac{-xz}{(x^2+y^2+z^2)} = -d_{xz}, \tag{3.14}$$

in agreement to what we concluded already. Repeating this analysis for the other two generating symmetries, we find

$$\begin{aligned} C_4 |d_{xz}\rangle &= |d_{yz}\rangle, & C_2' |d_{xz}\rangle &= -|d_{xz}\rangle, & \mathcal{I} |d_{xz}\rangle &= |d_{xz}\rangle, \\ C_4 |d_{yz}\rangle &= -|d_{xz}\rangle, & C_2' |d_{yz}\rangle &= |d_{yz}\rangle, & \mathcal{I} |d_{yz}\rangle &= |d_{yz}\rangle. \end{aligned} \tag{3.15}$$

We see that these two orbitals form the basis of a two-dimensional irrep, and comparison with Table 2.1 tells us that this is E_g, as both orbitals are symmetric under inversion. Using the results of Section 2.2.1, we can use (3.15) to determine the forms of the U_S matrices. Referring back to 2.2.1, we see that the coefficients given to us by (3.15) technically correspond to $U_S^{[o]*}$, but since they are

Orbital Pauli matrix	$C_4 : \eta_i$	ν_{C_4}	$C_2' : \eta_i$	$\nu_{C_2'}$	$I : \eta_i$	ν_I	Irrep
η_0	η_0	$+1$	η_0	$+1$	η_0	$+1$	A_{1g}
η_2	η_2	$+1$	$-\eta_2$	-1	η_2	$+1$	A_{2g}
η_3	$-\eta_3$	-1	η_3	$+1$	η_3	$+1$	B_{1g}
η_1	$-\eta_1$	-1	$-\eta_1$	-1	η_1	$+1$	B_{2g}

TABLE 3.2: The symmetry classification of the orbital Pauli matrices in D_{4h}. The irreducible representations are determined from Table 2.1.

all real-valued this is not a problem. We have

$$U_{C_4}^{[o]} = \begin{pmatrix} 0 & 1 \\ -1 & 0 \end{pmatrix} = i\eta_2, \tag{3.16}$$

$$U_{C_2'}^{[o]} = \begin{pmatrix} 1 & 0 \\ 0 & -1 \end{pmatrix} = \eta_3, \tag{3.17}$$

$$U_I^{[o]} = \begin{pmatrix} -1 & 0 \\ 0 & -1 \end{pmatrix} = -\eta_0. \tag{3.18}$$

We can now use these matrices to act on each of the orbital Pauli matrices with each of the generating symmetries via the matrix multiplication $U_S^{[o]\dagger}\eta_i U_S^{[o]}$, just as we did for spin. The results are summarised in Table 3.2, along with the irreducible representation to which each orbital Pauli matrix must therefore belong to.

3.1.3 Orbital $\otimes$ spin matrices

Having classified which irreducible representation each of the spin and orbital Pauli matrices belong to, we are now interested in the classification of each orbital $\otimes$ spin matrix as a whole. As an example of how to "combine" functions from different irreps, let us take $x^2 - y^2 \in B_{1g}$ and $z^3 \in A_{2u}$ (refer to Table 2.2). We can determine the irrep to which their product, $(x^2 - y^2)z^3$, belongs by applying the D_{4h} generating symmetries directly to this function, i.e.

$$\mathcal{C}_4 : (x^2 - y^2)z^3 = (y^2 - (-x)^2)z^3 = -(x^2 - y^2)z^3, \tag{3.19}$$

$$\mathcal{C}_2' : (x^2 - y^2)z^3 = (x^2 - (-y)^2)(-z)^3 = -(x^2 - y^2)z^3, \tag{3.20}$$

$$\mathcal{I} : (x^2 - y^2)z^3 = ((-x)^2 - (-y)^2)(-z)^3 = -(x^2 - y^2)z^3, \tag{3.21}$$

which tells us that it has the characters $\nu_{\mathcal{C}_4} = \nu_{\mathcal{C}_2'} = \nu_{\mathcal{I}} = -1$. Referencing Table 2.1 tells us that $(x^2 - y^2)z^3$ therefore belongs to B_{2u}. It turns out that this is true of *any* product of a function from B_{1g} with a function from A_{2u}. We write

$$B_{1g} \otimes A_{2u} = A_{2u} \otimes B_{1g} = B_{2u}.$$

The results of taking the product of functions belonging to any two irreps are tabulated in a *direct product table*, which is given for D_{4h} in Table 3.3. The product of two functions belonging to 1D irreps is a single function belonging to a 1D irrep. The product of a function from a 1D irrep with each of the basis functions belonging to a 2D irrep results in two functions that form the basis of a 2D irrep. Combining functions from two 2D irreps produces four functions belonging to 1D irreps, although if we take the four possible products between the basis functions of each irrep we will not necessarily end up with four functions that each belong to a 1D irrep. We may be required to

D_{4h}	A_{1g}	A_{2g}	B_{1g}	B_{2g}	E_g	A_{1u}	A_{2u}	B_{1u}	B_{2u}	E_u
A_{1g}	A_{1g}	A_{2g}	B_{1g}	B_{2g}	E_g	A_{1u}	A_{2u}	B_{1u}	B_{2u}	E_u
A_{2g}		A_{1g}	B_{2g}	B_{1g}	E_g	A_{2u}	A_{1u}	B_{2u}	B_{1u}	E_u
B_{1g}			A_{1g}	A_{2g}	E_g	B_{1u}	B_{2u}	A_{1u}	A_{2u}	E_u
B_{2g}				A_{1g}	E_g	B_{2u}	B_{1u}	A_{2u}	A_{1u}	E_u
E_g					$A_{1g}, A_{2g}, B_{1g}, B_{2g}$	E_u	E_u	E_u	E_u	$A_{1u}, A_{2u}, B_{1u}, B_{2u}$
A_{1u}						A_{1g}	A_{2g}	B_{1g}	B_{2g}	E_g
A_{2u}							A_{1g}	B_{2g}	B_{1g}	E_g
B_{1u}								A_{1g}	A_{2g}	E_g
B_{2u}									A_{1g}	E_g
E_u										$A_{1g}, A_{2g}, B_{1g}, B_{2g}$

TABLE 3.3: The direct product table for combining functions from different irreducible representations in D_{4h}.

take linear combinations in order to find resulting functions that have a definite character under each of the generating symmetries. The direct product table tells us which irreps each of these four functions will belong to, but not necessarily which belongs to which. We usually write, for example, $E_g \otimes E_u = A_{1u} \oplus A_{2u} \oplus B_{1u} \oplus B_{2u}$.

Returning to the orbital $\otimes$ spin matrices, it is a rather straightforward process to determine which irreps they belong to. For example, we already know from Tables 3.1 and 3.2 that $\sigma_3 \in A_{2g}$ and $\eta_1 \in B_{2g}$. We can then read off Table 3.3 that $\eta_1 \otimes \sigma_3$ belongs to B_{1g}. As a slightly more complicated example, we know that $\eta_0 \in A_{1g}$, while $\{\sigma_2, \sigma_2\} \in E_g$. Table 3.3 then tells us that the terms resulting from their products, $\eta_0 \otimes \sigma_1$ and $\eta_0 \otimes \sigma_2$, form a basis of an E_g irrep. Repeating this for each possible combination of orbital and spin, I summarise the results in Table 3.4. These apply to the orbital $\otimes$ spin parts of the terms that appear in both $H_{0,\boldsymbol{k}}$ and $\tilde{\Delta}_{\boldsymbol{k}}$.

3.2 Time-reversal

We now have forms for $U_S = U_S^{[\mathrm{o}]} \otimes U_S^{[\mathrm{s}]}$ for each of the D_{4h} generating symmetries. At this point it makes sense to also examine the form of U_T, the unitary matrix associated with time-reversal. We begin by examining the effect of time-reversal on spin states. From (1.1) we have $\Theta|\uparrow\rangle = |\downarrow\rangle$, and

Orbital $\otimes$ spin matrix	Irrep.
$\eta_0 \otimes \sigma_0$	A_{1g}
$\eta_2 \otimes \sigma_3$	A_{1g}
$\eta_0 \otimes \sigma_3$	A_{2g}
$\eta_2 \otimes \sigma_0$	A_{2g}
$\eta_3 \otimes \sigma_0$	B_{1g}
$\eta_1 \otimes \sigma_3$	B_{1g}
$\eta_3 \otimes \sigma_3$	B_{2g}
$\eta_1 \otimes \sigma_0$	B_{2g}
$\{\eta_0 \otimes \sigma_1,\ \eta_0 \otimes \sigma_2\}$	E_g
$\{\eta_2 \otimes \sigma_1,\ \eta_2 \otimes \sigma_2\}$	E_g
$\{\eta_3 \otimes \sigma_1,\ \eta_3 \otimes \sigma_2\}$	E_g
$\{\eta_1 \otimes \sigma_1,\ \eta_1 \otimes \sigma_2\}$	E_g

TABLE 3.4: The D_{4h} irreducible representations to which the orbital $\otimes$ spin matrices belong, as determined using Tables 3.1, 3.2, and 3.3.

$\Theta\,|\downarrow\rangle = -\,|\uparrow\rangle$. So with respect to the $\{\uparrow,\downarrow\}$ basis we have

$$U_T^{[\mathrm{s}]} = \begin{pmatrix} 0 & 1 \\ -1 & 0 \end{pmatrix} = i\sigma_2. \tag{3.22}$$

The orbital part of U_T is even easier to determine, because the d_{xz} and d_{yz} orbitals given in (3.11) and (3.12) are real-valued functions of spatial coordinates, which are unaffected by time-reversal. In the $\{\mathrm{d}_{xz}, \mathrm{d}_{yz}\}$ basis we must therefore have

$$U_T^{[\mathrm{o}]} = \begin{pmatrix} 1 & 0 \\ 0 & 1 \end{pmatrix} = \eta_0, \tag{3.23}$$

although it is worth noting that this conclusion would not necessarily hold in a different basis. For example, in the $\{\mathrm{d}_{xz} + i\mathrm{d}_{yz}, \mathrm{d}_{xz} - i\mathrm{d}_{yz}\}$ basis the complex conjugation of time-reversal would lead to nontrivial behaviour. Putting (3.22) and (3.23) together we obtain

$$U_T = \eta_0 \otimes i\sigma_2, \tag{3.24}$$

which is unitary, real-valued, and obeys

$$U_T^2 = -\mathbb{1}, \tag{3.25}$$

which is the result of $\Theta^2 = -1$ (refer to Section 1.2). Technically (3.25) should read $U_T U_T^* = -\mathbb{1}$, as

$$\Theta\Theta\,|\psi\rangle = \Theta U_T\,|\psi\rangle^* = U_T U_T^*\,|\psi\rangle = -\,|\psi\rangle \tag{3.26}$$

for an arbitrary single-particle state $|\psi\rangle$, but this is unimportant because U_T is real-valued. In fact, with the spin part of U_T fixed, this condition actually requires that U_T as a whole is real-valued, and therefore (3.25) holds for any two-orbital spin-$\frac{1}{2}$ system. Finally, it is worth noting that (3.25) in conjunction with the unitary nature of U_T implies that

$$U_T = -U_T^\dagger, \tag{3.27}$$

which can be seen by multiplying both sides of (3.25) with $U_T^\dagger$.

3.2.1 Implications for $\tilde{\Delta}$

At this point we could in theory use (2.29) and (2.30) to characterise how each orbital $\otimes$ spin part of H_0 and $\tilde{\Delta}$ transforms under time-reversal, although this would not provide us many useful insights. Instead, now that we have a form of U_T, we can restate (2.30) as

$$\Delta_{\boldsymbol{k}} \xrightarrow{\Theta} U_T^\dagger \Delta_{-\boldsymbol{k}}^* U_T = -U_T^\dagger \Delta_{\boldsymbol{k}}^\dagger U_T,$$

where the second step utilised (2.9). Substituting in $\Delta = \tilde{\Delta} U_T$ from (2.31) gives us

$$\tilde{\Delta}_{\boldsymbol{k}} U_T \xrightarrow{\Theta} -U_T^\dagger (\tilde{\Delta}_{\boldsymbol{k}} U_T)^\dagger U_T = -(U_T^\dagger)^2 \tilde{\Delta}_{\boldsymbol{k}}^\dagger U_T = \tilde{\Delta}_{\boldsymbol{k}}^\dagger U_T,$$

where we used (3.25) in the final step. Finally, noting that $U_T \xrightarrow{\Theta} U_T$ (which can be seen by setting $\tilde{\Delta} = \mathbb{1}$ above), we can conclude that

$$\tilde{\Delta}_{\boldsymbol{k}} \xrightarrow{\Theta} \tilde{\Delta}_{\boldsymbol{k}}^\dagger. \tag{3.28}$$

A similar argument also shows that

$$\tilde{\Delta}_{\boldsymbol{k}}^{\dagger} \xrightarrow{\Theta} \tilde{\Delta}_{\boldsymbol{k}}. \tag{3.29}$$

We introduced $\tilde{\Delta}$ in Section 2.2.1 because it transformed under point symmetry operations in a more convenient way than Δ. However, we now see that it also has the convenient property that $\tilde{\Delta}$ and $\tilde{\Delta}^{\dagger}$ are time-reversed counterparts. This useful result underscores the physical motivation for introducing $\tilde{\Delta}$ in the first place, and will play a crucial role in Chapter 5.

3.3 Restrictions to the model

In Chapter 2 we derived the general form of the Bogoliubov de Gennes Hamiltonian under the usual mean-field assumption. Now that we understand how the point symmetries and time-reversal act in our model of strontium ruthenate, I will enforce some physical constraints on $\mathcal{H}$ which will restrict the allowed forms of H_0 and Δ. In particular I will enforce that

1. $\mathcal{H}$ is Hermitian,
2. $\mathcal{H}$ obeys the fermionic exchange antisymmetry,
3. $\mathcal{H}_0$ has the full symmetry of the lattice (in particular, it is symmetric under spatial inversion),
4. $\mathcal{H}_0$ is symmetric under time-reversal, and
5. The dispersion is constant in the z direction, so we can restrict our analysis to the xy-plane.

The first two of these *must* be obeyed, while the last three are assumptions. It is generally safe to assume that the normal state of a crystalline solid will satisfy both the third and fourth assumptions, essentially by definition of the "normal state". The physical motivation for the final assumption was discussed in Chapter 1.

3.3.1 General form of H_0

Let us first consider the allowed form of H_0 under these restrictions. We begin by enforcing the first requirement, which tells us $\mathcal{H}^{\dagger} = \mathcal{H} \implies H_{\boldsymbol{k}}^{\dagger} = H_{\boldsymbol{k}}$. Examination of (2.16) shows us that this in turn requires $H_{0,\boldsymbol{k}}$ to be Hermitian. This is particularly easy to enforce when using (3.2), as the Pauli matrices themselves are Hermitian and linearly independent, so

$$H_{0,\boldsymbol{k}}^{\dagger} = H_{0,\boldsymbol{k}} \implies h_{\boldsymbol{k},\alpha\beta}^{*}\, \eta_{\alpha} \otimes \sigma_{\beta} = h_{\boldsymbol{k},\alpha\beta}\, \eta_{\alpha} \otimes \sigma_{\beta}. \tag{3.30}$$

We can hence conclude that the $h_{\boldsymbol{k},\alpha\beta}$ coefficients are real-valued.

The second requirement does not affect H_0, as the matrix elements of H_0 only appear in front of *single-particle* terms in $\mathcal{H}$, so we can move on to requirement three, that the normal state Hamiltonian has the full symmetry of the lattice. This is to say that $\mathcal{H}_0$ should be invariant under each of the D_{4h} point symmetries, which broadly implies that each term in (3.2) must independently belong to A_{1g}. Specifically, we require $\mathcal{H}_0$ to be symmetric under inversion. From (3.6) and (3.18) we know that inversion acts trivially on the orbital and spin degrees of freedom in our model, i.e. $U_I = \mathbb{1}_4$, so (2.27) can be written as

$$H_{0,\boldsymbol{k}} \xrightarrow{\mathcal{I}} H_{0,-\boldsymbol{k}}. \tag{3.31}$$

Enforcing H_0 as given by (3.2) to be *symmetric* under inversion simply requires the $h_{\boldsymbol{k},\alpha\beta}$ coefficients to be even functions of momentum:

$$H_{0,\boldsymbol{k}} = H_{0,-\boldsymbol{k}} \implies h_{\boldsymbol{k},\alpha\beta} = h_{-\boldsymbol{k},\alpha\beta}. \tag{3.32}$$

Using (2.29) we can write requirement four as $H_{0,\boldsymbol{k}} = U_T^\dagger H_{0,-\boldsymbol{k}}^* U_T$, where we have $U_T = \eta_0 \otimes i\sigma_2$ from (3.24). When applying this to (3.2), we find

$$\sum_{\alpha\beta} h_{\boldsymbol{k},\alpha\beta}\, \eta_\alpha \otimes \sigma_\beta = \sum_{\alpha\beta} h_{\boldsymbol{k},\alpha\beta}\, \eta_\alpha^* \otimes (\sigma_2 \sigma_\beta^* \sigma_2), \tag{3.33}$$

where I have also enforced $h_{\boldsymbol{k},\alpha\beta} \in \mathbb{R}$ and $h_{\boldsymbol{k},\alpha\beta} = h_{-\boldsymbol{k},\alpha\beta}$ from the previous arguments. On an initial examination this may appear unhelpful, as the equality only holds when we sum over all possible terms. However, we can simplify the problem at hand by tabulating the values of η_α^* and $\sigma_2\sigma_\beta^*\sigma_2$ for each value of α and β respectively:

α	0	1	2	3
η_α^*	η_0	η_1	$-\eta_2$	η_3

β	0	1	2	3
$\sigma_2\sigma_\beta^*\sigma_2$	σ_0	$-\sigma_1$	$-\sigma_2$	$-\sigma_3$

This tells us that $\eta_\alpha^* = \pm\eta_\alpha$, and $\sigma_2\sigma_\beta^*\sigma_2 = \pm\sigma_\beta$, and hence each term in the sum on the right hand side of (3.33) is equal to the corresponding term on the left hand side up to a factor of -1. As the Pauli matrices are linearly independent, we can therefore consider each term independently. Further, we see that there are only six permitted terms that satisfy (3.33), namely $\{\eta_0, \eta_1, \eta_3\} \otimes \sigma_0$ and $\eta_2 \otimes \{\sigma_1, \sigma_2, \sigma_3\}$. In summary, the general form of H_0 under these conditions is

$$H_0 = h_{00}\, \eta_0 \otimes \sigma_0 + h_{10}\, \eta_1 \otimes \sigma_0 + h_{30}\, \eta_3 \otimes \sigma_0 + h_{21}\, \eta_2 \otimes \sigma_1 + h_{22}\, \eta_2 \otimes \sigma_2 + h_{23}\, \eta_2 \otimes \sigma_3, \tag{3.34}$$

where each of the $h_{\alpha\beta}$ coefficients is an even function of momentum, and each term belongs to A_{1g}. Table 3.4 can be used to tell us which irrep each of the orbital $\otimes$ spin matrices in (3.34) belongs to. The direct product table, Table 3.3, tells us that the corresponding momentum-dependent coefficient must belong to the same irrep such that the product of the "momentum" and the "orbital $\otimes$ spin" terms belongs to A_{1g}, i.e.

H_0 term	Momentum irrep	Orbital $\otimes$ spin irrep
$h_{\boldsymbol{k},00}\, \eta_0 \otimes \sigma_0$	A_{1g}	A_{1g}
$h_{\boldsymbol{k},01}\, \eta_1 \otimes \sigma_0$	B_{2g}	B_{2g}
$h_{\boldsymbol{k},03}\, \eta_3 \otimes \sigma_0$	B_{1g}	B_{1g}
$\{h_{\boldsymbol{k},21}\, \eta_2 \otimes \sigma_1, h_{\boldsymbol{k},22}\, \eta_2 \otimes \sigma_2\}$	E_g	E_g
$h_{\boldsymbol{k},23}\, \eta_2 \otimes \sigma_3$	A_{1g}	A_{1g}

where the E_g terms are combined in such a way as to produce two overall A_{1g} terms.

We are now at a point where we can enforce assumption five, which restricts our model to two spatial dimensions, the xy-plane. By doing this we will be able to eliminate some of the terms from (3.34) by considering the σ_h mirror symmetry, which corresponds to reflection in the xy-plane. We focus on the behaviour of the momentum dependent coefficients, $h_{\boldsymbol{k},\alpha\beta}$ under σ_h, so make use of

$$\sigma_h : (k_x, k_y, k_z) = (k_x, k_y, -k_z). \tag{3.35}$$

Table 2.1 tells us that each of the 1D irreps has a character of $+1$ under σ_h, and therefore we have $h_{00,(k_x,k_y,k_z)} = h_{00,(k_x,k_y,-k_z)}$, and similarly for h_{01}, h_{03}, and h_{23}. This places no restriction on the

form of these coefficients in the xy-plane. However, let us now consider the E_g irrep, which has a character of -2 under σ_h. This is to say that

$$h_{21,(k_x,k_y,k_z)} = -h_{21,(k_x,k_y,-k_z)}, \tag{3.36}$$

and similarly for h_{22}. For $k_z = 0$, this tells us that

$$h_{21,(k_x,k_y,0)} = -h_{21,(k_x,k_y,0)}, \tag{3.37}$$

which requires $h_{21} = 0$ on the xy-plane. The same conclusion can be drawn for h_{22}. Since we are explicitly restricting our model to only this plane, we must exclude these terms from our model entirely. The final form of H_0 involves just four terms:

$$H_{0,\boldsymbol{k}} = \underbrace{h_{\boldsymbol{k},00}}_{A_{1g}}\,\underbrace{\eta_0 \otimes \sigma_0}_{A_{1g}} + \underbrace{h_{\boldsymbol{k},23}}_{A_{1g}}\,\underbrace{\eta_2 \otimes \sigma_3}_{A_{1g}} + \underbrace{h_{\boldsymbol{k},30}}_{B_{1g}}\,\underbrace{\eta_3 \otimes \sigma_0}_{B_{1g}} + \underbrace{h_{\boldsymbol{k},10}}_{B_{2g}}\,\underbrace{\eta_1 \otimes \sigma_0}_{B_{2g}}, \tag{3.38}$$

which can be shown to have the eigenvalues

$$E_{\boldsymbol{k}\pm} = h_{\boldsymbol{k},00} \pm \sqrt{h_{\boldsymbol{k},23}^2 + h_{\boldsymbol{k},30}^2 + h_{\boldsymbol{k},10}^2}. \tag{3.39}$$

These correspond to *four* possible eigenstates of H_0, which implies that H_0 has a two-fold degeneracy at each value of $\boldsymbol{k}$. The reason for this is addressed in Section 4.1, and is closely related to the spin-degeneracy discussed in Section 1.1.1.

Specific forms of the coefficients

All we know about the $h_{\alpha\beta}$ coefficients that appear in (3.38) is which irreducible representation they belong to. To give them specific forms, Taylor and Kallin [26] use a simple tight binding model to give $h_{00} + h_{30} = -2t_a \cos k_x - \mu$, $h_{00} - h_{30} = -2t_b \cos k_y - \mu$, and $h_{10} = 2t_c \sin k_x \sin k_y$, where $t_a, t_b, t_c > 0$ are hopping parameters. Assuming the simplest case in which spin-orbital coupling, described by h_{23}, is isotropic, we obtain

$$h_{\boldsymbol{k},00} = -t_1(\cos(k_x) + \cos(k_y)) - \mu, \tag{3.40}$$
$$h_{\boldsymbol{k},23} = \lambda, \tag{3.41}$$
$$h_{\boldsymbol{k},30} = -t_2(\cos(k_x) - \cos(k_y)), \tag{3.42}$$
$$h_{\boldsymbol{k},10} = 2t_3 \sin(k_x) \sin(k_y), \tag{3.43}$$

where $t_a = (t_1 + t_2)/2$, $t_b = (t_1 - t_2)/2$, $t_c = t_3$, and λ is a constant. Although momentum dependent spin-orbital coupling is possible, it is likely to be very small in strontium ruthenate [77]. It is fairly straightforward to verify that each of these expressions belongs to the correct irreducible representation (refer to Table 2.2). I choose the energy scale to be used throughout this thesis to be defined by $t_1 = 1$. Local density approximation analyses of the band structure of strontium ruthenate indicate that $\mu \approx t_1$, $t_3 \approx 0.1t_1$ [78], and $\lambda \approx 0.25t_1$ [79]. Taylor and Kallin take $t_2 = t_1$, but I choose $t_2 = 0.8t_1$ to better match experimental results by comparing the Fermi surface as calculated from our model to that measured in [55] (refer to Figure 1.2 B).

A "spaghetti plot" of the normal state band structure, and the normal state Fermi surface, as calculated with from (3.39) using (3.40)–(3.43), are presented in Figure 3.2. The two doubly-degenerate energy bands correspond to the α and β bands discussed in Section 1.2.2. The Fermi

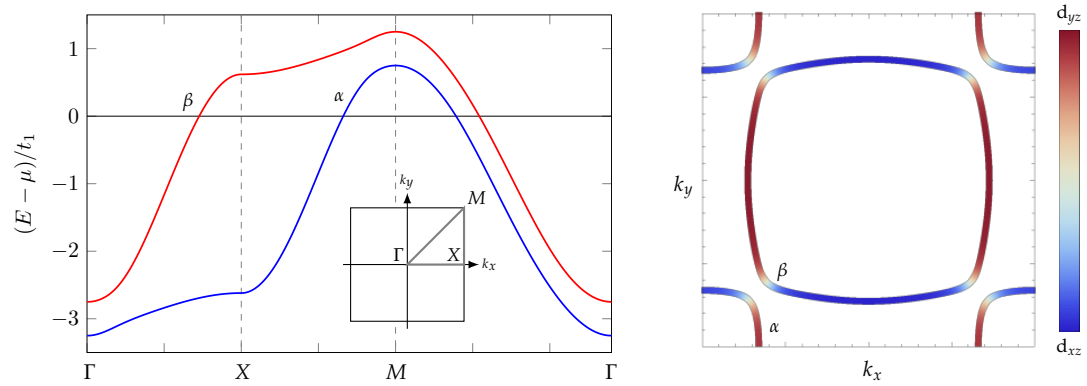

(A) Band structure (inset: high symmetry points in the first Brillouin zone)

(B) Fermi surface

FIGURE 3.2: The normal state energy spectrum of strontium ruthenate within our model. (A) is a "spaghatti plot" showing the dispersion of the two doubly-degenerate bands between specific high symmetry points (see inset), while (B) shows the orbital character of the bands at the Fermi surface.

surface in Figure 3.2 B is exact for our model, but corresponds to a 2D slice of the true Fermi surface in three dimensions (refer to Figure 1.2). The α and β bands arise from the hybridisation of the d_{xz} and d_{yz} orbitals, as indicated by the colour scheme in Figure 3.2 B. As mentioned above, I adjusted the value of t_2 to achieve agreement with Figure 1.2 B regarding the shape of the β sheet.

3.3.2 General form of $\tilde{\Delta}$

We now turn to the pairing potential, and see what we can determine about its form by enforcing the five assumptions from above. As has already been shown, enforcing the first requirement reduces to $H_{\boldsymbol{k}}^\dagger = H_{\boldsymbol{k}}$, which places no restriction on the form of Δ as the pairing part of the BdG Hamiltonian is Hermitian by construction. The second requirement is that $\mathcal{H}$ is antisymmetric under particle exchange, which was enforced in (2.9), but is restated in matrix form here:

$$\Delta_{\boldsymbol{k}}, = -\Delta_{-\boldsymbol{k}}^T. \tag{3.44}$$

Quite generally, this tells us that the terms that compose Δ must be of the form

$$\begin{cases} \textit{odd } \boldsymbol{k} \text{ dependence} \otimes \text{orbital-spin matrix that is } \textit{even} \text{ under transposition, or} \\ \textit{even } \boldsymbol{k} \text{ dependence} \otimes \text{orbital-spin matrix that is } \textit{odd} \text{ under transposition.} \end{cases} \tag{3.45}$$

Using the Pauli matrix decomposition, (3.3), we note that each of the Pauli matrices are even under transposition, with the exception of σ_2, which is odd, so (3.45) can be written

$$\begin{cases} \textit{odd } \boldsymbol{k} \text{ dependence} \otimes \{\{\eta_0, \eta_1, \eta_3\} \otimes \{\sigma_0, \sigma_1, \sigma_3\},\ \eta_2 \otimes \sigma_2\}, \text{ or} \\ \textit{even } \boldsymbol{k} \text{ dependence} \otimes \{\{\eta_0, \eta_1, \eta_3\} \otimes \sigma_2,\ \eta_2 \otimes \{\sigma_0, \sigma_1, \sigma_3\}\}. \end{cases} \tag{3.46}$$

Finally, when written in terms of $\tilde{\Delta}$, as defined in (2.31), (3.46) becomes

$$\begin{cases} \textit{odd } \boldsymbol{k} \text{ dependence} \otimes \{\{\eta_0, \eta_1, \eta_3\} \otimes \{\sigma_1, \sigma_2, \sigma_3\},\ \eta_2 \otimes \sigma_0, \}, \text{ or} \\ \textit{even } \boldsymbol{k} \text{ dependence} \otimes \{\{\eta_0, \eta_1, \eta_3\} \otimes \sigma_0,\ \eta_2 \otimes \{\sigma_1, \sigma_2, \sigma_3\}\}. \end{cases} \tag{3.47}$$

Unlike the normal state, the superconducting state is allowed to break time-reversal and crystal symmetries such as inversion, so when it comes to the form of $\tilde{\Delta}$ we have no need to enforce the third and fourth assumptions from above. However, $\tilde{\Delta}$ can still be written as a linear combination of individual terms belonging to irreducible representations of D_{4h}. At this point there is a lot of freedom as to the form of the momentum dependent coefficients, $\Delta_{\boldsymbol{k},\alpha\beta}$. In fact, there are an unlimited number of possibilities, so I approach this by *choosing* some simple forms for $\Delta_{\boldsymbol{k},\alpha\beta}$. When an even function of momentum is needed I take the trivial case $\Delta_{\boldsymbol{k},\alpha\beta} = 1$, which is s-wave and belongs to A_{1g}. When an odd function of momentum is needed I take $\Delta_{\boldsymbol{k},\alpha\beta}$ to be a linear combination of $\sin k_x a$ and $\sin k_y a$, which are p-wave, and form the basis of an E_u irrep. I choose $\{\sin k_x a, \sin k_y a\}$ rather than, say, $\{k_x, k_y\}$ so that the resulting states will be regularised to a square lattice with lattice constant a. A square lattice is appropriate when considering the projection of a tetragonal crystal into two dimensions. For simplicity I will set $a = 1$, essentially defining a length scale to be used throughout this thesis. These p-wave functions are justified in the context of constructing a chiral p-wave model of strontium ruthenate, although, as discussed in Section 1.3.1, there is recent experimental evidence against such a pairing state. This is not too much of an issue since the model we are constructing was only ever meant to be illustrative, and also justifies keeping the s-wave terms for now. Referring back to (3.47), we see that the form of the terms composing $\tilde{\Delta}$ are restricted to

$$\begin{cases} \{\sin k_x, \sin k_y\} \otimes \{\{\eta_0, \eta_1, \eta_3\} \otimes \sigma_0,\ \eta_2 \otimes \{\sigma_1, \sigma_2, \sigma_3\}\}, \text{ or} \\ 1 \otimes \{\{\eta_0, \eta_1, \eta_3\} \otimes \{\sigma_1, \sigma_2, \sigma_3\},\ \eta_2 \otimes \sigma_0\}. \end{cases} \tag{3.48}$$

In order to determine the resulting irrep of each term we can use the direct product table. This is rather easy for most terms in (3.48) for which we are taking the product between two 1D irreps, or a 2D irrep and a 1D irrep. For example, Table 3.4 tells us that $\eta_3 \otimes \sigma_0$ belongs to B_{1g}, and hence $1 \otimes \eta_3 \otimes \sigma_0$ does as well. Things becomes more complicated when we want to combine two 2D irreps, i.e. the E_u momentum irrep $\{\sin k_x a, \sin k_y a\}$ with one of the E_g orbital $\otimes$ spin matrices. As an example, let us consider $\{\sin k_x, \sin k_y\} \otimes \{\eta_0 \otimes \sigma_1,\ \eta_0 \otimes \sigma_2\}$. Table 3.3 tells us

$$E_u \otimes E_g = A_{1u} \oplus A_{2u} \oplus B_{1u} \oplus B_{2u}, \tag{3.49}$$

which is to say that we should expect four resulting terms, and that their irreps will be A_{1u}, A_{2u}, B_{1u}, and B_{2u}. Let us naively guess that the four terms will be $\sin k_x\ \eta_0 \otimes \sigma_1$, $\sin k_x\ \eta_0 \otimes \sigma_2$, $\sin k_y\ \eta_0 \otimes \sigma_1$, and $\sin k_y\ \eta_0 \otimes \sigma_2$. Unfortunately (3.49) does not tell us which of these terms belongs to which irrep, so we must consider the behaviour of each resulting term under the generating symmetries:

$\tilde{\Delta}$ term	$\mathcal{C}_4$	$\mathcal{C}_2'$	$\mathcal{I}$
$\sin k_x\ \eta_0 \otimes \sigma_1$	$\sin k_y\ \eta_0 \otimes \sigma_2$	$\sin k_x\ \eta_0 \otimes \sigma_1$	$-\sin k_x\ \eta_0 \otimes \sigma_1$
$\sin k_x\ \eta_0 \otimes \sigma_2$	$-\sin k_y\ \eta_0 \otimes \sigma_1$	$-\sin k_x\ \eta_0 \otimes \sigma_2$	$-\sin k_x\ \eta_0 \otimes \sigma_1$
$\sin k_y\ \eta_0 \otimes \sigma_1$	$-\sin k_x\ \eta_0 \otimes \sigma_2$	$-\sin k_y\ \eta_0 \otimes \sigma_1$	$-\sin k_y\ \eta_0 \otimes \sigma_1$
$\sin k_y\ \eta_0 \otimes \sigma_2$	$\sin k_x\ \eta_0 \otimes \sigma_1$	$\sin k_y\ \eta_0 \otimes \sigma_2$	$-\sin k_y\ \eta_0 \otimes \sigma_1$

At first glance there seems to be a problem here: we cannot assign a character to any of the terms under the $\mathcal{C}_4$ and $\mathcal{C}_2'$ symmetries. However, we have just been a bit narrow-minded: rather than dealing with the four terms presented here, we must instead consider linear combinations. By eye-balling the transformations under the generating symmetries we can determine that the following terms have definite characters under each of the generating symmetries, and hence we can determine which irrep they belong to:

$\tilde{\Delta}$ term	Irrep	Momentum	Orbital	Spin
$\eta_0 \otimes \sigma_0$	A_{1g}	s-wave (e)	e	singlet (o)
$\eta_2 \otimes \sigma_3$	A_{1g}	s-wave (e)	o	triplet (e)
$\eta_3 \otimes \sigma_0$	B_{1g}	s-wave (e)	e	singlet (o)
$\eta_1 \otimes \sigma_0$	B_{2g}	s-wave (e)	e	singlet (o)
$\{\eta_2 \otimes \sigma_1, \eta_2 \otimes \sigma_2\}$	E_g	s-wave (e)	o	triplet (e)
$\sin k_x\ \eta_3 \otimes \sigma_1 - \sin k_y\ \eta_3 \otimes \sigma_2$	A_{1u}	p-wave (o)	e	triplet (e)
$\sin k_x\ \eta_1 \otimes \sigma_2 + \sin k_y\ \eta_1 \otimes \sigma_1$	A_{1u}	p-wave (o)	e	triplet (e)
$\sin k_x\ \eta_0 \otimes \sigma_1 + \sin k_y\ \eta_0 \otimes \sigma_2$	A_{1u}	p-wave (o)	e	triplet (e)
$\sin k_x\ \eta_3 \otimes \sigma_2 + \sin k_y\ \eta_3 \otimes \sigma_1$	A_{2u}	p-wave (o)	e	triplet (e)
$\sin k_x\ \eta_1 \otimes \sigma_1 - \sin k_y\ \eta_1 \otimes \sigma_2$	A_{2u}	p-wave (o)	e	triplet (e)
$\sin k_x\ \eta_0 \otimes \sigma_2 - \sin k_y\ \eta_0 \otimes \sigma_1$	A_{2u}	p-wave (o)	e	triplet (e)
$\sin k_x\ \eta_3 \otimes \sigma_1 + \sin k_y\ \eta_3 \otimes \sigma_2$	B_{1u}	p-wave (o)	e	triplet (e)
$\sin k_x\ \eta_1 \otimes \sigma_2 - \sin k_y\ \eta_1 \otimes \sigma_1$	B_{1u}	p-wave (o)	e	triplet (e)
$\sin k_x\ \eta_0 \otimes \sigma_1 - \sin k_y\ \eta_0 \otimes \sigma_2$	B_{1u}	p-wave (o)	e	triplet (e)
$\sin k_x\ \eta_3 \otimes \sigma_2 - \sin k_y\ \eta_3 \otimes \sigma_1$	B_{2u}	p-wave (o)	e	triplet (e)
$\sin k_x\ \eta_1 \otimes \sigma_1 + \sin k_y\ \eta_1 \otimes \sigma_2$	B_{2u}	p-wave (o)	e	triplet (e)
$\sin k_x\ \eta_0 \otimes \sigma_2 + \sin k_y\ \eta_0 \otimes \sigma_1$	B_{2u}	p-wave (o)	e	triplet (e)
$\{\sin k_x\ \eta_0 \otimes \sigma_3,\ \sin k_y\ \eta_0 \otimes \sigma_3\}$	E_u	p-wave (o)	e	triplet (e)
$\{\sin k_x\ \eta_1 \otimes \sigma_3,\ \sin k_y\ \eta_1 \otimes \sigma_3\}$	E_u	p-wave (o)	e	triplet (e)
$\{\sin k_x\ \eta_2 \otimes \sigma_0,\ \sin k_y\ \eta_2 \otimes \sigma_0\}$	E_u	p-wave (o)	o	singlet (o)
$\{\sin k_x\ \eta_3 \otimes \sigma_3,\ \sin k_y\ \eta_3 \otimes \sigma_3\}$	E_u	p-wave (o)	e	triplet (e)

TABLE 3.5: Once we have restricted the form of the momentum-dependent coefficients, there are 26 pairing terms in our model. These are listed, along with the irreducible representation to which they belong, and the exchange symmetry of their momentum, orbital, and spin states.

$\tilde{\Delta}$ term	ν_{C_4}	$\nu_{C_2'}$	ν_I	Irrep
$\sin k_x\ \eta_0 \otimes \sigma_1 + \sin k_y\ \eta_0 \otimes \sigma_2$	1	1	−1	A_{1u}
$\sin k_x\ \eta_0 \otimes \sigma_2 + \sin k_y\ \eta_0 \otimes \sigma_1$	−1	−1	−1	B_{2u}
$\sin k_x\ \eta_0 \otimes \sigma_1 - \sin k_y\ \eta_0 \otimes \sigma_2$	−1	1	−1	B_{1u}
$\sin k_x\ \eta_0 \otimes \sigma_2 - \sin k_y\ \eta_0 \otimes \sigma_1$	1	−1	−1	A_{2u}

This process must be repeated for each combination of momentum and matrix terms in (3.48). The resulting terms, and the irreps they belong to, are presented in Table 3.5. For each term I have also stated whether the orbital degree of freedom is even or odd under particle exchange (implemented by matrix transposition), and whether it is spin-singlet or spin-triplet (which correspond to the spin degree of freedom being odd or even under particle exchange respectively). Note that the s-wave spin-triplet and p-wave spin-singlet states can only exist because the orbital degree is odd under particle exchange.

Finally, we want to restrict this model to two spatial dimensions. The momentum dependence of the even-parity terms was chosen to be 1, which belongs to A_{1g}. Table 2.1 tells us that A_{1g} terms have a character of $+1$ under the σ_h reflection, which is unsurprising. Similarly, the odd-parity terms have E_u momentum dependence, and therefore a character of $+2$ under σ_h. For this reason, unlike H_0, we are unable to eliminate any terms from Table 3.5.

3.4 Chiral pairing states

In this thesis I am ultimately interested in superconducting states with a non-zero anomalous Hall conductivity, which requires TRSB. As shown in Section 2.2.1, time-reversal is broken if $\tilde{\Delta} \neq \tilde{\Delta}^\dagger$. One might think that any of the states listed in Table 3.5 could be TRSB if they had a complex-valued

amplitude, such as $\tilde{\Delta} = \Delta_0 \eta_0 \otimes \sigma_0$ where $\Delta_0 \in \mathbb{C}$. However, as discussed in Section 2.1.1, we can always choose a gauge such that Δ_0 is real-valued, so this is not the case.

A chiral pairing state is one in which the phase of the pairing potential winds as $\boldsymbol{k}$ moves about some axis on the Fermi surface of the underlying material [42]. For example, the state

$$\tilde{\Delta} = \Delta_0(\sin k_x + i \sin k_y)\eta_0 \otimes \sigma_3, \tag{3.50}$$

constructed as a complex superposition of terms from the first E_u irrep in Table 3.5 undergoes a phase winding of 2π as we move in a loop about z axis. It breaks time-reversal symmetry no matter the phase of Δ_0, since $\tilde{\Delta}^\dagger = \Delta_0^*(\sin k_x - i \sin k_y)\eta_0 \otimes \sigma_3$. Before we continue, it is worth considering why a superconductor would even be chiral in the first place. Ultimately this comes down to a question of energy minimisation. The free energy of a superconducting state is given by Ginzburg–Landau theory, and is generically dependent on $\sim |\Delta_{\boldsymbol{k}}|^2$, averaged over the Fermi Surface [42]. This is why the opening of a band gap is essential for stabilising the superconducting state, as discussed in Section 1.1.1. Unconventional superconductors tend to develop momentum-dependent "nodes" in the gap. As an example, consider the fist A_{1u} state in Table 3.5, which vanishes at $\boldsymbol{k} = \boldsymbol{0}, (0, \pi), (\pi, 0)$, and (π, π). These are called *point nodes*. Nodal structure in the pairing potential is generally bad for superconductivity as it reduces the average gap magnitude. However, if two pairing states, say Δ_1 and Δ_2, happen to be degenerate it is possible to form the pairing state $a\Delta_1 + b\Delta_2$ as a linear superposition. Without going into the details, Ginzburg–Landau theory tells us that the free energy is always minimised by taking (a, b) to have one of the following forms [23]: $(\Delta_0, 0)$, $(0, \Delta_0)$, $(\Delta_0, \pm\Delta_0)$, or $(\Delta_0, \pm i\Delta_0)$, which limits the possible relative phase and magnitude of the two terms. The last of these, corresponding to a chiral state, maximises the gap magnitude over the Brillouin zone, and so will often be preferred from an energy minimisation point of view. A more precise analysis as to the preferred pairing state requires the microscopic details of a given system, but I am only trying to motivate why a chiral state might be favoured, as we already know they occur in strontium ruthenate (refer to Section 1.3).

3.4.1 Chiral states within 2D irreps

The easiest way to find degenerate pairing potentials is if they belong to the same two-dimensional irrep: if the symmetries of the crystal allow two states to be transformed into each other they must have the same energy. Further, a chiral state is the most natural way for a two-dimensional irrep to break time-reversal. As an example, consider the first of the E_u irreps from Table 3.5. A pairing state belonging to this irrep can be written completely generally as

$$\tilde{\Delta}_{\boldsymbol{k}} = \Delta_{0,x} \sin k_x \eta_0 \otimes \sigma_3 + \Delta_{0,y} \sin k_y \eta_0 \otimes \sigma_3, \tag{3.51}$$

where $\Delta_{0,x}$ and $\Delta_{0,y}$ are complex numbers. Currently there is complete freedom over the phase and magnitude of both $\Delta_{0,x}$ and $\Delta_{0,y}$, but the Ginzburg–Landau argument from above reduces the possibilities. In particular, I choose the $(\Delta_{0,x}, \Delta_{0,y}) = (\Delta_0, \pm i\Delta_0)$ chiral state. The $\pm$ cases are degenerate, so I choose the $+$ case, and we end up with (3.50). The other choice corresponds to the opposite *chirality*, which is to say the phase winds in the opposite direction. In terms of the polar Kerr effect the only difference would be that the reflected light would be rotated in the opposite direction. The exact same argument applies to pairing states constructed from all four of the E_u irreps. We can write a general E_u pairing state as

$$\tilde{\Delta}_{\boldsymbol{k}} = \Delta_{\boldsymbol{k},01}\eta_0 \otimes \sigma_3 + \Delta_{\boldsymbol{k},11}\eta_1 \otimes \sigma_3 + \Delta_{\boldsymbol{k},22}\eta_2 \otimes \sigma_0 + \Delta_{\boldsymbol{k},31}\eta_3 \otimes \sigma_3, \tag{3.52}$$

where

$$\Delta_{\boldsymbol{k},01} = \Delta_{0,01}(\sin k_x + i \sin k_y), \tag{3.53}$$
$$\Delta_{\boldsymbol{k},11} = \Delta_{0,11}(\sin k_y + i \sin k_x), \tag{3.54}$$
$$\Delta_{\boldsymbol{k},22} = \Delta_{0,22}(\sin k_x + i \sin k_y), \tag{3.55}$$
$$\Delta_{\boldsymbol{k},31} = \Delta_{0,31}(\sin k_x - i \sin k_y). \tag{3.56}$$

Note that once I chose the $\sin k_x + i \sin k_y$ form for Δ_{01}, the chirality of the other three terms was fixed by requiring that all four terms transform in exactly the same way under the D_{4h} symmetries. The chirality of $\Delta_{\boldsymbol{k},01}$ and $\Delta_{\boldsymbol{k},22}$ is opposite that of $\Delta_{\boldsymbol{k},11}$ and $\Delta_{\boldsymbol{k},31}$. There is still freedom over the relative magnitude and phase of all four terms, although this will be addressed in Chapter 6.

As well as the E_u irreps, Table 3.5 also includes one E_g irrep. Although it has trivial momentum dependence in the orbital-spin basis, it may have some explicit nontrivial momentum dependence when projected into a different basis. For this reason, a pairing state of the form

$$\tilde{\Delta} = \Delta_0 \left(\eta_2 \otimes \sigma_1 + i\eta_2 \otimes \sigma_2\right) \tag{3.57}$$

can be chiral. This state will be readdressed in the next chapter.

3.4.2 Chiral superpositions of 1D irreps

Although superconducting states belonging to the same multi-dimensional irrep are *required* to be degenerate, it is *possible* that any two states happen to be close enough in energy to form a chiral state [36]. These mixed-irrep states tend to be more likely in systems with some externally tunable parameter that affects the relative energy of the respective pairing states, and have been proposed in materials such as UTe_2 [80, 81], $U_{1-x}Th_xBe_{13}$ [82], and even strontium ruthenate [83, 84]. It is conceivable that the pairing state in strontium ruthenate is formed as a chiral superposition of say the first A_{1u} and the first A_{2u} terms in Table 3.5, i.e.

$$\tilde{\Delta}_{\boldsymbol{k}} = (\sin k_x + i \sin k_y)\eta_3 \otimes \sigma_1 \pm (i \sin k_x - \sin k_y)\eta_3 \otimes \sigma_2. \tag{3.58}$$

States of this form will be revisited in Chapter 6. Pairing states involving terms from, say, two different A_{1u} irreps are also plausible, but would not be chiral, so are irrelevant for our purposes.

Summary

This chapter has developed a simple two-orbital model of superconductivity in strontium ruthenate by utilising physical arguments to determine which terms can appear in the H_0 and Δ matrices. Simple, physically motivated momentum dependences were chosen for each term. By restricting the model to two dimensions we found four terms to be permitted in the normal state, along with 26 pairing terms. The possibility of chiral pairing states was examined due to their relevance to the anomalous Hall effect, and these will be further considered in the following chapters.

Chapter 4

Stability of the superconducting state

So far we have constructed a simple two-orbital model of superconductivity in strontium ruthenate, which includes the 26 pairing terms listed in Table 3.5. A general pairing state within this model could involve an arbitrary superposition of these terms, although experimental and theoretical results have motivated us to only consider chiral pairing states, which can be constructed as a complex superposition of two terms. However, an arbitrary chiral state will not necessarily exhibit an anomalous Hall conductivity, or even form a stable pairing state. The conditions that lead to a non-zero Hall conductivity are considered in the next chapter, while the stability of the various terms in Table 3.5 are the focus of this chapter.

Referring to Figure 1.1, and the related discussion in Section 1.1.2, we recall that a band gap can be opened either at the Fermi surface, corresponding to the pairing of electrons from the same normal state energy band, or away from the Fermi surface, corresponding to the pairing of electrons from different bands. The resulting pairing is said to be intra- or interband respectively, and a general superconducting state can involve both. Within the "weak-coupling" approximation, the opening of a band gap across the Fermi surface is essential for stabilising the superconducting state [32, 73] as it leads to a finite energy gap between the occupied and unoccupied states. A weak-coupling approach is justified in the case that the pairing potential is of a much smaller energy scale that the normal state parameters, or equivalently, when the critical temperature is much smaller than the Fermi temperature, which is the case for strontium ruthenate ($k_B T_c \approx 1.2 \times 10^{-4}$ eV [57] and $\epsilon_F \approx 0.4$ eV [26, 78]). A superconducting state with less intraband pairing will have a lower critical temperature, and ultimately the absence of intraband pairing implies that there will not be a transition to a superconducting state at all. On the other hand, interband pairing is generally considered to be detrimental to the formation of a superconducting state as it competes with the intraband pairing [31, 32].

In this section I will examine the presence of intra- and interband pairing in the terms included in our model. Unfortunately, the orbital-spin basis used to construct these terms does not directly provide us with information as to which energy band the paired electrons originate from, so we must consider the "pseudospin-band" basis, which is introduced in Section 4.1. The explicit transformation from a orbital-spin basis to the pseudospin-band basis can get complicated. Rather than working through these calculation, I will instead use the concept of *superconducting fitness* to examine the stability of the pairing terms in our model. This approach is introduced in Section 4.2, and allows us to gain insight into the intra- and interband nature of the pairing, all while working in the orbital-spin basis. While the superconducting fitness is a well understood, albeit relatively recent concept, the calculations and analysis in Section 4.2.1 are specific to our model and have not been performed before.

4.1 The pseudospin-band basis

Our model of strontium ruthenate involves three degrees of freedom: momentum, spin, and orbital. Each of the internal degrees of freedom have two possible values, so there must be four distinct eigenstates at each value of $\boldsymbol{k}$. In general, each of these eigenstates can have a different energy, but when it comes to the normal state we are subject to Kramer's theorem, which states that time-reversal symmetric systems with half-integer spin have doubly-degenerate eigenstates [33]. Specifically, the eigenstate $|\psi\rangle$ is degenerate with its time-reversed counterpart $\Theta|\psi\rangle$. This can be shown by writing the single-particle normal state eigenstates as $|\boldsymbol{k}, s, n\rangle$, i.e.

$$H_0|\boldsymbol{k}, s, n\rangle = E_{\boldsymbol{k}sn}|\boldsymbol{k}, s, n\rangle\,, \tag{4.1}$$

where, despite suggestive notation, we do not currently know how to interpret the s and n labels. As $\mathcal{H}_0$ is symmetric under time-reversal, we have $\Theta H_0 = H_0\Theta$, and hence

$$H_0\Theta|\boldsymbol{k}, s, n\rangle = \Theta H_0|\boldsymbol{k}, s, n\rangle = \Theta E_{\boldsymbol{k}sn}|\boldsymbol{k}, s, n\rangle = E_{\boldsymbol{k}sn}\Theta|\boldsymbol{k}, s, n\rangle\,, \tag{4.2}$$

where the last step is allowed because energy eigenvalues are real-valued. This says that the state $|\boldsymbol{k}, s, n\rangle$ is degenerate with the state $\Theta|\boldsymbol{k}, s, n\rangle$. Bear in mind that $\Theta|\boldsymbol{k}\rangle = |-\boldsymbol{k}\rangle$, so we have not yet unveiled a degeneracy at each value of $\boldsymbol{k}$, but we can go a step further because the normal state is also symmetric under spatial inversion. We therefore have

$$H_0\mathcal{I}\Theta|\boldsymbol{k}, s, n\rangle = \mathcal{I}\Theta H_0|\boldsymbol{k}, s, n\rangle = E_{\boldsymbol{k}sn}\mathcal{I}\Theta|\boldsymbol{k}, s, n\rangle\,, \tag{4.3}$$

which is to say that $|\boldsymbol{k}, s, n\rangle$ is degenerate with $\mathcal{I}\Theta|\boldsymbol{k}, s, n\rangle$. Noting that

$$\mathcal{I}\Theta|\boldsymbol{k}\rangle = \mathcal{I}|-\boldsymbol{k}\rangle = |\boldsymbol{k}\rangle\,, \tag{4.4}$$

we can conclude that the states $|s, n\rangle$ and $\mathcal{I}\Theta|s, n\rangle$ are degenerate *at each value of* $\boldsymbol{k}$. In other words, the $|\boldsymbol{k}, s, n\rangle$ eigenstates form two doubly-degenerate energy bands. This argument is entirely general, in the sense that it does not depend on how the orbital or spin degrees of freedom transform under inversion or time-reversal. I choose to let n label the energy band, which will be unaffected by both time-reversal and inversion. In the case of two energy bands, as we have here, it is convenient to write $|n\rangle = |\pm\rangle$, referring to the upper and lower bands given by (3.39). I refer to s as the *pseudospin*, because it is possible to choose a basis such that it transforms as spin does under both inversion and time-reversal[1] [86, 87], i.e.

$$\mathcal{I}|\boldsymbol{k}, s, n\rangle = |-\boldsymbol{k}, s, n\rangle\,, \tag{4.5}$$

$$\Theta|\boldsymbol{k}, s, n\rangle = s|-\boldsymbol{k}, -s, n\rangle\,, \tag{4.6}$$

where $s = \pm$ labels the two possible pseudospin states.

4.1.1 The gamma matrices and the flattened Hamiltonian

For the following discussion it will be convenient to introduce a set of five *gamma matrices*, $\{\gamma^i\}$, which are defined in Table 4.1 in terms of the orbital $\otimes$ spin matrices that appear in (3.34), and satisfy the following properties:

[1] This is true when the pseudospin is defined as a linear combination of the orbital and spin degrees of freedom, as is the case here. Other usages of the term "pseudospin" do not satisfy this criteria. See, for example, Ref. [85].

Orbital $\otimes$ spin matrix	Gamma matrix
$\eta_0 \otimes \sigma_0$	γ^0
$\eta_1 \otimes \sigma_0$	γ^1
$\eta_3 \otimes \sigma_0$	γ^2
$\eta_2 \otimes \sigma_1$	γ^3
$\eta_2 \otimes \sigma_2$	γ^4
$\eta_2 \otimes \sigma_3$	γ^5
$\eta_2 \otimes \sigma_0$	$i\gamma^1\gamma^2$
$\eta_1 \otimes \sigma_1$	$i\gamma^2\gamma^3$
$\eta_1 \otimes \sigma_2$	$i\gamma^2\gamma^4$
$\eta_1 \otimes \sigma_3$	$i\gamma^2\gamma^5$
$\eta_3 \otimes \sigma_1$	$i\gamma^3\gamma^1$
$\eta_0 \otimes \sigma_2$	$i\gamma^3\gamma^5$
$\eta_3 \otimes \sigma_2$	$i\gamma^4\gamma^1$
$\eta_0 \otimes \sigma_3$	$i\gamma^4\gamma^3$
$\eta_3 \otimes \sigma_3$	$i\gamma^5\gamma^1$
$\eta_0 \otimes \sigma_1$	$i\gamma^5\gamma^4$

TABLE 4.1: The definition of the gamma matrices used in this thesis (first six rows), along with expressions for the orbital $\otimes$ spin matrices that do not appear in H_0 in terms of these gamma matrices (last ten rows).

1. $(\gamma^i)^\dagger = \gamma^i$, i.e. they are Hermitian,
2. $(\gamma^i)^2 = \gamma^0$, and
3. $\gamma^i\gamma^j = -\gamma^j\gamma^i$ for $i \neq j$.

The last two of these properties further imply that

4. $[\gamma^i, \gamma^j] = 0$ for $i = j$ and $2\gamma^i\gamma^j$ for $i \neq j$, and
5. $\{\gamma^i, \gamma^j\} = 2\gamma^0\delta_{ij}$, where δ_{ij} is the Kronecker delta.

By design, H_0, as given by (3.34), can be written as a linear combination of all five gamma matrices, along with $\gamma^0 = \mathbb{1}$:

$$H_{0,\boldsymbol{k}} = \sum_{n=0}^{5} c_{\boldsymbol{k},n}\gamma^n, \tag{4.7}$$

where c_n are real-valued even functions of momentum. We identify $c_0 = h_{00}$, $c_1 = h_{10}$, $c_2 = h_{30}$, $c_3 = h_{21}$, $c_4 = h_{22}$, and $c_5 = h_{23}$. In fact, any two-orbital system that is symmetric under both inversion and time-reversal can be written in terms of a set of gamma matrices that satisfy these properties, although the specific matrices will depend on the details of the system. To understand why this is the case, note that (3.34) was derived in the case that $U_I = \eta_0 \otimes \sigma_0$ and $U_T = \eta_0 \otimes i\sigma_2$, which also happen to describe how the pseudospin-band eigenstates transform in (4.5) and (4.6). This is to say that H_0 can be written as (4.7) *in the pseudospin-band basis* for any two-orbital system with inversion and time-reversal symmetry. When transformed back to the orbital-spin basis the specific form of the gamma matrices may change (although not in our case), but they must still satisfy the properties outlined above.

For future reference it is convenient to define the "flattened" normal state Hamiltonian:

$$\tilde{H}_{0,\boldsymbol{k}} = \frac{H_{0,\boldsymbol{k}} - c_{\boldsymbol{k},0}\gamma^0}{|\boldsymbol{c}_{\boldsymbol{k}}|} = \sum_{n=1}^{5} \frac{c_{\boldsymbol{k},n}}{|\boldsymbol{c}_{\boldsymbol{k}}|}\gamma^n = \sum_{n=1}^{5} \hat{c}_{\boldsymbol{k},n}\gamma^n, \tag{4.8}$$

where $\boldsymbol{c} = (c_1, c_2, c_3, c_4, c_5)$ is a vector of the momentum-dependent coefficients, and $\hat{c}_{n,\boldsymbol{k}}$ are the corresponding unit vectors, such that

$$\sum_{n=1}^{5} \hat{c}_{\boldsymbol{k},n}^2 = 1. \tag{4.9}$$

Notationally, I will tend to drop the explicit $\boldsymbol{k}$ index from the $c_{n,\boldsymbol{k}}$ coefficients. Using the properties of the gamma matrices outlined above, we see that $\tilde{H}_0$ satisfies

$$\tilde{H}_0^2 = \gamma^0. \tag{4.10}$$

Further, from (3.39), the eigenvalues of H_0 are given by $E_{\boldsymbol{k}\pm} = c_0 \pm |\boldsymbol{c}|$, and therefore the flattened Hamiltonian satisfies the eponymous property that

$$\tilde{H}_{0,\boldsymbol{k}} |\boldsymbol{k}, s, \pm\rangle = \pm |\boldsymbol{k}, s, \pm\rangle , \tag{4.11}$$

where $|\pm\rangle$ indicates the band degree of freedom. Finally, (4.11) can be used to show that $\tilde{H}_0$ can be interpreted in terms of the projection operator onto the $|\pm\rangle$ band:

$$\mathcal{P}_\pm = \frac{\gamma^0 \pm \tilde{H}_0}{2}. \tag{4.12}$$

Once restricted to two spatial dimensions, we set $c_3 = c_4 = 0$ so as to obtain (3.38), in which case it is to be understood that $\hat{c}_i = c_i / \sqrt{c_1^2 + c_2^2 + c_5^2}$

4.2 The superconducting fitness functions

In the pseudospin-band basis the pairing potential is written in the general form

$$\Delta_{\boldsymbol{k}} = \begin{pmatrix} \Delta_{\boldsymbol{k},++} & \Delta_{\boldsymbol{k},+-} \\ \Delta_{\boldsymbol{k},-+} & \Delta_{\boldsymbol{k},--} \end{pmatrix}, \tag{4.13}$$

where $\Delta_{\pm\pm'} = \langle \pm | \, \Delta \, | \pm' \rangle$ are 2×2 matrices in pseudospin space. The overall strength of the pairing can be quantified by adding together $|\Delta_{ij}|^2$ for each element of Δ, i.e.

$$\mathrm{Tr}\{\Delta\Delta^\dagger\} = \mathrm{Tr}\{\Delta_{++}\Delta_{++}^\dagger + \Delta_{+-}\Delta_{+-}^\dagger + \Delta_{-+}\Delta_{-+}^\dagger + \Delta_{--}\Delta_{--}^\dagger\}, \tag{4.14}$$

where $\Delta_{\pm\pm'}^\dagger = \langle \pm | \, \Delta \, | \pm' \rangle^\dagger = \langle \pm' | \, \Delta^\dagger \, | \pm \rangle$, so

$$\begin{aligned} \mathrm{Tr}\{\Delta_{\pm\pm'}\Delta_{\pm\pm'}^\dagger\} &= \sum_{s,s'} \langle s, \pm | \, \Delta \, | s', \pm' \rangle \langle s', \pm' | \, \Delta^\dagger \, | s, \pm \rangle \\ &= \sum_{s,s'} \langle s | \, \mathcal{P}_\pm \Delta \mathcal{P}_{\pm'} \, | s' \rangle \langle s' | \, \mathcal{P}_{\pm'} \Delta^\dagger \mathcal{P}_\pm \, | s \rangle \\ &= \sum_{s} \langle s | \, \mathcal{P}_\pm \Delta \mathcal{P}_{\pm'} \mathcal{P}_{\pm'} \Delta^\dagger \mathcal{P}_\pm \, | s \rangle = \mathrm{Tr}\{\mathcal{P}_\pm \Delta \mathcal{P}_{\pm'} \mathcal{P}_{\pm'} \Delta^\dagger \mathcal{P}_\pm\}. \end{aligned}$$

Considering the intra- and interband contributions to (4.14) separately, we can write

$$\mathrm{Tr}\{\Delta_{++}\Delta_{++}^\dagger + \Delta_{--}\Delta_{--}^\dagger\} = \mathrm{Tr}\{\mathcal{P}_+\Delta\mathcal{P}_+\mathcal{P}_+\Delta^\dagger\mathcal{P}_+ + \mathcal{P}_-\Delta\mathcal{P}_-\mathcal{P}_-\Delta^\dagger\mathcal{P}_-\}, \tag{4.15}$$

$$\mathrm{Tr}\{\Delta_{+-}\Delta_{+-}^\dagger + \Delta_{-+}\Delta_{-+}^\dagger\} = \mathrm{Tr}\{\mathcal{P}_+\Delta\mathcal{P}_-\mathcal{P}_-\Delta^\dagger\mathcal{P}_+ + \mathcal{P}_-\Delta\mathcal{P}_+\mathcal{P}_+\Delta^\dagger\mathcal{P}_-\}. \tag{4.16}$$

Focussing on just the intraband pairing for now, we can use the cyclic nature of the trace and the fact that $\mathcal{P}_i\mathcal{P}_i = \mathcal{P}_i$ to write (4.15) as

$$\mathrm{Tr}\{\Delta_{++}\Delta_{++}^\dagger + \Delta_{--}\Delta_{--}^\dagger\} = \mathrm{Tr}\{\mathcal{P}_+\Delta\mathcal{P}_+\Delta^\dagger + \mathcal{P}_-\Delta\mathcal{P}_-\Delta^\dagger\}.$$

Substituting in (4.12) and (2.31) yields

$$\begin{aligned}\mathrm{Tr}\{\Delta_{++}\Delta_{++}^\dagger + \Delta_{--}\Delta_{--}^\dagger\} &= \frac{1}{4}\mathrm{Tr}\{(\gamma^0+\tilde{H}_0)\tilde{\Delta}U_T(\gamma^0+\tilde{H}_0)U_T^\dagger\tilde{\Delta}^\dagger + (\gamma^0-\tilde{H}_0)\tilde{\Delta}U_T(\gamma^0-\tilde{H}_0)U_T^\dagger\tilde{\Delta}^\dagger\}\\ &= \frac{1}{4}\mathrm{Tr}\{(\gamma^0+\tilde{H}_0)\tilde{\Delta}(\gamma^0+\tilde{H}_0)\tilde{\Delta}^\dagger + (\gamma^0-\tilde{H}_0)\tilde{\Delta}(\gamma^0-\tilde{H}_0)\tilde{\Delta}^\dagger\}\\ &= \frac{1}{4}\mathrm{Tr}\{2\tilde{H}_0\tilde{\Delta}\tilde{H}_0\tilde{\Delta}^\dagger + 2\tilde{\Delta}\tilde{\Delta}^\dagger\},\end{aligned}$$

where the second step used (2.29), and the fact that H_0 is symmetric under time-reversal. One may note that (2.29) tells us that H_0 actually transforms under time-reversal as $\Theta H_{0,\boldsymbol{k}}\Theta^{-1} = U_T^\dagger H_{0,-\boldsymbol{k}}^* U_T$, but (3.27) tells us that $U_T = -U_T^\dagger$, so they can be interchanged to give $\Theta H_{0,\boldsymbol{k}}\Theta^{-1} = U_T H_{0,-\boldsymbol{k}}^* U_T^\dagger$, as is used here. By exploiting the cyclic nature of the trace, and (4.10), it is fairly straightforward to show that this can be written as

$$\mathrm{Tr}\{\Delta_{++}\Delta_{++}^\dagger + \Delta_{--}\Delta_{--}^\dagger\} = \frac{1}{4}\mathrm{Tr}\{\left|[\tilde{H}_0,\tilde{\Delta}]_+\right|^2\}, \tag{4.17}$$

where $[\cdot,\cdot]_+ = \{\cdot,\cdot\}$ is the anticommutator. An analogous derivation can be used to show that the strength of the interband pairing is quantified by

$$\mathrm{Tr}\{\Delta_{++}\Delta_{++}^\dagger + \Delta_{--}\Delta_{--}^\dagger\} = \frac{1}{4}\mathrm{Tr}\{\left|[\tilde{H}_0,\tilde{\Delta}]_-\right|^2\}, \tag{4.18}$$

where $[\cdot,\cdot]_- = [\cdot,\cdot]$ is the commutator. Motivated by (4.17) and (4.18), I identify the *superconducting fitness* functions [32]

$$F_{\pm,\boldsymbol{k}} = [\tilde{H}_{0,\boldsymbol{k}},\tilde{\Delta}_{\boldsymbol{k}}]_\pm, \tag{4.19}$$

which quantify the presence of intra- and interband pairing respectively. From (4.14) we see that they satisfy

$$\mathrm{Tr}\{|F_+|^2\} + \mathrm{Tr}\{|F_-|^2\} = 4\,\mathrm{Tr}\{\Delta\Delta^\dagger\} = 4\,\mathrm{Tr}\{\tilde{\Delta}\tilde{\Delta}^\dagger\}, \tag{4.20}$$

where the second step used (2.31), and the unitary nature of U_T. This result emphasises the fact that the presence of interband pairing competes with intraband pairing, and is therefore detrimental to the formation of a stable superconducting state in the weak-coupling regime.

Although I have motivated their introduction via the pairing strength $\mathrm{Tr}\{\Delta\Delta^\dagger\}$, the fitness functions also explicitly control the formation of the superconducting instability in a single pairing channel via their presence in the "linearised gap equation" [31, 32]. In terms of our model, each row in Table 3.5 corresponds to a different pairing "channel". For convenience, these are reproduced in Table 4.2, along with each channel expressed in terms of the gamma matrices. In this chapter I will calculate $\mathrm{Tr}\{|F_{\pm,\boldsymbol{k}}|^2\}$ for each term in Table 3.5, which can be spilt into three "cases":

1. $\tilde{\Delta} = \Delta_0\gamma^0$,
2. $\tilde{\Delta} = \Delta_0\gamma^i$, and
3. $\tilde{\Delta} = \Delta_0(a\gamma^i\gamma^j \pm b\gamma^i\gamma^k)$,

where Δ_0 is some complex amplitude (not explicitly shown in Table 4.2), $i \neq j \neq k \in [1,5]$, and $a, b \in \mathbb{R}$. Any expressions in Table 4.2 that do not match one of these four cases exactly can easily

Case	$\tilde{\Delta}$ term		Irrep
1	$\eta_0 \otimes \sigma_0$	γ^0	A_{1g}
2	$\eta_2 \otimes \sigma_3$	γ^5	A_{1g}
	$\eta_3 \otimes \sigma_0$	γ^2	B_{1g}
	$\eta_1 \otimes \sigma_0$	γ^1	B_{2g}
	$\{\eta_2 \otimes \sigma_1, \eta_2 \otimes \sigma_2\}$	$\{\gamma^3, \gamma^4\}$	E_g
3	$\sin k_x\ \eta_3 \otimes \sigma_1 - \sin k_y\ \eta_3 \otimes \sigma_2$	$-i \sin k_x\ \gamma^1\gamma^3 + i \sin k_y\ \gamma^1\gamma^4$	A_{1u}
	$\sin k_x\ \eta_1 \otimes \sigma_2 + \sin k_y\ \eta_1 \otimes \sigma_1$	$i \sin k_x\ \gamma^2\gamma^4 + i \sin k_y\ \gamma^2\gamma^3$	A_{1u}
	$\sin k_x\ \eta_0 \otimes \sigma_1 + \sin k_y\ \eta_0 \otimes \sigma_2$	$-i \sin k_x\ \gamma^4\gamma^5 + i \sin k_y\ \gamma^3\gamma^5$	A_{1u}
	$\sin k_x\ \eta_3 \otimes \sigma_2 + \sin k_y\ \eta_3 \otimes \sigma_1$	$-i \sin k_x\ \gamma^1\gamma^4 - i \sin k_y\ \gamma^1\gamma^3$	A_{2u}
	$\sin k_x\ \eta_1 \otimes \sigma_1 - \sin k_y\ \eta_1 \otimes \sigma_2$	$i \sin k_x\ \gamma^2\gamma^3 - i \sin k_y\ \gamma^2\gamma^4$	A_{2u}
	$\sin k_x\ \eta_0 \otimes \sigma_2 - \sin k_y\ \eta_0 \otimes \sigma_1$	$i \sin k_x\ \gamma^3\gamma^5 + i \sin k_y\ \gamma^4\gamma^5$	A_{2u}
	$\sin k_x\ \eta_3 \otimes \sigma_1 + \sin k_y\ \eta_3 \otimes \sigma_2$	$-i \sin k_x\ \gamma^1\gamma^3 - i \sin k_y\ \gamma^1\gamma^4$	B_{1u}
	$\sin k_x\ \eta_1 \otimes \sigma_2 - \sin k_y\ \eta_1 \otimes \sigma_1$	$i \sin k_x\ \gamma^2\gamma^4 - i \sin k_y\ \gamma^2\gamma^3$	B_{1u}
	$\sin k_x\ \eta_0 \otimes \sigma_1 - \sin k_y\ \eta_0 \otimes \sigma_2$	$-i \sin k_x\ \gamma^4\gamma^5 - i \sin k_y\ \gamma^3\gamma^5$	B_{1u}
	$\sin k_x\ \eta_3 \otimes \sigma_2 - \sin k_y\ \eta_3 \otimes \sigma_1$	$-i \sin k_x\ \gamma^1\gamma^4 + i \sin k_y\ \gamma^1\gamma^3$	B_{2u}
	$\sin k_x\ \eta_1 \otimes \sigma_1 + \sin k_y\ \eta_1 \otimes \sigma_2$	$i \sin k_x\ \gamma^2\gamma^3 + i \sin k_y\ \gamma^2\gamma^4$	B_{2u}
	$\sin k_x\ \eta_0 \otimes \sigma_2 + \sin k_y\ \eta_0 \otimes \sigma_1$	$i \sin k_x\ \gamma^3\gamma^5 - i \sin k_y\ \gamma^4\gamma^5$	B_{2u}
	$\{\sin k_x, \sin k_y\}\ \eta_0 \otimes \sigma_3$	$-i\{\sin k_x, \sin k_y\}\ \gamma^3\gamma^4$	E_u
	$\{\sin k_y, \sin k_x\}\ \eta_1 \otimes \sigma_3$	$i\{\sin k_x, \sin k_y\}\ \gamma^2\gamma^5$	E_u
	$\{\sin k_x, \sin k_y\}\ \eta_2 \otimes \sigma_0$	$i\{\sin k_x, \sin k_y\}\ \gamma^1\gamma^2$	E_u
	$\{\sin k_x, \sin k_y\}\ \eta_3 \otimes \sigma_3$	$-i\{\sin k_x, \sin k_y\}\ \gamma^1\gamma^5$	E_u

TABLE 4.2: When written in terms of the gamma matrices, the pairing terms listed in Table 3.5 can be split into three cases: the trivial even-parity state, the nontrivial even-parity states, and the odd-parity states.

be transformed such that they do by adding some overall phase to Δ_0 with no loss of generality. Without going into the details, I also note that in the context of the linearised gap equation, the application of $F_{-,k}$ is restricted by the requirement that

$$\mathrm{Tr}\{\tilde{H}(\tilde{\Delta}\tilde{\Delta}^\dagger + \tilde{\Delta}^\dagger\tilde{\Delta})\} = 0. \tag{4.21}$$

Before we calculate the fitness functions we must first verify that (4.21) holds for each case considered. Given that the eigenvalues of $\tilde{H}_0$ are given by (4.11) to be ± 1, we see that one way that this will be satisfied is if $\tilde{\Delta}\tilde{\Delta}^\dagger \propto \gamma^0$. Remembering that the gamma matrices are Hermitian, and $\gamma^i\gamma^i = \gamma^0$, it is trivial to show that $\tilde{\Delta}\tilde{\Delta}^\dagger = |\Delta_0|^2\gamma^0$ for the first two cases. For the third we have

$$\begin{aligned}
\tilde{\Delta}\tilde{\Delta}^\dagger &= |\Delta_0|^2(a\gamma^i\gamma^j \pm b\gamma^i\gamma^k)(a\gamma^j\gamma^i \pm b\gamma^k\gamma^i) \\
&= |\Delta_0|^2(a^2\gamma^0 \pm ab\gamma^i\gamma^j\gamma^k\gamma^i \pm ab\gamma^i\gamma^k\gamma^j\gamma^i + b^2\gamma^0) \\
&= |\Delta_0|^2(a^2\gamma^0 \pm ab\gamma^i\gamma^j\gamma^k\gamma^i \mp ab\gamma^i\gamma^j\gamma^k\gamma^i + b^2\gamma^0) \\
&= |\Delta_0|^2(a^2 + b^2)\gamma^0,
\end{aligned} \tag{4.22}$$

where we used $\gamma^i\gamma^j = -\gamma^j\gamma^i$. We can conclude that this requirement is satisfied by all pairing potentials in Table 4.2. This is not to say that linear combinations of these terms will necessarily satisfy $\tilde{\Delta}\tilde{\Delta}^\dagger \propto \gamma^0$, but our goal is to understand the stability of the different channels individually.

4.2.1 Calculation of fitness functions

We can now proceed with the calculation of the fitness functions for each of the three cases outlined above, in order to learn about the nature of intra- and interband pairing in each of the pairing channels listed in Table 4.2. The results will be summarised in Table 4.4 at the end of this chapter.

Case one: $\tilde{\Delta} = \Delta_0\gamma^0$

We begin by considering the trivial pairing state $\tilde{\Delta} = \Delta_0\gamma^0$. The interband fitness function is given by (4.19) to be $F_{-,\boldsymbol{k}} = [\tilde{H}_0, \tilde{\Delta}]$. Taking $\tilde{H}_0$ as given in (4.8), we have

$$F_- = \Delta_0 \sum_{n=1}^{5} \hat{c}_n[\gamma^n, \gamma^0] = 0, \tag{4.23}$$

because the commutator of any matrix with the identity must be zero. We therefore trivially have $\mathrm{Tr}\{|F_-|^2\} = 0$, and can use (4.20) to write

$$\mathrm{Tr}\{|F_+|^2\} = 4\,\mathrm{Tr}\{\tilde{\Delta}\tilde{\Delta}^\dagger\} = 4\,\mathrm{Tr}\{|\Delta_0|^2\gamma^0\} = 16|\Delta_0|^2, \tag{4.24}$$

where we used the form of $\tilde{\Delta}\tilde{\Delta}^\dagger$ identified above.

These results imply that this pairing channel is "completely fit", in the sense that the pairing is entirely intraband. This is unsurprising because (2.31) tells us that $\tilde{\Delta} \propto \gamma^0 \implies \Delta \propto U_T$, which is to say that this channel only pairs time-reversed states. Due to the Kramer's degeneracy discussed above, these must belong to the same band. Further, the intraband fitness, (4.24), is dependent on only the amplitude of $\tilde{\Delta}$, meaning that it is isotropic and has no nodes. This means that, in addition to belonging to a 1D irrep, this pairing channel is unlikely to form part of a chiral pairing state in order to minimise its free energy. In terms of the polar Kerr effect, we can essentially ignore it.

Case two: $\tilde{\Delta} = \Delta_0\gamma^i$

We now calculate F_+ for the case that $\tilde{\Delta} = \Delta_0\gamma^i$, where $i \in [1, 5]$, which corresponds to the five nontrivial even-parity terms in Table 4.2. Using $\{\gamma^i, \gamma^j\} = 2\gamma^0\delta_{ij}$, we have

$$F_+ = \Delta_0 \sum_{n=1}^{5} \hat{c}_n\{\gamma^n, \gamma^i\} = 2\Delta_0\hat{c}_i\gamma^0, \tag{4.25}$$

and therefore

$$\mathrm{Tr}\{|F_+|^2\} = \mathrm{Tr}\{4|\Delta_0|^2\hat{c}_i^2\gamma^0\} = 16|\Delta_0|^2\hat{c}_i^2. \tag{4.26}$$

Using (4.20), and remembering that $\tilde{\Delta}\tilde{\Delta}^\dagger = |\Delta_0|^2\gamma^0$, we then have

$$\mathrm{Tr}\{|F_-|^2\} = 16|\Delta_0|^2 - 16|\Delta_0|\hat{c}_i^2 = 16|\Delta_0|^2 \sum_{n\neq i} \hat{c}_n^2, \tag{4.27}$$

where the last step used (4.9).

These results tell us that, in general, these pairing channels have some level of "unfitness", in the sense that they can have interband pairing. The actual details depend on the interplay between the normal state and the pairing potential: the value of i is determined by the pairing channel while the form of the $\hat{c}_n$ coefficients is dependent on the normal state. For example, the $\Delta_0\gamma^3$ and $\Delta_0\gamma^4$ pairing states belonging to the E_g irrep have *no* intraband pairing, since $c_3 = c_4 = 0$ in the two-dimensional form of H_0, so (4.26) is vanishing. For this reason, I will ignore these terms from our model as the Fermi surface does not destabilise under a weak-coupling instability.

The remaining even-parity pairing channels have both intra- and interband pairing. As an example, consider the $\tilde{\Delta} = \Delta_0\gamma^5$ pairing channel. The intraband fitness is given by (4.26) to be dependent on $c_5^2 = h_{23}^2$. Taking the form of h_{23} from (3.41), we see that the intraband fitness is isotropic. Conversely, the interband fitness is given by (4.27) to be dependent on $c_1^2 + c_2^2 = h_{10}^2 + h_{30}^2$.

Function	Nodes in first Brillouin zone	
$\sin^2 k_x$	$k_x = n\pi$	Fig. 4.1 A
$\sin^2 k_y$	$k_y = n\pi$	Fig. 4.1 B
$\sin^2 k_x + \sin^2 k_y$	$\boldsymbol{k} = (n\pi, m\pi)$	Fig. 4.1 C
$h_{10}^2 \sim \sin^2 k_x \sin^2 k_y$	$k_x = n\pi$, or $k_y = n\pi$	Fig. 4.1 D
$h_{30}^2 \sim (\cos k_x - \cos k_y)^2$	$k_x = \pm k_y$	Fig. 4.1 E
$h_{23}^2 = \lambda^2$	none	-
$h_{10}^2 + h_{30}^2$	$\boldsymbol{k} = 0$, or $\boldsymbol{k} = (\pi, \pi)$	Fig. 4.1 F
$h_{30}^2 + h_{23}^2$	none	-
$h_{23}^2 + h_{10}^2$	none	-

TABLE 4.3: The zeros (nodes) within the first Brillouin zone of various functions that appear in the superconducting fitness expressions (refer to Table 4.4). These are used to determine the nodal structure of the intra- and interband pairing for each pairing channel, and are shown visually in Figure 4.1.

From (3.42) and (3.43) we see that this goes as $t_2(\cos k_x - \cos k_y)^2 + 2t_3 \sin^2 k_x \sin^2 k_y$, which is rather nontrivial. In particular, Table 4.3 tells us that it has nodes at $\boldsymbol{k} = 0$ and $\boldsymbol{k} = (\pi, \pi)$, which is to say that the pairing is purely intraband at these points. There may also be additional "accidental nodes" if specific values of t_2 and t_3 lead to $t_2(\cos k_x - \cos k_y)^2 = -2t_3 \sin k_x^2 \sin k_y^2$ at some momentum points.

The corresponding results for all the pairing channels are summarised in Table 4.4, which is accompanied by Figure 4.1 to provide a visualisation of the nodal structure of various terms. Note in particular that the $\Delta_0\eta_3 \otimes \sigma_0$ and $\Delta_0\eta_1 \otimes \sigma_0$ pairing states have nontrivial intraband nodal structure. For example, the $\eta_3 \otimes \sigma_0$ channel has vanishing intraband pairing along the $k_x = \pm k_y$ lines in momentum space. It is quite plausible that, provided they were brought close enough in energy, these states could form a chiral state of the form $\Delta_0(\eta_3 \otimes \sigma_0 \pm i\eta_1 \otimes \sigma_0)$, so as to maximise the intraband gap magnitude.

Case three: $\tilde{\Delta} = \Delta_0(a\gamma^i\gamma^j + b\gamma^i\gamma^k)$

The third and final case, $\tilde{\Delta} = \Delta_0(a\gamma^i\gamma^j + b\gamma^i\gamma^k)$ for $i \neq j \neq k \in [1,5]$ and $a, b \in \mathbb{R}$, is the most complicated we have to consider, and includes all the odd-parity pairing channels. Using the identity $[A, BC] = \{A, B\}C - B\{A, C\}$, we can calculate the intraband fitness to be

$$\begin{aligned} F_- &= \Delta_0 \sum_n \hat{c}_n \left(a[\gamma^n, \gamma^i\gamma^j] + b[\gamma^n, \gamma^i\gamma^k] \right) \\ &= \Delta_0 \sum_n \hat{c}_n \left(a\{\gamma^n, \gamma^i\}\gamma^j - a\gamma^i\{\gamma^n, \gamma^j\} + b\{\gamma^n, \gamma^i\}\gamma^k - b\gamma^i\{\gamma^n, \gamma^k\} \right) \\ &= 2\Delta_0 \left(a\hat{c}_i\gamma^j - a\hat{c}_j\gamma^i + b\hat{c}_i\gamma^k - b\hat{c}_k\gamma^i \right), \end{aligned} \tag{4.28}$$

where we used $\{\gamma^i, \gamma^j\} = 2\delta_{ij}\gamma^0$. Continuing with the calculation, we can write $\mathrm{Tr}\{|F_-|^2\}$ as

$$4|\Delta_0|^2 \,\mathrm{Tr}\Big\{ \left(a\hat{c}_i\gamma^j - a\hat{c}_j\gamma^i + b\hat{c}_i\gamma^k - b\hat{c}_k\gamma^i \right) \left(a^*\hat{c}_i\gamma^j - a^*\hat{c}_j\gamma^i + b^*\hat{c}_i\gamma^k - b^*\hat{c}_k\gamma^i \right) \Big\}. \tag{4.29}$$

The argument of the trace in this expression can be expanded into 16 terms:

$$\begin{aligned} &a^2\hat{c}_i^2\gamma^0 - a^2\hat{c}_i\hat{c}_j\gamma^j\gamma^i + ab\hat{c}_i^2\gamma^j\gamma^k - ab\hat{c}_i\hat{c}_k\gamma^j\gamma^i - a^2\hat{c}_j\hat{c}_i\gamma^i\gamma^j + a^2\hat{c}_j^2\gamma^0 - ab\hat{c}_j\hat{c}_i\gamma^i\gamma^k + ab\hat{c}_j\hat{c}_k\gamma^0 \\ &+ ab\hat{c}_i^2\gamma^k\gamma^j - ab\hat{c}_i\hat{c}_j\gamma^k\gamma^i + b^2\hat{c}_i^2\gamma^0 - b^2\hat{c}_i\hat{c}_k\gamma^k\gamma^i - ab\hat{c}_k\hat{c}_i\gamma^i\gamma^j + ab\hat{c}_k\hat{c}_j\gamma^0 - b^2\hat{c}_k\hat{c}_i\gamma^i\gamma^k + b^2\hat{c}_k^2\gamma^0, \end{aligned} \tag{4.30}$$

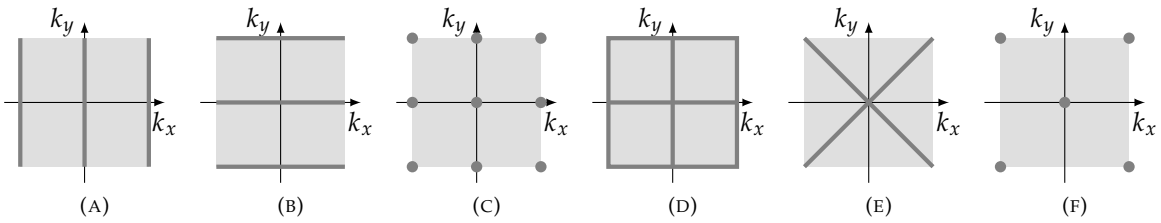

FIGURE 4.1: The zeros (nodes) in the first Brillouin zone of various functions listed in Table 4.3.

many of which cancel out because $\gamma^i\gamma^j = -\gamma^j\gamma^i$ for $i \neq j$. These have been colour coded, leaving us with only the terms proportional to γ^0:

$$\begin{aligned}\mathrm{Tr}\{|F_-|^2\} &= 4|\Delta_0|^2\,\mathrm{Tr}\left\{\left(a^2\hat{c}_i^2 + a^2\hat{c}_j^2 + b^2\hat{c}_i^2 + b^2\hat{c}_k^2 + 2ab\hat{c}_j\hat{c}_k\right)\gamma^0\right\} \\ &= 16|\Delta_0|^2\left(a^2\hat{c}_i^2 + a^2\hat{c}_j^2 + b^2\hat{c}_i^2 + b^2\hat{c}_k^2 + 2ab\hat{c}_j\hat{c}_k\right) \\ &= 16|\Delta_0|^2\left([a^2+b^2]\hat{c}_i^2 + [a\hat{c}_j + b\hat{c}_k]^2\right).\end{aligned} \tag{4.31}$$

In order to determine $\mathrm{Tr}\{|F_+|^2\}$ we use (4.20) and (4.22) to obtain

$$\begin{aligned}\mathrm{Tr}\{|F_+|^2\} &= 16|\Delta_0|^2(a^2+b^2) - 16|\Delta_0|^2\left([a^2+b^2]\hat{c}_i^2 + [a\hat{c}_j + b\hat{c}_k]^2\right), \\ &= 16|\Delta_0|^2\left(a^2\sum_{n\neq i,j}\hat{c}_n^2 + b^2\sum_{n\neq i,k}\hat{c}_n^2 - 2ab\hat{c}_j\hat{c}_k\right).\end{aligned} \tag{4.32}$$

These results apply to the odd-parity pairing channels, and the specific forms of $\mathrm{Tr}\{|F_\pm|^2\}$, along with the resulting intra- and interband nodal structure for each channel, are shown in Table 4.4. We see that all of these states have momentum-dependent intraband nodes. It is quite plausible that any of these channels will form chiral states so as to minimise their free energy, either within a 2D irrep, or as the superposition of terms from two 1D irreps.

Summary

Of all the terms in Table 4.4, it is only the E_g channels that we can ignore due to the lack of intraband pairing, although in the context of chiral pairing states we will also ignore the two A_{1g} pairing channels due to the isotropic nature of their intraband pairing. This leaves us with 22 possible pairing terms in our model of strontium ruthenate: those belonging to the B_{1g}, B_{2g}, A_{1u}, A_{2u}, B_{1u}, B_{2u}, and E_u irreps. Among other results, the role of interband pairing is considered in more detail in the next chapter, specifically in Section 5.3.2, and we will return to this model in Chapter 6.

$\tilde{\Delta}$ term	Irrep	$\mathrm{Tr}\{\lvert F_+\rvert^2\}/16\lvert\Delta_0\rvert^2$	Intraband nodes	$\mathrm{Tr}\{\lvert F_-\rvert^2\}/16\lvert\Delta_0\rvert^2$	Interband nodes
$\eta_0 \otimes \sigma_0$	A_{1g}	1	no nodes	0	no pairing
$\eta_2 \otimes \sigma_3$	A_{1g}	$\hat{h}_{23}^2$	no nodes	$\hat{h}_{30}^2 + \hat{h}_{10}^2$	$\boldsymbol{k} = \mathbf{0}$ or $(\pm\pi, \pm\pi)$
$\eta_3 \otimes \sigma_0$	B_{1g}	$\hat{h}_{30}^2$	$k_x = \pm k_y$	$\hat{h}_{23}^2 + \hat{h}_{10}^2$	no nodes
$\eta_1 \otimes \sigma_0$	B_{2g}	$\hat{h}_{10}^2$	$k_x = n\pi$ or $k_y = n\pi$	$\hat{h}_{23}^2 + \hat{h}_{30}^2$	no nodes
$\{\eta_2 \otimes \sigma_1, \eta_2 \otimes \sigma_2\}$	E_g	0	no pairing	1	no nodes
$\sin k_x\, \eta_3 \otimes \sigma_1 - \sin k_y\, \eta_3 \otimes \sigma_2$	A_{1u}	$(\sin^2 k_x + \sin^2 k_y)(\hat{h}_{23}^2 + \hat{h}_{30}^2)$	$\boldsymbol{k} = (n\pi, m\pi)$	$(\sin^2 k_x + \sin^2 k_y)\hat{h}_{10}^2$	$k_x = n\pi$ or $k_y = n\pi$
$\sin k_x\, \eta_1 \otimes \sigma_2 + \sin k_y\, \eta_1 \otimes \sigma_1$	A_{1u}	$(\sin^2 k_x + \sin^2 k_y)(\hat{h}_{23}^2 + \hat{h}_{10}^2)$	$\boldsymbol{k} = (n\pi, m\pi)$	$(\sin^2 k_x + \sin^2 k_y)\hat{h}_{30}^2$	$\boldsymbol{k} = (n\pi, m\pi)$
$\sin k_x\, \eta_0 \otimes \sigma_1 + \sin k_y\, \eta_0 \otimes \sigma_2$	A_{1u}	$(\sin^2 k_x + \sin^2 k_y)(\hat{h}_{30}^2 + \hat{h}_{10}^2)$	$\boldsymbol{k} = (n\pi, m\pi)$	$(\sin^2 k_x + \sin^2 k_y)\hat{h}_{23}^2$	$\boldsymbol{k} = (n\pi, m\pi)$
$\sin k_x\, \eta_3 \otimes \sigma_2 + \sin k_y\, \eta_3 \otimes \sigma_1$	A_{2u}	$(\sin^2 k_x + \sin^2 k_y)(\hat{h}_{23}^2 + \hat{h}_{30}^2)$	$\boldsymbol{k} = (n\pi, m\pi)$	$(\sin^2 k_x + \sin^2 k_y)\hat{h}_{10}^2$	$k_x = n\pi$ or $k_y = n\pi$
$\sin k_x\, \eta_1 \otimes \sigma_1 - \sin k_y\, \eta_1 \otimes \sigma_2$	A_{2u}	$(\sin^2 k_x + \sin^2 k_y)(\hat{h}_{23}^2 + \hat{h}_{10}^2)$	$\boldsymbol{k} = (n\pi, m\pi)$	$(\sin^2 k_x + \sin^2 k_y)\hat{h}_{30}^2$	$\boldsymbol{k} = (n\pi, m\pi)$
$\sin k_x\, \eta_0 \otimes \sigma_2 - \sin k_y\, \eta_0 \otimes \sigma_1$	A_{2u}	$(\sin^2 k_x + \sin^2 k_y)(\hat{h}_{30}^2 + \hat{h}_{10}^2)$	$\boldsymbol{k} = (n\pi, m\pi)$	$(\sin^2 k_x + \sin^2 k_y)\hat{h}_{23}^2$	$\boldsymbol{k} = (n\pi, m\pi)$
$\sin k_x\, \eta_3 \otimes \sigma_1 + \sin k_y\, \eta_3 \otimes \sigma_2$	B_{1u}	$(\sin^2 k_x + \sin^2 k_y)(\hat{h}_{23}^2 + \hat{h}_{30}^2)$	$\boldsymbol{k} = (n\pi, m\pi)$	$(\sin^2 k_x + \sin^2 k_y)\hat{h}_{10}^2$	$k_x = n\pi$ or $k_y = n\pi$
$\sin k_x\, \eta_1 \otimes \sigma_2 - \sin k_y\, \eta_1 \otimes \sigma_1$	B_{1u}	$(\sin^2 k_x + \sin^2 k_y)(\hat{h}_{23}^2 + \hat{h}_{10}^2)$	$\boldsymbol{k} = (n\pi, m\pi)$	$(\sin^2 k_x + \sin^2 k_y)\hat{h}_{30}^2$	$\boldsymbol{k} = (n\pi, m\pi)$
$\sin k_x\, \eta_0 \otimes \sigma_1 - \sin k_y\, \eta_0 \otimes \sigma_2$	B_{1u}	$(\sin^2 k_x + \sin^2 k_y)(\hat{h}_{30}^2 + \hat{h}_{10}^2)$	$\boldsymbol{k} = (n\pi, m\pi)$	$(\sin^2 k_x + \sin^2 k_y)\hat{h}_{23}^2$	$\boldsymbol{k} = (n\pi, m\pi)$
$\sin k_x\, \eta_3 \otimes \sigma_2 - \sin k_y\, \eta_3 \otimes \sigma_1$	B_{2u}	$(\sin^2 k_x + \sin^2 k_y)(\hat{h}_{23}^2 + \hat{h}_{30}^2)$	$\boldsymbol{k} = (n\pi, m\pi)$	$(\sin^2 k_x + \sin^2 k_y)\hat{h}_{10}^2$	$k_x = n\pi$ or $k_y = n\pi$
$\sin k_x\, \eta_1 \otimes \sigma_1 + \sin k_y\, \eta_1 \otimes \sigma_2$	B_{2u}	$(\sin^2 k_x + \sin^2 k_y)(\hat{h}_{23}^2 + \hat{h}_{10}^2)$	$\boldsymbol{k} = (n\pi, m\pi)$	$(\sin^2 k_x + \sin^2 k_y)\hat{h}_{30}^2$	$\boldsymbol{k} = (n\pi, m\pi)$
$\sin k_x\, \eta_0 \otimes \sigma_2 + \sin k_y\, \eta_0 \otimes \sigma_1$	B_{2u}	$(\sin^2 k_x + \sin^2 k_y)(\hat{h}_{30}^2 + \hat{h}_{10}^2)$	$\boldsymbol{k} = (n\pi, m\pi)$	$(\sin^2 k_x + \sin^2 k_y)\hat{h}_{23}^2$	$\boldsymbol{k} = (n\pi, m\pi)$
$\{\sin k_x, \sin k_y\}\, \eta_0 \otimes \sigma_3$	E_u	$\{\sin^2 k_x, \sin^2 k_y\}$	$\{k_x = n\pi, k_y = n\pi\}$	0	no pairing
$\{\sin k_x, \sin k_y\}\, \eta_1 \otimes \sigma_3$	E_u	$\{\sin^2 k_x, \sin^2 k_y\}\hat{h}_{10}^2$	$k_x = n\pi$ or $k_y = m\pi$	$\{\sin^2 k_x, \sin^2 k_y\}(\hat{h}_{23}^2 + \hat{h}_{30}^2)$	$\{k_x = n\pi, k_y = n\pi\}$
$\{\sin k_x, \sin k_y\}\, \eta_2 \otimes \sigma_0$	E_u	$\{\sin^2 k_x, \sin^2 k_y\}\hat{h}_{23}^2$	$\{k_x = n\pi, k_y = n\pi\}$	$\{\sin^2 k_x, \sin^2 k_y\}(\hat{h}_{30}^2 + \hat{h}_{10}^2)$	$\{k_x = n\pi, k_y = n\pi\}$
$\{\sin k_x, \sin k_y\}\, \eta_3 \otimes \sigma_3$	E_u	$\{\sin^2 k_x, \sin^2 k_y\}\hat{h}_{30}^2$	$\{k_x = \pm k_y$ or $n\pi, k_y = \pm k_x$ or $n\pi\}$	$\{\sin^2 k_x, \sin^2 k_y\}(\hat{h}_{23}^2 + \hat{h}_{10}^2)$	$\{k_x = n\pi, k_y = n\pi\}$

TABLE 4.4: The intra- and interband pairing structure of each pairing channel included in our model of strontium ruthenate. The intra- and interband pairing is quantified by the $\mathrm{Tr}\{\lvert F_\pm\rvert^2\}$ functions, as determined in the text. The nodal structure is inferred using Table 4.3, and can be visualised with the help of Figure 4.1.

Chapter 5

Anomalous Hall conductivity

The preceding chapters have been spent constructing a model of superconductivity in strontium ruthenate. This will be put aside for now, so that we can consider the Hall conductivity in a general system, but we will return to our model in Chapter 6, where we apply the results obtained here.

As discussed in Section 1.2, the polar Kerr effect can be used as an experimental probe for time-reversal symmetry breaking in bulk superconductors. The anomalous Hall conductivity of the superconductor in question plays a central role in determining the respective Kerr angle. However, the presence of a non-zero anomalous Hall conductivity requires further conditions in addition to the breaking of time-reversal symmetry. My aim in this chapter is to further understand the conditions required for a two-band superconductor to exhibit a non-zero anomalous Hall conductivity due to intrinsic mechanisms.

In Section 5.1 I perform an exact calculation of the Hall conductivity in the linear response regime, while Section 5.2 focusses on an approximate result that applies in the high-frequency, small-gap limit. This approximation encapsulates many of the details of the exact result, while simplifying the calculations. It is also directly applicable to some experimental endeavours. I take advantage of this result in Section 5.3 to derive a necessary condition for a non-vanishing Hall conductivity which applies to a rather general set of models. The work presented in Section 5.3 is new, and comprises some of the core results of this thesis.

5.1 Exact calculation of the Hall conductivity

As discussed in Section 1.2.2, the Hall conductivity is defined as the antisymmetric part of the conductivity tensor,

$$\sigma_H(\omega) = \frac{\sigma_{xy}(\omega) - \sigma_{yx}(\omega)}{2}. \tag{5.1}$$

Calculation of the conductivity tensor for an arbitrary applied field is difficult, so the usual approach is to consider the linear response regime, in which the applied electric field has a small enough magnitude such that the current is directly proportional to its intensity. The name given to the set of correlation functions that describe linear responses are *Kubo formulas*, and the Kubo formula for electrical conductivity can be shown to be given by [88]

$$\sigma_{ij}(\omega) = \frac{i}{\omega}\left(\pi_{ij}(\omega) + \frac{n_0 q^2}{m}\delta_{ij}\right), \tag{5.2}$$

where π_{ij} is the correlator between the i and j components of the current, n_0, q, and m are the number density, charge, and mass of the charge carriers, and δ_{ij} is the Kronecker delta. By convention, all

frequencies are in units of $\hbar$. We see that the Hall conductivity can be written as

$$\sigma_H(\omega) = \frac{i}{2\omega}\left[\pi_{xy}(\omega) - \pi_{yx}(\omega)\right], \tag{5.3}$$

which is particularly convenient because correlation functions are well understood in many-body physics. In this section we will use these well known results to derive a form of the Hall conductivity in terms of Green's functions, which can be calculated directly from the BdG Hamiltonian, making the resulting expression useful for both analytical and numerical calculations. We approach this via the Matsubara formalism, in which the Matsubara current-current correlator is given by [88]

$$\pi_{ij}(i\omega_n) = \int_0^\beta d\tau\, e^{i\omega_n\tau}\pi_{ij}(\tau), \tag{5.4}$$

where $\omega_n = 2n\pi/\beta$ is a *bosonic* Matsubara frequency, τ is imaginary time,

$$\pi_{ij}(\tau) = -\frac{1}{N}\left\langle \mathcal{T}_\tau \mathcal{J}_i(\tau)\mathcal{J}_j(0)\right\rangle, \tag{5.5}$$

is the imaginary-time current-current correlator, N is the number of lattice points, $\mathcal{T}_\tau$ is the imaginary-time-ordering operator, and $\mathcal{J}_i$ is the i component of the current operator. At the end of our calculation we can determine the real-frequency correlator, $\pi_{ij}(\omega)$, via analytic continuation of the Matsubara frequencies, i.e. [89]

$$\pi_{ij}(\omega) = \lim_{i\omega_n\to\omega+i0^+}\pi_{ij}(i\omega_n), \tag{5.6}$$

where 0^+ is a positive infinitesimal.

The current operator: The current operator can be written as

$$\mathcal{J}_j = \frac{e}{i}[r_j, \mathcal{H}_0] = e\frac{\partial\mathcal{H}_0}{\partial k_j}, \tag{5.7}$$

where $\boldsymbol{r}$ is the position operator, and only the noninteracting normal state Hamiltonian is present because the interaction Hamiltonian (which gives rise to the superconducting potential in the mean-field approximation) commutes with $\boldsymbol{r}$. Substituting in $\mathcal{H}_0$ as given by (2.13) (with the constant term dropped), we can write this as

$$\mathcal{J}_i = \frac{e}{2}\sum_{\boldsymbol{k}}\left(\frac{\partial H_{0,\boldsymbol{k},\alpha_1\alpha_2}}{\partial k_i}\hat{a}^\dagger_{\boldsymbol{k}\alpha_1}\hat{a}_{\boldsymbol{k}\alpha_2} - \frac{\partial H_{0,-\boldsymbol{k},\alpha_2\alpha_1}}{\partial k_i}\hat{a}_{-\boldsymbol{k}\alpha_1}\hat{a}^\dagger_{-\boldsymbol{k}\alpha_2}\right), \tag{5.8}$$

where the α_1 and α_2 indices run over the four possible orbital $\otimes$ spin states. As usual, repeated indices are summed over. Defining the "electron" and "hole" velocity matrices respectively as

$$v^{ei}_{\boldsymbol{k}} = \frac{\partial H_{0,\boldsymbol{k}}}{\partial k_i} \tag{5.9}$$

and

$$v^{hi}_{\boldsymbol{k}} = -\frac{\partial H^T_{0,-\boldsymbol{k}}}{\partial k_i}, \tag{5.10}$$

we can write

$$\mathcal{J}_i = \frac{e}{2}\sum_{k}\left(v^{ei}_{k,\alpha_1\alpha_2}\hat{a}^\dagger_{k\alpha_1}\hat{a}_{k\alpha_2} + v^{hi}_{k,\alpha_1\alpha_2}\hat{a}_{-k\alpha_1}\hat{a}^\dagger_{-k\alpha_2}\right). \tag{5.11}$$

It may appear odd that we differentiate between electron and hole contributions in the context of $\mathcal{H}_0$, but ultimately this result will be applied to a superconducting state.

The imaginary-time correlation function: Substituting the current operator as given by (5.11) into (5.5), we write the imaginary-time current-current correlator as

$$\begin{aligned}\pi_{ij}(\tau) = -\frac{e^2}{4N}\sum_{k,k'}\Big(&v^{ei}_{k,\alpha_1\alpha_2}v^{ej}_{k',\beta_1\beta_2}\langle\mathcal{T}_\tau\hat{a}^\dagger_{k\alpha_1}(\tau)\hat{a}_{k\alpha_2}(\tau)\hat{a}^\dagger_{k'\beta_1}(0)\hat{a}_{k'\beta_2}(0)\rangle\\ &+ v^{ei}_{k,\alpha_1\alpha_2}v^{hj}_{k',\beta_1\beta_2}\langle\mathcal{T}_\tau\hat{a}^\dagger_{k\alpha_1}(\tau)\hat{a}_{k\alpha_2}(\tau)\hat{a}_{-k'\beta_1}(0)\hat{a}^\dagger_{-k'\beta_2}(0)\rangle\\ &+ v^{hi}_{k,\alpha_1\alpha_2}v^{ej}_{k',\beta_1\beta_2}\langle\mathcal{T}_\tau\hat{a}_{-k\alpha_1}(\tau)\hat{a}^\dagger_{-k\alpha_2}(\tau)\hat{a}^\dagger_{k'\beta_1}(0)\hat{a}_{k'\beta_2}(0)\rangle\\ &+ v^{hi}_{k,\alpha_1\alpha_2}v^{hj}_{k',\beta_1\beta_2}\langle\mathcal{T}_\tau\hat{a}_{-k\alpha_1}(\tau)\hat{a}^\dagger_{-k\alpha_2}(\tau)\hat{a}_{-k'\beta_1}(0)\hat{a}^\dagger_{-k'\beta_2}(0)\rangle\Big).\end{aligned} \tag{5.12}$$

When faced with expectation values of multiple creation and annihilation operators, the usual approach in the context of a single-particle Hamiltonian is to apply Wick's theorem [88, 90] in order to express them in terms of products of expectation values of *pairs* of operators. As an example, the first term in (5.12) can be written as

$$\begin{aligned}-\frac{e^2}{4N}\sum_{k,k'}v^{ei}_{k,\alpha_1\alpha_2}v^{ej}_{k',\beta_1\beta_2}\Big(&\langle\mathcal{T}_\tau\hat{a}^\dagger_{k\alpha_1}(\tau)\hat{a}_{k\alpha_2}(\tau)\rangle\langle\mathcal{T}_\tau\hat{a}^\dagger_{k'\beta_1}(0)\hat{a}_{k'\beta_2}(0)\rangle\\ &+\langle\mathcal{T}_\tau\hat{a}_{k\alpha_2}(\tau)\hat{a}_{k'\beta_2}(0)\rangle\langle\mathcal{T}_\tau\hat{a}^\dagger_{k'\beta_1}(0)\hat{a}^\dagger_{k\alpha_1}(\tau)\rangle - \langle\mathcal{T}_\tau\hat{a}_{k\alpha_2}(\tau)\hat{a}^\dagger_{k'\beta_1}(0)\rangle\langle\mathcal{T}_\tau\hat{a}_{k'\beta_2}(0)\hat{a}^\dagger_{k\alpha_1}(\tau)\rangle\Big).\end{aligned} \tag{5.13}$$

The other three terms in (5.12) can be written as analogous expressions, but for now I will focus on simplifying this term. Note that both operators in the expectation values in the first term of (5.13) have the same imaginary-time argument, so we can drop the imaginary-time-ordering in order to obtain

$$-\frac{e^2}{4N}\left(\sum_{k}v^{ei}_{k,\alpha_1\alpha_2}\langle\hat{a}^\dagger_{k\alpha_1}\hat{a}_{k\alpha_2}\rangle\right)\left(\sum_{k'}v^{ej}_{k',\beta_1\beta_2}\langle\hat{a}^\dagger_{k'\beta_1}\hat{a}_{k'\beta_2}\rangle\right).$$

Now let us consider the $v^{ei}_{k,\alpha_1\alpha_2}\langle\hat{a}^\dagger_{k\alpha_1}\hat{a}_{k\alpha_2}\rangle$ term. The following argument would also apply to the other bracket. Note from (2.1) that $\mathcal{H}_0$ contains terms of the form $H_{0,k,\alpha_1\alpha_2}\hat{a}^\dagger_{k\alpha_1}\hat{a}_{k\alpha_2}$. From the discussion in Section 2.2.1, we see that $\langle\hat{a}^\dagger_{k\alpha_1}\hat{a}_{k\alpha_2}\rangle$ must have the same parity as $H_{0,k,\alpha_1\alpha_2}$. At the same time, $v^{ei}_{k,\alpha_1\alpha_2}$ is defined in (5.9) in terms of a momentum derivative of $H_{0,k}$, so will have parity opposite that of $H_{0,k,\alpha_1\alpha_2}$. For this reason, no matter the parity of the $H_{0,k,\alpha_1\alpha_2}$, the $v^{ei}_{k,\alpha_1\alpha_2}\langle\hat{a}^\dagger_{k\alpha_1}\hat{a}_{k\alpha_2}\rangle$ term will be odd under inversion, and will therefore vanish under the sum over momentum. This is easiest to see when inversion acts trivially on the internal degrees of freedom (as is the case in our model of strontium ruthenate), because inversion simplifies to $k \to -k$ in this case. However, the same argument applies even if inversion does affect the orbital degree of freedom, as we still sum over all α_1 and α_2 values. This result allows us to drop the first term from (5.13).

We can further simplify (5.13) by noting that there are strict restrictions on the momentum values that lead to non-zero expectation values. Terms like $\hat{a}^\dagger_{k\alpha_1}\hat{a}_{k'\alpha_2}$ only appear in (2.1) when $k = k'$, so we can conclude that $\langle\hat{a}^\dagger_{k\alpha_1}(\tau)\hat{a}_{k'\alpha_2}(\tau')\rangle = 0$ unless $k = k'$. Similarly, (2.2) tells us that $\langle\hat{a}^\dagger_{k\alpha_1}(\tau)\hat{a}^\dagger_{k'\alpha_2}(\tau')\rangle = \langle\hat{a}_{k\alpha_1}(\tau)\hat{a}_{k'\alpha_2}(\tau')\rangle = 0$ unless $k = -k'$. Applying these results allows us to

write (5.13) as a sum over only a single momentum value:

$$(5.13) = -\frac{e^2}{4N}\sum_{\boldsymbol{k}}\Big(v^{ei}_{\boldsymbol{k},\alpha_1\alpha_2} v^{ej}_{-\boldsymbol{k},\beta_1\beta_2} \langle \mathcal{T}_\tau \hat{a}_{\boldsymbol{k}\alpha_2}(\tau)\hat{a}_{-\boldsymbol{k}\beta_2}(0)\rangle \langle \mathcal{T}_\tau \hat{a}^\dagger_{-\boldsymbol{k}\beta_1}(0)\hat{a}^\dagger_{\boldsymbol{k}\alpha_1}(\tau)\rangle \\ - v^{ei}_{\boldsymbol{k},\alpha_1\alpha_2} v^{ej}_{\boldsymbol{k},\beta_1\beta_2} \langle \mathcal{T}_\tau \hat{a}_{\boldsymbol{k}\alpha_2}(\tau)\hat{a}^\dagger_{\boldsymbol{k}\beta_1}(0)\rangle \langle \mathcal{T}_\tau \hat{a}_{\boldsymbol{k}\beta_2}(0)\hat{a}^\dagger_{\boldsymbol{k}\alpha_1}(\tau)\rangle\Big). \quad (5.14)$$

The other three terms in (5.12) can be simplified in much the same way, and resulting the expression for the imaginary-time current-current correlator is

$$\begin{aligned}\pi_{ij}(\tau) = -\frac{e^2}{4N}\sum_{\boldsymbol{k}}\Big(& v^{ei}_{\boldsymbol{k},\alpha_1\alpha_2} v^{ej}_{-\boldsymbol{k},\beta_1\beta_2} \langle \mathcal{T}_\tau \hat{a}_{\boldsymbol{k}\alpha_2}(\tau)\hat{a}_{-\boldsymbol{k}\beta_2}(0)\rangle \langle \mathcal{T}_\tau \hat{a}^\dagger_{-\boldsymbol{k}\beta_1}(0)\hat{a}^\dagger_{\boldsymbol{k}\alpha_1}(\tau)\rangle \\ & - v^{ei}_{\boldsymbol{k},\alpha_1\alpha_2} v^{ej}_{\boldsymbol{k},\beta_1\beta_2} \langle \mathcal{T}_\tau \hat{a}_{\boldsymbol{k}\alpha_2}(\tau)\hat{a}^\dagger_{\boldsymbol{k}\beta_1}(0)\rangle \langle \mathcal{T}_\tau \hat{a}_{\boldsymbol{k}\beta_2}(0)\hat{a}^\dagger_{\boldsymbol{k}\alpha_1}(\tau)\rangle \\ & + v^{ei}_{\boldsymbol{k},\alpha_1\alpha_2} v^{hj}_{-\boldsymbol{k},\beta_1\beta_2} \langle \mathcal{T}_\tau \hat{a}_{\boldsymbol{k}\alpha_2}(\tau)\hat{a}^\dagger_{\boldsymbol{k}\beta_2}(0)\rangle \langle \mathcal{T}_\tau \hat{a}_{\boldsymbol{k}\beta_1}(0)\hat{a}^\dagger_{\boldsymbol{k}\alpha_1}(\tau)\rangle \\ & - v^{ei}_{\boldsymbol{k},\alpha_1\alpha_2} v^{hj}_{\boldsymbol{k},\beta_1\beta_2} \langle \mathcal{T}_\tau \hat{a}_{\boldsymbol{k}\alpha_2}(\tau)\hat{a}_{-\boldsymbol{k}\beta_1}(0)\rangle \langle \mathcal{T}_\tau \hat{a}^\dagger_{-\boldsymbol{k}\beta_2}(0)\hat{a}^\dagger_{\boldsymbol{k}\alpha_1}(\tau)\rangle \\ & + v^{hi}_{\boldsymbol{k},\alpha_1\alpha_2} v^{ej}_{-\boldsymbol{k},\beta_1\beta_2} \langle \mathcal{T}_\tau \hat{a}^\dagger_{-\boldsymbol{k}\alpha_2}(\tau)\hat{a}_{-\boldsymbol{k}\beta_2}(0)\rangle \langle \mathcal{T}_\tau \hat{a}^\dagger_{-\boldsymbol{k}\beta_1}(0)\hat{a}_{-\boldsymbol{k}\alpha_1}(\tau)\rangle \\ & - v^{hi}_{\boldsymbol{k},\alpha_1\alpha_2} v^{ej}_{\boldsymbol{k},\beta_1\beta_2} \langle \mathcal{T}_\tau \hat{a}^\dagger_{-\boldsymbol{k}\alpha_2}(\tau)\hat{a}^\dagger_{\boldsymbol{k}\beta_1}(0)\rangle \langle \mathcal{T}_\tau \hat{a}_{\boldsymbol{k}\beta_2}(0)\hat{a}_{-\boldsymbol{k}\alpha_1}(\tau)\rangle \\ & + v^{hi}_{\boldsymbol{k},\alpha_1\alpha_2} v^{hj}_{-\boldsymbol{k},\beta_1\beta_2} \langle \mathcal{T}_\tau \hat{a}^\dagger_{-\boldsymbol{k}\alpha_2}(\tau)\hat{a}^\dagger_{\boldsymbol{k}\beta_2}(0)\rangle \langle \mathcal{T}_\tau \hat{a}_{\boldsymbol{k}\beta_1}(0)\hat{a}_{-\boldsymbol{k}\alpha_1}(\tau)\rangle \\ & - v^{hi}_{\boldsymbol{k},\alpha_1\alpha_2} v^{hj}_{\boldsymbol{k},\beta_1\beta_2} \langle \mathcal{T}_\tau \hat{a}^\dagger_{-\boldsymbol{k}\alpha_2}(\tau)\hat{a}_{-\boldsymbol{k}\beta_1}(0)\rangle \langle \mathcal{T}_\tau \hat{a}^\dagger_{-\boldsymbol{k}\beta_2}(0)\hat{a}_{-\boldsymbol{k}\alpha_1}(\tau)\rangle\Big). \quad (5.15)\end{aligned}$$

From (5.9) and (5.10) we see that $v^{hi}_{\boldsymbol{k},\alpha_1\alpha_2} = -v^{ei}_{-\boldsymbol{k},\alpha_2\alpha_1}$. This allows us to write, for example, the first term in (5.15) as

$$v^{ei}_{\boldsymbol{k},\alpha_1\alpha_2} v^{ej}_{-\boldsymbol{k},\beta_1\beta_2} \langle \mathcal{T}_\tau \hat{a}^\dagger_{\boldsymbol{k}\alpha_1}(\tau)\hat{a}^\dagger_{-\boldsymbol{k}\beta_1}(0)\rangle \langle \mathcal{T}_\tau \hat{a}_{-\boldsymbol{k}\beta_2}(0)\hat{a}_{\boldsymbol{k}\alpha_2}(\tau)\rangle \\ = -v^{hi}_{\boldsymbol{k},\alpha_1\alpha_2} v^{ej}_{\boldsymbol{k},\beta_1\beta_2} \langle \mathcal{T}_\tau \hat{a}^\dagger_{\boldsymbol{k}\alpha_1}(\tau)\hat{a}^\dagger_{-\boldsymbol{k}\beta_2}(0)\rangle \langle \mathcal{T}_\tau \hat{a}_{-\boldsymbol{k}\beta_1}(0)\hat{a}_{\boldsymbol{k}\alpha_2}(\tau)\rangle.$$

Close examination shows us that this is equal to the fourth term in (5.15). In fact, we also find that the second term is equal to the third, the fifth is equal to the eighth, and the sixth is equal to the seventh. Putting these together yields

$$\begin{aligned}\pi_{ij}(\tau) = \frac{e^2}{2N}\sum_{\boldsymbol{k}}\Big(& v^{ei}_{\boldsymbol{k},\alpha_1\alpha_2} v^{ej}_{\boldsymbol{k},\beta_1\beta_2} \langle \mathcal{T}_\tau \hat{a}_{\boldsymbol{k}\alpha_2}(\tau)\hat{a}^\dagger_{\boldsymbol{k}\beta_1}(0)\rangle \langle \mathcal{T}_\tau \hat{a}_{\boldsymbol{k}\beta_2}(0)\hat{a}^\dagger_{\boldsymbol{k}\alpha_1}(\tau)\rangle \\ & + v^{ei}_{\boldsymbol{k},\alpha_1\alpha_2} v^{hj}_{\boldsymbol{k},\beta_1\beta_2} \langle \mathcal{T}_\tau \hat{a}_{\boldsymbol{k}\alpha_2}(\tau)\hat{a}_{-\boldsymbol{k}\beta_1}(0)\rangle \langle \mathcal{T}_\tau \hat{a}^\dagger_{-\boldsymbol{k}\beta_2}(0)\hat{a}^\dagger_{\boldsymbol{k}\alpha_1}(\tau)\rangle \\ & + v^{hi}_{\boldsymbol{k},\alpha_1\alpha_2} v^{ej}_{\boldsymbol{k},\beta_1\beta_2} \langle \mathcal{T}_\tau \hat{a}^\dagger_{-\boldsymbol{k}\alpha_2}(\tau)\hat{a}^\dagger_{\boldsymbol{k}\beta_1}(0)\rangle \langle \mathcal{T}_\tau \hat{a}_{\boldsymbol{k}\beta_2}(0)\hat{a}_{-\boldsymbol{k}\alpha_1}(\tau)\rangle \\ & + v^{hi}_{\boldsymbol{k},\alpha_1\alpha_2} v^{hj}_{\boldsymbol{k},\beta_1\beta_2} \langle \mathcal{T}_\tau \hat{a}^\dagger_{-\boldsymbol{k}\alpha_2}(\tau)\hat{a}_{-\boldsymbol{k}\beta_1}(0)\rangle \langle \mathcal{T}_\tau \hat{a}^\dagger_{-\boldsymbol{k}\beta_2}(0)\hat{a}_{-\boldsymbol{k}\alpha_1}(\tau)\rangle\Big). \quad (5.16)\end{aligned}$$

If we pay careful attention to the indices, we see that each term in (5.16) is suggestive of a trace. It is not difficult to verify that we can write

$$\begin{aligned}\pi_{ij}(\tau) = \frac{e^2}{2N}\sum_{\boldsymbol{k}}\Big(&\mathrm{Tr}\Big\{v^{ei}_{\boldsymbol{k}}\langle\mathcal{T}_\tau\Psi^e_{\boldsymbol{k}}(\tau)\Psi^{e\dagger}_{\boldsymbol{k}}(0)\rangle v^{ej}_{\boldsymbol{k}}\langle\mathcal{T}_\tau\Psi^e_{\boldsymbol{k}}(0)\Psi^{e\dagger}_{\boldsymbol{k}}(\tau)\rangle\Big\}\\ &+\mathrm{Tr}\Big\{v^{ei}_{\boldsymbol{k}}\langle\mathcal{T}_\tau\Psi^e_{\boldsymbol{k}}(\tau)\Psi^{h\dagger}_{\boldsymbol{k}}(0)\rangle v^{hj}_{\boldsymbol{k}}\langle\mathcal{T}_\tau\Psi^h_{\boldsymbol{k}}(0)\Psi^{e\dagger}_{\boldsymbol{k}}(\tau)\rangle\Big\}\\ &+\mathrm{Tr}\Big\{v^{hi}_{\boldsymbol{k}}\langle\mathcal{T}_\tau\Psi^h_{\boldsymbol{k}}(\tau)\Psi^{e\dagger}_{\boldsymbol{k}}(0)\rangle v^{ej}_{\boldsymbol{k}}\langle\mathcal{T}_\tau\Psi^e_{\boldsymbol{k}}(0)\Psi^{h\dagger}_{\boldsymbol{k}}(\tau)\rangle\Big\}\\ &+\mathrm{Tr}\Big\{v^{hi}_{\boldsymbol{k}}\langle\mathcal{T}_\tau\Psi^h_{\boldsymbol{k}}(\tau)\Psi^{h\dagger}_{\boldsymbol{k}}(0)\rangle v^{hj}_{\boldsymbol{k}}\langle\mathcal{T}_\tau\Psi^h_{\boldsymbol{k}}(0)\Psi^{h\dagger}_{\boldsymbol{k}}(\tau)\rangle\Big\}\Big),\end{aligned} \tag{5.17}$$

where the "electron" and "hole" spinors are given by

$$\Psi^e_{\boldsymbol{k}} = \begin{pmatrix}\hat{a}_{\boldsymbol{k}x\uparrow} & \hat{a}_{\boldsymbol{k}x\downarrow} & \hat{a}_{\boldsymbol{k}y\uparrow} & \hat{a}_{\boldsymbol{k}y\downarrow}\end{pmatrix}^T \tag{5.18}$$

and

$$\Psi^h_{\boldsymbol{k}} = \begin{pmatrix}\hat{a}^\dagger_{-\boldsymbol{k}x\uparrow} & \hat{a}^\dagger_{-\boldsymbol{k}x\downarrow} & \hat{a}^\dagger_{-\boldsymbol{k}y\uparrow} & \hat{a}^\dagger_{-\boldsymbol{k}y\downarrow}\end{pmatrix}^T \tag{5.19}$$

respectively. Finally, by noting that the full Nambu spinor, (3.1), can be written as $\Psi_{\boldsymbol{k}} = \begin{pmatrix}\Psi^e_{\boldsymbol{k}} & \Psi^h_{\boldsymbol{k}}\end{pmatrix}^T$, it is again straightforward to verify that we can write

$$\pi_{ij}(\tau) = \frac{e^2}{2N}\sum_{\boldsymbol{k}}\mathrm{Tr}\left\{\begin{pmatrix}v^{ei}_{\boldsymbol{k}} & 0\\ 0 & v^{hi}_{\boldsymbol{k}}\end{pmatrix}\left\langle\mathcal{T}_\tau\Psi_{\boldsymbol{k}}(\tau)\Psi^\dagger_{\boldsymbol{k}}(0)\right\rangle\begin{pmatrix}v^{ej}_{\boldsymbol{k}} & 0\\ 0 & v^{hj}_{\boldsymbol{k}}\end{pmatrix}\left\langle\mathcal{T}_\tau\Psi_{\boldsymbol{k}}(0)\Psi^\dagger_{\boldsymbol{k}}(\tau)\right\rangle\right\} \tag{5.20}$$

$$= \frac{e^2}{2N}\sum_{\boldsymbol{k}}\mathrm{Tr}\Big\{v^i_{\boldsymbol{k}}\mathcal{G}_{\boldsymbol{k}}(\tau)v^j_{\boldsymbol{k}}\mathcal{G}_{\boldsymbol{k}}(-\tau)\Big\}, \tag{5.21}$$

where we have defined the full velocity matrix as

$$v^i_{\boldsymbol{k}} = \begin{pmatrix}v^{ei}_{\boldsymbol{k}} & 0\\ 0 & v^{hi}_{\boldsymbol{k}}\end{pmatrix}, \tag{5.22}$$

and have introduced the imaginary-time Nambu Green's function [89]

$$\mathcal{G}_{\boldsymbol{k}}(\tau_1-\tau_2) = -\left\langle\mathcal{T}_\tau\Psi_{\boldsymbol{k}}(\tau_1)\Psi^\dagger_{\boldsymbol{k}}(\tau_2)\right\rangle, \tag{5.23}$$

which is an 8×8 matrix.

The Matsubara correlation function: Substituting (5.21) into (5.4) yields the following form of the Matsubara current-current correlator:

$$\pi_{ij}(i\omega_n) = \frac{e^2}{2N}\sum_{\boldsymbol{k}}\int_0^\beta d\tau\, e^{i\omega_n\tau}\,\mathrm{Tr}\Big\{v^i_{\boldsymbol{k}}\mathcal{G}_{\boldsymbol{k}}(\tau)v^j_{\boldsymbol{k}}\mathcal{G}_{\boldsymbol{k}}(-\tau)\Big\}. \tag{5.24}$$

Our final stage of working will be undertaken with the aim of expressing this conveniently in terms of Matsubara Green's functions, $\mathcal{G}_{\boldsymbol{k},i\nu_m}$, which will get rid of the integral in (5.24). To proceed, we require the following identity [88]:

$$\mathcal{G}_{\boldsymbol{k}}(\tau) = \frac{1}{\beta}\sum_m \mathcal{G}_{\boldsymbol{k},i\nu_m}e^{-i\nu_m\tau}, \tag{5.25}$$

where $\nu_m = (2m+1)\pi/\beta$ is a *fermionic* Matsubara frequency, corresponding to the single-particle excitations described by the BdG Hamiltonian. This gives us

$$\pi_{ij}(i\omega_n) = \frac{e^2}{2N}\sum_{\boldsymbol{k}}\frac{1}{\beta^2}\sum_{l,m}\int_0^\beta d\tau\, e^{i\omega_n\tau}\,\mathrm{Tr}\Big\{v^i_{\boldsymbol{k}}\mathcal{G}_{\boldsymbol{k},i\nu_l}e^{-i\nu_l\tau}v^j_{\boldsymbol{k}}\mathcal{G}_{\boldsymbol{k},i\nu_m}e^{i\nu_m\tau}\Big\} \tag{5.26}$$

$$= \frac{e^2}{2N}\sum_{\boldsymbol{k}}\frac{1}{\beta^2}\sum_{l,m}\mathrm{Tr}\Big\{v^i_{\boldsymbol{k}}\mathcal{G}_{\boldsymbol{k},i\nu_l}v^j_{\boldsymbol{k}}\mathcal{G}_{\boldsymbol{k},i\nu_m}\Big\}\int_0^\beta d\tau\, e^{i(\omega_n-\nu_l+\nu_m)\tau}, \tag{5.27}$$

where the integral in (5.27) is given by

$$\int_0^\beta d\tau\, e^{i(\omega_n-\nu_l+\nu_m)\tau} = \beta\delta_{\nu_l,\omega_n+\nu_m}. \tag{5.28}$$

Substituting this result back into (5.27) yields

$$\pi_{ij}(i\omega_n) = \frac{e^2}{2N}\sum_{\boldsymbol{k}}\frac{1}{\beta}\sum_{m}\mathrm{Tr}\Big\{v^i_{\boldsymbol{k}}\mathcal{G}_{\boldsymbol{k},i\omega_n+i\nu_m}v^j_{\boldsymbol{k}}\mathcal{G}_{\boldsymbol{k},i\nu_m}\Big\}. \tag{5.29}$$

The Hall conductivity: The real-frequency current-current correlator, $\pi_{ij}(\omega)$, can be calculated from (5.29) via the analytic continuation (5.6). The Hall conductivity is then given by (5.3) to be

$$\sigma_H(\omega) = \frac{ie^2}{4N\omega}\lim_{i\omega_n\to\omega+i0^+}\sum_{\boldsymbol{k}}\frac{1}{\beta}\sum_{m}\mathrm{Tr}\Big\{\Big[v^x_{\boldsymbol{k}}\mathcal{G}_{\boldsymbol{k},i\omega_n+i\nu_m}v^y_{\boldsymbol{k}} - v^y_{\boldsymbol{k}}\mathcal{G}_{\boldsymbol{k},i\omega_n+i\nu_m}v^x_{\boldsymbol{k}}\Big]\,\mathcal{G}_{\boldsymbol{k},i\nu_m}\Big\}. \tag{5.30}$$

The only assumption explicitly used in deriving this result was that the normal state has definite parity, although we must remember that the Kubo formula used as a starting point only applies in the linear response regime. This expression differs by a factor of one half compared to that used elsewhere in the literature [22, 26]. This is not an inconsistency, but arises because the BdG Hamiltonian in those works can be block-diagonalised into two sectors, each of which contribute equally to the trace in (5.30). Other authors choose to express (5.30) in terms of just one of these sectors, whereas I write it in terms of the full Nambu Green's function so that our results will apply generally, even when the Hamiltonian cannot be block-diagonalised in such a way.

5.2 High-frequency, small-gap approximation

We will return to (5.30) in Chapter 6, but for now we turn our attention to an approximate form of the Hall conductivity in the *high-frequency, small-gap limit*. The physical relevance of this limit is discussed below. In general, the Green's function that appears in (5.30) can be related to the Green's function of the normal state by Dyson's equation

$$\mathcal{G} = \mathcal{G}_0 + \mathcal{G}_0 H_\Delta \mathcal{G}, \tag{5.31}$$

where $\mathcal{G}_0$ is the Nambu Green's function corresponding to the normal state (i.e. just the block diagonal parts of $\mathcal{G}$), and

$$H_\Delta \equiv \begin{pmatrix} 0 & \Delta \\ \Delta^\dagger & 0 \end{pmatrix} \tag{5.32}$$

is the pairing part of the BdG Hamiltonian. The small-gap limit can be taken by expanding (5.31) up to second order in H_Δ, i.e.

$$\mathcal{G} \approx \mathcal{G}_0 + \mathcal{G}_0 H_\Delta \mathcal{G}_0 + \mathcal{G}_0 H_\Delta \mathcal{G}_0 H_\Delta \mathcal{G}_0, \tag{5.33}$$

which is equivalent to dropping all terms higher than second order in the gap magnitude (although it does not necessarily mean that all second-order terms are kept). Similarly, we can take the high-frequency limit by dropping all the remaining terms with a frequency dependence of lower order than ω^{-2}. This process is performed by Brydon et al. in [27], where they obtain the following approximation for the Matsubara current-current correlator in the high-frequency, small-gap limit:

$$\pi_{xy}(i\omega_n) \approx \frac{e^2}{2i\omega_n} \frac{1}{N} \sum_{\boldsymbol{k}} \frac{1}{\beta} \sum_m \mathrm{Tr}\Big\{ (v^x_{\boldsymbol{k}} v^y_{\boldsymbol{k}} - v^y_{\boldsymbol{k}} v^x_{\boldsymbol{k}}) \mathcal{G}_{0,\boldsymbol{k},i\nu_m} H_{\Delta,\boldsymbol{k}} \mathcal{G}_{0,\boldsymbol{k},i\nu_m} H_{\Delta,\boldsymbol{k}} \mathcal{G}_{0,\boldsymbol{k},i\nu_m} \Big\}. \tag{5.34}$$

Technically, this expression differs by a factor of one half from that of Brydon et al., for the same reason as for (5.30). Within this limit we also find $\pi_{xy}(i\omega_n) = -\pi_{yx}(i\omega_n)$, so (5.3) yields the following expression for the Hall conductivity

$$\sigma_H(\omega) \approx \frac{ie^2}{2\omega^2} \frac{1}{N} \sum_{\boldsymbol{k}} \frac{1}{\beta} \sum_m \mathrm{Tr}\Big\{ (v^x_{\boldsymbol{k}} v^y_{\boldsymbol{k}} - v^y_{\boldsymbol{k}} v^x_{\boldsymbol{k}}) \mathcal{G}_{0,\boldsymbol{k},i\nu_m} H_{\Delta,\boldsymbol{k}} \mathcal{G}_{0,\boldsymbol{k},i\nu_m} H_{\Delta,\boldsymbol{k}} \mathcal{G}_{0,\boldsymbol{k},i\nu_m} \Big\}, \tag{5.35}$$

where the $i0^+$ part of the analytic continuation has been dropped because it will never contribute unless $\omega = 0$, which falls outside the high-frequency limit.

The remainder of this section is dedicated to gaining a better understanding of the velocity term and the Green's function that appear in (5.35). This involves introducing some assumptions, so the results we obtain will not be completely general, although they will still apply to a large class of systems, including our model of strontium ruthenate.

The velocity term: To begin, it is notationally convenient to define the following "wedge product":

$$[a \wedge b] = a^x b^y - a^y b^x. \tag{5.36}$$

In particular, we have

$$[v^e_{\boldsymbol{k}} \wedge v^e_{\boldsymbol{k}}] = v^{ex}_{\boldsymbol{k}} v^{ey}_{\boldsymbol{k}} - v^{ey}_{\boldsymbol{k}} v^{ex}_{\boldsymbol{k}} \tag{5.37}$$

and

$$[v^h_{\boldsymbol{k}} \wedge v^h_{\boldsymbol{k}}] = v^{hx}_{\boldsymbol{k}} v^{hy}_{\boldsymbol{k}} - v^{hy}_{\boldsymbol{k}} v^{hx}_{\boldsymbol{k}}. \tag{5.38}$$

We can see how these two expressions are related by noting that

$$\begin{aligned}
[v^h \wedge v^h] &= \frac{\partial H^T_{0,-\boldsymbol{k}}}{\partial k_x} \frac{\partial H^T_{0,-\boldsymbol{k}}}{\partial k_y} - \frac{\partial H^T_{0,-\boldsymbol{k}}}{\partial k_y} \frac{\partial H^T_{0,-\boldsymbol{k}}}{\partial k_x} \\
&= U_I^T \left(\frac{\partial H^T_{0,\boldsymbol{k}}}{\partial k_x} \frac{\partial H^T_{0,\boldsymbol{k}}}{\partial k_y} - \frac{\partial H^T_{0,\boldsymbol{k}}}{\partial k_y} \frac{\partial H^T_{0,\boldsymbol{k}}}{\partial k_x} \right) U_I^* \\
&= U_I^T \left(\frac{\partial H_{0,\boldsymbol{k}}}{\partial k_y} \frac{\partial H_{0,\boldsymbol{k}}}{\partial k_x} - \frac{\partial H_{0,\boldsymbol{k}}}{\partial k_x} \frac{\partial H_{0,\boldsymbol{k}}}{\partial k_y} \right)^T U_I^* = -U_I^T [v^e_{\boldsymbol{k}} \wedge v^e_{\boldsymbol{k}}]^T U_I^*,
\end{aligned} \tag{5.39}$$

where we assumed that H_0 is symmetric under inversion, and therefore $U_I^T H_{0,\boldsymbol{k}}^T U_I^* = H_{0,-\boldsymbol{k}}^T$, which can be seen by taking the transpose of (2.27). We can therefore write

$$v_{\boldsymbol{k}}^x v_{\boldsymbol{k}}^y - v_{\boldsymbol{k}}^y v_{\boldsymbol{k}}^x = \begin{pmatrix} v_{\boldsymbol{k}}^{ex} v_{\boldsymbol{k}}^{ey} - v_{\boldsymbol{k}}^{ey} v_{\boldsymbol{k}}^{ex} & 0 \\ 0 & v_{\boldsymbol{k}}^{hx} v_{\boldsymbol{k}}^{hy} - v_{\boldsymbol{k}}^{hy} v_{\boldsymbol{k}}^{hx} \end{pmatrix} = \begin{pmatrix} [v_{\boldsymbol{k}}^e \wedge v_{\boldsymbol{k}}^e] & 0 \\ 0 & -U_I^T [v_{\boldsymbol{k}}^e \wedge v_{\boldsymbol{k}}^e]^T U_I^* \end{pmatrix}, \tag{5.40}$$

which will make working with (5.35) easier.

The Green's function: The normal state Green's function can be written in Nambu space as [89]

$$\mathcal{G}_{0,\boldsymbol{k},i\nu_m} = \begin{pmatrix} \mathcal{G}^e_{0,\boldsymbol{k},i\nu_m} & 0 \\ 0 & \mathcal{G}^h_{0,\boldsymbol{k},i\omega_n} \end{pmatrix} = \left[i\nu_m \mathbb{1}_8 - \begin{pmatrix} H_{0,\boldsymbol{k}} & 0 \\ 0 & -H_{0,-\boldsymbol{k}}^T \end{pmatrix} \right]^{-1}, \tag{5.41}$$

where $\mathcal{G}^e_{0,\boldsymbol{k},i\nu_m}$ and $\mathcal{G}^h_{0,\boldsymbol{k},i\nu_m}$ are the "electron" and "hole" parts of the Green's function respectively. A block diagonal matrix can be inverted block by block, so these are decoupled, and we can write

$$\mathcal{G}^e_{0,\boldsymbol{k},i\nu_m} = [i\nu_m \mathbb{1}_4 - H_{0,\boldsymbol{k}}]^{-1}, \tag{5.42}$$
$$\mathcal{G}^h_{0,\boldsymbol{k},i\nu_m} = [i\nu_m \mathbb{1}_4 + H_{0,-\boldsymbol{k}}^T]^{-1}. \tag{5.43}$$

An alternative way of writing (5.42) is as a sum over projection operators:

$$\mathcal{G}^e_{0,\boldsymbol{k},i\nu_m} = \sum_{s,n} \frac{\mathcal{P}_{\boldsymbol{k},s,n}}{i\nu_m - E_{\boldsymbol{k},s,n}} = \sum_{s,n} \frac{|\boldsymbol{k},s,n\rangle \langle \boldsymbol{k},s,n|}{i\nu_m - E_{\boldsymbol{k},s,n}}, \tag{5.44}$$

where I have labelled the eigenstates of $H_{0,\boldsymbol{k}}$ with momentum, pseudospin, and band indices, as outlined in Section 4.1. Assuming that we can write $H_{0,\boldsymbol{k}}$ as in (4.7), the pseudospin degeneracy of the normal state means that there are only two energy bands, and we can write [32]

$$\mathcal{G}^e_{0,\boldsymbol{k},i\nu_m} = \sum_s \frac{\mathcal{P}_{\boldsymbol{k},s,+}}{i\nu_m - E_{\boldsymbol{k}+}} + \frac{\mathcal{P}_{\boldsymbol{k},s,-}}{i\nu_m - E_{\boldsymbol{k}-}} = \frac{\mathbb{1} + \tilde{H}_{0,\boldsymbol{k}}}{2(i\nu_m - E_{\boldsymbol{k}+})} + \frac{\mathbb{1} - \tilde{H}_{0,\boldsymbol{k}}}{2(i\nu_m - E_{\boldsymbol{k}-})}, \tag{5.45}$$

where E_+ is the energy of the "upper" band, E_- is the energy of the "lower" band, $\tilde{H}_0$ is defined in (4.8), and the projection operators have been given by (4.12). We can rearrange (5.45) slightly in order to decompose $G^e_{0,\boldsymbol{k},i\nu_m}$ in terms of $\tilde{H}_0$ and the identity matrix as follows:

$$\begin{aligned} \mathcal{G}^e_{0,\boldsymbol{k},i\nu_m} &= \frac{1}{2}\left[(i\nu_m - E_{\boldsymbol{k}+})^{-1}(\mathbb{1} + \tilde{H}_{0,\boldsymbol{k}})\right] + \frac{1}{2}\left[(i\nu_m - E_{\boldsymbol{k}-})^{-1}(\mathbb{1} - \tilde{H}_{0,\boldsymbol{k}})\right] \\ &= \frac{1}{2}\left[(i\nu_m - E_{\boldsymbol{k}+})^{-1} + (i\nu_m - E_{\boldsymbol{k}-})^{-1}\right]\mathbb{1} + \frac{1}{2}\left[(i\nu_m - E_{\boldsymbol{k}-})^{-1} - (i\nu_m - E_{\boldsymbol{k}-})^{-1}\right]\tilde{H}_{0,\boldsymbol{k}}. \end{aligned}$$

By generalising this result, we can also show that the hole-type Green's function is given by

$$\begin{aligned} \mathcal{G}^h_{0,\boldsymbol{k},i\nu_m} &= \frac{\mathbb{1} + \tilde{H}^T_{0,-\boldsymbol{k}}}{2(i\nu_m + E_{\boldsymbol{k}+})} + \frac{\mathbb{1} - \tilde{H}^T_{0,-\boldsymbol{k}}}{2(i\nu_m + E_{\boldsymbol{k}-})} \\ &= \frac{1}{2}\left[(i\nu_m + E_{\boldsymbol{k}+})^{-1} + (i\nu_m + E_{\boldsymbol{k}-})^{-1}\right]\mathbb{1} + \frac{1}{2}\left[(i\nu_m + E_{\boldsymbol{k}-})^{-1} - (i\nu_m + E_{\boldsymbol{k}-})^{-1}\right]\tilde{H}^T_{0,-\boldsymbol{k}}. \end{aligned}$$

For convenience, we will abbreviate these expressions by writing

$$\mathcal{G}^e_{0,\boldsymbol{k},i\nu_m} = a_{\boldsymbol{k},m}\mathbb{1} + b_{\boldsymbol{k},m}\tilde{H}_{0,\boldsymbol{k}}, \tag{5.46}$$
$$\mathcal{G}^h_{0,\boldsymbol{k},i\nu_m} = c_{\boldsymbol{k},m}\mathbb{1} + d_{\boldsymbol{k},m}\tilde{H}^T_{0,-\boldsymbol{k}}, \tag{5.47}$$

where

$$a_{\boldsymbol{k},m} = \frac{1}{2}\left[(i\nu_m - E_{\boldsymbol{k},+})^{-1} + (i\nu_m - E_{\boldsymbol{k},-})^{-1}\right], \tag{5.48}$$

$$b_{\boldsymbol{k},m} = \frac{1}{2}\left[(i\nu_m - E_{\boldsymbol{k},+})^{-1} - (i\nu_m - E_{\boldsymbol{k},-})^{-1}\right], \tag{5.49}$$

$$c_{\boldsymbol{k},m} = \frac{1}{2}\left[(i\nu_m + E_{\boldsymbol{k},+})^{-1} + (i\nu_m + E_{\boldsymbol{k},-})^{-1}\right], \tag{5.50}$$

$$d_{\boldsymbol{k},m} = \frac{1}{2}\left[(i\nu_m + E_{\boldsymbol{k},+})^{-1} - (i\nu_m + E_{\boldsymbol{k},-})^{-1}\right]. \tag{5.51}$$

5.3 Time-reversal-odd bilinears

As discussed in Chapter 1, a necessary condition for a non-zero Hall conductivity is broken time-reversal symmetry. In fact, the whole reason we are interested in the Hall conductivity is in the context of detecting TRSB via the polar Kerr effect. However, in addition to TRSB, there are additional conditions that must be met in order for a given system to exhibit a non-zero Hall conductivity, and identifying these in various models has been the focus of much theoretical work [22, 26, 27, 49, 50, 91]. For example, in chiral superconductors time-reversal is broken in the relative momentum coordinate of the Cooper pair, so it is necessary for this to be coupled to the experimentally accessible centre-of-mass momentum in order for an intrinsic Hall conductivity to be present. This is achieved, for example, in multiband superconductors (refer to the discussion in Section 1.2.2), which we are considering here. As an additional example, Taylor and Kallin have used a multiband model of strontium ruthenate to show that a further necessary condition is the presence of interband pairing [26]. The exact assumptions under which these various results apply is not always clear, especially when they are derived for a specific model. For this reason, there is still some debate over precisely which conditions are required.

When examining the anomalous Hall conductivity on a simplified model of the Honeycomb lattice, Brydon et al. argued for the introduction of some time-reversal symmetry breaking combination of products of $\tilde{\Delta}_{\boldsymbol{k}}$ and $\tilde{\Delta}_{\boldsymbol{k}}^\dagger$ [27]. As well as necessarily breaking time-reversal, the resulting bilinear would be independent of the overall phase of $\tilde{\Delta}$, which is not experimentally observable. The simplest such bilinear is $\tilde{\Delta}_{\boldsymbol{k}}\tilde{\Delta}_{\boldsymbol{k}}^\dagger$, and as noted in Section 3.2, $\tilde{\Delta}_{\boldsymbol{k}}$ and $\tilde{\Delta}_{\boldsymbol{k}}^\dagger$ are time-reversed counterparts. For this reason, Brydon et al. motivated the following *time-reversal-odd bilinear* (TROB) [27]:

$$\tilde{\Delta}_{\boldsymbol{k}}\tilde{\Delta}_{\boldsymbol{k}}^\dagger - \tilde{\Delta}_{\boldsymbol{k}}^\dagger\tilde{\Delta}_{\boldsymbol{k}}, \tag{5.52}$$

which selects just the time-reversal-odd part of $\tilde{\Delta}_{\boldsymbol{k}}\tilde{\Delta}_{\boldsymbol{k}}^\dagger$. The TROB defined in (5.52) is not necessarily unique; any function of the form $\tilde{\Delta}_{\boldsymbol{k}} f_{\boldsymbol{k}} \tilde{\Delta}_{\boldsymbol{k}}$, where $f_{\boldsymbol{k}}$ is time-reversal symmetric, would also be odd under time-reversal and independent of the overall phase of $\tilde{\Delta}$. In this section I follow this line of reasoning by further investigating the role of TROBs in determining the presence of a non-vanishing intrinsic Hall conductivity more generally.

I will deal with the high-frequency, small-gap approximation introduced in the previous section, as this leads to more analytically tractable expressions to work with. At the end I will discuss the applicability of my result away from this limit. To begin, substituting (5.32), (5.40), and (5.41) into (5.35), we find the Hall conductivity in this limit can be written as

$$\sigma_H(\omega) \approx \frac{ie^2}{2\omega^2}\frac{1}{N}\sum_{\boldsymbol{k}}\frac{1}{\beta}\sum_m \mathrm{Tr}\Big\{[v^e \wedge v^e]\,\mathcal{G}_0^e\,\Delta\,\mathcal{G}_0^h\,\Delta^\dagger\,\mathcal{G}_0^e - U_I^T[v^e \wedge v^e]^T U_I^*\,\mathcal{G}_0^h\,\Delta^\dagger\,\mathcal{G}_0^e\,\Delta\,\mathcal{G}_0^h\Big\}, \tag{5.53}$$

where I have dropped explicit momentum and frequency indices for convenience. The main part of this expression is the trace, which can be written as

$$\mathrm{Tr}\Big\{[v^e\wedge v^e]\,\mathcal{G}_0^e\,\tilde{\Delta}U_T\,\mathcal{G}_0^h\,U_T^\dagger\tilde{\Delta}^\dagger\,\mathcal{G}_0^e\Big\}-\mathrm{Tr}\Big\{U_I^T[v^e\wedge v^e]^TU_I^*\,\mathcal{G}_0^h\,U_T\tilde{\Delta}^\dagger\,\mathcal{G}_0^e\,\tilde{\Delta}U_T^\dagger\,\mathcal{G}_0^h\Big\},$$

where I have used $\Delta=\tilde{\Delta}U_T$ from (2.31), and $U_T=-U_T^\dagger$ from (3.27). By inserting $U_T^\dagger U_T=\mathbb{1}$ and taking advantage of the cyclic nature of the trace, we can write this as

$$\underbrace{\mathrm{Tr}\Big\{[v^e\wedge v^e]\,\mathcal{G}_0^e\,\tilde{\Delta}\,U_T\mathcal{G}_0^hU_T^\dagger\,\tilde{\Delta}^\dagger\,\mathcal{G}_0^e\Big\}}_{(*)}-\underbrace{\mathrm{Tr}\Big\{U_T^\dagger U_I^T[v^e\wedge v^e]^TU_I^*U_T\,U_T^\dagger\mathcal{G}_0^hU_T\,\tilde{\Delta}^\dagger\,\mathcal{G}_0^e\,\tilde{\Delta}\,U_T^\dagger\mathcal{G}_0^hU_T\Big\}}_{(\dagger)}.$$

This expression can be simplified in two useful ways:

1. Firstly, inversion commutes with time-reversal, so we can use (2.35) to write

$$U_T^\dagger U_I^T[v^e\wedge v^e]^TU_I^*U_T=U_I^\dagger U_T^\dagger[v^e\wedge v^e]^TU_TU_I.$$

We then have

$$\begin{aligned}U_I^\dagger U_T^\dagger[v^e\wedge v^e]^TU_TU_I&=U_I^\dagger U_T^\dagger\left(\frac{\partial H_{0,\boldsymbol{k}}^T}{\partial k_y}\frac{\partial H_{0,\boldsymbol{k}}^T}{\partial k_x}-\frac{\partial H_{0,\boldsymbol{k}}^T}{\partial k_x}\frac{\partial H_{0,\boldsymbol{k}}^T}{\partial k_y}\right)U_TU_I\\&=U_I^\dagger U_T^\dagger\left(\frac{\partial H_{0,\boldsymbol{k}}^*}{\partial k_y}\frac{\partial H_{0,\boldsymbol{k}}^*}{\partial k_x}-\frac{\partial H_{0,\boldsymbol{k}}^*}{\partial k_x}\frac{\partial H_{0,\boldsymbol{k}}^*}{\partial k_y}\right)U_TU_I,\end{aligned}$$

where $H_0^T=H_0^*$ arises from the fact that H_0 is Hermitian. We recognise $U_T^\dagger H_{0,\boldsymbol{k}}^*U_T$ from (2.29) as the result of applying time-reversal to $H_{0,-\boldsymbol{k}}$. Assuming H_0 is symmetric under time-reversal, we see that

$$U_I^\dagger U_T^\dagger[v^e\wedge v^e]^TU_TU_I=U_I^\dagger\left(\frac{\partial H_{0,-\boldsymbol{k}}}{\partial k_y}\frac{\partial H_{0,-\boldsymbol{k}}}{\partial k_x}-\frac{\partial H_{0,-\boldsymbol{k}}}{\partial k_x}\frac{\partial H_{0,-\boldsymbol{k}}}{\partial k_y}\right)U_I.$$

Similarly, we recognise $U_I^\dagger H_{0,-\boldsymbol{k}}U_I$ from (2.27) as the result of applying inversion to $H_{0,\boldsymbol{k}}$. Assuming H_0 is symmetric under inversion we can conclude that

$$U_I^\dagger U_T^\dagger[v^e\wedge v^e]^TU_TU_I=\left(\frac{\partial H_{0,\boldsymbol{k}}}{\partial k_y}\frac{\partial H_{0,\boldsymbol{k}}}{\partial k_x}-\frac{\partial H_{0,\boldsymbol{k}}}{\partial k_x}\frac{\partial H_{0,\boldsymbol{k}}}{\partial k_y}\right)=-[v^e\wedge v^e].\tag{5.54}$$

2. Secondly, using $\mathcal{G}_0^h$ as defined in (5.47), we have

$$U_T^\dagger\mathcal{G}_0^hU_T=U_T^\dagger(c_{\boldsymbol{k},m}\mathbb{1}+d_{\boldsymbol{k},m}\tilde{H}_{0,-\boldsymbol{k}}^T)U_T=c_{\boldsymbol{k},m}\mathbb{1}+d_{\boldsymbol{k},m}U_T^\dagger\tilde{H}_{0,-\boldsymbol{k}}^TU_T,$$

where we can again use (2.29), the assumption that the normal state is symmetric under time-reversal, and the Hermiticity of H_0 to conclude that

$$U_T^\dagger\mathcal{G}_0^hU_T=c_{\boldsymbol{k},m}\mathbb{1}+d_{\boldsymbol{k},m}\tilde{H}_{0,\boldsymbol{k}}.\tag{5.55}$$

Using these results we can write

$$(*) = \quad \mathrm{Tr}\Big\{[v^e \wedge v^e]\ (a\mathbb{1} + b\tilde{H}_{0,k})\ \tilde{\Delta}\ (c\mathbb{1} + d\tilde{H}_{0,k})\ \tilde{\Delta}^\dagger\ (a\mathbb{1} + b\tilde{H}_{0,k})\Big\}, \tag{5.56}$$

$$(\dagger) = -\mathrm{Tr}\Big\{[v^e \wedge v^e]\ (c\mathbb{1} + d\tilde{H}_{0,k})\ \tilde{\Delta}^\dagger\ (a\mathbb{1} + b\tilde{H}_{0,k})\ \tilde{\Delta}\ (c\mathbb{1} + d\tilde{H}_{0,k})\Big\}, \tag{5.57}$$

where I have dropped the explicit indices on the a, b, c, and d coefficients for convenience. The advantage these expressions have over the trace in (5.53) is that both $(*)$ and $(\dagger)$ are now expressed in terms of $[v^e \wedge v^e]$ and $\tilde{H}_{0,k}$, rather than mixing in $[v^e \wedge v^e]^T$ and $\tilde{H}^T_{0,-k}$ as well. By decomposing these expression further, we obtain

$$\begin{aligned}
(*) = \quad & a^2 c\,\mathrm{Tr}\Big\{[v^e \wedge v^e]\tilde{\Delta}\tilde{\Delta}^\dagger\Big\} && + a^2 d\,\mathrm{Tr}\Big\{[v^e \wedge v^e]\tilde{\Delta}\tilde{H}_{0,k}\tilde{\Delta}^\dagger\Big\} \\
& + b^2 c\,\mathrm{Tr}\Big\{[v^e \wedge v^e]\tilde{H}_{0,k}\tilde{\Delta}\tilde{\Delta}^\dagger\tilde{H}_{0,k}\Big\} && + b^2 d\,\mathrm{Tr}\Big\{[v^e \wedge v^e]\tilde{H}_{0,k}\tilde{\Delta}\tilde{H}_{0,k}\tilde{\Delta}^\dagger\tilde{H}_{0,k}\Big\} \\
& + abc\,\mathrm{Tr}\Big\{[v^e \wedge v^e]\tilde{\Delta}\tilde{\Delta}^\dagger\tilde{H}_{0,k}\Big\} && + abd\,\mathrm{Tr}\Big\{[v^e \wedge v^e]\tilde{\Delta}\tilde{H}_{0,k}\tilde{\Delta}^\dagger\tilde{H}_{0,k}\Big\} \\
& + abc\,\mathrm{Tr}\Big\{[v^e \wedge v^e]\tilde{H}_{0,k}\tilde{\Delta}\tilde{\Delta}^\dagger\Big\} && + abd\,\mathrm{Tr}\Big\{[v^e \wedge v^e]\tilde{H}_{0,k}\tilde{\Delta}\tilde{H}_{0,k}\tilde{\Delta}^\dagger\Big\},
\end{aligned}$$

and

$$\begin{aligned}
(\dagger) = \quad & -ac^2\,\mathrm{Tr}\Big\{[v^e \wedge v^e]\tilde{\Delta}^\dagger\tilde{\Delta}\Big\} && - bc^2\,\mathrm{Tr}\Big\{[v^e \wedge v^e]\tilde{\Delta}^\dagger\tilde{H}_{0,k}\tilde{\Delta}\Big\} \\
& - ad^2\,\mathrm{Tr}\Big\{[v^e \wedge v^e]\tilde{H}_{0,k}\tilde{\Delta}^\dagger\tilde{\Delta}\tilde{H}_{0,k}\Big\} && - bd^2\,\mathrm{Tr}\Big\{[v^e \wedge v^e]\tilde{H}_{0,k}\tilde{\Delta}^\dagger\tilde{H}_{0,k}\tilde{\Delta}\tilde{H}_{0,k}\Big\} \\
& - acd\,\mathrm{Tr}\Big\{[v^e \wedge v^e]\tilde{\Delta}^\dagger\tilde{\Delta}\tilde{H}_{0,k}\Big\} && - bcd\,\mathrm{Tr}\Big\{[v^e \wedge v^e]\tilde{\Delta}^\dagger\tilde{H}_{0,k}\tilde{\Delta}\tilde{H}_{0,k}\Big\} \\
& - acd\,\mathrm{Tr}\Big\{[v^e \wedge v^e]\tilde{H}_{0,k}\tilde{\Delta}^\dagger\tilde{\Delta}\Big\} && - bcd\,\mathrm{Tr}\Big\{[v^e \wedge v^e]\tilde{H}_{0,k}\tilde{\Delta}^\dagger\tilde{H}_{0,k}\tilde{\Delta}\Big\}.
\end{aligned}$$

Now, these two expressions are very similar, but differ in two crucial ways. Firstly, the order of $\tilde{\Delta}$ and $\tilde{\Delta}^\dagger$ are reversed, which is promisingly reminiscent of the TROB defined in (5.52). Secondly, a and c are swapped, and b and d are swapped. Examination of (5.48)–(5.51) show us that $a \to -c$ and $b \to -d$ when $\nu_m \to -\nu_m$, so let us consider the sum over m that appears in (5.53). As an example, the first term from each of $(*)$ and $(\dagger)$ contribute

$$\sum_m a_m^2 c_m\,\mathrm{Tr}\Big\{[v^e \wedge v^e]\tilde{\Delta}\tilde{\Delta}^\dagger\Big\} + \sum_m a_m c_m^2\,\mathrm{Tr}\Big\{[v^e \wedge v^e]\tilde{\Delta}^\dagger\tilde{\Delta}\Big\}$$

to the $\sum_m \mathrm{Tr}\{\cdots\} = \sum_m[(*) - (\dagger)]$ part of (5.53). Since the sum over m runs from $-\infty$ to ∞ we can take $\nu_m \to -\nu_m$ in the second term and it will not affect our result. This gives us

$$\sum_m a_m^2 c_m\,\mathrm{Tr}\Big\{[v^e \wedge v^e](\tilde{\Delta}\tilde{\Delta}^\dagger - \tilde{\Delta}^\dagger\tilde{\Delta})\Big\},$$

which is promising as it contains the TROB defined in (5.52). If we repeat this process for the second term in each of $(*)$ and $(\dagger)$ we obtain the following contribution:

$$\sum_m a_m^2 d_m\,\mathrm{Tr}\Big\{[v^e \wedge v^e](\tilde{\Delta}\tilde{H}_0\tilde{\Delta}^\dagger - \tilde{\Delta}^\dagger\tilde{H}_0\tilde{\Delta})\Big\}, \tag{5.58}$$

where $\tilde{H}_0$ is assumed to be evaluated at momentum $\boldsymbol{k}$ for the rest of this chapter. This expression does *not* contain the TROB defined in (5.52), but note that $\tilde{\Delta}\tilde{H}_0\tilde{\Delta}^\dagger - \tilde{\Delta}^\dagger\tilde{H}_0\tilde{\Delta}$ is still a time-reversal-odd bilinear. If we repeat this process for all the terms in $(*)$ and $(\dagger)$ we obtain the resulting

expression for the Hall conductivity:

$$\sigma_H(\omega) \approx \frac{ie^2}{2\omega^2}\frac{1}{N}\sum_{\boldsymbol{k}}\frac{1}{\beta}\sum_{m}(\ddagger), \tag{5.59}$$

where

$$\begin{aligned}(\ddagger) = a^2c\,\mathrm{Tr}\{[v^e\wedge v^e]\ \mathrm{TROB}_1\} + a^2d\,\mathrm{Tr}\{[v^e\wedge v^e]\ \mathrm{TROB}_2\}\\ + b^2c\,\mathrm{Tr}\{\tilde{H}_0[v^e\wedge v^e]\tilde{H}_0\ \mathrm{TROB}_1\} + b^2d\,\mathrm{Tr}\{\tilde{H}_0[v^e\wedge v^e]\tilde{H}_0\ \mathrm{TROB}_2\}\\ + abc\,\mathrm{Tr}\{\{\tilde{H}_0,[v^e\wedge v^e]\}\ \mathrm{TROB}_1\} + abd\,\mathrm{Tr}\{\{\tilde{H}_0,[v^e\wedge v^e]\}\ \mathrm{TROB}_2\},\end{aligned} \tag{5.60}$$

and

$$\mathrm{TROB}_1 \equiv \tilde{\Delta}\tilde{\Delta}^\dagger - \tilde{\Delta}^\dagger\tilde{\Delta}, \tag{5.61}$$

$$\mathrm{TROB}_2 \equiv \tilde{\Delta}\tilde{H}_0\tilde{\Delta}^\dagger - \tilde{\Delta}^\dagger\tilde{H}_0\tilde{\Delta}. \tag{5.62}$$

This result is exact in the high-frequency, small-gap limit, in the sense that (5.59) is equal to (5.35), which shows that these TROBs play a central role in determining the Hall conductivity. However, the main advantage of this result is not that we have restated (5.35), but rather that the TROBs themselves provide a quick test as to whether a given model of a superconductor might have a non-vanishing intrinsic Hall conductivity. If both TROBs are vanishing there will be no intrinsic Hall conductivity, so the existence of $\mathrm{TROB}_1 \neq 0$ or $\mathrm{TROB}_2 \neq 0$ is a *necessary* condition for a non-zero intrinsic Hall conductivity. This is a useful result because these TROBs are straightforward to calculate, which means that this requirement is easy to test for. On the other hand, it is important to note that this requirement is not a *sufficient* condition for a non-zero intrinsic Hall conductivity as it is possible for (5.59) to be vanishing even if one of the TROBs is non-zero, although this outcome probably requires fine-tuning.

Another useful feature of these TROBs is that the requirement for at least one of them to be non-zero implies not only that time-reversal is broken, but also that the TRSB can be communicated to the centre-of-mass coordinate. This can be seen by noting that in a single-band system both $\tilde{\Delta}$ and $\tilde{H}_0$ are written as the linear combination of Pauli matrices, in which case $\mathrm{TROB}_1 = \mathrm{TROB}_2 = 0$. This is to say that the TROBs require a multiband system in order to be non-vanishing, in which case we already know that the relative and centre-of-mass momentum coordinates are coupled. This means that our new condition for a non-vanishing Hall conductivity is *at least* as specific as these two conditions combined. On the other hand, it is not obvious if a non-vanishing TROB also implies the presence of interband pairing, in alignment with the condition identified in [26]. An in depth discussion about the relationship between these two conditions is presented in Section 5.3.2.

It may appear as though there is some kind of imbalance between electrons and holes in (5.59). Specifically, v^e appears while v^h does not, and the a and b coefficients occur more often than c and d. This imbalance is not actually an issue, and can be easily explained. First of all, v^e appears exclusively because (5.39) was used to write $[v^h\wedge v^h]$ in terms of $[v^e\wedge v^e]$. We could equally easily have chosen to invert this in order to write (5.59) exclusively in terms of v^h. Similarly, the over-emphasis of a and b arises from taking $\nu_m \to -\nu_m$ in the $(\dagger)$ terms when summing over m. If we had instead chosen to take $\nu_m \to -\nu_m$ in the $(*)$ terms, c and d would be emphasised instead.

5.3.1 Applicability of the TROB result

There are a few results that were assumed in the derivation that yielded (5.59) and the results pertaining to the TROBs that come along with it. All of these apply to our model of strontium ruthenate, but it is worth explicitly stating them, and discussing how generally they apply. To begin, it goes without saying that (5.59) only applies to systems that can be described by the mean-field superconducting Hamiltonian introduced in Section 2.1, and which have two internal degrees of freedom, each with two possible states. We have also used the fact that the Hamiltonian is Hermitian and obeys the fermionic exchange antisymmetry, and that time-reversal obeys $\Theta^2 = -\mathbb{1}$, each of which are physically required to be true. When it comes to calculating the Hall conductivity we have imposed the following assumptions:

1. *The intensity of the incoming light is restricted to the linear response regime*. This assumption was introduced right from the beginning, when we wrote the Hall conductivity in terms of the current-current correlator in (5.2). As was noted in Section 1.2, this regime is applicable to experiments [42], and, in any case, can be obtained by reducing the intensity of the beam.

2. *Measurements are taken in the high-frequency, small-gap limit*. This limit was introduced in Section 5.2, and applies to all results since. The "high-frequency" aspect is valid in the context of many experimental endeavours, and specifically to strontium ruthenate, as we will see in the next chapter. In any case, it can be obtained by using higher frequency light. The "small-gap" aspect can be obtained by taking measurements very close to the critical temperature, although it is unclear in general what range of temperatures it is valid over. The TROBs themselves still have some utility away from these limits, which is discussed in detail below.

3. *The normal state is symmetric under time-reversal*. This assumption was used explicitly to obtain (5.39), (5.54), and (5.55), and implicitly when we used the pseudospin degeneracy to write the Green's function as (5.45). As has been discussed previously, it is almost universally true that the normal state will be time-reversal symmetric. If the normal state were not symmetric under time-reversal, we might expect an anomalous Hall conductivity above the critical temperature. This could occur if the normal state was ferromagnetic for example, but this falls outside the scope of $\mathcal{H}_0$ as defined as a single-particle operator in (2.1).

4. *The normal state has an inversion centre, and is symmetric under inversion*. Similarly to the previous assumption, these are used explicitly to obtain (5.39) and (5.54), and implicitly in (5.45). These assumptions are somewhat restrictive because there are many superconducting systems which do not have an inversion centre, such as $LaNiC_2$ [92]. Our results do not apply to such systems. However, in crystal lattices that do have an inversion centre, the "normal state" does tend to be symmetric under inversion.

Application away from the high-frequency, small-gap limit

Although (5.59) only applies in the high-frequency, small-gap limit, the TROBs still have some utility away from this regime. To understand why, we begin by recalling that the small-gap limit is taken by dropping all terms that are of higher order than $\sim |\Delta|^2$. If we moved away from this limit (by decreasing the temperature), we would be required to include higher order terms in (5.33), although it would will leave the small-gap contribution unaffected. Although not impossible, it is unlikely that higher-order corrections would cancel out the small-gap contribution. For this reason, we can say that if either TROB is non-vanishing there will *probably* by a non-zero intrinsic Hall conductivity, even away from the small-gap limit. Unfortunately, the converse statement is not

true: if both TROBs are vanishing we cannot necessarily say that this implies a vanishing Hall conductivity away from the small-gap limit.

When we move away from the high-frequency limit a similar argument applies. If either TROB is non-zero it is likely that there will be a non-vanishing Hall conductivity, even away from the high-frequency limit, because it is unlikely that corrections to (5.59) will cancel out the high-frequency contribution. Further, unlike the small-gap approximation, the converse statement also holds: if both TROBs are vanishing there is probably no Hall conductivity at any frequency. To understand why this is the case we require the following two results [93, 94]:

$$\sigma_{H,\text{high-}\omega}(\omega) \propto \left\langle [\mathcal{J}_x, \mathcal{J}_y] \right\rangle , \tag{5.63}$$

and

$$\int_{-\infty}^{\infty} \omega \, \mathrm{Im}\{\sigma_H(\omega)\} \, \mathrm{d}\omega \propto \left\langle [\mathcal{J}_x, \mathcal{J}_y] \right\rangle . \tag{5.64}$$

From these we can conclude that

$$\sigma_{H,\text{high}-\omega}(\omega) \propto \int_{-\infty}^{\infty} \omega \, \mathrm{Im}\{\sigma_H(\omega)\} \, \mathrm{d}\omega. \tag{5.65}$$

It is unlikely that this integral over all frequencies will vanish unless the Hall conductivity is vanishing at all frequencies. If both TROBs are vanishing then we know that the Hall conductivity is equal to zero at high frequencies, and is therefore probably vanishing at all frequencies.

None of the arguments put forward in this section have been water-tight as they have all relied on balances of likelihoods. The key point is that just because (5.59) only applies in the high-frequency, small-gap limit does not mean that the TROBs I have identified have no use applicability outside of this regime.

5.3.2 Contribution from intraband pairing

As mentioned in Section 5.3, one of the necessary conditions for a non-zero Hall conductivity identified by Taylor and Kallin was the presence of interband pairing. This is a bit of a cause for concern because there is nothing in (5.59) that seems to indicate that intraband pairing does not contribute to the Hall conductivity. This apparent contradiction can be understood by realising that, while (5.59) applies rather generally, the results of Taylor and Kallin are specific to a certain model, which just so happens to be restricted in such a way that intraband pairing does not contribute to the intrinsic Hall conductivity. If we include just the E_u pairing potentials from Table 4.2, the model of strontium ruthenate introduced in Chapters 2 and 3 of this thesis turns out to be a generalised version of Taylor and Kallin's (the model in [26] takes $h_{23} = 0$ and $\Delta_{22} = 0$). In this section I will show why intraband pairing does not contribute within the E_u pairing states in our model, which will by extension explain Taylor and Kallin's result.

I begin by explicitly writing the traces in (5.59) in terms of the eigenstates of the normal state Hamiltonian. As discussed in Section 4.1, these are $|\boldsymbol{k}, s, \pm\rangle$, where $\pm$ indicates the two possible energy bands, and s is pseudospin. As an example, let us consider the first term in (5.59):

$$\mathrm{Tr}\{[v^e \wedge v^e] \, \mathrm{TROB}_1\} = \sum_{\sigma,\pm} \langle \sigma, \pm | \, [v^e \wedge v^e] \, \mathrm{TROB}_1 \, | \sigma, \pm \rangle , \tag{5.66}$$

where the momentum degree of freedom is not included in the trace as the momentum states are explicitly summed over in (5.59). At a given $\boldsymbol{k}$ point, the identity is $\mathbb{1} = \sum_{s,\pm} |s, \pm\rangle \langle s, \pm|$, which

can be inserted to obtain

$$\mathrm{Tr}\{[v^e \wedge v^e]\,\mathrm{TROB}_1\} = \sum_{s,\pm}\sum_{s',\pm'} \langle s,\pm|\,[v^e \wedge v^e]\,|s',\pm'\rangle\,\langle s',\pm'|\,\mathrm{TROB}_1\,|s,\pm\rangle\,. \tag{5.67}$$

As a second example, we can apply the same process to the second term in (5.59) in order to obtain

$$\mathrm{Tr}\{\tilde{H}_0[v^e \wedge v^e]\tilde{H}_0\,\mathrm{TROB}_1\} = \sum_{s,\pm}\sum_{s',\pm'} \langle s,\pm|\,\tilde{H}_0[v^e \wedge v^e]\tilde{H}_0\,|s',\pm'\rangle\,\langle s',\pm'|\,\mathrm{TROB}_1\,|s,\pm\rangle\,. \tag{5.68}$$

This expression differs from (5.67) by the presence of $\tilde{H}_0$. Applying (4.11) we have

$$\mathrm{Tr}\{\tilde{H}_0[v^e \wedge v^e]\tilde{H}_0\,\mathrm{TROB}_1\} = \sum_{s,\pm}\sum_{s',\pm'} \pm\pm'\,\langle s,\pm|\,[v^e \wedge v^e]\,|s',\pm'\rangle\,\langle s',\pm'|\,\mathrm{TROB}_1\,|s,\pm\rangle\,. \tag{5.69}$$

Applying the same process to each term in (5.59), we obtain the following result:

$$\begin{aligned}(\ddagger) = \sum_{s,\pm}\sum_{s',\pm'} \Big[& a^2 c\,\mathrm{Tr}_{1,\pm\pm'} \pm abc\,\mathrm{Tr}_{1,\pm\pm'} \pm' abc\,\mathrm{Tr}_{1,\pm\pm'} \pm\pm' b^2 c\,\mathrm{Tr}_{1,\pm\pm'} \\ & + a^2 d\,\mathrm{Tr}_{2,\pm\pm'} \pm abd\,\mathrm{Tr}_{2,\pm\pm'} \pm' abd\,\mathrm{Tr}_{2,\pm\pm'} \pm\pm' b^2 d\,\mathrm{Tr}_{2,\pm\pm'}\Big],\end{aligned} \tag{5.70}$$

where I have introduced the shorthand notation

$$\mathrm{Tr}_{i,\pm\pm'} \equiv \langle s,\pm|\,[v^e \wedge v^e]\,|s',\pm'\rangle\,\langle s',\pm'|\,\mathrm{TROB}_i\,|s,\pm\rangle\,, \tag{5.71}$$

which has allowed us to express (5.70) rather compactly. We can explicitly carry out the sum over the band index in order to write

$$\begin{aligned}(\ddagger) = \sum_{s,s'} \Big[& a^2 c(\mathrm{Tr}_{1,++} + \mathrm{Tr}_{1,+-} + \mathrm{Tr}_{1,-+} + \mathrm{Tr}_{1,--}) + a^2 d(\mathrm{Tr}_{2,++} + \mathrm{Tr}_{2,+-} + \mathrm{Tr}_{2,-+} + \mathrm{Tr}_{2,--}) \\ & + abc(\mathrm{Tr}_{1,++} + \mathrm{Tr}_{1,+-} - \mathrm{Tr}_{1,-+} - \mathrm{Tr}_{1,--}) + abd(\mathrm{Tr}_{2,++} + \mathrm{Tr}_{2,+-} - \mathrm{Tr}_{2,-+} - \mathrm{Tr}_{2,--}) \\ & + abc(\mathrm{Tr}_{1,++} - \mathrm{Tr}_{1,+-} + \mathrm{Tr}_{1,-+} - \mathrm{Tr}_{1,--}) + abd(\mathrm{Tr}_{2,++} - \mathrm{Tr}_{2,+-} + \mathrm{Tr}_{2,-+} - \mathrm{Tr}_{2,--}) \\ & + b^2 c(\mathrm{Tr}_{1,++} - \mathrm{Tr}_{1,+-} - \mathrm{Tr}_{1,-+} + \mathrm{Tr}_{1,--}) + b^2 d(\mathrm{Tr}_{2,++} - \mathrm{Tr}_{2,+-} - \mathrm{Tr}_{2,-+} + \mathrm{Tr}_{2,--})\Big].\end{aligned} \tag{5.72}$$

Regrouping these terms in a convenient manner yields

$$\begin{aligned}(\ddagger) = \sum_{s,s'} \Big[& (a+b)^2 c\,\mathrm{Tr}_{1,++} + (a^2-b^2)c(\mathrm{Tr}_{1,+-} + \mathrm{Tr}_{1,-+}) + (a-b)^2 c\,\mathrm{Tr}_{1,--} \\ & + (a+b)^2 d\,\mathrm{Tr}_{2,++} + (a^2-b^2)d(\mathrm{Tr}_{2,+-} + \mathrm{Tr}_{1,-+}) + (a-b)^2 d\,\mathrm{Tr}_{2,--}\Big].\end{aligned} \tag{5.73}$$

At this point we refer to (5.48)–(5.51) in order to write

$$a = g^e_+ + g^e_-, \qquad b = g^e_+ - g^e_-, \qquad c = g^h_+ + g^h_-, \qquad d = g^h_+ - g^h_-, \tag{5.74}$$

where

$$g^e_{\boldsymbol{k},m,\pm} = \frac{1}{2}\frac{1}{i\nu_m - E_{\boldsymbol{k}\pm}}, \qquad g^h_{\boldsymbol{k},m,\pm} = \frac{1}{2}\frac{1}{i\nu_m + E_{\boldsymbol{k}\pm}}, \tag{5.75}$$

although I will drop the explicit momentum and frequency indices for convenience. Substituting these into (5.73) yields

$$\begin{aligned}(\ddagger) = 4\sum_{s,s'}&(g^e_+)^2(g^h_+ + g^h_-)\,\mathrm{Tr}_{1,++} + (g^e_+)^2(g^h_+ - g^h_-)\,\mathrm{Tr}_{2,++} \\ &+ (g^e_+ g^e_-)(g^h_+ + g^h_-)(\mathrm{Tr}_{1,+-} + \mathrm{Tr}_{1,-+}) + (g^e_+ g^e_-)(g^h_+ - g^h_-)(\mathrm{Tr}_{2,+-} + \mathrm{Tr}_{2,-+}) \\ &+ (g^e_-)^2(g^h_+ + g^h_-)\,\mathrm{Tr}_{1,--} + (g^e_-)^2(g^h_+ - g^h_-)\,\mathrm{Tr}_{2,--}]. \end{aligned} \tag{5.76}$$

This change in notation is useful because the $\pm$ index on the g coefficients in each term indicates which band the Green's functions that appear in that term belong to. Terms involving only g^e_+ and g^h_+, or only g^e_- and g^h_-, can only involve intraband pairing, while any expression that involves a mixture of g_+ and g_- terms must involve interband pairing. We can immediately see that $\mathrm{Tr}_{i,+-}$ and $\mathrm{Tr}_{i,-+}$ always correspond to interband pairing, while the $\mathrm{Tr}_{i,++}$ and $\mathrm{Tr}_{i,--}$ terms can involve intraband contributions. The purely intraband part of (5.76) is therefore given by

$$(\ddagger)_{\text{intra}} = 4\sum_{s,s'}\left[(g^e_+)^2 g^h_+(\mathrm{Tr}_{1,++} + \mathrm{Tr}_{2,++}) + (g^e_-)^2 g^h_-(\mathrm{Tr}_{1,--} - \mathrm{Tr}_{2,--})\right] \tag{5.77}$$

$$= 4\sum_{s,s'}\sum_{\pm}(g^e_\pm)^2 g^h_\pm(\mathrm{Tr}_{1,\pm\pm} \pm \mathrm{Tr}_{2,\pm\pm}). \tag{5.78}$$

So far this derivation has been general to systems subject to the assumptions outlined in Section 5.3.1. We know that, in general, pseudospin is a degree of freedom that transforms in the same way as spin under inversion and time-reversal, and it turns out that within our model, i.e. with H_0 as given by (3.38), the pseudospin is actually just the spin, so the eigenstates of H_0 are $|\boldsymbol{k}, \sigma, \pm\rangle$. To see why this is the case, note that (3.38) is purely diagonal in spin. It therefore commutes with the spin operator $\mathcal{S}_z = \eta_0 \otimes \sigma_3$, and we can conclude that they share a common set of eigenstates, i.e. the spin states $|\sigma\rangle$. I will now show that in this case the intraband contribution to the Hall conductivity is vanishing (at least in the high-frequency, small-gap limit). To approach this, let us see how we can simplify the

$$\mathrm{Tr}_{i,\pm\pm} = \sum_{\sigma,\sigma'}\langle\sigma,\pm|\,[v^e \wedge v^e]\,|\sigma',\pm\rangle\,\langle\sigma',\pm|\,\mathrm{TROB}_i\,|\sigma,\pm\rangle \tag{5.79}$$

terms that appear in (5.78). (5.79) consists of four terms (one for each value of σ and σ'), but we note that since H_0 is diagonal in spin, so too is $[v^e \wedge v^e]$. This implies that the spin off-diagonal terms must vanish, and hence we have

$$\mathrm{Tr}_{i,\pm\pm} = \sum_{\sigma}\langle\sigma,\pm|\,[v^e \wedge v^e]\,|\sigma,\pm\rangle\,\langle\sigma,\pm|\,\mathrm{TROB}_i\,|\sigma,\pm\rangle\,, \tag{5.80}$$

and therefore

$$\mathrm{Tr}_{1,\pm\pm} \pm \mathrm{Tr}_{2,\pm\pm} = \sum_{\sigma}\langle\sigma,\pm|\,[v^e \wedge v^e]\,|\sigma,\pm\rangle\,\langle\sigma,\pm|\,\mathrm{TROB}_1 \pm \mathrm{TROB}_2\,|\sigma,\pm\rangle\,. \tag{5.81}$$

To understand why the intraband contribution vanishes, it will suffice to show that

$$\langle\sigma,\pm|\,\mathrm{TROB}_1 \pm \mathrm{TROB}_2\,|\sigma,\pm\rangle \tag{5.82}$$

is equal to zero. Of course, this is not the only way the intraband contribution could vanish (for example, we could conceive of a situation where contributions from both spins were required in order for (5.81) to vanish), but we can see that if (5.82) vanishes, then so too must (5.78). In order to

achieve this we use the defining TROB expressions (5.61) and (5.62) to write

$$\mathrm{TROB}_1 \pm \mathrm{TROB}_2 = \tilde{\Delta}(1 \pm \tilde{H}_0)\tilde{\Delta}^\dagger - \tilde{\Delta}^\dagger(1 \pm \tilde{H}_0)\tilde{\Delta} = 2\left(\tilde{\Delta}\mathcal{P}_\pm\tilde{\Delta}^\dagger - \tilde{\Delta}^\dagger\mathcal{P}_\pm\tilde{\Delta}\right), \tag{5.83}$$

where we have used the band projection operators as defined in (4.12). When substituted into (5.82), we obtain

$$2\left\langle \sigma, \pm\right| \left[\tilde{\Delta}\mathcal{P}_\pm\tilde{\Delta}^\dagger - \tilde{\Delta}^\dagger\mathcal{P}_\pm\tilde{\Delta}\right] \left|\sigma, \pm\right\rangle .$$

Inserting the identity in the form $\mathbb{1} = \sum_\sigma \left(\left|\sigma,+\right\rangle\left\langle\sigma,+\right| + \left|\sigma,-\right\rangle\left\langle\sigma,-\right|\right)$, we can write

$$\begin{aligned} 2\sum_{\sigma'}\Big[&\left\langle \sigma, \pm\right| \left[\tilde{\Delta}\mathcal{P}_\pm \left|\sigma',+\right\rangle\left\langle\sigma',+\right| \tilde{\Delta}^\dagger - \tilde{\Delta}^\dagger\mathcal{P}_\pm \left|\sigma',+\right\rangle\left\langle\sigma',+\right| \tilde{\Delta}\right] \left|\sigma,\pm\right\rangle \\ &+ \left\langle \sigma', \pm\right| \left[\tilde{\Delta}\mathcal{P}_\pm \left|\sigma',-\right\rangle\left\langle\sigma,-\right| \tilde{\Delta}^\dagger - \tilde{\Delta}^\dagger\mathcal{P}_\pm \left|\sigma',+\right\rangle\left\langle\sigma',+\right| \tilde{\Delta}\right] \left|\sigma,\pm\right\rangle \Big]. \end{aligned}$$

By acting the projection operators on their neighbouring kets, we see that the first line vanishes when $\left|\pm\right\rangle \to \left|-\right\rangle$, while the second line vanishes when $\left|\pm\right\rangle \to \left|+\right\rangle$, so in either case we have

$$4\sum_{\sigma'}\left[\left\langle\sigma,\pm\right| \tilde{\Delta} \left|\sigma',\pm\right\rangle \left\langle\sigma',\pm\right| \tilde{\Delta}^\dagger \left|\sigma,\pm\right\rangle - \left\langle\sigma,\pm\right| \tilde{\Delta}^\dagger \left|\sigma',\pm\right\rangle \left\langle\sigma',\pm\right| \tilde{\Delta} \left|\sigma,\pm\right\rangle\right].$$

In general this could be non-zero, but we can see that it vanishes in particular if $\tilde{\Delta}$ is diagonal in spin. In conclusion, there is no intraband contribution to the Hall conductivity when both H_0 and $\tilde{\Delta}$ are diagonal in spin, as is the case for pairing within the E_u irreps in Table 4.2. Of course, this is not to say that this is the only case in which intraband pairing will not contribute, but it explains the conclusions of Taylor and Kallin. It is worth noting that this result could not be derived from the TROBs alone, but instead required the full expression for the Hall conductivity in the high-frequency, small-gap limit, (5.59).

Summary

The main result of this chapter was the identification of the two time-reversal-odd bilinears, (5.61) and (5.62), and their relationship to the presence of an intrinsic anomalous Hall conductivity in a given model. A necessary condition for a non-vanishing Hall conductivity in the high-frequency, small-gap limit is that these two TROBs are non-zero. Away from the high-frequency, small-gap limit this necessary condition no longer holds, as correction terms may contribute to the Hall conductivity even if (5.59) is vanishing. However, we can still say that if both TROBs are non-vanishing there will *probably* be a non-zero Hall conductivity at any given frequency and temperature. In the next chapter I will apply these results to our model of strontium ruthenate.

Chapter 6

Hall conductivity in strontium ruthenate

In Chapters 2–4 we constructed a simple model of superconductivity in strontium ruthenate, eventually restricting ourselves to 22 pairing channels: those belonging to the B_{1g}, B_{2g}, A_{1u}, A_{2u}, B_{1u}, B_{2u}, and E_u irreps listed in Table 4.2. This model was put aside in Chapter 5, so as to consider the Hall conductivity in a general class of systems. In this chapter we return to our model in order to consider the Hall conductivity in strontium ruthenate in particular. The focus of this chapter will be on pairing terms belonging to the E_u irreps. I did also consider the superposition of pairing potentials from different one-dimensional irreps, but I was unable to stabilise these within our model. This is discussed in more detail in Section 6.2.2.

A summary of the model containing just the E_u channels is provided in Section 6.1. In particular, I present the two TROBs introduced in Chapter 5, and use these to gain insight into which states might exhibit a non-zero Hall conductivity. I motivate two specific models, which will be examined in detail in this chapter. In Section 6.2 I calculate the amplitudes of the pairing potentials as a function of temperature, by minimising the free energy of each model. These are then used in Section 6.3 to calculate the Hall conductivity as a function of temperature and frequency within each model. Both the exact and the high-frequency, small-gap results of Chapter 5 are examined, and, in addition, I introduce a form of the Hall conductivity in the high-frequency limit alone.

6.1 E_u pairing states

As mentioned above, I choose to limit the pairing in our model to the E_u terms from Table 4.2. The justification for this choice is that it is natural for pairing terms from the same multi-dimensional irrep to form chiral states, whereas the superposition of terms from different irreps requires fine-tuning (refer to Section 3.4). A general superconducting state consisting of these terms has

$$H_{0,\boldsymbol{k}} = h_{\boldsymbol{k},00}\eta_0 \otimes \sigma_0 + h_{\boldsymbol{k},23}\eta_2 \otimes \sigma_3 + h_{\boldsymbol{k},30}\eta_3 \otimes \sigma_0 + h_{\boldsymbol{k},10}\eta_1 \otimes \sigma_0, \tag{6.1}$$

$$\tilde{\Delta}_{\boldsymbol{k}} = \Delta_{\boldsymbol{k},01}\eta_0 \otimes \sigma_3 + \Delta_{\boldsymbol{k},11}\eta_1 \otimes \sigma_3 + \Delta_{\boldsymbol{k},22}\eta_2 \otimes \sigma_0 + \Delta_{\boldsymbol{k},31}\eta_3 \otimes \sigma_3, \tag{6.2}$$

where the $h_{\boldsymbol{k},\eta\sigma}$ coefficients are given by (3.40)–(3.43) to be

$$h_{\boldsymbol{k},00} = -t_1(\cos(k_x) + \cos(k_y)) - \mu, \tag{6.3}$$

$$h_{\boldsymbol{k},23} = \lambda, \tag{6.4}$$

$$h_{\boldsymbol{k},30} = -t_2(\cos(k_x) - \cos(k_y)), \tag{6.5}$$

$$h_{\boldsymbol{k},10} = 2t_3 \sin(k_x)\sin(k_y), \tag{6.6}$$

with t_1 defining the energy scale, such that we can take $t_2 = 0.8t_1$, $t_3 = 0.1t_1$, $\mu = t_1$, and $\lambda = 0.4t_1$. The chiral $\Delta_{\boldsymbol{k},\eta\sigma}$ coefficients are given in (3.53)–(3.56) as

$$\Delta_{\boldsymbol{k},01} = \Delta_{0,01}(\sin k_x + i \sin k_y), \tag{6.7}$$
$$\Delta_{\boldsymbol{k},11} = \Delta_{0,11}(\sin k_y + i \sin k_x), \tag{6.8}$$
$$\Delta_{\boldsymbol{k},22} = \Delta_{0,22}(\sin k_x + i \sin k_y), \tag{6.9}$$
$$\Delta_{\boldsymbol{k},31} = \Delta_{0,31}(\sin k_x - i \sin k_y), \tag{6.10}$$

where the amplitudes $\Delta_{0,\nu}$ are complex numbers.

6.1.1 Spin sectors

Having restricted ourselves to these pairing terms, it turns out that we can write our Hamiltonian in a convenient way that will save us some computational effort below. Because H_0 and $\tilde{\Delta}$ are purely diagonal in spin (and therefore Δ is purely off-diagonal), we are able to decompose (2.15) in terms of two smaller spinors:

$$\mathcal{H} = \mathcal{H}^{\uparrow} + \mathcal{H}^{\downarrow} = \frac{1}{2}\sum_{\boldsymbol{k}} \Psi_{\boldsymbol{k}}^{\uparrow\dagger} H_{\boldsymbol{k}}^{\uparrow} \Psi_{\boldsymbol{k}}^{\uparrow} + \frac{1}{2}\sum_{\boldsymbol{k}} \Psi_{\boldsymbol{k}}^{\downarrow\dagger} H_{\boldsymbol{k}}^{\downarrow} \Psi_{\boldsymbol{k}}^{\downarrow}, \tag{6.11}$$

where

$$\Psi_{\boldsymbol{k}}^{\uparrow} = \begin{pmatrix} \hat{a}_{\boldsymbol{k}x\uparrow} & \hat{a}_{\boldsymbol{k}y\uparrow} & \hat{a}^{\dagger}_{-\boldsymbol{k}x\downarrow} & \hat{a}^{\dagger}_{-\boldsymbol{k}y\downarrow} \end{pmatrix}^{T}, \tag{6.12}$$

and

$$\Psi_{\boldsymbol{k}}^{\downarrow} = \begin{pmatrix} \hat{a}_{\boldsymbol{k}x\downarrow} & \hat{a}_{\boldsymbol{k}y\downarrow} & \hat{a}^{\dagger}_{-\boldsymbol{k}x\uparrow} & \hat{a}^{\dagger}_{-\boldsymbol{k}y\uparrow} \end{pmatrix}^{T}. \tag{6.13}$$

We see that $\Psi_{\boldsymbol{k}}^{\uparrow}$ corresponds to only spin-up electrons (and spin-down holes), while the converse is true for $\Psi_{\boldsymbol{k}}^{\downarrow}$. We have effectively decoupled the two spin species in the Hamiltonian. Neither $H_{\boldsymbol{k}}^{\uparrow}$ nor $H_{\boldsymbol{k}}^{\downarrow}$ are true BdG Hamiltonians because, rather than obeying (2.16), they each have the form

$$\begin{pmatrix} H_{0,\boldsymbol{k}} & \Delta_{\boldsymbol{k}} \\ \Delta_{\boldsymbol{k}}^{\dagger} & -H_{0,-\boldsymbol{k}} \end{pmatrix}, \tag{6.14}$$

with

$$H_{0,\boldsymbol{k}}^{\uparrow} = h_{\boldsymbol{k},00}\eta_0 + h_{\boldsymbol{k},10}\eta_1 + h_{\boldsymbol{k},23}\eta_2 + h_{\boldsymbol{k},30}\eta_3, \tag{6.15}$$
$$\Delta_{\boldsymbol{k}}^{\uparrow} = \Delta_{\boldsymbol{k},01}\eta_0 + \Delta_{\boldsymbol{k},11}\eta_1 + \Delta_{\boldsymbol{k},22}\eta_2 + \Delta_{\boldsymbol{k},31}\eta_3, \tag{6.16}$$

in the spin-up sector, and

$$H_{0,\boldsymbol{k}}^{\downarrow} = h_{\boldsymbol{k},00}\eta_0 + h_{\boldsymbol{k},10}\eta_1 - h_{\boldsymbol{k},23}\eta_2 + h_{\boldsymbol{k},30}\eta_3, \tag{6.17}$$
$$\Delta_{\boldsymbol{k}}^{\downarrow} = \Delta_{\boldsymbol{k},01}\eta_0 + \Delta_{\boldsymbol{k},11}\eta_1 - \Delta_{\boldsymbol{k},22}\eta_2 + \Delta_{\boldsymbol{k},31}\eta_3, \tag{6.18}$$

in the spin-down sector. The difference between the two sectors is the sign of the h_{23} and Δ_{22} terms. If these terms were excluded from our model, the BdG Hamiltonian would be independent of spin.

The utility of this decomposition can be seen by writing

$$\mathcal{H}^{\uparrow} = \frac{1}{2}\sum_{\boldsymbol{k}} \begin{pmatrix} \hat{a}^{\dagger}_{\boldsymbol{k}i\uparrow} & \hat{a}_{-\boldsymbol{k}i\downarrow} \end{pmatrix} \begin{pmatrix} H^{\uparrow}_{0,\boldsymbol{k},ij} & \Delta^{\uparrow}_{\boldsymbol{k},ij} \\ \Delta^{\uparrow *}_{\boldsymbol{k},ij} & -H^{\uparrow}_{0,\boldsymbol{k},ij} \end{pmatrix} \begin{pmatrix} \hat{a}_{\boldsymbol{k}j\uparrow} \\ \hat{a}^{\dagger}_{-\boldsymbol{k}j\downarrow} \end{pmatrix} \tag{6.19}$$

$$= \frac{1}{2}\sum_{\boldsymbol{k}} \begin{pmatrix} \hat{a}^{\dagger}_{\boldsymbol{k}i\uparrow} & \hat{a}_{-\boldsymbol{k}i\downarrow} \end{pmatrix} \begin{pmatrix} H^{\downarrow}_{0,\boldsymbol{k},ji} & \Delta^{\downarrow}_{\boldsymbol{k},ji} \\ \Delta^{\downarrow *}_{\boldsymbol{k},ji} & -H^{\downarrow}_{0,\boldsymbol{k},ji} \end{pmatrix} \begin{pmatrix} \hat{a}_{\boldsymbol{k}j\uparrow} \\ \hat{a}^{\dagger}_{-\boldsymbol{k}j\downarrow} \end{pmatrix}, \tag{6.20}$$

where we have used $H_{0,-\boldsymbol{k}} = H_{0,\boldsymbol{k}}$, and the second line is achieved by noting that $H^{\downarrow}_0$ and $\Delta^{\downarrow}$ are related to their spin-up counterparts via matrix transposition. Applying the fermionic anticommutation relations, we obtain

$$\mathcal{H}^{\uparrow} = \frac{1}{2}\sum_{\boldsymbol{k}} \left[\begin{pmatrix} \hat{a}_{\boldsymbol{k}i\uparrow} & \hat{a}^{\dagger}_{-\boldsymbol{k}i\downarrow} \end{pmatrix} \begin{pmatrix} -H^{\downarrow}_{0,\boldsymbol{k},ij} & -\Delta^{\downarrow *}_{\boldsymbol{k},ij} \\ -\Delta^{\downarrow}_{\boldsymbol{k},ij} & H^{\downarrow}_{0,\boldsymbol{k},ij} \end{pmatrix} \begin{pmatrix} \hat{a}^{\dagger}_{\boldsymbol{k}j\uparrow} \\ \hat{a}_{-\boldsymbol{k}j\downarrow} \end{pmatrix} \right] + \mathrm{Tr} \begin{pmatrix} H^{\downarrow}_{0,\boldsymbol{k},ii} & 0 \\ 0 & -H^{\downarrow}_{0,\boldsymbol{k},ii} \end{pmatrix}, \tag{6.21}$$

where the trace term is obviously vanishing. Taking $\boldsymbol{k} \to -\boldsymbol{k}$ under the summation, while noting that $H_{0,-\boldsymbol{k}} = H_{0,\boldsymbol{k}}$ and $\Delta_{-\boldsymbol{k}} = -\Delta_{\boldsymbol{k}}$, we have

$$\mathcal{H}^{\uparrow} = \frac{1}{2}\sum_{\boldsymbol{k}} \begin{pmatrix} \hat{a}_{-\boldsymbol{k}i\uparrow} & \hat{a}^{\dagger}_{\boldsymbol{k}i\downarrow} \end{pmatrix} \begin{pmatrix} -H^{\downarrow}_{0,\boldsymbol{k},ij} & \Delta^{\downarrow *}_{\boldsymbol{k},ij} \\ \Delta^{\downarrow}_{\boldsymbol{k},ij} & H^{\downarrow}_{0,\boldsymbol{k},ij} \end{pmatrix} \begin{pmatrix} \hat{a}^{\dagger}_{-\boldsymbol{k}j\uparrow} \\ \hat{a}_{\boldsymbol{k}j\downarrow} \end{pmatrix}. \tag{6.22}$$

Finally, we can reorder the spinors to find that *the Hamiltonian is the same in each spin sector*:

$$\mathcal{H}^{\uparrow} = \frac{1}{2}\sum_{\boldsymbol{k}} \begin{pmatrix} \hat{a}^{\dagger}_{\boldsymbol{k}i\downarrow} & \hat{a}_{-\boldsymbol{k}i\uparrow} \end{pmatrix} \begin{pmatrix} H^{\downarrow}_{0,\boldsymbol{k},ij} & \Delta^{\downarrow}_{\boldsymbol{k},ij} \\ \Delta^{\downarrow *}_{\boldsymbol{k},ij} & -H^{\downarrow}_{0,\boldsymbol{k},ij} \end{pmatrix} \begin{pmatrix} \hat{a}_{\boldsymbol{k}j\downarrow} \\ \hat{a}^{\dagger}_{-\boldsymbol{k}j\uparrow} \end{pmatrix} = \mathcal{H}^{\downarrow}. \tag{6.23}$$

This result can be substituted into (6.11) to show that that the mean-field Hamiltonian can be written entirely in terms of one sector, i.e.

$$\mathcal{H}^{\mathrm{MF}} = \sum_{\boldsymbol{k}} \Psi^{\uparrow\dagger}_{\boldsymbol{k}} H^{\uparrow}_{\boldsymbol{k}} \Psi^{\uparrow}_{\boldsymbol{k}} = \sum_{\boldsymbol{k}} \Psi^{\downarrow\dagger}_{\boldsymbol{k}} H^{\downarrow}_{\boldsymbol{k}} \Psi^{\downarrow}_{\boldsymbol{k}}. \tag{6.24}$$

This is particularly convenient for numerical calculations as it means we can deal with 4×4 matrices, rather than the full 8×8 BdG Hamiltonian. This decomposition is the same as that mentioned briefly at the end of Section 5.1, and, as mentioned there, each spin sector contributes equally to the Hall conductivity. The assumptions behind it (i.e. that H_0 and $\tilde{\Delta}$ are diagonal in spin) are the same as those that predicated the discussion in Section 5.3.2, which showed that interband pairing is required within this model.

6.1.2 Insights from the TROBs

Using H_0 and $\tilde{\Delta}$ as given by (6.1) and (6.2), the TROBs, (5.61) and (5.62), can be calculated to be

$$\mathrm{TROB}_1 = 4\,\mathrm{Im}\{\Delta_{31}\Delta^{*}_{22}\}\eta_1 \otimes \sigma_3 + 4\,\mathrm{Im}\{\Delta_{11}\Delta^{*}_{31}\}\eta_2 \otimes \sigma_0 + 4\,\mathrm{Im}\{\Delta_{22}\Delta^{*}_{11}\}\eta_3 \otimes \sigma_3, \tag{6.25}$$

and

$$\begin{aligned}\mathrm{TROB}_2 = 4(\hat{h}_{10}\,\mathrm{Im}\{\Delta_{22}\Delta_{31}^*\} + \hat{h}_{30}\,\mathrm{Im}\{\Delta_{11}\Delta_{22}^*\} + \hat{h}_{23}\,\mathrm{Im}\{\Delta_{31}\Delta_{11}^*\})\eta_0\otimes\sigma_3 \\ + 4(\hat{h}_{30}\,\mathrm{Im}\{\Delta_{01}\Delta_{22}^*\} + \hat{h}_{23}\,\mathrm{Im}\{\Delta_{31}\Delta_{01}^*\})\eta_1\otimes\sigma_3 + 4(\hat{h}_{10}\,\mathrm{Im}\{\Delta_{01}\Delta_{31}^*\} + \hat{h}_{30}\,\mathrm{Im}\{\Delta_{11}\Delta_{01}^*\})\eta_2\otimes\sigma_0 \\ + 4(\hat{h}_{23}\,\mathrm{Im}\{\Delta_{01}\Delta_{11}^*\} + \hat{h}_{10}\,\mathrm{Im}\{\Delta_{22}\Delta_{01}^*\})\eta_3\otimes\sigma_3, \quad (6.26)\end{aligned}$$

where I have dropped the explicit momentum indices from the $\Delta_{\boldsymbol{k},\eta\sigma}$ and $\hat{h}_{\boldsymbol{k},\eta\sigma}$ terms for convenience. We note that the momentum dependence of each term in TROB_1 and TROB_2 is real-valued, implying that the TRSB arises from the orbital-spin structure of each term. We can understand the terms that appear by noting that $\eta_0\otimes\sigma_3$, $\eta_1\otimes\sigma_3$, and $\eta_3\otimes\sigma_3$ break time-reversal because they correspond to a spin polarisation (which might be orbitally dependent). Meanwhile, the eigenstates of η_2 are the definite-angular-momentum states $\mathrm{d}_{xz}\pm i\mathrm{d}_{yz}$, so we can understand the $\eta_2\otimes\sigma_0$ term as an analogous orbital angular-momentum polarisation. (6.25) and (6.26) could now be used to calculate the Hall conductivity in the high-frequency, small-gap limit using (5.59), but the resulting expression is prohibitively complicated. I will instead take the time to exemplify how these TROBs on their own can be used to gain insight into the necessary conditions for a non-zero Hall conductivity within this model.

The most important take away is that each term in TROB_1 and TROB_2 involves two pairing channels. This means that a pairing potential involving just one of the chiral E_u pairing channels is not sufficient to lead to a non-zero Hall conductivity. On the other hand, it might be possible to obtain a non-zero Hall conductivity if we include just two of the four channels in our model. It is also worth noting that, except in very particular cases, if TROB_1 is nonzero, so too will TROB_2 be. The converse statement does not apply. In Chapter 4 we found that the orbitally trivial channel, Δ_{01}, involves purely intraband pairing (refer to Table 4.4). At the same time, we showed in Section 5.3.2 that a necessary condition for the Hall conductivity, within the E_u pairing states considered here, is the presence of interband pairing. While TROB_1 is independent of Δ_{01}, this channel does appear in TROB_2, indicating that it can contribute to the Hall conductivity. This is not an issue because it always appears along with one of the orbitally nontrival pairing channels, which each involve some degree of interband pairing.

6.1.3 Pairing potential ansatz

Rather than providing an exhaustive analysis of the Hall conductivity within this model, using the pairing potential given by (6.2), I will instead focus on two specific sub-models. In each case I choose to include just two terms in the pairing potential, as this is the minimum number required to obtain non-vanishing TROBs. For the first model I include just Δ_{01} and Δ_{31}, in which case the pairing potential is given by

$$\Delta_{\boldsymbol{k}} = \Delta_{0,01}(\sin k_x + i\sin k_y)\eta_0\otimes\sigma_1 + \Delta_{0,31}(\sin k_x - i\sin k_y)\eta_3\otimes\sigma_1, \quad (6.27)$$

where $\Delta_{0,01}, \Delta_{0,31}\in\mathbb{C}$. We have the freedom to choose the overall phase of the pairing potential, so I take $\Delta_{0,01}\in\mathbb{R}^+$. Further, by a similar argument as that used in Section 3.4, the lowest-order Ginzburg–Landau expansion can be used to show that the free energy of the superconducting state will be minimised by taking $\Delta_{0,31}\in\mathbb{R}$ [36]. The magnitude of the pairing in each channel remains free, but we have been able to restrict the relative phase between the channels such that (6.27) only involves two free parameters. I will refer to (6.27) as the *triplet-triplet* model because each channel involved describes purely spin-triplet pairing. Additionally, this model corresponds

to purely intraorbital pairing, as both η_0 and η_3 are diagonal. The pairing of electrons from the d_{xz} orbital is of the form $(\Delta_{0,01} + \Delta_{0,31}) \sin k_x + i(\Delta_{0,01} - \Delta_{0,31}) \sin k_y$, which is predominantly dependent on $\sin k_x$ for $\Delta_{0,31} > 0$. Similarly, the d_{yz} pairing is predominantly $\sim \sin k_y$. The physical motivation behind this choice arises from a simple model of strontium ruthenate with one-dimensional bands corresponding to each orbital [95], which can essentially be obtained by ignoring the band hybridisation present in Figure 3.2 B. In this model, the d_{xz} band is one-dimensional (in the x direction) so we would expect pairing in this band to only depend on the x component of momentum. Similarly, the d_{yz} band would be expected to only have k_y dependence, which would essentially be the case in this model when $\Delta_{0,01} \approx \Delta_{0,31}$. This model is also that considered by Taylor and Kallin [26].

Our second case, which I will dub the *singlet-triplet* model, is given by

$$\Delta_{\boldsymbol{k}} = \Delta_{0,22}(\sin k_x + i \sin k_y)\eta_2 \otimes \sigma_2 + \Delta_{0,31}(\sin k_x - i \sin k_y)\eta_3 \otimes \sigma_1, \tag{6.28}$$

where I take $\Delta_{0,22} \in \mathbb{R}^+$ and $\Delta_{0,31} \in \mathbb{R}$ by the same arguments as above. Unlike the triplet-triplet model, there is no specific physical motivation behind this choice. I include it here because it involves an odd-momentum spin-singlet term, which means it is a case in which the orbital degree of freedom needs to be taken into account in order for fermionic antisymmetry to be obeyed. Even among such unconventional states more attention has been focussed on even-momentum spin-triplet states [77, 96, 97] like the A_{1g} and E_g terms in Table 4.4 (I have argued that they can be excluded from our two-orbital model, but analogous terms can be included in three-orbital models). I choose this model involving Δ_{22} out of curiosity regarding its exotic pairing structure.

The band structure for each of these models is presented in Figure 6.1. In these plots the magnitude of the pairing in each channel has been chosen so as to be large enough to emphasise the opening of band gaps, and is not physically realistic. Both intra- and interband gaps can be seen, the magnitudes of which are highly dependent on the model. For example, the triplet-triplet model opens a large intraband and a small interband gap between the X and M points, while the opposite is true in the singlet-triplet model. While the intra- and interband pairing present in each of these models can be determined using the superconducting fitness, the connection to nodal structures presented in Table 4.4 is not particular clear, due to the presence of two pairing channels here.

Within the triplet-triplet model the pairing in each spin sector, as given by (6.16) and (6.18), is the same, which is to say that it is independent of the spin. For this reason, the pseudospin degeneracy is not lifted in the superconducting state, as evidenced by the presence of just four energy bands in Figure 6.1 A. One outcome of this is that the eigenvalues within each spin sector have the form

$$E_i = \{E_1, E_2, E_3 = -E_1, E_4 = -E_2\}, \tag{6.29}$$

analogous to those of a 4×4 BdG Hamiltonian. This is not the case in the singlet-triplet model, due to the sign change of the Δ_{22} term between (6.16) and (6.18). Although the eigenvalues of the overall BdG Hamiltonian still come in $\pm$ pairs, this is not true within each spin sector. The resulting lifting of the pseudospin degeneracy is observed between the M and Γ points.

6.2 Pairing potential amplitudes

We would now like to proceed with calculating the Hall conductivity within the triplet-triplet and singlet-triplet models. In Section 3.3.1 we identified some reasonable values for parameters which can be used to construct H_0, but we do not currently have values for the pairing amplitudes $\Delta_{0,01}$,

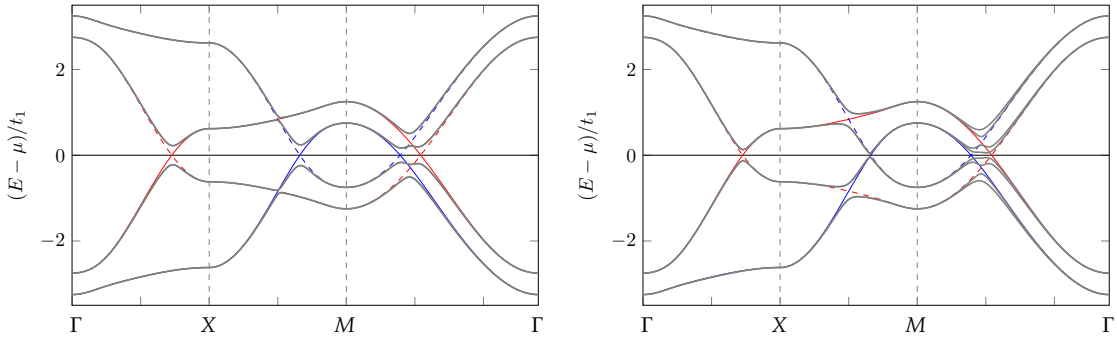

(A) triplet-triplet model (B) singlet-triplet model

FIGURE 6.1: The band structure between high symmetry points in both the triplet-triplet and singlet-triplet models. Solid grey lines indicate the energy spectrum of the superconducting state, while solid (dashed) red and blue lines indicate the normal state electronic (particle-hole reversed) dispersion of each band. For the purposes of visualisation the gap amplitude was taken to be $\Delta_0/t_1 = 0.15$ in each channel.

$\Delta_{0,31}$, and $\Delta_{0,22}$. One approach would be to simply choose physically reasonable values for each of these amplitudes which we would then feed into the calculation of the Hall conductivity for each model. However, I choose instead to self-consistently determine the pairing amplitudes by minimising the free energy of the system while treating the amplitudes as variational parameters. As we will see, this approach still requires us to *choose* somewhat arbitrary values associated with the interaction potential, but it has the advantage that we will be able to extract the temperature dependence of the gap amplitudes, and ultimately the Hall conductivity.

6.2.1 Minimising the free energy

In the absence of an external magnetic field it is most appropriate to consider the Helmholtz free energy of the superconducting state. This can be calculated from the partition function

$$Z = \sum_j e^{-\beta\epsilon_j}, \tag{6.30}$$

where ϵ_j is the energy of the j^{th} many-particle state of the full system. Working in the mean-field regime, the Hamiltonian is given by (2.15) to be

$$\mathcal{H}^{\text{MF}} = \frac{1}{2}\sum_{\boldsymbol{k}} \Psi_{\boldsymbol{k}}^\dagger H_{\boldsymbol{k}} \Psi_{\boldsymbol{k}} = \tilde{\sum_{\boldsymbol{k}}} \Psi_{\boldsymbol{k}}^\dagger H_{\boldsymbol{k}} \Psi_{\boldsymbol{k}}, \tag{6.31}$$

where $\tilde{\sum}_{\boldsymbol{k}}$ refers to a sum over one half of the Brillouin zone, as discussed at the start of Chapter 2. One may think that the energies of the system will therefore be

$$\epsilon_j = \tilde{\sum_{\boldsymbol{k}}} \sum_{\alpha,\pm} E_{\boldsymbol{k}\alpha\pm} n_{\boldsymbol{k}\alpha\pm,j},$$

where $E_{\boldsymbol{k}\alpha\pm} = \pm E_{\boldsymbol{k}\alpha}$ are the eigenvalues of the BdG Hamiltonian, $H_{\boldsymbol{k}}$ (the $\pm$ arises from the reflection of the energy bands for the hole states), and $n_{\boldsymbol{k}\alpha\pm,j}$ is the occupancy of the $\{\boldsymbol{k},\alpha,\pm\}$ single-particle state in the j^{th} many-particle state of the full system. However, this is not quite correct: when we were constructing the mean-field Hamiltonian in Sections 2.1.1 and 2.1.2 we dropped two "constant" terms, one from $\mathcal{H}_0$, and the other from $\mathcal{H}_{\text{int}}$. For our purposes at the time it was justified to neglect both of these terms as they only contribute to an overall shift in the energy

of the system. But we now wish to compare the free energy of different pairing states, so we must reintroduce the term we dropped from $\mathcal{H}_{\text{int}}$. We still exclude the term we dropped from $\mathcal{H}_0$ as it remains unchanged between different superconducting states. The correct form of ϵ_j is therefore

$$\epsilon_j = \tilde{\sum_{\boldsymbol{k}}} \sum_{\alpha\pm} \pm E_{\boldsymbol{k}\alpha} n_{\boldsymbol{k}\alpha\pm,j} - K, \tag{6.32}$$

where K is given in (2.7) to be

$$K = \frac{1}{2}\frac{1}{N} \sum_{\boldsymbol{k},\boldsymbol{k}'} V_{\boldsymbol{k},\boldsymbol{k}',\alpha_1\alpha_2,\alpha_3\alpha_4} \langle \hat{a}^\dagger_{-\boldsymbol{k}\alpha_1} \hat{a}^\dagger_{\boldsymbol{k}\alpha_2} \rangle \, \langle \hat{a}_{\boldsymbol{k}'\alpha_3} \hat{a}_{-\boldsymbol{k}'\alpha_4} \rangle. \tag{6.33}$$

We can conclude that the correct form of the partition function is therefore

$$Z = e^{\beta K} \tilde{\prod_{\boldsymbol{k}}} \prod_{\alpha,\pm} \sum_j e^{\mp \beta E_{\boldsymbol{k}\alpha} n_{\boldsymbol{k},\alpha,\pm,j}} = e^{\beta K} \tilde{\prod_{\boldsymbol{k}}} \prod_{\alpha,\pm} (1 + e^{\mp \beta E_{\boldsymbol{k}\alpha}}), \tag{6.34}$$

where we used the fact that the occupancy of a given single-particle fermionic state can be either zero or one, and $\tilde{\prod}$ refers to a product across half the Brillouin zone. We can use

$$\prod_{\pm} \ln\left(1 + e^{\mp \beta E_{\boldsymbol{k}\alpha}}\right) = \left(1 + e^{-\beta E_{\boldsymbol{k}\alpha}}\right)\left(1 + e^{\beta E_{\boldsymbol{k}\alpha}}\right) = \left(e^{-\beta E_{\boldsymbol{k}\alpha}/2} + e^{\beta E_{\boldsymbol{k}\alpha}/2}\right)^2$$

in order to write the Helmholtz free energy as

$$F = -\frac{1}{\beta} \ln Z = -\frac{1}{\beta} \tilde{\sum_{\boldsymbol{k}}} \sum_{\alpha} \ln \left[\left(e^{-\beta E_{\boldsymbol{k}\alpha}/2} + e^{\beta E_{\boldsymbol{k}\alpha}/2} \right)^2 \right] - K \tag{6.35}$$

$$= -\frac{2}{\beta} \tilde{\sum_{\boldsymbol{k}}} \sum_{\alpha} \ln \left[2 \cosh(\beta E_{\boldsymbol{k}\alpha}/2) \right] - K. \tag{6.36}$$

Finally, we can use $\tilde{\sum}_{\boldsymbol{k}} = \frac{1}{2} \sum_{\boldsymbol{k}}$ in order to write

$$F = -\frac{1}{\beta} \sum_{\boldsymbol{k},\alpha} \ln \left[2 \cosh(\beta E_{\boldsymbol{k}\alpha}/2) \right] - K. \tag{6.37}$$

Evaluating the constant term

In principle, a microscopic theory of the pairing in strontium ruthenate could be used to calculate K from (6.33), but is well beyond the scope of this thesis. Instead, I adopt a phenomenological interaction potential which describes pairing within each channel, as well as between channels. Allowing for an arbitrary number of channels, we write

$$V_{\boldsymbol{k},\boldsymbol{k}',\alpha_1\alpha_2,\alpha_3\alpha_4} = \sum_{\nu,\nu'} \lambda_{\nu\nu'} f_{\nu,\boldsymbol{k},\alpha_1\alpha_2} f^*_{\nu',\boldsymbol{k}',\alpha_4\alpha_3}, \tag{6.38}$$

where $\lambda_{\nu\nu'}$ is the interaction strength for the process that destroys a Cooper pair in the ν' channel and creates one in the ν channel. This interaction is attractive for $\lambda_{\nu\nu'} < 0$, and must satisfy

$$\lambda_{\nu\nu'} = \lambda^*_{\nu'\nu} \tag{6.39}$$

so that the Hamiltonian is Hermitian. The f terms are matrices which describe the momentum, orbital, and spin dependence of each channel. Fermionic antisymmetry, (2.4), requires that

$$f_{\nu,\boldsymbol{k},\alpha_1\alpha_2} = -f_{\nu,-\boldsymbol{k},\alpha_2,\alpha_1}. \tag{6.40}$$

We can substitute (6.38) into (2.8) in order to write the pairing potential as

$$\Delta_{\boldsymbol{k},ij} = -\frac{1}{N}\sum_{\nu,\nu'}\lambda_{\nu\nu'}\sum_{\boldsymbol{k}'}\langle \hat{a}_{\boldsymbol{k}'\alpha_3} f^*_{\boldsymbol{k}',\nu',\alpha_4\alpha_3}\hat{a}_{-\boldsymbol{k}'\alpha_4}\rangle f_{\nu,\boldsymbol{k},ji}, \tag{6.41}$$

which can easily be deconstructed into a pairing potential *per channel*:

$$\Delta_{\nu,\boldsymbol{k},ij} = -\frac{1}{N}\sum_{\nu'}\lambda_{\nu\nu'}\sum_{\boldsymbol{k}'}\langle \hat{a}_{\boldsymbol{k}'\alpha_3} f^*_{\boldsymbol{k}',\nu',\alpha_4\alpha_3}\hat{a}_{-\boldsymbol{k}'\alpha_4}\rangle f_{\nu,\boldsymbol{k},ji}. \tag{6.42}$$

Seeing as $f_{\nu,\boldsymbol{k},ji}$ describes the momentum, orbital, and spin dependence of the pairing potential in the ν channel, the *amplitude* of the pairing potential in this channel is

$$\Delta_{0,\nu} = -\frac{1}{N}\sum_{\nu'}\lambda_{\nu\nu'}\sum_{\boldsymbol{k}'}\langle \hat{a}_{\boldsymbol{k}'\alpha_3} f^*_{\boldsymbol{k}',\nu',\alpha_4\alpha_3}\hat{a}_{-\boldsymbol{k}'\alpha_4}\rangle. \tag{6.43}$$

It will be useful to note that we can write the complex conjugate of $\Delta_{0,\nu}$ as

$$\begin{aligned}\Delta^*_{0,\nu} &= -\frac{1}{N}\sum_{\nu'}\lambda^*_{\nu\nu'}\sum_{\boldsymbol{k}'}\langle \hat{a}^\dagger_{-\boldsymbol{k}'\alpha_4} f_{\boldsymbol{k}',\nu',\alpha_4\alpha_3}\hat{a}^\dagger_{\boldsymbol{k}'\alpha_3}\rangle \\ &= -\frac{1}{N}\sum_{\nu'}\lambda^*_{\nu\nu'}\sum_{\boldsymbol{k}'}\langle \hat{a}^\dagger_{-\boldsymbol{k}'\alpha_1} f_{\boldsymbol{k}',\nu',\alpha_1\alpha_2}\hat{a}^\dagger_{\boldsymbol{k}'\alpha_2}\rangle.\end{aligned} \tag{6.44}$$

In addition to the pairing potential, I also define the following term:

$$\Delta_\nu = -\frac{\lambda_\nu}{N}\sum_{\boldsymbol{k}}\langle \hat{a}_{\boldsymbol{k}\alpha_3} f^*_{\boldsymbol{k},\nu',\alpha_4\alpha_3}\hat{a}_{-\boldsymbol{k}\alpha_4}\rangle, \tag{6.45}$$

along with its complex conjugate

$$\Delta^*_\nu = -\frac{\lambda_\nu}{N}\sum_{\boldsymbol{k}}\langle \hat{a}^\dagger_{-\boldsymbol{k}\alpha_1} f_{\boldsymbol{k},\nu',\alpha_1\alpha_2}\hat{a}^\dagger_{\boldsymbol{k}\alpha_2}\rangle, \tag{6.46}$$

where I have denoted $\lambda_{\nu\nu} = \lambda_\nu$, and (6.39) implies that $\lambda^*_\nu = \lambda_\nu$. While Δ_ν has specifically been defined to be similar to $\Delta_{0,\nu}$, it is not the amplitude of a pairing potential, but it will play an important role when it comes to numerically minimising the free energy.

We now have all the ingredients required to write K in a convenient form. If we substitute (6.38) into (6.33) we obtain

$$K = \frac{1}{2}\sum_{\nu,\nu'}\lambda_{\nu\nu'}\sum_{\boldsymbol{k},\boldsymbol{k}'}\langle \hat{a}^\dagger_{-\boldsymbol{k}\alpha_1} f_{\boldsymbol{k},\nu,\alpha_1\alpha_2}\hat{a}^\dagger_{\boldsymbol{k}\alpha_2}\rangle\ \langle \hat{a}_{\boldsymbol{k}'\alpha_3} f^*_{\boldsymbol{k}',\nu',\alpha_4\alpha_3}\hat{a}_{-\boldsymbol{k}'\alpha_4}\rangle. \tag{6.47}$$

Further substituting in Δ_ν and Δ^*_ν, we can write

$$K = \frac{N}{2}\sum_{\nu,\nu'}\frac{\lambda_{\nu\nu'}}{\lambda_\nu\lambda_{\nu'}}\Delta^*_\nu\Delta_{\nu'}, \tag{6.48}$$

which is significantly easier to deal with than (6.33). In order to use (6.48) when minimising the

free energy with respect to the pairing amplitudes we need to be able to express Δ_ν in terms of $\Delta_{0,\nu'}$, which can be done by comparing (6.43) and (6.45). If there is only one pairing channel, the two expressions are equivalent. In the case of two pairing channels, as is the case in the models we are dealing with, we have

$$\Delta_{0,1} = \Delta_1 + \frac{\lambda_{12}}{\lambda_2}\Delta_2, \qquad \Delta_{0,2} = \Delta_2 + \frac{\lambda_{12}}{\lambda_1}\Delta_1, \tag{6.49}$$

and K is given by

$$K = \frac{N}{2}\left(\frac{|\Delta_1|^2}{\lambda_1} + \frac{|\Delta_2|^2}{\lambda_2} + \frac{\lambda_{12}\Delta_1^*\Delta_2}{\lambda_1\lambda_2} + \frac{\lambda_{21}\Delta_1\Delta_2^*}{\lambda_1\lambda_2}\right).$$

We can then write the free energy as

$$F = -\frac{1}{\beta}\sum_{k,\alpha}\ln\left[2\cosh(\beta E_{k\alpha}/2)\right] - \frac{N}{2}\left(\frac{|\Delta_1|^2}{\lambda_1} + \frac{|\Delta_2|^2}{\lambda_2} + \frac{\lambda_{12}\Delta_1^*\Delta_2}{\lambda_1\lambda_2} + \frac{\lambda_{21}\Delta_1\Delta_2^*}{\lambda_1\lambda_2}\right). \tag{6.50}$$

It is possible to generalise these results to larger numbers of pairing channels, but this would serve no purpose for us here.

6.2.2 Numerical results

We can use (6.50) in conjunction with (6.49) to minimise the free energy with respect to $\Delta_{0,1}$ and $\Delta_{0,2}$ in our models of strontium ruthenate. There are a few details to keep in mind when performing these numerical calculations, which are discussed in Appendix A.1. In the absence of a microscopic theory, we must still choose reasonable values for the interaction strengths. Rather than aiming for quantitative predictions, I choose these so as to demonstrate some representative cases. The only physical consideration behind our choices is that the resulting gap magnitudes and critical temperatures should be of roughly the correct order of magnitude.

Triplet-triplet model: For the triplet-triplet model I choose two sets of interaction strengths:

1. $\lambda_{01}/t_1 = -0.2, \lambda_{31}/t_1 = -0.265, \lambda_{01,31}/t_1 = 0.03$, resulting in the coexistence of gaps of a similar magnitude in each channel, as shown in Figure 6.2 A. These parameters were fine-tuned so as to exhibit the non-monotonic temperature dependence of the gaps present in this plot: below $k_BT/t_1 \approx 0.01$ there is competition between the channels resulting in a reduction in $|\Delta_{0,31}|$. The inter-channel interaction strength is taken to be real-valued for simplicity. It is also taken to be repulsive, which explains the competition between the two channels.

2. $\lambda_{01}/t_1 = -0.2, \lambda_{31}/t_1 = -0.06, \lambda_{01,31}/t_1 = 0.03$, corresponding to much weaker pairing in one channel compared to the other (and a correspondingly smaller gap magnitude). The resulting gap magnitudes are shown in Figure 6.2 B. Similar sets of interaction strengths were examined, none of which exhibited the non-monotonic behaviour of Figure 6.2 A. Presumably this is because the Δ_{31} channel is too weak to compete with the Δ_{01} channel. The inter-channel interaction strength is taken to be the same as above.

A more comprehensive survey of the interaction strengths is always possible, but I focus on these two representative cases. In both cases the critical temperature of the two-channel chiral state occurs around $k_BT/t_1 = 1.3 \times 10^{-2}$. Noting that experimental results indicate $t_1 \approx 0.4\,\text{eV}$ [78], this corresponds to $T_c \approx 60\,\text{K}$, significantly larger than experimentally measured values around 1.5 K [57]. This might appear worrying at first glance, but note that with these parameters we still

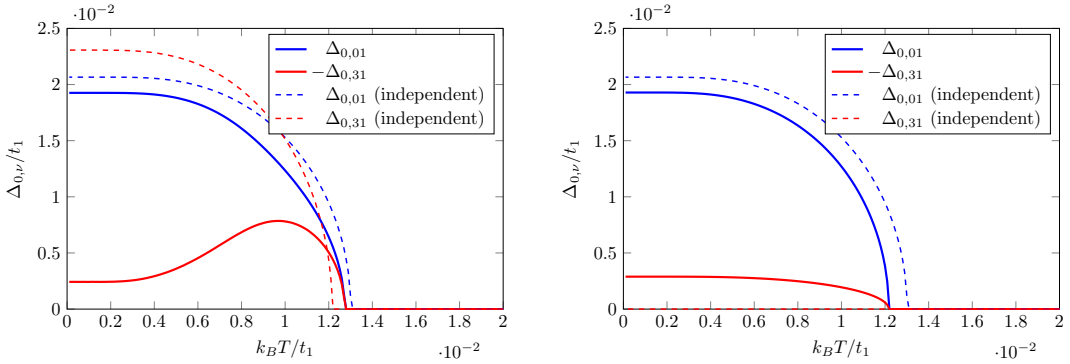

(A) $\lambda_{01}/t_1 = -0.2, \lambda_{31}/t_1 = -0.265, \lambda_{01,31}/t_1 = 0.03$ (B) $\lambda_{01}/t_1 = -0.2, \lambda_{31}/t_1 = -0.06, \lambda_{01,31}/t_1 = 0.03$

FIGURE 6.2: Pairing potential amplitudes as a function of temperature in the triplet-triplet model. Solid lines indicate the full state, while dashed lines indicate the amplitude in the presence of only one pairing channel. Calculated using $N = 500 \times 500$ lattice points and 200 temperature values.

have $\Delta_{0,\nu} \ll t_1$, placing us well within the weak-coupling regime. Further decreasing the critical temperature (and the gap magnitudes along with it) to be more physical would not qualitatively change our results, while coming with significant numerical costs (refer to the discussion in Appendix A.3).

The dashed lines in Figure 6.2 show the "independent" gap amplitudes, i.e. those in the case that only one channel is present. For the second set of parameters, the Δ_{31} channel interaction is too weak for its critical temperature to be visible on the scale used in the plot. In all cases the independent amplitudes exhibit the typical $\sqrt{1 - T/T_c}$ behaviour below T_c. For both sets of parameters the critical temperature of the triplet-triplet model is lower than that of the Δ_{01} channel on its own, implying that the triplet-triplet pairing state (6.27) is unlikely to be realised. However, this is dependent on the specific interaction strengths chosen, and should not be taken as a general conclusion regarding the triplet-triplet model.

Note that we have $\Delta_{0,31} < 0$ for both sets of interaction strengths. This contradicts the justification for the triplet-triplet model outlined in Section 6.1.3. While this means that our interaction strengths are physically dubious, we are only going for qualitative results anyway, so it should not present much of an issue. We will see below that the frequency-dependence of the Hall conductivity does not qualitatively depend on the magnitude or temperature dependence of the gaps.

Singlet-triplet model: For the singlet-triplet model I have chosen to deal with just a single set of interaction strengths: $\lambda_{22} = -0.45/t_1, \lambda_{31} = -0.25/t_1, \lambda_{01,31} = 0.01/t_1$. These were selected such that the two channels had similar gap magnitudes, as shown in Figure 6.3. They were fine-tuned such that the critical temperature was similar to those in the triplet-triplet models above. A range of inter-channel interaction strengths was surveyed, with no non-monotonic behaviour observed.

Chiral superposition of 1D irreps: As noted in Section 3.4.2, it is possible to form a chiral state from the complex superposition of two pairing potentials, each belonging to a different one-dimensional irrep. In addition to the triplet-triplet and singlet-triplet models considered so far, I also attempted to construct states of the following forms: $A_{1u} + iA_{2u}$, $B_{1u} + iB_{2u}$, and $B_{1g} + iB_{2g}$. These have been notably absent from the discussion so far because, when numerically minimising the free energy for these states, I was unable to find any set of interaction strengths such that a coexistence between two such channels was stable. The energetically favoured state only ever involved the opening of a gap in a single channel. This is not a general result, and must be

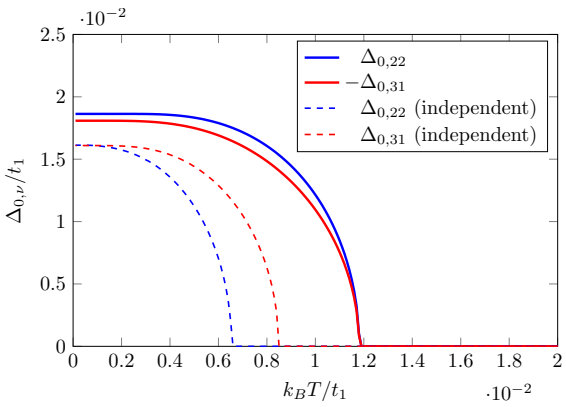

FIGURE 6.3: Pairing potential amplitudes as a function of temperature in the singlet-triplet model, with the interactions strengths $\lambda_{22} = -0.45, \lambda_{31} = -0.25$ and $\lambda_{01,31} = 0.01$. Solid lines indicate the full state, while dashed lines indicate the amplitude in the presence of only one pairing channel. Calculated using $N = 500 \times 500$ lattice points and 200 temperature values.

somewhat related to the details of this specific model. I did not have time to examine this further, but it is an interesting observation in itself, especially in light of recent proposals of such a state in strontium ruthenate [83, 84].

6.3 Hall conductivity

6.3.1 Exact result

Now that we have calculated the amplitudes of the pairing potentials, they can be used to numerically construct the BdG Hamiltonian, and in turn to calculate the Hall conductivity using (5.30), which is reproduced here for convenience:

$$\sigma_H(\omega) = \frac{ie^2}{4N\omega} \lim_{i\omega_n \to \omega + i0^+} \sum_{\boldsymbol{k}} \frac{1}{\beta} \sum_m \mathrm{Tr}\Big\{ \Big[v^x_{\boldsymbol{k}} \mathcal{G}_{\boldsymbol{k}, i\omega_n + i\nu_m} v^y_{\boldsymbol{k}} - v^y_{\boldsymbol{k}} \mathcal{G}_{\boldsymbol{k}, i\omega_n + i\nu_m} v^x_{\boldsymbol{k}} \Big] \mathcal{G}_{\boldsymbol{k}, i\nu_m} \Big\}.$$

It would be possible to calculate the Matsubara Green's functions directly using (5.41), but this would leave us with the problem of how to numerically perform the Matsubara summation and the analytic continuation in (5.30). Instead, we need to do a bit more analytic work in order to write the Hall conductivity in a form that can be calculated numerically. We begin by using (5.44) to write the Matsubara Green's functions as

$$\mathcal{G}_{\boldsymbol{k}, i\nu_m} = \sum_{\alpha, \pm} \frac{|\boldsymbol{k}, \alpha, \pm\rangle \langle \boldsymbol{k}, \alpha, \pm|}{i\nu_m - E_{\boldsymbol{k}\alpha\pm}}, \tag{6.51}$$

where $E_{\boldsymbol{k}\alpha\pm} = \pm E_{\boldsymbol{k}\alpha}$, and α enumerates the four particle-like eigenstates of $H_{\boldsymbol{k}}$. We can then write

$$v^i_{\boldsymbol{k}} \mathcal{G}_{\boldsymbol{k}, i\omega_n + i\nu_m} v^j_{\boldsymbol{k}} \mathcal{G}_{\boldsymbol{k}, i\nu_m} = \sum_{\substack{\alpha, \alpha' \\ \pm, \pm'}} \frac{v^i_{\boldsymbol{k}} |\boldsymbol{k}, \alpha, \pm\rangle \langle \boldsymbol{k}, \alpha, \pm| v^j_{\boldsymbol{k}} |\boldsymbol{k}, \alpha', \pm'\rangle \langle \boldsymbol{k}, \alpha', \pm'|}{(i\omega_n + i\nu_m - E_{\boldsymbol{k}\alpha\pm})(i\nu_m - E_{\boldsymbol{k}\alpha'\pm'})}, \tag{6.52}$$

and therefore

$$\mathrm{Tr}\Big\{ v^i_{\boldsymbol{k}} \mathcal{G}_{\boldsymbol{k}, i\omega_n + i\nu_m} v^j_{\boldsymbol{k}} \mathcal{G}_{\boldsymbol{k}, i\nu_m} \Big\} = \sum_{\substack{\alpha, \alpha' \\ \pm, \pm'}} \frac{\langle \boldsymbol{k}, \alpha, \pm| v^i_{\boldsymbol{k}} |\boldsymbol{k}, \alpha', \pm'\rangle \langle \boldsymbol{k}, \alpha', \pm'| v^j_{\boldsymbol{k}} |\boldsymbol{k}, \alpha, \pm\rangle}{(i\nu_m - E_{\boldsymbol{k}\alpha\pm})(i\omega_n + i\nu_m - E_{\boldsymbol{k}\alpha'\pm'})}, \tag{6.53}$$

where we have used $\langle \boldsymbol{k}, \alpha, \pm | \boldsymbol{k}, \alpha', \pm' \rangle = \delta_{\alpha\alpha'}\delta_{\pm\pm'}$. Substituting this result into (5.30) yields

$$\sigma_H(\omega) = \frac{ie^2}{4N\omega} \sum_{\boldsymbol{k}} \sum_{\substack{\alpha,\alpha' \\ \pm,\pm'}} \Bigg[\left(\lim_{i\omega_n \to \omega + i0^+} \frac{1}{\beta} \sum_m \frac{1}{(i\nu_m - E_{\boldsymbol{k}\alpha\pm})(i\omega_n + i\nu_m - E_{\boldsymbol{k}\alpha'\pm'})} \right)$$
$$\times \left(\langle \boldsymbol{k}, \alpha, \pm | v_{\boldsymbol{k}}^x | \boldsymbol{k}, \alpha', \pm' \rangle \langle \boldsymbol{k}, \alpha', \pm' | v_{\boldsymbol{k}}^y | \boldsymbol{k}, \alpha, \pm \rangle - \langle \boldsymbol{k}, \alpha, \pm | v_{\boldsymbol{k}}^y | \boldsymbol{k}, \alpha', \pm' \rangle \langle \boldsymbol{k}, \alpha', \pm' | v_{\boldsymbol{k}}^x | \boldsymbol{k}, \alpha, \pm \rangle \right) \Bigg],$$

where we have conveniently been able to pull out the $i\nu_m$ dependence into a single term. Using $\langle \psi | \mathcal{O} | \psi \rangle^* = \langle \psi | \mathcal{O}^\dagger | \psi \rangle$, we note that the second line can be written as

$$2i \operatorname{Im} \left\{ \langle \boldsymbol{k}, \alpha, \pm | v_{\boldsymbol{k}}^x | \boldsymbol{k}, \alpha', \pm' \rangle \langle \boldsymbol{k}, \alpha', \pm' | v_{\boldsymbol{k}}^y | \boldsymbol{k}, \alpha, \pm \rangle \right\}$$

because the velocity matrices are Hermitian. Carrying out the Matsubara summation yields

$$\sigma_H(\omega) = \frac{e^2}{4N\omega} \sum_{\boldsymbol{k}} \sum_{\substack{\alpha,\alpha' \\ \pm,\pm'}} \Bigg[\frac{\tanh\left(\frac{E_{\boldsymbol{k}\alpha\pm}\beta}{2}\right) - \tanh\left(\frac{E_{\boldsymbol{k}\alpha'\pm'}\beta}{2}\right)}{E_{\boldsymbol{k}\alpha\pm} - E_{\boldsymbol{k}\alpha'\pm'} + \omega + i0^+}$$
$$\times \operatorname{Im} \left\{ \langle \boldsymbol{k}, \alpha, \pm | v_{\boldsymbol{k}}^x | \boldsymbol{k}, \alpha', \pm' \rangle \langle \boldsymbol{k}, \alpha', \pm' | v_{\boldsymbol{k}}^y | \boldsymbol{k}, \alpha, \pm \rangle \right\} \Bigg], \quad (6.54)$$

which is suitable for numerical calculations because $E_{\boldsymbol{k}\alpha\pm}$ and $|\boldsymbol{k}, \alpha, \pm\rangle$ can be easily calculated by numerical diagonalisation of the BdG Hamiltonian. The infinitesimal must be approximated by a "small" float. I take this to be $0^+ = 10^{-3}$, the validity of which is addressed in Section 6.3.4. Further analytic calculations with (6.54) are essentially impossible due to the complexity of the expression.

Numerical calculations of (6.54) as a function of frequency and temperature in both the triplet-triplet and singlet-triplet models are presented in Section 6.3.4, but before we continue it is worth noting an important analytic result that can be ascertained from (6.54). In particular, consider the

$$\frac{1}{E_{\boldsymbol{k}\alpha\pm} - E_{\boldsymbol{k}\alpha'\pm'} + \omega + i0^+} = \frac{E_{\boldsymbol{k}\alpha\pm} - E_{\boldsymbol{k}\alpha'\pm'} + \omega}{(E_{\boldsymbol{k}\alpha\pm} - E_{\boldsymbol{k}\alpha'\pm'} + \omega)^2 + (0^+)^2} - \frac{i0^+}{(E_{\boldsymbol{k}\alpha\pm} - E_{\boldsymbol{k}\alpha'\pm'} + \omega)^2 + (0^+)^2}$$

part, for which we have

$$\frac{1}{E_{\boldsymbol{k}\alpha\pm} - E_{\boldsymbol{k}\alpha'\pm'} + \omega + i0^+} \xrightarrow{0^+ \to 0} \frac{1}{E_{\boldsymbol{k}\alpha\pm} - E_{\boldsymbol{k}\alpha'\pm'} + \omega} - i\pi\delta(E_{\boldsymbol{k}\alpha\pm} - E_{\boldsymbol{k}\alpha'\pm'} + \omega). \quad (6.55)$$

The imaginary part of the Hall conductivity is determined by this delta function, i.e. there are only contributions at the frequency ω from terms in the sum for which $\omega = E_{\boldsymbol{k}\alpha'\pm'} - E_{\boldsymbol{k}\alpha\pm}$. This turns out to imply that the imaginary part of the Hall conductivity will vanish below some finite frequency. To see why, I note first that

1. If $E_{\boldsymbol{k}\alpha\pm} = E_{\boldsymbol{k}\alpha'\pm'}$ then the tanh terms in (6.54) cancel, so there is no contribution to the imaginary part of the Hall conductivity at exactly zero frequency.

We could, however, still imagine the energy difference between two bands approaching zero, allowing for contributions to the imaginary part of the Hall conductivity at arbitrarily small frequencies. For example, if we refer to Figure 6.1 B, there are momentum values between the M and Γ points in which the spin degeneracy between two bands is lifted, but only by a very small amount. However, it turns out that

2. The $\{\alpha, \pm; \alpha, \mp\}$ contributions vanish because the velocity matrix is block-diagonal in particle-hole space, and hence $\langle \alpha, \pm | \, v^x \, | \alpha, \mp \rangle = 0$ in (6.54).

3. The contribution from the $\{\boldsymbol{k}, \alpha, \alpha', +, +\}$ term cancels with the $\{-\boldsymbol{k}, \alpha', \alpha, -, -\}$ term even for $\alpha \neq \alpha'$, since $v^{hi}_{\boldsymbol{k},\alpha_1\alpha_2} = -v^{ei}_{-\boldsymbol{k},\alpha_2\alpha_1}$, and the velocity matrices are Hermitian.

Together these mean that contributions to (6.54) must involve an electron-like band and a different hole-like band, i.e. only $\{\alpha, \pm; \alpha', \mp\}$ contributions are permitted, for $\alpha \neq \alpha'$. The corresponding energy bands are separated from each other by a finite energy gap, so we can conclude that the imaginary part of the Hall conductivity will vanish below some finite frequency. The energy separation between these bands is determined by the normal state parameters, so we expect this "cutoff frequency" to be on the order of $\hbar\omega \sim t_1$.

6.3.2 High-frequency, small-gap limit

In addition to this exact result, we can use (5.59) to evaluate the Hall conductivity in the high-frequency, small-gap limit for both the triplet-triplet and singlet-triplet models. The details of the calculations are not particularly enlightening, but are easily performed using software packages such as Mathematica.

Triplet-triplet model: By taking $v^x_{23} = v^y_{23} = 0$ (as h_{23} is constant in our model), we can evaluate (5.59) with the triplet-triplet pairing potential, (6.27), in order to obtain

$$\sigma_H(\omega) \approx \frac{16e^2}{\omega^2} \frac{1}{N} \sum_{\boldsymbol{k}} h_{10}[v_{10} \wedge v_{30}] \, \mathrm{Im}\{\Delta^*_{01}\Delta_{31}\} \frac{1}{\beta} \sum_{m=-\infty}^{\infty} \frac{1}{(E_+^2 + \nu_m^2)(E_-^2 + \nu_m^2)}, \tag{6.56}$$

where $E_\pm$ are the normal state eigenenergies. Only TROB_2 contributes to this expression because the triplet-triplet model involves Δ_{01} (refer to the discussion is Section 6.1.2). Performing the Matsubara summation yields

$$\sigma_H(\omega) \approx \frac{8e^2}{\omega^2} \frac{1}{N} \sum_{\boldsymbol{k}} h_{10}[v_{10} \wedge v_{30}] \, \mathrm{Im}\{\Delta^*_{01}\Delta_{31}\} \frac{E_+ \tanh\left(\frac{E_-\beta}{2}\right) - E_- \tanh\left(\frac{E_+\beta}{2}\right)}{E_+E_-(E_+^2 - E_-^2)}. \tag{6.57}$$

Singlet-triplet model: Similarly, in the singlet-triplet model we have

$$\sigma_H(\omega) \approx \frac{128e^2}{\omega^2} \frac{1}{N} \sum_{\boldsymbol{k}} h_{00}h_{10}h_{23}[v_{10} \wedge v_{30}] \, \mathrm{Im}\{\Delta^*_{22}\Delta_{31}\} \frac{1}{\beta} \sum_{m=-\infty}^{\infty} \frac{\nu_m^2}{(E_+^2 + \nu_m^2)^2(E_-^2 + \nu_m^2)^2}, \tag{6.58}$$

where the Matsubara summation can be carried out in order to obtain

$$\begin{aligned}\sigma_H(\omega) \approx \frac{16e^2}{\omega^2} \frac{1}{N} \sum_{\boldsymbol{k}} & h_{00}h_{10}h_{23}[v_{10} \wedge v_{30}] \, \mathrm{Im}\{\Delta^*_{22}\Delta_{31}\} \\ & \times \frac{E_+ \, \mathrm{sech}^2(\frac{E_-\beta}{2}) \left[(E_+^2 - E_-^2)E_-\beta + (E_+^2 + 3E_-^2)\sinh(E_-\beta)\right] - \{E_+ \leftrightarrow E_-\}}{E_+E_-(E_+^2 - E_-^2)^3}.\end{aligned} \tag{6.59}$$

There are contributions from both TROBs to this expression.

6.3.3 High-frequency approximation

In addition to the high-frequency, small-gap limit considered by the TROB result, we will briefly consider the Hall conductivity in the high-frequency limit alone. This has the well known form [93]

$$\sigma_H(\omega) \approx \frac{i}{N\omega^2} \left\langle [\mathcal{J}_x, \mathcal{J}_y] \right\rangle, \tag{6.60}$$

where, unlike the calculation of the current-current correlator (5.5), the two current operators are evaluated at the *same* imaginary-time. The expectation value is taken with respect to the eigenstates of the BdG Hamiltonian, in contrast to the eigenstates of H_0 used in the high-frequency, small-gap limit. In order to calculate (6.60) we must first calculate the commutator between $\mathcal{J}_x$ and $\mathcal{J}_y$. The most convenient way to approach this is to rewrite (5.11) as

$$\mathcal{J}_i = \frac{e}{2} \sum_k \Psi_k^\dagger v_k^i \Psi_k = e \sum_k \Psi_k^{\uparrow\dagger} v_k^{\uparrow i} \Psi_k^\uparrow, \tag{6.61}$$

where v_k^i is defined in terms of (5.9) and (5.10) in (5.22), the Nambu spinor Ψ_k is given in (3.1), and the spin-up and spin-down spinors are given in (6.12) and (6.13) respectively. We have been able to write this in terms of a single spin sector be exploiting (6.24). We want to calculate

$$[\mathcal{J}_x, \mathcal{J}_y] = e^2 \sum_{k,k'} \left[\Psi_k^{\uparrow\dagger} v_k^{\uparrow x} \Psi_k^\uparrow, \Psi_{k'}^{\uparrow\dagger} v_{k'}^{\uparrow y} \Psi_{k'}^\uparrow \right]. \tag{6.62}$$

It can be shown that, for H_0 as given in (6.1), we can write

$$\begin{aligned}[\mathcal{J}_x, \mathcal{J}_y] = -2e^2 \sum_k \{ &[v_{10} \wedge v_{30}](\Psi_{k,1}^{\uparrow\dagger}\Psi_{k,2}^\uparrow - \Psi_{k,2}^{\uparrow\dagger}\Psi_{k,1}^\uparrow + \Psi_{k,3}^{\uparrow\dagger}\Psi_{k,4}^\uparrow - \Psi_{k,4}^{\uparrow\dagger}\Psi_{k,3}^\uparrow) \\ &+ i[v_{30} \wedge v_{23}](\Psi_{k,1}^{\uparrow\dagger}\Psi_{k,2}^\uparrow + \Psi_{k,2}^{\uparrow\dagger}\Psi_{k,1}^\uparrow + \Psi_{k,3}^{\uparrow\dagger}\Psi_4^\uparrow + \Psi_{k,4}^{\uparrow\dagger}\Psi_{k,3}^\uparrow) \\ &+ i[v_{23} \wedge v_{10}](\Psi_{k,1}^{\uparrow\dagger}\Psi_{k,1}^\uparrow - \Psi_{k,2}^{\uparrow\dagger}\Psi_{k,2}^\uparrow + \Psi_{k,3}^{\uparrow\dagger}\Psi_{k,3}^\uparrow - \Psi_{k,4}^{\uparrow\dagger}\Psi_{k,4}^\uparrow)\}, \end{aligned} \tag{6.63}$$

where $\Psi_{k,i}^\sigma$ is the i^{th} component of Ψ_k^σ. The derivation of (6.63) is rather involved, so I will not present it here. However, it can be verified to be the same as the result presented in Appendix C of [22] by making the following notational substitutions: $\partial_{k_i}\xi_k = v_{00}^i$, $\partial_{k_i} g_k = v_{30}^i$, $\partial_{k_i} \operatorname{Re}\{\epsilon_k\} = v_{10}^i$, and $\partial_{k_i} \operatorname{Im}\{\epsilon_k\} = v_{23}^i$. As h_{23} is constant in our model, we can set $v_{23}^x = v_{23}^y = 0$, and write

$$[\mathcal{J}_x, \mathcal{J}_y] = -2e^2 \sum_k \{[v_{10} \wedge v_{30}](\Psi_{k,1}^{\uparrow\dagger}\Psi_{k,2}^\uparrow - \Psi_{k,2}^{\uparrow\dagger}\Psi_{k,1}^\uparrow + \Psi_{k,3}^{\uparrow\dagger}\Psi_{k,4}^\uparrow - \Psi_{k,4}^{\uparrow\dagger}\Psi_{k,3}^\uparrow)\}. \tag{6.64}$$

We can then use the fermionic anticommutation relations and the fact that $v_k = -v_{-k}$ to show that

$$\Psi_{k,1}^{\uparrow\dagger}\Psi_{k,2}^\uparrow - \Psi_{k,2}^{\uparrow\dagger}\Psi_{k,1}^\uparrow + \Psi_{k,3}^{\uparrow\dagger}\Psi_{k,4}^\uparrow - \Psi_{k,4}^{\uparrow\dagger}\Psi_{k,3}^\uparrow = \Psi_{k,1}^{\downarrow\dagger}\Psi_{k,2}^\downarrow - \Psi_{k,2}^{\downarrow\dagger}\Psi_{k,1}^\downarrow + \Psi_{k,3}^{\downarrow\dagger}\Psi_{k,4}^\downarrow - \Psi_{k,4}^{\downarrow\dagger}\Psi_{k,3}^\downarrow,$$

and therefore we can write (6.64) as

$$\begin{aligned}[\mathcal{J}_x, \mathcal{J}_y] = -e^2 \sum_k \{ &[v_{10} \wedge v_{30}](\Psi_{k,1}^{\uparrow\dagger}\Psi_{k,2}^\uparrow - \Psi_{k,2}^{\uparrow\dagger}\Psi_{k,1}^\uparrow + \Psi_{k,3}^{\uparrow\dagger}\Psi_{k,4}^\uparrow - \Psi_{k,4}^{\uparrow\dagger}\Psi_{k,3}^\uparrow \\ &+ \Psi_{k,1}^{\downarrow\dagger}\Psi_{k,2}^\downarrow - \Psi_{k,2}^{\downarrow\dagger}\Psi_{k,1}^\downarrow + \Psi_{k,3}^{\downarrow\dagger}\Psi_{k,4}^\downarrow - \Psi_{k,4}^{\downarrow\dagger}\Psi_{k,3}^\downarrow)\}. \end{aligned} \tag{6.65}$$

As an aside, I note that this can be written as

$$[\mathcal{J}_x, \mathcal{J}_y] = -e^2 \sum_{\boldsymbol{k}} [v_{10} \wedge v_{30}] \Psi_{\boldsymbol{k}}^\dagger (\tau_0 \otimes \eta_2 \otimes \sigma_0) \Psi_{\boldsymbol{k}}, \tag{6.66}$$

which implies that the orbital angular-momentum polarisation matrix, $\eta_2 \otimes \sigma_0$, mentioned in the context of the TROBs in Section 6.1.2, is critical when it comes to generating an anomalous Hall conductivity in the high-frequency limit of our model. This result is unsurprising because we have set the v_{23} velocity terms to be vanishing in our model, which means that the only nontrivial components of the velocity matrix, and therefore the current operator, are proportional to η_1 and η_3 (i.e. v_{10} and v_{30}). In turn, the only way that these can be combined nontrivially in the commutator considered here is as an η_2 term. Due to the small value of the momentum-dependent spin-orbit coupling in strontium ruthenate [77], it is fairly safe to extend this argument to strontium ruthenate in general, even outside of our model.

When it comes to calculating $\langle [\mathcal{J}_x, \mathcal{J}_y] \rangle$ we can set $\tau = 0$ in (5.23) and (5.25) to show that

$$\langle \Psi_{\boldsymbol{k},i}^\dagger \Psi_{\boldsymbol{k},j} \rangle = -\langle \Psi_{\boldsymbol{k},j} \Psi_{\boldsymbol{k},i}^\dagger \rangle = \frac{1}{\beta} \sum_m \mathcal{G}_{\boldsymbol{k},i\nu_m,ji}, \tag{6.67}$$

for $i \neq j$. This is true in general, and applies to each spin sector independently, so we have

$$\langle [\mathcal{J}_x, \mathcal{J}_y] \rangle = -e^2 \sum_{\boldsymbol{k}} \frac{1}{\beta} \sum_m [v_{10} \wedge v_{30}] (\mathcal{G}_{21}^\uparrow - \mathcal{G}_{12}^\uparrow + \mathcal{G}_{43}^\uparrow - \mathcal{G}_{34}^\uparrow + \mathcal{G}_{21}^\downarrow - \mathcal{G}_{12}^\downarrow + \mathcal{G}_{43}^\downarrow - \mathcal{G}_{34}^\downarrow), \tag{6.68}$$

where I have dropped the explicit momentum and frequency indices from the Green's functions for convenience. In practice we can calculate

$$\langle [\mathcal{J}_x, \mathcal{J}_y] \rangle - e^2 \sum_{\boldsymbol{k}} \frac{1}{\beta} \sum_m [v_{10} \wedge v_{30}] (\mathcal{G}_{21}^\uparrow - \mathcal{G}_{12}^\uparrow + \mathcal{G}_{43}^\uparrow - \mathcal{G}_{34}^\uparrow) + \{h_{23} \to -h_{23}, \Delta_{22} \to -\Delta_{22}\}, \tag{6.69}$$

seeing as the spin sectors differ only by the sign of h_{23} and Δ_{22}. We substitute (6.69) into (6.60) in order to determine the high-frequency approximation of the Hall conductivity.

Triplet-triplet model: When we evaluate (6.69) for the triplet-triplet model we obtain

$$\sigma_H(\omega) \approx \frac{16e^2}{N\omega^2} \sum_{\boldsymbol{k}} \frac{1}{\beta} \sum_m \frac{h_{10} [v_{10} \wedge v_{30}] \operatorname{Im}\{\Delta_{01}^* \Delta_{31}\}}{(i\nu_m - E_1)(i\nu_m - E_2)(i\nu_m - E_3)(i\nu_m - E_4)}, \tag{6.70}$$

where $\{E_i\}$ are the four eigenvalues of $H_{\boldsymbol{k}}^\uparrow$. These are too complicated to present here, but I note that $H_{\boldsymbol{k}}^\downarrow$ has the same set of eigenvalues, as discussed in Section 6.1.3. Carrying out the Matsubara summation yields

$$\sigma_H(\omega) \approx \frac{-8e^2}{N\omega^2} \sum_{\boldsymbol{k}} h_{10} [v_{10} \wedge v_{30}] \operatorname{Im}\{\Delta_{01}^* \Delta_{31}\} \sum_{i=1}^4 \sum_{j \neq i} \left(\frac{\tanh\left(\frac{E_i \beta}{2}\right)}{(E_i - E_j)} \right). \tag{6.71}$$

This is a particularly nice result because the core part of its similarity to the high-frequency, small-gap approximation (6.57). The only difference between the two expressions is the eigenvalues that appear: if we take $E_1 \to E_+$, $E_2 \to -E_+$, $E_3 \to E_-$, and $E_+ \to -E_-$, we exactly replicate the high-frequency, small-gap approximation. The physical motivation behind this set of substitutions can be understood by the following argument: as noted in Section 6.1.3, the eigenvalues of each

spin sector in the triplet-triplet model take the form $\{E_1, E_2, E_3 = -E_1, E_4 = -E_2\}$. If the pairing potential is set to zero within these eigenvalues, they must take the form $\{\pm E_+, \pm E_-\}$, where $E_\pm$ are the eigenvalues of H_0. This seems to indicate that, at least in this case, the small-gap limit can be applied to the high-frequency limit by setting $\Delta_\nu \to 0$ in each of the (time-reversal symmetric) eigenenergies, while leaving the TRSB contribution from the gaps unchanged.

Singlet-triplet pairing: Evaluating (6.69) for the singlet-triplet model yields

$$\sigma_H(\omega) \approx \frac{-128e^2}{N\omega^2} \sum_{\boldsymbol{k}} \frac{1}{\beta} \sum_m \frac{h_{00}h_{10}h_{23}[v_{10} \wedge v_{30}] \operatorname{Im}\{\Delta_{22}^* \Delta_{31}\} \nu_m^2}{\prod_{i=1}^8 (i\nu_m - E_i)}, \tag{6.72}$$

where $\{E_i\}$ are now the eight eigenvalues of the full BdG Hamiltonian. Unlike the triplet-triplet model, the eigenvalues of the spin-up Hamiltonian are not the same as those of the spin-down Hamiltonian. Just as for the triplet-triplet case, we note that the core part of this result is the same as in the high-frequency, small-gap limit. It is only the dependence on the eigenvalues that is different because they are dependent on the gaps. Unfortunately, (6.72) was not evaluated numerically because the Matsubara summation is not analytically tractable, and we did not have sufficient time to implement the otherwise necessary numerical evaluation.

6.3.4 Numerical results

We now turn to numerically calculating the Hall conductivity, using (5.30) as well as the approximate results (6.57), (6.59), and (6.71). All three of the sets of interaction strengths introduced in Section 6.2.2 are considered here: two corresponding to the triplet-triplet model, and one to the singlet-triplet model.

Triplet-triplet model: Figure 6.4 shows the Hall conductivity as a function of both frequency and temperature for the triplet-triplet model with the first set of interaction strengths, corresponding to the pairing potential amplitudes shown in Figure 6.2 A. As noted in Section 6.3.1, the imaginary part of the Hall conductivity vanishes below some finite frequency. The frequency at which this occurs is $\hbar\omega \approx t_1/2$, in accordance with the prediction that it be determined by the normal state parameters. Close examination of the plots actually indicates small but non-zero values of the imaginary Hall conductivity about zero frequency. This is a numerical artefact which arises from taking a finite value of 0^+ for these calculations. This also explains the spike in the imaginary Hall conductivity at $\hbar\omega \approx t_1/2$, which is most obvious in Figure 6.4 A. A smaller numerical value of 0^+ would be preferable, but would come at significant numerical costs. As we are not aiming for quantitative results, this choice suffices.

The temperatures at which Figures 6.4 A–6.4 C are calculated at are chosen to coincide with qualitatively different gaps (with respect to the competition between the two channels exhibited in Figure 6.2 A). Qualitatively, the frequency dependence of the Hall conductivity at all three temperatures is very similar, indicating that competition between the gaps has little affect on the frequency response of the Hall conductivity. This is not necessarily a general result that would apply to other models. Conversely, the magnitude of the Hall response has a strong temperature dependence, as shown in Figures 6.4 D–6.4 F. In all three of these plots the magnitude of the Hall response appears to follow the temperature dependence of the gaps from Figure 6.2 A, which is consistent with the Hall conductivity scaling with $\Delta_{0,01}\Delta_{0,31}^*$ in (6.57) and (6.71).

The approximate results show good agreement with the exact result above $\hbar\omega/t_1 \approx 1$, which essentially defines the region in which the high-frequency approximation is valid. They do not

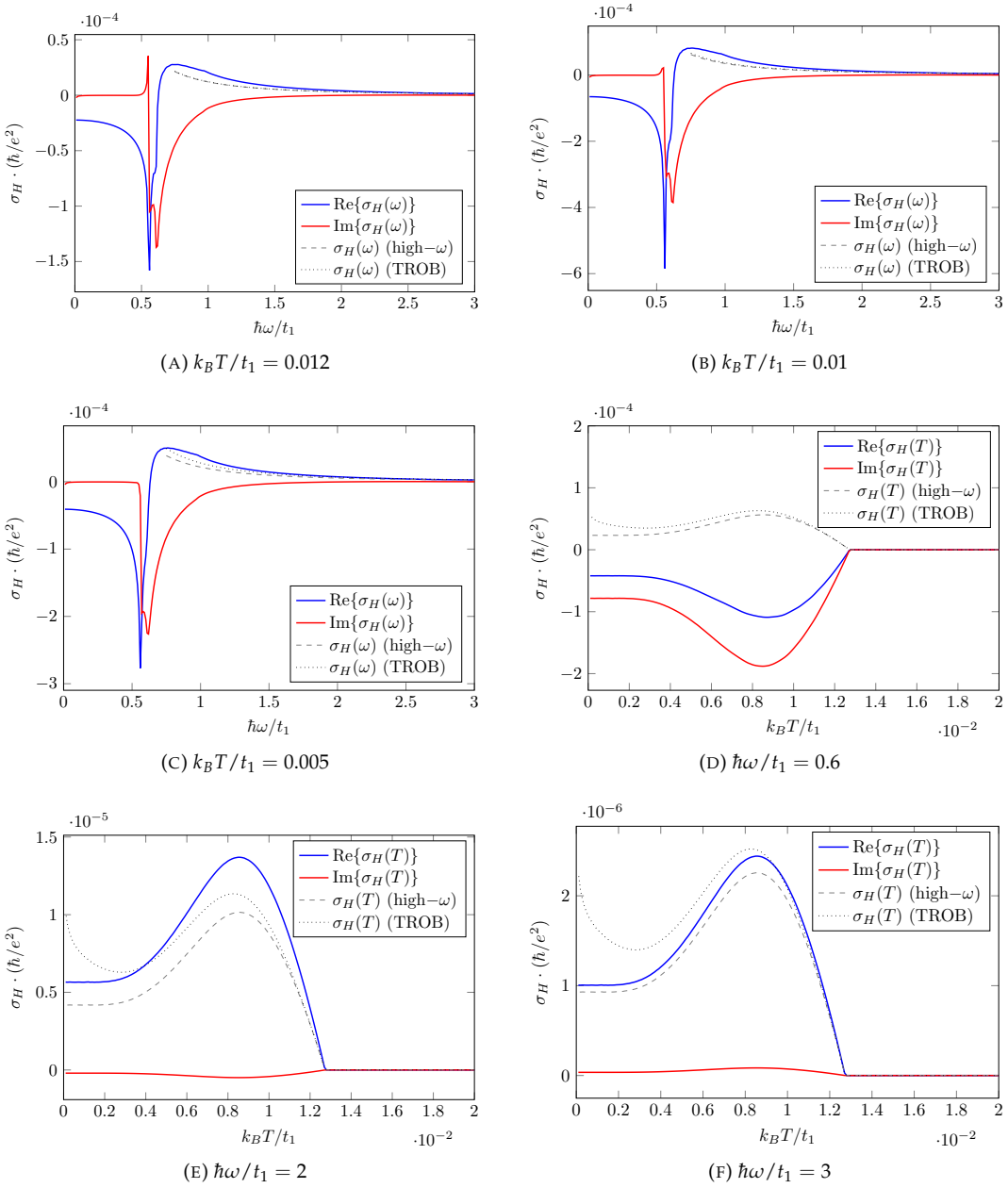

(A) $k_BT/t_1 = 0.012$ (B) $k_BT/t_1 = 0.01$

(C) $k_BT/t_1 = 0.005$ (D) $\hbar\omega/t_1 = 0.6$

(E) $\hbar\omega/t_1 = 2$ (F) $\hbar\omega/t_1 = 3$

FIGURE 6.4: The Hall conductivity as a function of frequency (A–C) and temperature (D–F) in the triplet-triplet model using the first set of interaction strengths ($\lambda_{01}/t_1 = -0.2, \lambda_{31}/t_1 = -0.265, \lambda_{01,31}/t_1 = 0.03$). The real (imaginary) part of the exact result is shown as a solid blue (red) line, while the high-frequency and high-frequency, small-gap approximations are shown as dashed and dotted lines respectively. Calculated using $N = 5000 \times 5000$ lattice points, the numerical approximation $0^+ = 0.001$ for a positive infinitesimal, 300 frequency values, and 200 temperature values respectively.

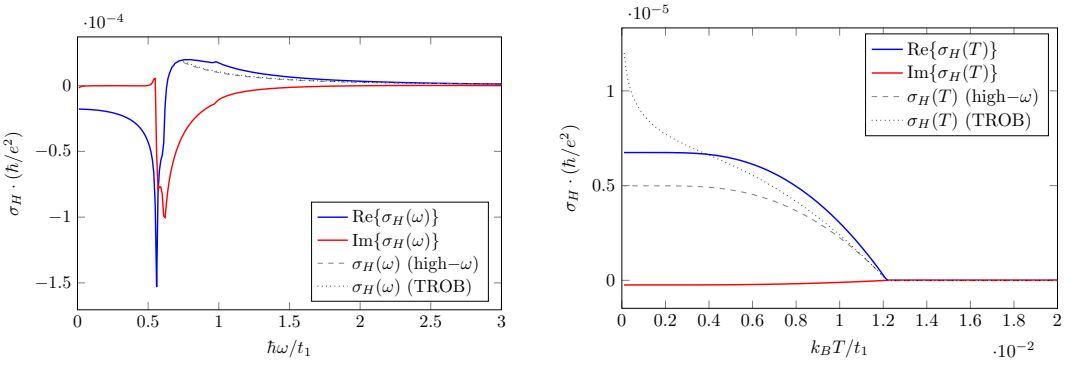

(A) $\sigma_H(\omega)$ for $k_BT/t_1 = 0.01$ (B) $\sigma_H(T)$ for $\hbar\omega/t_1 = 2$

FIGURE 6.5: The Hall conductivity as a function of frequency and temperature in the triplet-triplet model using the second set of interaction strengths ($\lambda_{01}/t_1 = -0.2, \lambda_{31}/t_1 = -0.06, \lambda_{01,31}/t_1 = 0.03$). The real (imaginary) part of the exact result is shown as a solid blue (red) line, while the high-frequency and high-frequency, small-gap approximations are shown as dashed and dotted lines respectively. Calculated using $N = 5000 \times 5000$ lattice points, the numerical approximation $0^+ = 0.001$ for a positive infinitesimal, 300 frequency values, and 200 temperature values respectively.

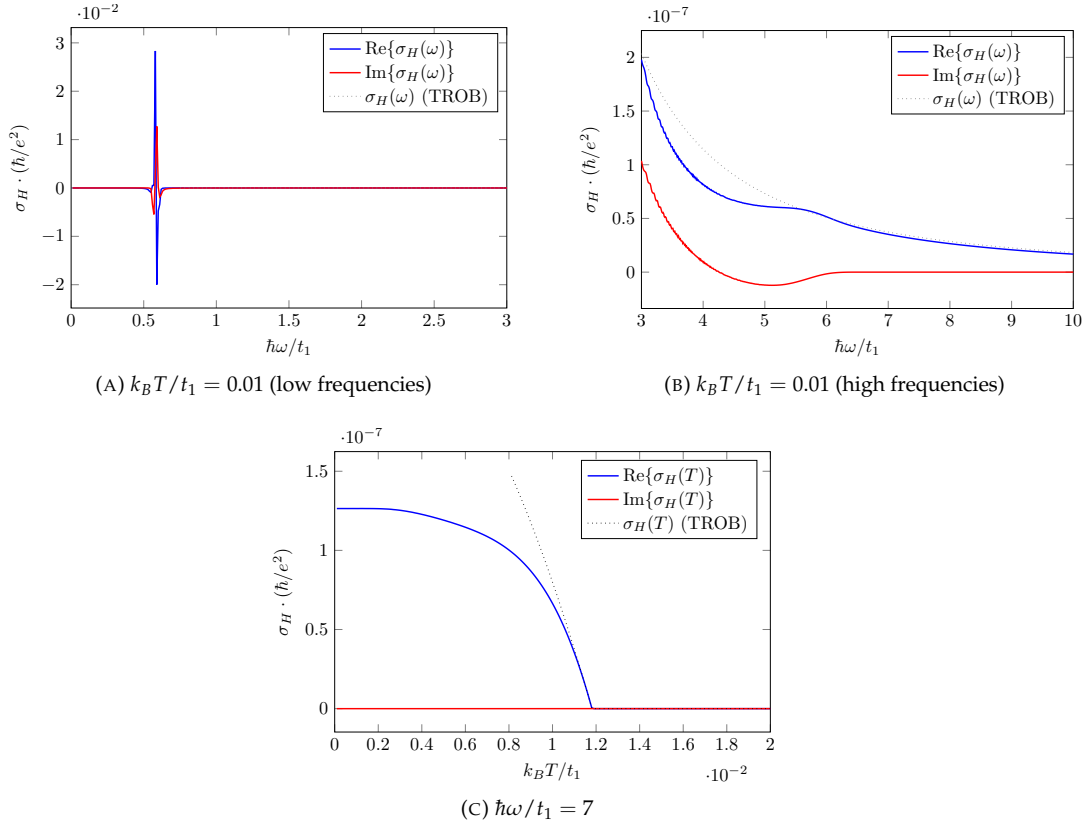

(A) $k_BT/t_1 = 0.01$ (low frequencies) (B) $k_BT/t_1 = 0.01$ (high frequencies)

(C) $\hbar\omega/t_1 = 7$

FIGURE 6.6: The Hall conductivity as a function of frequency (A and B) and temperature (C) in the singlet-triplet model using the interaction strengths $\lambda_{22}/t_1 = -0.45, \lambda_{31}/t_1 = -0.25$, and $\lambda_{01,31}/t_1 = 0.01$. The real (imaginary) part of the exact result is shown as a solid blue (red) line, while the high-frequency, small-gap approximation is shown as a dotted line. Calculated using $N = 5000 \times 5000$ lattice points, the numerical approximation $0^+ = 0.001$ for a positive infinitesimal, 1000 frequency values, and 200 temperature values respectively.

match at all in Figure 6.4 D, which is unsurprising as this is calculated at $\hbar\omega/t_1 = 0.6$. The high-frequency, small-gap approximation generally matches the high-frequency approximation well, although it diverges at small temperatures. This can be understood by inspection of (6.57) and (6.71). In the high-frequency limit (6.71) involves the eigenenergies of the spin-up sector, E_i. These exhibit a gap about $E = 0$. Meanwhile, the normal state eigenenergies E_+ and E_-, which have no such band gap, appear in (6.57). Let us consider what occurs at momentum values in which $E_- \to 0$ in the $\tanh(E_-/2T)$ part of (6.57):

$$\frac{\tanh(E_-/2T)}{E_-(E_+^2 - E_-^2)} \xrightarrow{E_- \to 0} \frac{1}{2TE_+^2}. \tag{6.73}$$

As T becomes small this diverges, leading to an overestimation of the Hall conductivity at small temperatures in the high-frequency, small-gap limit. The same argument applies to the $\tanh(E_+/2T)$ term in the $E_+ \to 0$ limit. Understandably, quantitative agreement between the approximate and exact results is strongest at the highest frequency considered here, in Figure 6.4 F.

Taking $t_1 \approx 0.4\,\text{eV}$ [78], the frequency $\hbar\omega/t_1 = 2$ used in 6.4 E corresponds to that used by Xia et al. when measuring the polar Kerr effect in strontium ruthenate [57]. At least within this model, the high-frequency, small-gap limit is experimentally appropriate, except at the lowest temperatures. I do not want to over emphasise the importance of this point however, because this model was never intended for quantitative predictions.

For comparison, Figure 6.5 shows the Hall conductivity in the triplet-triplet model as a function of frequency and of temperature for the alternative set of interaction strengths. We see no qualitative differences in this case, except that the temperature dependence shown in Figure 6.5 B is monotonically increasing because it follows the pairing potential amplitudes shown in Figure 6.2 B

Singlet-triplet pairing model: Figures 6.6 A and 6.6 B show the Hall conductivity of the singlet-triplet model as a function of frequency on two different energy scales. The conductivity is large within a narrow range of frequencies compared to the triplet-triplet case. In Figure 6.6 A the high-frequency limit, (6.59), appears to be vanishing, although Figure 6.6 B shows that it is fact just very small, and in strong agreement with (6.54) above $\hbar\omega/t_1 \approx 5.5$. This is an important qualitative difference between this model and the triplet-triplet model, and goes to show that the experimental applicability of the approximate results are highly dependent on the details of the system. As noted in Section 6.3.3, I was unable to write the high-frequency approximation in a form that leant itself to numerical calculations, so it cannot be shown here for comparison.

The Hall conductivity is shown as a function of temperature in 6.6 C. The exact result behaves as expected. The frequency used for these calculations is $\hbar\omega/t_1 = 7$, which falls in the high-frequency regime, as indicated by 6.6 B. Even here the high-frequency, small-gap approximation is in quantitative agreement for only a small range of temperatures. It rapidly diverges as we move away from the critical temperature.

Summary

In this chapter we used the TROBs identified in Chapter 5 in order to construct two specific models of strontium ruthenate that might exhibit a non-vanishing Hall conductivity. This was subsequently calculated exactly, and in the high-frequency, and high-frequency, small-gap limits. These approximate calculations gave qualitatively (and sometimes even quantitatively) accurate results within their respective limits.

Chapter 7

Conclusions and outlook

In this thesis I have considered intrinsic contributions to the anomalous Hall conductivity of two-band superconductors in the linear-response regime. In particular, I considered the role of time-reversal-odd bilinear functions of the pairing potential, and identified two such TROBs which play a central role in determining the intrinsic anomalous Hall conductivity in the high-frequency, small-gap limit. Although the concept of a TROB was introduced in a previous work [27], I have generalised its applicability and clarified its role in the anomalous Hall conductivity. The importance of these TROBs is not that they can be used to explicitly calculate the Hall conductivity, but rather that they provide a *necessary condition for a non-vanishing Hall conductivity*. At least one of the TROBs must be non-vanishing in order for a given system to exhibit intrinsic contributions to the anomalous Hall conductivity in the high-frequency, small-gap limit. Because these TROBs are straightforward to calculate, they provide an easy mechanism to test whether a given model might exhibit a Hall conductivity, which is useful when it comes to developing theoretical models to explain observations of the polar Kerr effect in materials of interest. As an illustrative example, I constructed a two-orbital model of strontium ruthenate, and utilised the TROBs to constrain the pairing states to be consistent with an anomalous Hall conductivity.

Although the TROBs only act as a necessary condition for an anomalous Hall conductivity in the high-frequency, small-gap limit, they are informative even outside of this regime. The high-frequency, small-gap approximation of the Hall conductivity is obtained by neglecting certain terms, and it is unlikely for these to exactly cancel with the terms that are kept. If the Hall conductivity is non-zero in the high-frequency, small-gap limit, it is probably also non-vanishing in general. This is somewhat exemplified in Chapter 6, where both of the models considered have a non-zero Hall conductivity in general. It is a useful result because the relevance of the high-frequency, small-gap limit to experimental endeavours is dependent on the details of the system in question. For example, the high-frequency approximation is valid at frequencies used in previous experiments [57], but this is not the case for the singlet-triplet model. If both TROBs are vanishing on the other hand, we cannot make claims about the Hall conductivity in general, because higher order corrections to (5.59) could conceivably contribute (although they would be expected to be on the order of $\sim |\Delta|^4$, so should be much smaller). This is an unfortunate restriction on the applicability of my result, especially because the temperature range over which the small-gap approximation is valid is unclear in general. For example, the validity of the small-gap approximation is quite good at all but the lowest temperatures in the triplet-triplet model, but only for a small range of temperatures is the singlet-triplet model. A generalisation away from the small-gap limit would be desirable, and is plausibly within reach. I note that there is a close connection between the high-frequency and the high-frequency, small-gap forms of the Hall conductivity in our model of strontium ruthenate, so it is plausible that the same TROBs provide a necessary condition for the Hall conductivity in the high-frequency limit alone. Of course, a complete generalisation away from

even the high-frequency limit would be preferred, but the feasibility of this is questionable due to the analytic work that would be involved: despite our simple model including just four terms in each of the normal state and pairing potential, analytical calculations of the exact anomalous Hall conductivity were basically impossible. This is a testament to the highly nontrivial nature of the anomalous Hall conductivity.

A perhaps more attainable goal would be the generalisation of my result to systems that do not have a centre of inversion, or to multiband superconductors with more than two energy bands. This would significantly broaden the class of systems to which the resulting argument would apply, such as the noncentrosymmetric superconductor $LaNiC_2$ [92], or a more realistic three-band model of strontium ruthenate [97]. It is unclear exactly how much additional work would be required to approach these generalisations because the assumptions we would be required to drop were fairly central to my derivation. Future work could also investigate the relationship between the TROBs and other necessary conditions for a Hall conductivity identified in specific models, or try to identify further physical conditions from them. For example, we know that the TROBs encapsulate both the condition that time-reversal symmetry is broken and that it is communicated to the centre-of-mass coordinate, but further physically meaningful conditions may be able to be extracted in the context of a given system. On the other hand, the requirement of interband pairing identified by Taylor and Kallin [91] could not be related to the TROBs alone, but required the full form of (5.59). Finally, it is worth emphasising that I have solely considered contributions to the Hall conductivity from intrinsic mechanisms. There has been much theoretical work providing insight into the mechanisms which can lead to a Hall conductivity via impurity scattering [34, 45–48]. It would be interesting to study these extrinsic contributions in a system where we also have the intrinsic Hall conductivity studied here.

Appendix A

Numerical considerations

This appendix deals with the issues that arise when actually performing the numerical calculations presented in Chapter 6. Sections A.1 and A.2 deal with how to simplify and speed up the calculations, while A.3 deals with the accuracy of the results.

A.1 Minimising the free energy

In Chapter 6 we determined (6.50) as the free energy of a superconducting state with two pairing channels. In order to determine the amplitude of each pairing channel, to be used in the calculation of the Hall conductivity, we had to minimise (6.50) with respect to these amplitudes. In this section I will outline how I approached this numerically, as there are a number of results that can be used to simplify the calculation.

Momentum summation: First of all, let us address which values of $\boldsymbol{k} = (k_x, k_y)$ are to be used in the summation, which should cover all the points in the first Brillouin zone. For a two-dimensional square lattice with $N_{\text{lat}} = N \times N$ sites[1] and lattice constant a, the periodic boundary conditions $k_x N a = 1$ and $k_y N a = 1$ require that

$$(k_x, k_y) = \left(\frac{(2n_x - N)\pi}{Na}, \frac{(2n_y - N)\pi}{Na} \right), \qquad 0 \leq n_x, n_y \leq N - 1. \tag{A.1}$$

These points are shown in Figure A.1 A for $N = 10$. One of the easiest ways to speed up the calculation is by decreasing the number of momentum points we sum over. By transforming the coordinates given in (A.1) to

$$(k_x, k_y) = \left(\frac{(2n_x - N + 1)\pi}{Na}, \frac{(2n_y - N + 1)\pi}{Na} \right), \qquad 0 \leq n_x, n_y \leq N - 1, \tag{A.2}$$

as shown in Figure A.1 B, we can then exploit the symmetries of D_{4h} in order to sum over only the shaded region shown in Figure A.1 C, which is only one eighth of the Brillouin zone[2]. (A.2) can be motivated by noting that

$$\frac{1}{N^2} \sum_{\boldsymbol{k}} \xrightarrow{N \to \infty} \int \frac{dk_x}{2\pi/a} \frac{dk_y}{2\pi/a},$$

[1] Throughout this thesis N has referred to the total number of lattice points, but for the purposes of this appendix it refers to the number of lattice points *per dimension*.

[2] The transformation from (A.1) to (A.2) is not actually necessary to take advantage of the symmetries of the lattice, as long as the $\boldsymbol{k}$ points situated on the edge of the Brillouin zone are correctly accounted for. (A.2) *is* more convenient when it comes to dealing with these edge points, but if I was to perform these calculations again, I would directly sum over one eighth of the points shown in Figure A.1 A.

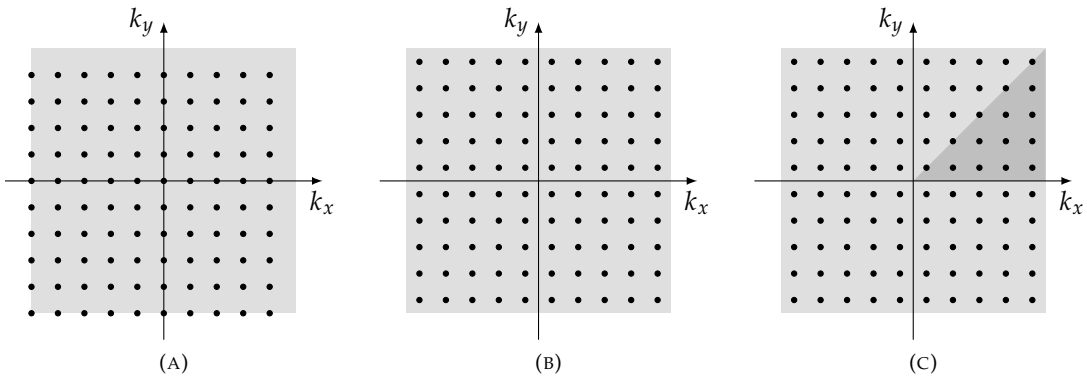

FIGURE A.1: Restricting the momentum values we sum over in the first Brillouin zone.

for $\boldsymbol{k}$ given by *either* (A.1) or (A.2), so for sufficiently large N the difference between these sums should vanish. We can therefore replace the $\sum_{k,\alpha}$ in (6.50) with $8\sum'_{k,\alpha}$, where $\sum'_{k,\alpha}$ is understood to refer to a sum over $\boldsymbol{k}$ values in the shaded region of A.1 C. Note that contributions to the free energy from momentum points on the diagonal edge of the shaded region must be multiplied by one half to avoid double-counting.

Splitting the Hamiltonian into sectors: Aside from the sum over momentum, one of the slowest steps in the numerical calculation of (6.50) is the determination of the eigenvalues and eigenvectors of the 8×8 matrix H_k. Within the triplet-triplet model this step can be sped up by splitting the Hamiltonian $\mathcal{H}$ into the two spin sectors discussed in Section 6.1.1. From (6.24), we can write

$$\mathcal{H}^{\mathrm{MF}} = \frac{1}{2}\sum_{k} \Psi_k^\dagger H_k \Psi_k = \sum_{k} \Psi_k^{\uparrow\dagger} H_k^{\uparrow} \Psi_k^{\uparrow}, \tag{A.3}$$

where $H_k^{\uparrow}$ is a 4×4 matrix, and $\Psi_k^{\uparrow}$ is a 4×1 spinor. Because the eigenvalues of $H_k^{\uparrow}$ come in $\pm$ pairs (refer to Section 6.1.3), we are able to replace the eigenvalues in (6.50) with those of $H_k^{\uparrow}$, as long as we remember to multiply the result by two in order to account for the fact that we no longer have a factor of one half out the front in (A.3). Of course, this only applies to the summation term in (6.50), as K is *in addition* to (2.15). Unfortunately, when it comes to the singlet-triplet model the eigenvalues within a single spin sector do not come in $\pm$ pairs, so we cannot make use of this result because (6.50) was derived assuming this was the case.

The logarithm: As part of determining (6.50), the computer will have to calculate $\cosh(\beta E_{k\alpha}/2)$, which could cause issues for $E_{k\alpha} \gg k_B T$, because cosh grows exponentially. It is safer to use

$$\ln\left[2\cosh(\beta E_{k\alpha}/2)\right] = \ln\left[\mathrm{e}^{\beta E_{k\alpha}/2}\left(1+\mathrm{e}^{-\beta E_{k\alpha}}\right)\right] = \frac{\beta E_{k\alpha}}{2} + \ln\left[1+\mathrm{e}^{-\beta E_{k\alpha}}\right].$$

Intensive free energy: The free energy, F, is an extensive quantity, which is to say that it will increase with the number of lattice points, N_{lat}. It is more convenient to consider the specific free energy, $f = F/N_{\mathrm{lat}}$, which is an *intensive* quantity.

Pairing potential ansatz: In Section 6.1.3 we used a free energy argument in order to restrict the relative phase between the pairing channels. This considerably speeds up the numerical minimisation routine as it is being performed with respect to two parameters rather than four.

Interaction strengths: The interaction strengths, $\lambda_{\nu\nu'}$, are generally allowed to be complex-valued, although subject to $\lambda_{\nu\nu'} = \lambda^*_{\nu'\nu}$ (see (6.39)), which requires $\lambda_{\nu\nu} \equiv \lambda_\nu$ to be real-valued. In all the calculations I have additionally taken $\lambda_{\nu\nu'}$ to be real, which gives $\lambda_{\nu\nu'} = \lambda_{\nu'\nu}$.

Final expression: In summary, we can express the free energy in the triplet-triplet model as

$$f = -\frac{8}{N^2}\sum_{\boldsymbol{k}}{}' \sum_{\alpha} \left[E_{\boldsymbol{k}\alpha} + \frac{2}{\beta}\ln\left(1 + e^{-\beta E_{\boldsymbol{k}\alpha}}\right)\right] - \frac{1}{2}\left(\frac{\Delta_1^2}{\lambda_1} + \frac{\Delta_2^2}{\lambda_2} + \frac{\lambda_{12}}{\lambda_1\lambda_2}(\Delta_1\Delta_2 + \Delta_1\Delta_2)\right), \tag{A.4}$$

where $E_{\boldsymbol{k}\alpha}$ are understood to be the two positive eigenvalues of the 4×4 matrix $H^{\uparrow}_{\boldsymbol{k}}$ and $\sum'_{\boldsymbol{k}}$ refers to a sum over one eighth of the first Brillouin zone, as shown in Figure A.1 C. When it comes to the singlet-triplet model we must associate an additional factor of one half with the first term in (A.4), and understand $E_{\boldsymbol{k}\alpha}$ to be the four positive eigenvalues of the 8×8 matrix $H_{\boldsymbol{k}}$. This is the expression that I minimise numerically with respect to the amplitudes of the two pairing channels. While it would be fairly straightforward to express (A.4) directly in terms of $\Delta_{0,1}$ and $\Delta_{0,2}$ using (6.49), it is easier to instead minimise (A.4) in terms of the variational parameters Δ_1 and Δ_2, and calculate $\Delta_{0,1}$ and $\Delta_{0,2}$ at the end. When taking this approach we must express $E_{\boldsymbol{k}\alpha}$ in terms of Δ_1 and Δ_2, rather than directly in terms of $\Delta_{0,1}$ and $\Delta_{0,2}$, in order to be consistent. The minimisation is performed using a Nelder–Mead method, implemented in the `Optim.jl` package for Julia. Examples of the code used to calculate and minimise the free energy can be found in Appendices B.1 and B.2.

A.2 Calculating the Hall conductivity

The efficiency of the code when it comes to calculating the Hall conductivity can be improved in much the same ways as for the free energy. We can reduce the number of momentum values we need to sum over by exploiting the lattice symmetries in order to sum over only one eighth of the Brillouin zone. For both the triplet-triplet and the singlet-triplet models we can replace the BdG Hamiltonian with $H^{\uparrow}_{\boldsymbol{k}}$ by exploiting (A.3). The resulting expression is a modified version of (6.54):

$$\sigma_H(\omega) = \frac{2e^2}{iN\omega}\sum_{\boldsymbol{k}}{}' \sum_{\alpha,\alpha'} \left[\frac{\tanh\left(\frac{E_{\boldsymbol{k}\alpha}\beta}{2}\right) - \tanh\left(\frac{E_{\boldsymbol{k}\alpha'}\beta}{2}\right)}{E_{\boldsymbol{k}\alpha} - E_{\boldsymbol{k}\alpha'} + \omega + i0^+} \times \left(\langle \boldsymbol{k},\alpha|\, v^x_{\boldsymbol{k}}\, |\boldsymbol{k},\alpha'\rangle \langle \boldsymbol{k},\alpha'|\, v^y_{\boldsymbol{k}}\, |\boldsymbol{k},\alpha\rangle - \langle \boldsymbol{k},\alpha|\, v^y_{\boldsymbol{k}}\, |\boldsymbol{k},\alpha'\rangle \langle \boldsymbol{k},\alpha'|\, v^x_{\boldsymbol{k}}\, |\boldsymbol{k},\alpha\rangle\right)\right], \tag{A.5}$$

where $E_{\boldsymbol{k}\alpha}$ and $|\boldsymbol{k},\alpha\rangle$ are understood to be the eigenvalues and eigenstates of the 4×4 matrix $H^{\uparrow}_{\boldsymbol{k}}$, and $\tilde{\sum}_{\boldsymbol{k}}$ refers to a sum over one eighth of the first Brillouin zone, as shown in Figure A.1 C. The momentum sum speed up can also be applied to the approximate results, (6.57), (6.59), and (6.71). An example of the code used to calculate both the exact and approximate forms of the Hall conductivity can be found in Appendix B.3.

A.3 Numerical accuracy

When performing numerical calculations there are a number of errors which we would like to minimise. One source of error is that approximations must be made, such as being unable to take 0^+ to be truly infinitesimal (see discussion in Chapter 6), and being unable to take N to be infinite. Another source of error is introduced in the optimisation step used to minimise the free energy.

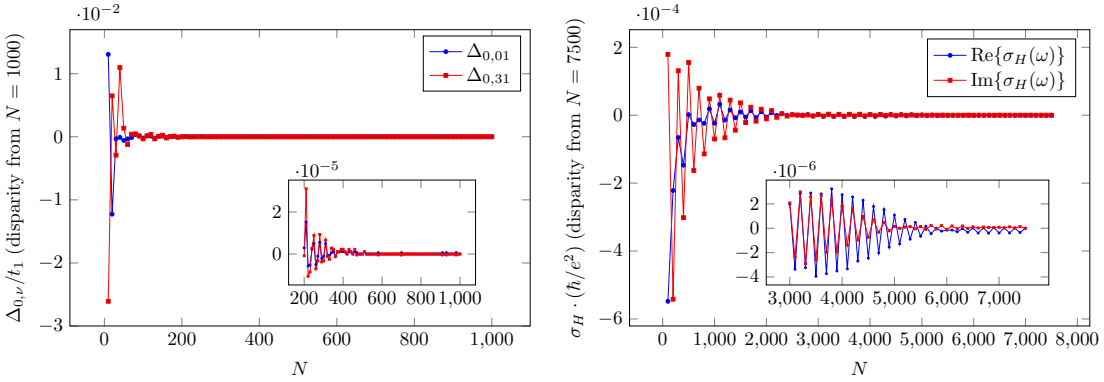

(A) Pairing potentials

(B) Hall conductivity

FIGURE A.2: The convergence of the pairing potential amplitudes with respect to N. The triplet-triplet pairing model discussed in Chapter 6 was used, taking $k_BT/t_1 = 0.01$, $\hbar\omega/t_1 = 0.6$, and $0^+ = 0.001$.

Numerical optimisation routines must decide on an some "convergence criterion". The pairing potentials that minimise the free energy can never be determined with absolute precision by a numerical algorithm. Instead, we must verify that the convergence criterion is small enough such that the error is negligible for our purposes.

Convergence with respect to N: In order to test for convergence, I calculated both the pairing potentials and the Hall conductivity using a range of values of N. For these calculations I used the triplet-triplet model with the first set of interaction strengths, and took $k_BT/t_1 = 0.01$, $\hbar\omega/t_1 = 0.6$, and $0^+ = 0.001$. For the pairing potentials I varied N between 50 and 1000. The results are shown in Figure A.2 A. For each value of N I plot the *disparity* between the calculation with that value of N from that calculated with $N = 1000$. This is not to presuppose that the $N = 1000$ calculation is correct, but allows us to see how this disparity decreases as N is increased. For the Hall conductivity I took N from 100 to 7500. The results are shown in A.2 B. Again, I plot the disparity of each calculation with respect to the $N = 7500$ calculation.

We observe that the pairing potentials are well converged by $N = 400$, and after $N = 500$ there is negligible improvement. Figure 6.2 indicates that the pairing amplitudes are on the order of 10^{-2}, which means that by $N = 500$ the error is well less than one in one hundred. The Hall conductivity does not converge as fast, although by $N = 5000$ the disparity is on the order of 10^{-6}. Figure 6.4 indicates that the Hall conductivity is on the order of 10^{-4} at $k_BT/t_1 = 0.01$ and $\hbar\omega/t_1 = 0.6$, which means that the error is also on the order of one in one hundred. For this reason, despite Figure A.2 B indicating that the Hall conductivity has not converged as far as it could have by $N = 5000$, I made the decision that this would be sufficient for our purposes. The error should not be enough to mask any qualitative features, although it probably explains the numerical artefacts at high frequencies in Figure 6.6 B for example.

It is worth noting that, for both the pairing amplitudes and the Hall conductivity calculations, the convergence with respect to N is dependent on the gap magnitudes. Smaller gap magnitudes require a larger value of N (i.e. a finer momentum resolution) to reach convergence. This is because of the $E_{k\alpha}$ eigenvalues, which appear in both (A.4) and (A.5). Convergence is reached when the energy difference between neighbouring momentum points is negligible compared to the gap magnitudes, which requires a finer resolution when these magnitudes are smaller. As noted in Chapter 6, the gap magnitudes used there correspond to a critical temperature approximately forty times larger than the experimentally observed value. If I had aimed for a more physical value

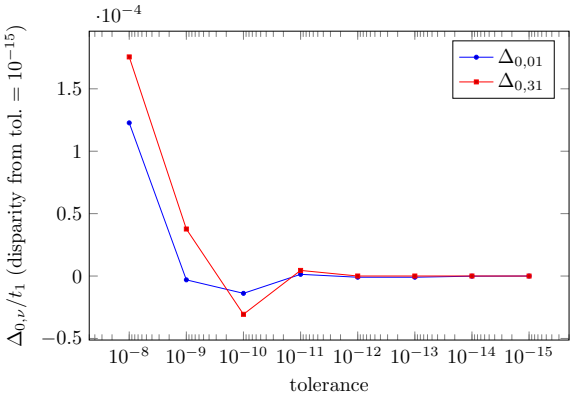

FIGURE A.3: The convergence of the pairing potential amplitudes with respect to the tolerance of the Nelder–Mead algorithm. The triplet-triplet pairing model discussed in Chapter 6 was used, taking $k_B T/t_1 = 0.01$.

(by reducing the interaction strengths) the corresponding gap magnitudes would then require a much finer momentum resolution. As noted in the text, the values I did use were still in the weak-coupling regime, so I did not feel that it was necessary to go to this additional effort.

Convergence criterion in the optimisation routine: The Nelder–Mead algorithm performs numerical optimisation of multi-dimensional functions using simplex optimisation. I will not go into the specifics of the convergence criterion it implements, although it can be found in the original paper [98]. The `Optim.jl` package alters the convergence criterion directly by setting the "tolerance", which is taken to be 10^{-8} by default. In order to see if this was sufficient I calculated the pairing potentials (again, for the triplet-triplet model with the first set of interaction strengths, and $k_B T/t_1 = 0.01$) for a range of tolerances between 10^{-8} and 10^{-15}. Figure A.3 plots the disparity of each calculation with respect to the tol. $= 10^{-15}$ calculation. We see that significant improvements can be made by decreasing the tolerance from 10^{-8}. By tol. $= 10^{-12}$ the result is essentially unaffected by any further decrease. For this reason I set the tolerance to be 10^{-12} in my calculations. I could have probably justified a larger tolerance, but each order of magnitude came with only a small increase in calculation time.

Appendix B

Code samples

This appendix provides examples of the code used for the numerical calculations in Chapter 6. Where the code is specific to an individual model the triplet-triplet model outlined in Section 6.1 is used. The code is written entirely in Julia, using the `LinearAlgebra.jl` and `Optim.jl` packages.

B.1 Calculating the free energy

The following function was used to convert between $\Delta_{0,1}, \Delta_{0,2}$ and Δ_1, Δ_2(refer to Section 6.2).

```
Δconversion(Δ0) = [Δ0[1] + Δ0[2]*λ[3]/λ[2], Δ0[2] + Δ0[1]*λ[3]/λ[1]]
```

When it came to calculating the free energy, the single-particle Hamiltonian was constructed in the spin-up sector and used to calculate the relevant eigenvalues. The form of the free energy as implemented in this code differs slightly from (6.50). See Appendix A.1 for an explanation of some of the techniques implemented here to speed up the calculation.

```
function f(Δ0)
  fsum = 0.0;
  for nx in N/2:N-1, ny in N/2:nx
        #calculate momentum values
        kx = (2*nx-N+1)*pi/N
        ky = (2*ny-N+1)*pi/N

        #don't double count diagonals of the B zone
        BZdiagonal = (nx == ny ? 0.5 : 1.0)

        #construct normal state Hamiltonian
        h00 = -t1*(cos(kx)+cos(ky)) - μ;
        h10 =2*t3*(sin(kx)*sin(ky));
        h30 = -t2*(cos(kx)-cos(ky));
        h23 = soc

        #construct pairing potential
        Δ01 = Δconversion(Δ0)[1]*(sin(kx)+im*sin(ky));
        Δ31 = Δconversion(Δ0)[2]*(sin(kx)-im*sin(ky));

        #explicitly construct one sector of HBdG
        Hbdg = [h00+h30 h10-im*h23 Δ01+Δ31 0;
```

```
                h10+im*h23 h00-h30 0 Δ01-Δ31;
                conj(Δ01)+conj(Δ31) 0 -h00-h30 -h10+im*h23;
                0 conj(Δ01)-conj(Δ31) -h10-im*h23 -h00+h30]

        #calculate eigenvalues of HBdG
        evals = eigvals(Hbdg)

        #sum over positive e-values (± is taken into account in the formula)
        for α in 3:4
          fsum += (evals[α]+(2/β)*log(1+exp(-β*evals[α])))*BZdiagonal
        end
  end
  return -8/(N^2)*fsum - 0.5*(Δ0[1]^2/λ[1] + Δ0[2]^2/λ[2] + λ[3]/
 ↪(λ[1]*λ[2])*2*Δ0[1]*Δ0[2])
end
```

Note: the `t1`, `t2`, `t3`, and `soc` parameters are defined in global scope; `soc` is referred to as λ in this thesis.

B.2 Minimising the free energy

The default Nelder-Mead algorithm as implemented by `Optim.jl` was used to minimise the free energy with respect to the pairing potential amplitudes. As discussed in Appendix A.3, the default tolerance was not found to be sufficient.

```
Δoptim(Δ0init,tol)  = optimize(f,Δ0init,Optim.Options(g_tol=tol)).minimizer
```

Note: the `tol` parameter is defined in global scope to be `10e-12`, as discussed in Appendix A.3.

The following code was used to calculate the pairing potentials as a function of temperature. The initial guess supplied to the optimisation algorithm was updated at each temperature. For this I supplied the "optimised" values from the previous temperature plus some noise. Updating the initial guess meant the optimisation could be more efficient, while the noise reduced the chance of getting stuck in a local minimum.

```
function Tsweep(T1,T2,NT,tol)
  Trange = range(T2,stop=T1,length=NT) #runs from high to low temperature
  Δ0init  = [0.0,0.0] #initial guess (is updated for each temperature)
  Δ0optims  = zeros(NT,2)

  for (i,T) in enumerate(Trange)
        global β = 1.0/T #global scope such that it can be accessed by f in optimize()
        Δ0optims[i,:]  = Δconversion(Δoptim(Δ0init,tol))
        Δ0init  = Δ0optims[i,:] .*(0.9.+rand(2)./10) #update initial guess (with noise)
  end
  return Trange, Δ0optims
end
```

B.3 Calculating the Hall conductivity

The following code sample shows how the Hall conductivity was calculated as a function of frequency, via explicit construction of the single-particle Hamiltonian in the spin-up sector. The approximate results are also calculated. As for the free energy, the form of the Hall conductivity implemented here differs slightly from (6.54). See Appendix A.2 for an explanation as to why. Analogous code was used to calculate the Hall conductivity as a function of temperature, but is not included here.

```
function σHω(;Nmax::Int, temp::Float64, ωmax::Int, deltaomega::Float64, zeroplus::
 ↪Float64)
  hall = zeros(ωmax) .+ 0im #the exact result
  approxhall  = zeros(ωmax) #the high-ω approximation
  approx2hall = zeros(ωmax) #the high-ω, small-Δ approximation

  temp = 1/β

  for nx in Nmax/2:Nmax-1
    for ny in Nmax/2:nx #sum over one eighth of B zone
          kx = (2*nx-Nmax+1)*pi/Nmax
          ky = (2*ny-Nmax+1)*pi/Nmax

          #don't double count diagonals of the B zone
          BZdiagonal = (nx == ny ? 0.5 : 1.0)

          #construct normal state Hamiltonian
          h00 = -t1*(cos(kx)+cos(ky)) - μ;
          h10 =2*t3*(sin(kx)*sin(ky));
          h30 = -t2*(cos(kx)-cos(ky));
          h23 = soc

          #calculate eigenvalues of normal state Hamiltonian
          Ea = h00+sqrt(h10^2+h30^2+h23^2)
          Eb = h00-sqrt(h10^2+h30^2+h23^2)

          #construct pairing potential
          Δ01 = Δ0[1]*(sin(kx)+im*sin(ky));
          Δ31 = Δ0[2]*(sin(kx)-im*sin(ky));

          #explicitly construct one sector of HBdG
          Hbdg = [h00+h30 h10-im*h23 Δ01+Δ31 0;
                  h10+im*h23 h00-h30 0 Δ01-Δ31;
                  conj(Δ01)+conj(Δ31) 0 -h00-h30 -h10+im*h23;
                  0 conj(Δ01)-conj(Δ31) -h10-im*h23 -h00+h30]

          #calculate eigenvectors and values of HBdG
          evecs = eigvecs(Hbdg)
          evals = eigvals(Hbdg)

          #construct velocity terms (vx5 and vy5 = 0)
```

```
        v00x =  t1*sin(kx);
        v00y =  t1*sin(ky);
        v10x =2*t3*cos(kx)*sin(ky);
        v10y =2*t3*sin(kx)*cos(ky);
        v30x =  t2*sin(kx);
        v30y = -t2*sin(ky);
        Vx = v00x*kron(σ0,σ0) + v10x*kron(σ0,σ1) + v30x*kron(σ0,σ3) #in one sector
        Vy = v00y*kron(σ0,σ0) + v10y*kron(σ0,σ1) + v30y*kron(σ0,σ3)

        Threads.@threads for iω in 1:ωmax

          ω = iω*deltaomega + im*zeroplus

          for hi in 1:4, hj in 1:4
            hall[iω] += (dot(evecs[:,hi],Vx*evecs[:,hj])*dot(evecs[:,hj],Vy*evecs[:,hi]) - dot(evecs[:,hi],Vy*evecs[:,hj])*dot(evecs[:,hj],Vx*evecs[:,hi])) *␣
↪(tanh(evals[hi]/(2*temp)) - tanh(evals[hj]/(2*temp)))/(real(ω)*(evals[hi] - evals[hj]␣
↪+ ω)) * BZdiagonal
          end #end hi, hj sum

          approxhall[iω]  += h10*(v10x*v30y-v10y*v30x)*imag(conj(Δ01)*Δ31) *␣
↪(tanh(evals[1]/(2*temp))/
↪((evals[1]-evals[2])*(evals[1]-evals[3])*(evals[1]-evals[4])) + tanh(evals[2]/
↪(2*temp))/((evals[2]-evals[1])*(evals[2]-evals[3])*(evals[2]-evals[4])) +␣
↪tanh(evals[3]/(2*temp))/((evals[3]-evals[1])*(evals[3]-evals[2])*(evals[3]-evals[4]))␣
↪+ tanh(evals[4]/(2*temp))/
↪((evals[4]-evals[1])*(evals[4]-evals[2])*(evals[4]-evals[3])))* BZdiagonal / real(ω)^2
          approx2hall[iω] +=␣
↪h10*(v10x*v30y-v10y*v30x)*imag(conj(Δ01)*Δ31)*(Ea*tanh(Eb/(2*temp))-Eb*tanh(Ea/
↪(2*temp)))/(Ea*Eb*(Ea^2-Eb^2)*real(ω)^2) * BZdiagonal;
        end #end ω loop
    end #end ny sum
  end #end nx sum

  return 8*2*hall/(8*im*Nmax^2),   #exact result (x8 for k sum, x2 for one sector)
    8*approxhall*(-8)/Nmax^2, #high-ω approximation (x8 for k sum)
    8*approx2hall*8/Nmax^2,   #high-ω, small-Δ approximation (x8 for k sum)
    (1:ωmax)*deltaomega      #the vector of frequencies
end
```

Note: the vector of optimised pairing potentials `Δ0` is defined in global scope. Additionally, the `σ0`, `σ1`, and `σ3` variables used in the definition of `Vx` and `Vy` are the relevant Pauli matrices.

Bibliography

[1] H. Kamerlingh Onnes, "Further experiments with liquid helium. C. On the change of electric resistance of pure metals at very low temperatures etc. IV. The resistance of pure mercury at helium temperatures", *Through Measurement to Knowledge*, ed. by Robert S. Cohen, Kostas Gavroglu, and Yorgos Goudaroulis, vol. 124, Series Title: Boston Studies in the Philosophy of Science, Dordrecht: Springer Netherlands, 1991, pp. 261–263, DOI: 10.1007/978-94-009-2079-8_15 (cit. on p. 1).

[2] B. T. Matthias, T. H. Geballe, and V. B. Compton, "Superconductivity", *Rev. Mod. Phys.* 35 (1 1963), pp. 1–22, DOI: 10.1103/RevModPhys.35.1 (cit. on p. 1).

[3] W. Meissner and R. Ochsenfeld, "Ein neuer Effekt bei Eintritt der Supraleitfähigkeit", *Naturwissenschaften* 21 (Nov. 1933), pp. 787–788, DOI: 10.1007/BF01504252 (cit. on p. 1).

[4] V. L. Ginzburg and L. D. Landau, "On the Theory of Superconductivity", *On Superconductivity and Superfluidity: A Scientific Autobiography*, ed. by Vitaly L. Ginzburg, Berlin, Heidelberg: Springer, 2009, pp. 113–137, DOI: 10.1007/978-3-540-68008-6_4 (cit. on p. 1).

[5] F. London, H. London, and Frederick Alexander Lindemann, "The electromagnetic equations of the supraconductor", *Proceedings of the Royal Society of London. Series A - Mathematical and Physical Sciences* 149 (Mar. 1935), Publisher: Royal Society, pp. 71–88, DOI: 10.1098/rspa.1935.0048 (cit. on p. 1).

[6] Leon N. Cooper, "Bound Electron Pairs in a Degenerate Fermi Gas", *Phys. Rev.* 104 (Nov. 1956), Publisher: American Physical Society, pp. 1189–1190, DOI: 10.1103/PhysRev.104.1189 (cit. on p. 1).

[7] J. Bardeen, L. N. Cooper, and J. R. Schrieffer, "Microscopic Theory of Superconductivity", *Phys. Rev.* 106 (Apr. 1957), Publisher: American Physical Society, pp. 162–164, DOI: 10.1103/PhysRev.106.162 (cit. on p. 1).

[8] J. Bardeen, L. N. Cooper, and J. R. Schrieffer, "Theory of Superconductivity", *Phys. Rev.* 108 (Dec. 1957), Publisher: American Physical Society, pp. 1175–1204, DOI: 10.1103/PhysRev.108.1175 (cit. on p. 1).

[9] James F. Annett, *Superconductivity, Superfluids and Condensates*, Oxford University Press, 2004 (cit. on pp. 1, 2, 12).

[10] F. Steglich, C. D. Bredl, W. Lieke, U. Rauchschwalbe, and G. Sparn, "Heavy fermion superconductivity", *Physica B+C* 126 (Nov. 1984), pp. 82–91, DOI: 10.1016/0378-4363(84)90148-7 (cit. on p. 2).

[11] G. R. Stewart, "Heavy-fermion systems", *Rev. Mod. Phys.* 56 (Oct. 1984), Publisher: American Physical Society, pp. 755–787, DOI: 10.1103/RevModPhys.56.755 (cit. on p. 2).

[12] T Kloss, X Montiel, V S de Carvalho, H Freire, and C Pépin, "Charge orders, magnetism and pairings in the cuprate superconductors", *Reports on Progress in Physics* 79 (2016), p. 084507, DOI: 10.1088/0034-4885/79/8/084507 (cit. on p. 2).

[13] N. P. Armitage, P. Fournier, and R. L. Greene, "Progress and perspectives on electron-doped cuprates", *Rev. Mod. Phys.* 82 (3 2010), pp. 2421–2487, DOI: 10.1103/RevModPhys.82.2421 (cit. on p. 2).

[14] G. R. Stewart, "Unconventional superconductivity", *Advances in Physics* 66 (2017), pp. 75–196, DOI: 10.1080/00018732.2017.1331615 (cit. on p. 2).

[15] B.D. White, J.D. Thompson, and M.B. Maple, "Unconventional superconductivity in heavy-fermion compounds", *Physica C: Superconductivity and its Applications* 514 (2015), Superconducting Materials: Conventional, Unconventional and Undetermined, pp. 246 –278, DOI: https://doi.org/10.1016/j.physc.2015.02.044 (cit. on p. 2).

[16] Robert Joynt and Louis Taillefer, "The superconducting phases of UPt_3", *Rev. Mod. Phys.* 74 (1 2002), pp. 235–294, DOI: 10.1103/RevModPhys.74.235 (cit. on p. 2).

[17] G. R. Stewart, "Superconductivity in iron compounds", *Rev. Mod. Phys.* 83 (4 2011), pp. 1589–1652, DOI: 10.1103/RevModPhys.83.1589 (cit. on p. 2).

[18] Qimiao Si, Rong Yu, and Elihu Abrahams, "High-temperature superconductivity in iron pnictides and chalcogenides", *Nature Reviews Materials* 1 (2016), p. 16017, DOI: https://doi.org/10.1038/natrevmats.2016.17 (cit. on p. 2).

[19] Wosnitza J., "Quasi-Two-Dimensional Organic Superconductors", *Journal of Low Temperature Physics* 146 (2007), pp. 641–667, DOI: https://doi.org/10.1007/s10909-006-9282-9 (cit. on p. 2).

[20] C. C. Tsuei and J. R. Kirtley, "Pairing symmetry in cuprate superconductors", *Rev. Mod. Phys.* 72 (4 2000), pp. 969–1016, DOI: 10.1103/RevModPhys.72.969 (cit. on p. 3).

[21] Guolin Yang and Kazumi Maki, "Impurity scattering in f-wave superconductor UPt_3", *Physica C: Superconductivity* 341-348 (Nov. 2000), pp. 1955–1956, DOI: 10.1016/S0921-4534(00)01421-0 (cit. on p. 3).

[22] Zhiqiang Wang, John Berlinsky, Gertrud Zwicknagl, and Catherine Kallin, "Intrinsic ac anomalous Hall effect of nonsymmorphic chiral superconductors with an application to UPt_3", *Phys. Rev. B* 96 (Nov. 2017), p. 174511, DOI: 10.1103/PhysRevB.96.174511 (cit. on pp. 3, 5, 48, 51, 74).

[23] Valdimir P. Mineev and Krill V. Samokhin, *Introduction to Unconventional Superconductivity*, Gordon and Breach, 1999 (cit. on pp. 3, 9, 11, 13, 31).

[24] S. Raghu, Xiao-Liang Qi, Chao-Xing Liu, D. J. Scalapino, and Shou-Cheng Zhang, "Minimal two-band model of the superconducting iron oxypnictides", *Phys. Rev. B* 77 (June 2008), p. 220503, DOI: 10.1103/PhysRevB.77.220503 (cit. on p. 3).

[25] Yi Gao, Wu-Pei Su, and Jian-Xin Zhu, "Interorbital pairing and its physical consequences for iron pnictide superconductors", *Phys. Rev. B* 81 (10 2010), p. 104504, DOI: 10.1103/PhysRevB.81.104504 (cit. on p. 3).

[26] Edward Taylor and Catherine Kallin, "Intrinsic Hall Effect in a Multiband Chiral Superconductor in the Absence of an External Magnetic Field", *Phys. Rev. Lett.* 108 (Apr. 2012), p. 157001, DOI: 10.1103/PhysRevLett.108.157001 (cit. on pp. 3, 5, 6, 27, 33, 48, 51, 54, 56, 65).

[27] P. M. R. Brydon, D. S. L. Abergel, D. F. Agterberg, and Victor M. Yakovenko, "Loop Currents and Anomalous Hall Effect from Time-Reversal Symmetry-Breaking Superconductivity on the Honeycomb Lattice", *Phys. Rev. X* 9 (Aug. 2019), p. 031025, DOI: 10.1103/PhysRevX.9.031025 (cit. on pp. 3, 5, 49, 51, 81).

[28] Jun Goryo, Yoshiki Imai, W. B. Rui, Manfred Sigrist, and Andreas P. Schnyder, "Surface magnetism in a chiral *d*-wave superconductor with hexagonal symmetry", *Phys. Rev. B* 96 (14 2017), p. 140502, DOI: 10.1103/PhysRevB.96.140502 (cit. on p. 3).

[29] Tomáš Bzdušek and Manfred Sigrist, "Robust doubly charged nodal lines and nodal surfaces in centrosymmetric systems", *Phys. Rev. B* 96 (15 2017), p. 155105, DOI: 10.1103/PhysRevB.96.155105 (cit. on p. 3).

[30] Youichi Yanase and Ken Shiozaki, "Möbius topological superconductivity in UPt_3", *Phys. Rev. B* 95 (22 2017), p. 224514, DOI: 10.1103/PhysRevB.95.224514 (cit. on p. 3).

[31] Aline Ramires and Manfred Sigrist, "Identifying detrimental effects for multiorbital superconductivity: Application to Sr_2RuO_4", *Phys. Rev. B* 94 (Sept. 2016), p. 104501, DOI: 10.1103/PhysRevB.94.104501 (cit. on pp. 3, 33, 37).

[32] Aline Ramires, Daniel F. Agterberg, and Manfred Sigrist, "Tailoring T_c by symmetry principles: The concept of superconducting fitness", *Phys. Rev. B* 98 (July 2018), p. 024501, DOI: 10.1103/PhysRevB.98.024501 (cit. on pp. 3, 33, 37, 50).

[33] J. J. Sakurai and Jim J. Napolitano, *Modern Quantum Mechanics*, 2 edition, Boston: Pearson, July 2010 (cit. on pp. 3, 34).

[34] Elio J. König and Alex Levchenko, "Kerr Effect from Diffractive Skew Scattering in Chiral $p_x \pm ip_y$ Superconductors", *Phys. Rev. Lett.* 118 (Jan. 2017), p. 027001, DOI: 10.1103/PhysRevLett.118.027001 (cit. on pp. 4, 5, 82).

[35] Andrew Peter Mackenzie and Yoshiteru Maeno, "The superconductivity of Sr_2RuO_4 and the physics of spin-triplet pairing", *Rev. Mod. Phys.* 75 (May 2003), pp. 657–712, DOI: 10.1103/RevModPhys.75.657 (cit. on pp. 4, 6, 7, 13).

[36] Manfred Sigrist and Kazuo Ueda, "Phenomenological theory of unconventional superconductivity", *Rev. Mod. Phys.* 63 (2 1991), pp. 239–311, DOI: 10.1103/RevModPhys.63.239 (cit. on pp. 4, 32, 64).

[37] Vyacheslav G. Storchak, Jess H. Brewer, and Stephen F.J. Cox, "Muonium formation via charge transport in solids and liquids", *Hyperfine Interactions* 105 (1997), pp. 189–201, DOI: https://doi.org/10.1023/A:1012643119286 (cit. on p. 4).

[38] G. M. Luke, Y. Fudamoto, K. M. Kojima, M. I. Larkin, J. Merrin, B. Nachumi, Y. J. Uemura, Y. Maeno, Z. Q. Mao, Y. Mori, H. Nakamura, and M. Sigrist, "Time-reversal symmetry-breaking superconductivity in Sr_2RuO_4", *Nature* 394 (Aug. 1998), Number: 6693 Publisher: Nature Publishing Group, pp. 558–561, DOI: 10.1038/29038 (cit. on pp. 4, 6).

[39] A. Bhattacharyya, D. T. Adroja, J. Quintanilla, A. D. Hillier, N. Kase, A. M. Strydom, and J. Akimitsu, "Broken time-reversal symmetry probed by muon spin relaxation in the caged type superconductor $Lu_5Rh_6Sn_{18}$", *Phys. Rev. B* 91 (6 2015), p. 060503, DOI: 10.1103/PhysRevB.91.060503 (cit. on p. 4).

[40] Aharon Kapitulnik, Jing Xia, Elizabeth Schemm, and Alexander Palevski, "Polar Kerr effect as probe for time-reversal symmetry breaking in unconventional superconductors", *New J. Phys.* 11 (May 2009), Publisher: IOP Publishing, p. 055060, DOI: 10.1088/1367-2630/11/5/055060 (cit. on pp. 4, 6).

[41] Petros N. Argyres, "Theory of the Faraday and Kerr Effects in Ferromagnetics", *Phys. Rev.* 97 (Jan. 1955), pp. 334–345, DOI: 10.1103/PhysRev.97.334 (cit. on p. 4).

[42] Catherine Kallin and John Berlinsky, "Chiral superconductors", *Rep. Prog. Phys.* 79 (May 2016), p. 054502, DOI: 10.1088/0034-4885/79/5/054502 (cit. on pp. 4–6, 31, 55).

[43] E. H. Hall, "On a New Action of the Magnet on Electric Currents", *American Journal of Mathematics* 2 (1879), pp. 287–292 (cit. on p. 5).

[44] Rahul Roy and Catherine Kallin, "Collective modes and electromagnetic response of a chiral superconductor", *Phys. Rev. B* 77 (May 2008), p. 174513, DOI: 10.1103/PhysRevB.77.174513 (cit. on p. 5).

[45] Jun Goryo, "Impurity-induced polar Kerr effect in a chiral p-wave superconductor", *Phys. Rev. B* 78 (Aug. 2008), p. 060501, DOI: 10.1103/PhysRevB.78.060501 (cit. on pp. 5, 82).

[46] Roman M. Lutchyn, Pavel Nagornykh, and Victor M. Yakovenko, "Frequency and temperature dependence of the anomalous ac Hall conductivity in a chiral $p_x + ip_y$ superconductor with impurities", *Phys. Rev. B* 80 (Sept. 2009), p. 104508, DOI: 10.1103/PhysRevB.80.104508 (cit. on pp. 5, 82).

[47] Songci Li, A. V. Andreev, and B. Z. Spivak, "Anomalous transport phenomena in $p_x + ip_y$ superconductors", *Phys. Rev. B* 92 (10 2015), p. 100506, DOI: 10.1103/PhysRevB.92.100506 (cit. on pp. 5, 82).

[48] Yu Li, Zhiqiang Wang, and Wen Huang, "Anomalous Hall effect in chiral superconductors from impurity superlattices", *arXiv e-prints* (Sept. 2019), arXiv:1909.08012 (cit. on pp. 5, 82).

[49] K. I. Wysokiński, James F. Annett, and B. L. Györffy, "Intrinsic Optical Dichroism in the Chiral Superconducting State of Sr_2RuO_4", *Phys. Rev. Lett.* 108 (Feb. 2012), p. 077004, DOI: 10.1103/PhysRevLett.108.077004 (cit. on pp. 5, 6, 51).

[50] Martin Gradhand, Karol I. Wysokinski, James F. Annett, and Balazs L. Györffy, "Kerr rotation in the unconventional superconductor Sr_2RuO_4", *Phys. Rev. B* 88 (9 2013), p. 094504, DOI: 10.1103/PhysRevB.88.094504 (cit. on pp. 5, 6, 51).

[51] Joshua Robbins, James F. Annett, and Martin Gradhand, "Effect of spin-orbit coupling on the polar Kerr effect in Sr_2RuO_4", *Phys. Rev. B* 96 (14 2017), p. 144503, DOI: 10.1103/PhysRevB.96.144503 (cit. on p. 5).

[52] Joynt Robert and Wu Wen-Chin, "Superconductivity in Empty Bands and Multiple Order Parameter Chirality", *Scientific Reports* 7 (2017), p. 12968, DOI: https://doi.org/10.1038/s41598-017-13426-9 (cit. on p. 5).

[53] N. E. Hussey, A. P. Mackenzie, J. R. Cooper, Y. Maeno, S. Nishizaki, and T. Fujita, "Normal-state magnetoresistance of Sr_2RuO_4", *Phys. Rev. B* 57 (Mar. 1998), Publisher: American Physical Society, pp. 5505–5511, DOI: 10.1103/PhysRevB.57.5505 (cit. on p. 6).

[54] C. N. Veenstra, Z.-H. Zhu, M. Raichle, B. M. Ludbrook, A. Nicolaou, B. Slomski, G. Landolt, S. Kittaka, Y. Maeno, J. H. Dil, I. S. Elfimov, M. W. Haverkort, and A. Damascelli, "Spin-Orbital Entanglement and the Breakdown of Singlets and Triplets in Sr_2RuO_4 Revealed by Spin- and Angle-Resolved Photoemission Spectroscopy", *Phys. Rev. Lett.* 112 (Mar. 2014), Publisher: American Physical Society, p. 127002, DOI: 10.1103/PhysRevLett.112.127002 (cit. on p. 6).

[55] A. Tamai, M. Zingl, E. Rozbicki, E. Cappelli, S. Riccò, A. de la Torre, S. McKeown Walker, F. Y. Bruno, P. D. C. King, W. Meevasana, M. Shi, M. Radović, N. C. Plumb, A. S. Gibbs, A. P. Mackenzie, C. Berthod, H. U. R. Strand, M. Kim, A. Georges, and F. Baumberger, "High-Resolution Photoemission on Sr_2RuO_4 Reveals Correlation-Enhanced Effective Spin-Orbit Coupling and Dominantly Local Self-Energies", *Phys. Rev. X* 9 (June 2019), Publisher: American Physical Society, p. 021048, DOI: 10.1103/PhysRevX.9.021048 (cit. on pp. 6, 27).

[56] Tamio Oguchi, "Electronic band structure of the superconductor Sr_2RuO_4", *Phys. Rev. B* 51 (Jan. 1995), Publisher: American Physical Society, pp. 1385–1388, DOI: 10.1103/PhysRevB.51.1385 (cit. on p. 6).

[57] Jing Xia, Yoshiteru Maeno, Peter T. Beyersdorf, M. M. Fejer, and Aharon Kapitulnik, "High Resolution Polar Kerr Effect Measurements of Sr_2RuO_4: Evidence for Broken Time-Reversal Symmetry in the Superconducting State", *Phys. Rev. Lett.* 97 (Oct. 2006), p. 167002, DOI: 10.1103/PhysRevLett.97.167002 (cit. on pp. 6, 7, 33, 69, 79, 81).

[58] A. P. Mackenzie, R. K. W. Haselwimmer, A. W. Tyler, G. G. Lonzarich, Y. Mori, S. Nishizaki, and Y. Maeno, "Extremely Strong Dependence of Superconductivity on Disorder in Sr_2RuO_4", *Phys. Rev. Lett.* 80 (Jan. 1998), Publisher: American Physical Society, pp. 161–164, DOI: 10.1103/PhysRevLett.80.161 (cit. on p. 6).

[59] Naoki Kikugawa, Andrew Peter Mackenzie, and Yoshiteru Maeno, "Effects of In-Plane Impurity Substitution in Sr_2RuO_4", *J. Phys. Soc. Jpn.* 72 (Feb. 2003), Publisher: The Physical Society of Japan, pp. 237–240, DOI: 10.1143/JPSJ.72.237 (cit. on p. 6).

[60] P. W. Anderson, "Theory of dirty superconductors", *Journal of Physics and Chemistry of Solids* 11 (Sept. 1959), pp. 26–30, DOI: 10.1016/0022-3697(59)90036-8 (cit. on p. 6).

[61] I. I. Mazin and David J. Singh, "Ferromagnetic Spin Fluctuation Induced Superconductivity in Sr_2RuO_4", *Phys. Rev. Lett.* 79 (4 1997), pp. 733–736, DOI: 10.1103/PhysRevLett.79.733 (cit. on p. 6).

[62] K. Miyake and O. Narikiyo, "Model for Unconventional Superconductivity of Sr_2RuO_4: Effect of Impurity Scattering on Time-Reversal Breaking Triplet Pairing with a Tiny Gap", *Phys. Rev. Lett.* 83 (7 1999), pp. 1423–1426, DOI: 10.1103/PhysRevLett.83.1423 (cit. on p. 6).

[63] M. Braden, W. Reichardt, S. Nishizaki, Y. Mori, and Y. Maeno, "Structural stability of Sr_2RuO_4", *Phys. Rev. B* 57 (2 1998), pp. 1236–1240, DOI: 10.1103/PhysRevB.57.1236 (cit. on p. 6).

[64] C. Lupien, W. A. MacFarlane, Cyril Proust, Louis Taillefer, Z. Q. Mao, and Y. Maeno, "Ultrasound Attenuation in Sr_2RuO_4: An Angle-Resolved Study of the Superconducting Gap Function", *Phys. Rev. Lett.* 86 (26 2001), pp. 5986–5989, DOI: 10.1103/PhysRevLett.86.5986 (cit. on p. 6).

[65] Sayak Ghosh, Arkady Shekhter, F. Jerzembeck, N. Kikugawa, Dmitry A. Sokolov, Manuel Brando, A. P. Mackenzie, Clifford W. Hicks, and B. J. Ramshaw, *Thermodynamic Evidence for a Two-Component Superconducting Order Parameter in Sr_2RuO_4*, 2020 (cit. on p. 6).

[66] Sarah B. Etter, Hirono Kaneyasu, Matthias Ossadnik, and Manfred Sigrist, "Limiting mechanism for critical current in topologically frustrated Josephson junctions", *Phys. Rev. B* 90 (July 2014), Publisher: American Physical Society, p. 024515, DOI: 10.1103/PhysRevB.90.024515 (cit. on p. 6).

[67] C. Kallin and A. J. Berlinsky, "Is Sr_2RuO_4 a chiral p-wave superconductor?", *J. Phys.: Condens. Matter* 21 (Mar. 2009), Publisher: IOP Publishing, p. 164210, DOI: 10.1088/0953-8984/21/16/164210 (cit. on p. 7).

[68] "Spin-triplet superconductivity in Sr_2RuO_4 identified by ^{17}O Knight shift", *Nature* 396 (1998), pp. 658–660, DOI: https://doi.org/10.1038/25315 (cit. on p. 7).

[69] J. A. Duffy, S. M. Hayden, Y. Maeno, Z. Mao, J. Kulda, and G. J. McIntyre, "Polarized-Neutron Scattering Study of the Cooper-Pair Moment in Sr_2RuO_4", *Phys. Rev. Lett.* 85 (25 2000), pp. 5412–5415, DOI: 10.1103/PhysRevLett.85.5412 (cit. on p. 7).

[70] K. Ishida, H. Mukuda, Y. Kitaoka, Z. Q. Mao, H. Fukazawa, and Y. Maeno, "Ru NMR probe of spin susceptibility in the superconducting state of Sr_2RuO_4", *Phys. Rev. B* 63 (6 2001), p. 060507, DOI: 10.1103/PhysRevB.63.060507 (cit. on p. 7).

[71] A. Pustogow, Yongkang Luo, A. Chronister, Y.-S. Su, D. A. Sokolov, F. Jerzembeck, A. P. Mackenzie, C. W. Hicks, N. Kikugawa, S. Raghu, E. D. Bauer, and S. E. Brown, "Constraints on the superconducting order parameter in Sr_2RuO_4 from oxygen-17 nuclear magnetic resonance", *Nature* 574 (Oct. 2019), Number: 7776 Publisher: Nature Publishing Group, pp. 72–75, DOI: 10.1038/s41586-019-1596-2 (cit. on p. 7).

[72] Kenji Ishida, Masahiro Manago, Katsuki Kinjo, and Yoshiteru Maeno, "Reduction of the ^{17}O Knight Shift in the Superconducting State and the Heat-up Effect by NMR Pulses on Sr_2RuO_4", *J. Phys. Soc. Jpn.* 89 (Mar. 2020), Publisher: The Physical Society of Japan, p. 034712, DOI: 10.7566/JPSJ.89.034712 (cit. on p. 7).

[73] Manfred Sigrist, "Introduction to Unconventional Superconductivity", *AIP Conference Proceedings* 789 (2005), 165–243, DOI: 10.1063/1.2080350 (cit. on pp. 9, 33).

[74] John N. Lalena, "From quartz to quasicrystals: probing nature's geometric patterns in crystalline substances", *Crystallography Reviews* 12 (Apr. 2006), Publisher: Taylor & Francis, pp. 125–180, DOI: 10.1080/08893110600838528 (cit. on p. 13).

[75] Tetsurō Inui, Yukito Tanabe, and Y. Onodera, *Group theory and its applications in physics*, 2d, corrected printing, with new exercises and 77 figures, Springer series in solid-state sciences, New York: Springer-Verlag, 1996 (cit. on p. 16).

[76] Richard P Feynman, Robert B Leighton, and Matthew Sands, *The Feynman lectures on physics Vol. 3, Vol. 3*, OCLC: 963647846, Reading, Mass.: Addison-Wesley, 1965 (cit. on p. 20).

[77] Han Gyeol Suh, Henri Menke, P. M. R. Brydon, Carsten Timm, Aline Ramires, and Daniel F. Agterberg, "Stabilizing even-parity chiral superconductivity in Sr_2RuO_4", *Phys. Rev. Research* 2 (3 2020), p. 032023, DOI: 10.1103/PhysRevResearch.2.032023 (cit. on pp. 27, 65, 75).

[78] Emil J. Rozbicki, James F. Annett, Jean-René Souquet, and Andrew P. Mackenzie, "Spin–orbit coupling and k-dependent Zeeman splitting in strontium ruthenate", *J. Phys.: Condens. Matter* 23 (Feb. 2011), Publisher: IOP Publishing, p. 094201, DOI: 10.1088/0953-8984/23/9/094201 (cit. on pp. 27, 33, 69, 79).

[79] M. W. Haverkort, I. S. Elfimov, L. H. Tjeng, G. A. Sawatzky, and A. Damascelli, "Strong Spin-Orbit Coupling Effects on the Fermi Surface of Sr_2RuO_4 and Sr_2RhO_4", *Phys. Rev. Lett.* 101 (July 2008), Publisher: American Physical Society, p. 026406, DOI: 10.1103/PhysRevLett.101.026406 (cit. on p. 27).

[80] Shunichiro Kittaka, Yusei Shimizu, Toshiro Sakakibara, Ai Nakamura, Dexin Li, Yoshiya Homma, Fuminori Honda, Dai Aoki, and Kazushige Machida, "Orientation of point nodes and nonunitary triplet pairing tuned by the easy-axis magnetization in UTe_2", *Phys. Rev. Research* 2 (3 2020), p. 032014, DOI: 10.1103/PhysRevResearch.2.032014 (cit. on p. 32).

[81] Andriy H. Nevidomskyy, "Stability of a Nonunitary Triplet Pairing on the Border of Magnetism in UTe_2", *arXiv e-prints* (Jan. 2020), arXiv:2001.02699 (cit. on p. 32).

[82] Manfred Sigrist and T. M. Rice, "Phenomenological theory of the superconductivity phase diagram of $U_{1-x}Th_xBe_{13}$", *Phys. Rev. B* 39 (4 1989), pp. 2200–2216, DOI: 10.1103/PhysRevB.39.2200 (cit. on p. 32).

[83] A. T. Rømer, D. D. Scherer, I. M. Eremin, P. J. Hirschfeld, and B. M. Andersen, "Knight Shift and Leading Superconducting Instability from Spin Fluctuations in Sr_2RuO_4", *Phys. Rev. Lett.* 123 (24 2019), p. 247001, DOI: 10.1103/PhysRevLett.123.247001 (cit. on pp. 32, 71).

[84] Steven Allan Kivelson, Andrew Chang Yuan, Brad Ramshaw, and Ronny Thomale, "A proposal for reconciling diverse experiments on the superconducting state in Sr_2RuO_4", *npj Quantum Materials* 5 (2020), p. 43, DOI: https://doi.org/10.1038/s41535-020-0245-1 (cit. on pp. 32, 71).

[85] R. Winkler and U. Zülicke, "Time reversal of pseudo-spin 1/2 degrees of freedom", *Phys. Lett. A* 374 (2010), pp. 4003 –4006, DOI: https://doi.org/10.1016/j.physleta.2010.08.008 (cit. on p. 34).

[86] Sungkit Yip, "Pseudospin bases for a model of Cu:Bi_2Se_3", *arXiv e-prints* (Sept. 2016), arXiv:1609.04152 (cit. on p. 34).

[87] Jörn W. F. Venderbos, Vladyslav Kozii, and Liang Fu, "Odd-parity superconductors with two-component order parameters: Nematic and chiral, full gap, and Majorana node", *Phys. Rev. B* 94 (18 2016), p. 180504, DOI: 10.1103/PhysRevB.94.180504 (cit. on p. 34).

[88] Gerald D. Mahan, *Many-Particle Physics*, 3rd ed., 1980 (cit. on pp. 43–45, 47).

[89] Henrik Bruus and Karsten Flensberg, *Many-Body Quantum Theory in Condensed Matter Physics*, Oxford University Press, 2004 (cit. on pp. 44, 47, 50).

[90] G. C. Wick, "The Evaluation of the Collision Matrix", *Phys. Rev.* 80 (Oct. 1950), Publisher: American Physical Society, pp. 268–272, DOI: 10.1103/PhysRev.80.268 (cit. on p. 45).

[91] Edward Taylor and Catherine Kallin, "Anomalous Hall conductivity of clean Sr_2RuO_4 at finite temperatures", *Journal of Physics: Conference Series* 449 (2013), p. 012036, DOI: 10.1088/1742-6596/449/1/012036 (cit. on pp. 51, 82).

[92] A. D. Hillier, J. Quintanilla, and R. Cywinski, "Evidence for Time-Reversal Symmetry Breaking in the Noncentrosymmetric Superconductor $LaNiC_2$", *Phys. Rev. Lett.* 102 (11 2009), p. 117007, DOI: 10.1103/PhysRevLett.102.117007 (cit. on pp. 55, 82).

[93] B. Sriram Shastry, Boris I. Shraiman, and Rajiv R. P. Singh, "Faraday rotation and the Hall constant in strongly correlated Fermi systems", *Phys. Rev. Lett.* 70 (Mar. 1993), pp. 2004–2007, DOI: 10.1103/PhysRevLett.70.2004 (cit. on pp. 56, 74).

[94] Ekkehard Lange and Gabriel Kotliar, "Magneto-optical Sum Rules Close to the Mott Transition", *Phys. Rev. Lett.* 82 (Feb. 1999), Publisher: American Physical Society, pp. 1317–1320, DOI: 10.1103/PhysRevLett.82.1317 (cit. on p. 56).

[95] S. Raghu, A. Kapitulnik, and S. A. Kivelson, "Hidden Quasi-One-Dimensional Superconductivity in Sr_2RuO_4", *Phys. Rev. Lett.* 105 (13 2010), p. 136401, DOI: 10.1103/PhysRevLett.105.136401 (cit. on p. 65).

[96] Oskar Vafek and Andrey V. Chubukov, "Hund Interaction, Spin-Orbit Coupling, and the Mechanism of Superconductivity in Strongly Hole-Doped Iron Pnictides", *Phys. Rev. Lett.* 118 (8 2017), p. 087003, DOI: 10.1103/PhysRevLett.118.087003 (cit. on p. 65).

[97] Henri Menke, "Superconductivity in strongly spin-orbit coupled systems", PhD thesis, University of Otago, 2020, (submitted) (cit. on pp. 65, 82).

[98] J. A. Nelder and R. Mead, "A Simplex Method for Function Minimization", *The Computer Journal* 7 (Jan. 1965), pp. 308–313, DOI: 10.1093/comjnl/7.4.308 (cit. on p. 87).